Organic and organometallic heterocyclic luminescent materials : towards OLED applications

Michaela Fecková

UNIVERSITÉ DE RENNES 1

UNIVERSITY OF PARDUBICE

THESE DE DOCTORAT DE

L'UNIVERSITE DE RENNES 1
ET UNIVERSITY OF PARDUBICE

ECOLE DOCTORALE N° 596
Matière, Molécules, Matériaux
Spécialité : *Chimie Moléculaire et Macromoléculaire*

Par
Michaela FECKOVÁ

Matériaux luminescents hétérocycliques organiques et organométalliques: vers des applications OLEDs

Thèse présentée et soutenue à Pardubice, le jeudi 17 juin 2021
Unité de recherche : Institut des Sciences Chimiques de Rennes – UMR CNRS 6226 – ISCR
Équipe : Organométalliques : Matériaux et Catalyse (OMC)
UFR Sciences et Propriétés de la Matière – Université de Rennes 1
Institute of Organic Chemistry and Technology,
Faculty of Chemical Technology – University of Pardubice

Rapporteurs avant soutenance :

Dr Julien Massue	CNRS researcher with habilitation, Université de Strasbourg
Dr Vítežslav Zima	Senior researchers with habilitation

Composition du Jury :

Président :	Prof Miroslav Lugwig	Vice-Rector, University of Pardubice
Examinateurs :	Dr Jeanne Crassous	CNRS Director of research, Université de Rennes 1
	Dr Christine Paul-Roth	Associate Professor, INSA de Rennes
	Dr Pavel Drabina	Associate Professor, University of Pardubice
	Dr Jean-Luc Fillaut	CNRS Director of research, Université de Rennes 1
	Dr Roman Jambor	Professor, University of Pardubice
	Dr Julien Massue	CNRS researcher with habilitation, Université de Strasbourg
	Dr Vítežslav Zima	Senior researchers with habilitation

Direction de la thèse :

Dir. de thèse :	Dr Sylvain Achelle	Associate Professor, Université de Rennes 1
	Prof Filip Bureš	Head of the department, University of Pardubice
Co-encadrant :	Dr Pascal le Poul	Associate Professor, Université de Rennes 1

ACKNOWLEDGEMENT

This thesis is a result of Cotutelle doctorate, collaboration of University of Rennes 1 (France) and University of Pardubice (Czech Republic), and work of many researchers. At this point, I would like to say a few words of thanks.

First and foremost, I would like to express my sincere gratitude to my patient and supportive supervisors, Assoc. Prof. Sylvain Achelle, Ph.D., Prof. Filip Bureš, Ph.D. and Assoc. Prof. Pascal le Poul, Ph.D., without whom I would not be able to complete this work. I am deeply grateful to S. Achelle for providing help not only on an academic but also on a personal level. I would also like to thank the other members of the French laboratory, Prof. Françoise Robin-le Guen, Ph.D., Assoc. Prof. Sébastien Gauthier, Ph.D., Assoc. Prof. Nolwenn Cabon, Ph.D., Raphaël Durand, Ph.D. and Mariia Hruzd, for their advice and ideas and for creating positive and friendly atmosphere in the lab.

In addition, I would like to thank all members of Bureš group for their help, optimistic and friendly attitude, namely, Jiří Tydlitát, Ph.D. for HR-MALDI-MS measurements, Milan Klikar, Ph.D. for DSC analysis and Patrik Pařík, Ph.D. for NMR measurements.

I would like to offer my special thanks to Thierry Roisnel, Ph.D. from Université de Rennes 1 for X-ray analysis, Assoc. Prof. Mihalis Fakis, Ph.D. and his research group from University of Patras (Greece) for fluorescence dynamics measurements, Julien Boixel, Ph.D. (Université de Rennes 1) for emission lifetime measurement, Dr. Jean-Pierre Malval and Dr. Arnaud Spangenberg, Université de Haute Alsace (France), for two-photon absorption measurement and Prof. Oldřich Pytela, DrSc. (University of Pardubice), Prof. Jean-Yves Saillard, Assoc. Prof. Samia Kahlal, Claudine Katan, Ph.D. and Assoc. Prof. Arnaud Fihey, Ph.D. (Université de Rennes 1) for theoretical calculations.

From the bottom of my heart I would like to thank my family, partner and friends for being an endless source of support and encouragement throughout my studies.

Last but not least, my great appreciation belongs to the Région Bretagne and University of Pardubice for founding this work.

RÉSUMÉ

« Matériaux luminescents hétérocycliques organiques et organométalliques: vers des applications OLEDs »

Ce manuscrit de cinq chapitres suivi d'une partie expérimentale décrit les résultats des travaux concernant des matériaux luminescents organiques et organométalliques à base de pyrimidine adaptés pour des applications potentielles dans le domaine de la technologie des diodes électroluminescentes organiques (OLEDs). Le premier chapitre a été consacré à la définition des concepts généraux et des termes, des quantités physiques et des phénomènes utilisés pour la description de la luminescence. Des relations structure-propriétés photophysiques des composés organiques ainsi que l'effet de facteurs environnementaux sur la luminescence ont également été discutés. La deuxième moitié du premier chapitre contient la description des semi-conducteurs organiques dans le contexte de la technologie OLED. La structure générale des dispositifs OLED, les principes de fonctionnement et les principales caractéristiques d'une OLED sont également inclus. En fin de compte, trois types d'OLED ont été distingués en fonction du mécanisme d'émission de photons.

Le deuxième chapitre débute par la description de l'hétérocycle pyrimidine et de son rôle dans les matériaux organiques. Par la suite, des chromophores fluorescents de type « push-pull » ont été présentés dans le contexte de l'influence des changements structurels sur leurs propriétés photophysiques. Un bref aperçu des principales voies réactionnelles pour la synthèse de chromophores à base de pyrimidine a conclu la première partie du deuxième chapitre. L'objectif principal de la deuxième partie est de présenter une large gamme d'applications des matériaux pyrimidiniques luminescents. Des sondes fluorescentes pour la détection de la polarité des solvants, la présence de cations métalliques, d'explosifs nitrés et pour la bioimagerie ont été présentées. Quelques exemples d'émission de lumière blanche par protonation partielle de chromophores pyrimidines ont également été inclus. Enfin, la fin du deuxième chapitre a été consacrée à l'utilisation de luminophores organiques et organométalliques pyrimidiniques dans les dispositifs OLED.

Les résultats de ce travail doctoral expérimental ont été résumés en trois chapitres, qui ont été organisés en fonction du motif structurel principal, et par conséquent des caractéristiques photophysiques différentes, de chaque série. L'organisation de chaque chapitre est similaire, la synthèse des molécules finales est tout d'abord décrite suivie des résultats des mesures thermiques DSC et de la description de structures cristallines. L'accent a été mis sur les

propriétés photophysiques des dérivés finaux et chaque chapitre s'est terminé par des résultats de calculs théoriques.

Le troisème chapitre concerne la synthèse et l'étude de fluorophore de type 4,6-di(arylvinyl)- et 2,4,6-tri(arylvinyl)pyrimidines (*Figure R1*).

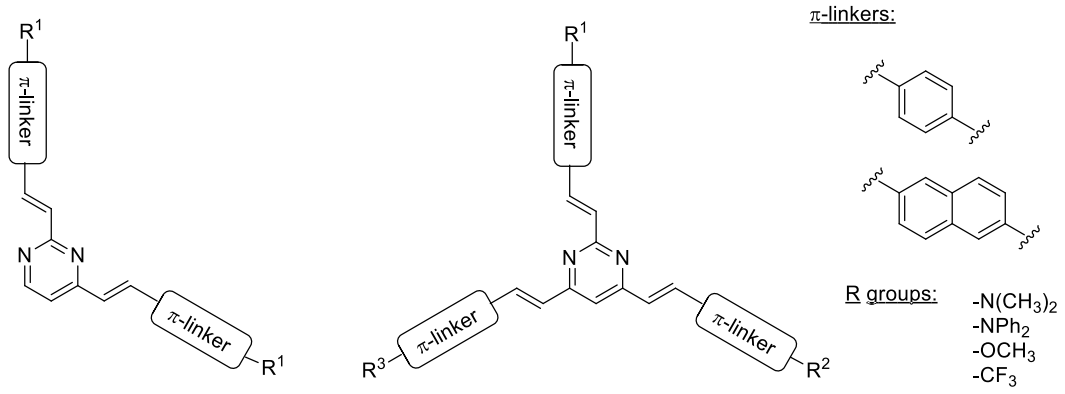

Figure R1. *Structure des 2,4-di(arylvinyl) et des 2,4,6-tri(arylvinyl)pyrimidine étudiées.*

Les 2,4-distyrylpyrimidines ont été synthétisées à partir de la 2-chloro-4-méthylpyrimidine en deux étapes. La première étape est un couplage de Suzuki-Miyaura en présence d'acide styrylboronique formé insitu à partir des alcynes correspondant. La deuxième étape est une condensation de Knoevenagel d'un aldehyde sur le groupement méthyle. Quatre chromophores de ce type ont été obtenus. Les 2,4,6-tristyrylpyrimidines ont été synthétisées à partir de la 2-chloro-4,6-diméthylpyrimidine ou de la 2,4-dichloro-6-méthylpyrimidine en deux ou trois étapes respectivement. Dans le premier cas, les chromophores sont obtenus par un couplage de Suzuki suivi d'une double condensation de Knoevenagel. Les substituants en C4 et C6 sont alors identiques. Dans le second cas, un monocouplage de Suzuki est réalisé régiosélectivement sur la position C4 de la pyrimidine, suivi d'un second couplage de Suzuki sur la position C2 de la pyrimidine et enfin une condensation de Knoevenagel d'un aldehyde peut être réalisée sur le méthyl en position C6 (*Schème R1*). Un total de 21 2,4,6-tristyrylpyrimidines ont ainsi été obtenues.

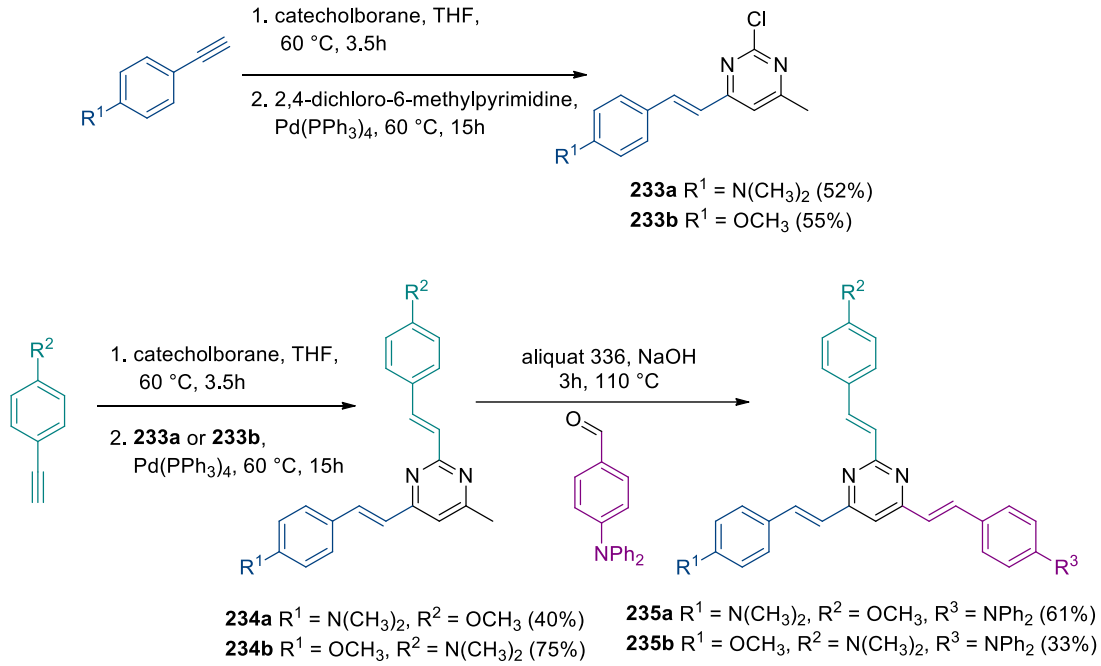

Schème R1. *Synthèse des 2,4,6-tristyrylpyrimidines* ***235***

Le cycle pyrimidine ne présente pas de symétrie C3 et de ce fait apporte des propriétés optiques intéressantes et peu communes par rapport aux chromophores tripodaux classiques avec une symétrie C3. Généralement, le comportement photophysique est donné par la nature des substituants périphériques attachés en position C4 / C6 de la pyrimidine. Cependant, lorsque le substituant C2 est un groupe électro-donneur plus fort que les substituants en position C4/ C6, le transfert de charge intramoléculaire est prédominant sur la branche en position C2 et dépend donc de celui-ci. Dans le dichlorométhane, des rendements quantiques de fluorescence modérés à élevés ont été observés pour les chromophores cibles. La solvatochromie d'émission des chromophores a été étudiée. Alors que l'augmentation de la polarité du solvant a un effet limité sur la position des maxima d'absorption, les bandes d'émission ont été décalées vers le rouge, une caractéristique typique d'un transfert de charge intramoléculaire. Les spectres d'émission du composé **232k** sont présentés sur la *Figure R2*. Dans le cas de solvant polaire, le transfert de charge intramoléculaire entre les unités electro-donneuses périphériques et le noyau pyrimidinique central augmente l'interaction dipôle-dipôle entre le chromophore et les molécules de solvant, ce qui entraîne une relaxation du solvant et une diminution de l'énergie de l'état excité.

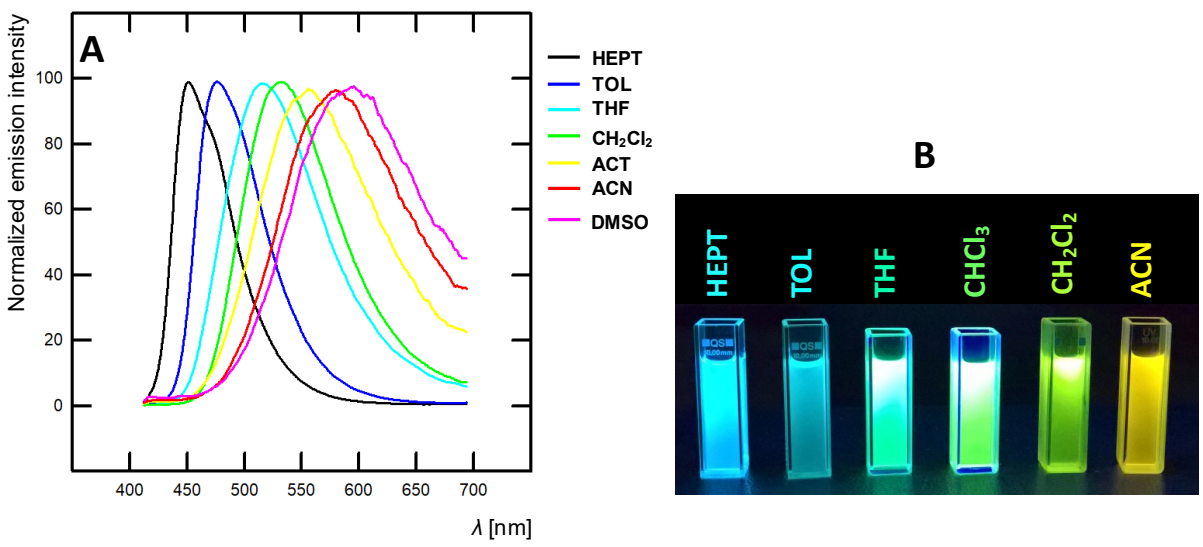

Figure R2. *(A) spectres d'émission normalisés du composé* ***232k*** *dans differents solvants. (B) Photographie du composé* ***232k*** *en solution dans différents solvants sous irradiation UV (lampe portable λ = 254 nm).*

Les propriétés d'absorption et d'émission ont été étudiées lors de l'ajout d'acide. Pour les dérivés amino-substitués, la protonation a conduit à une extinction spectaculaire de l'émission. Cependant, dans le cas des dérivés finaux avec des groupes méthoxy périphériques, la protonation a conduit à la formation d'une nouvelle bande d'émission décalée vers le rouge. Un exemple de modification du spectre d'émission lors de l'addition d'acide est présenté *Figure R3*.

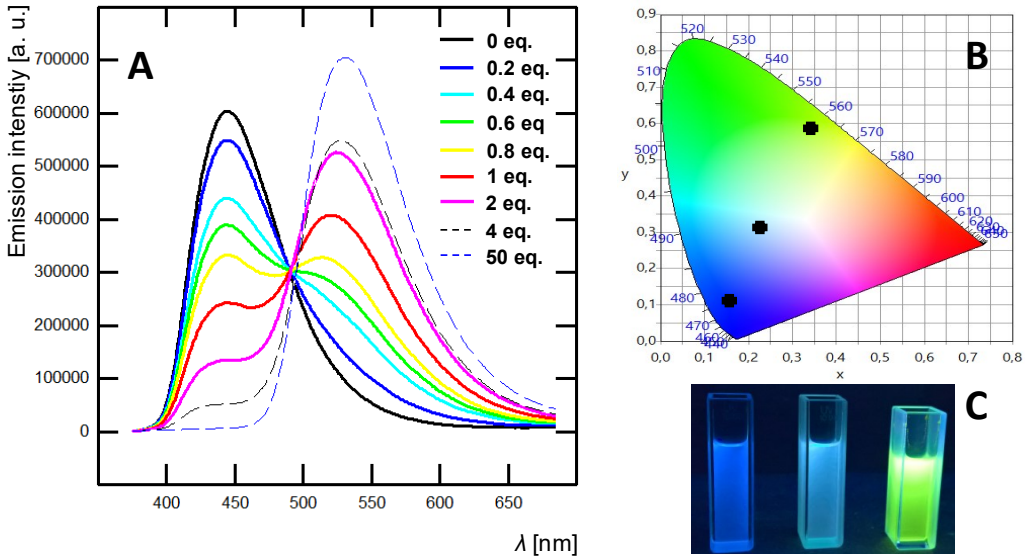

Figure R3. *(A) Spectre d'émission du composé* ***232q*** *après ajout progressif d'acide camphorsulphonique dans CH_2Cl_2 (λ(exc) = 380 nm). (B) 1931 diagramme des coordonnées chromatiques CIE des solutions de* ***232q*** *neutre, partiellement et complètement protonné dans CH_2Cl_2. (C) Photographie de solutions de* ***232q*** après ajout progressif d'acide *sous irradiation UV (lampe portable λ = 254 nm).*

Ce troisième chapitre se termine par la comparaison des propriétes photophysiques linéaires et non linéaires (absorption biphotonique) des styrylpyrimidines en fonction du nombre de branche. Par rapport à la grande majorité des systèmes tripodaux existants, les 2,4,6-tristyrylpyrimidines étudiées ici n'ont pas de symétrie C3. Pour cette raison, les spectres d'absorption mono et biphonotique des 4,6-distyrylpyrimidines et des 2,4,6-tristyrylpyrimidines sont similaires. Fait intéressant, alors que les spectres d'absorption à un photon des systèmes à une branche par rapport à ceux à deux ou trois branches sont décalés spectralement, il n'y a presque pas de décalage spectral dans la région spectrale principale 2PA. Une amélioration des réponses non linéaires est observée lorsque le nombre de branche est augmenté. Nous avons donc développé ici une stratégie qui améliore l'absorption biphotonique tout en maintenant la position spectrale. Plus précisément, des valeurs de section efficace d'absorption biphotonique atteignant 500 GM dans le dichlorométhane ont été obtenues pour le chromophore de structure A– (π – D)$_3$ avec trois groupements donneurs de type NPh_2 (*Figure R4*).

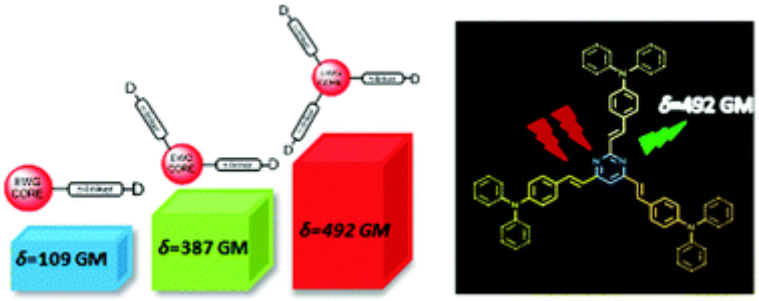

Figure R4. *Sections efficaces d'absorption biphotonique des N,N-diphénylaminostyrylpyrimidines en fonction du nombre de branche sur la pyrimidine.*

Dans le quatrième chapitre, une série de six nouveaux chromophores avec un hétérocycle pyrimidinique électro-attracteur comme unité centrale de retrait d'électrons a été préparée. Le groupement acridine a été connecté à la position pyrimidine C2 via un lien 1,4-phénylène et les positions C4 (C6) ont été étendues par un système conjugué arylvinyle avec des groupements électro-donneurs périphériques méthoxy ou diphénylamino (*Figure R5*). L'encombrement stérique du groupement acridine conduit à une géométrie twistée, comme le montre les structures par diffraction aux RX obtenues.

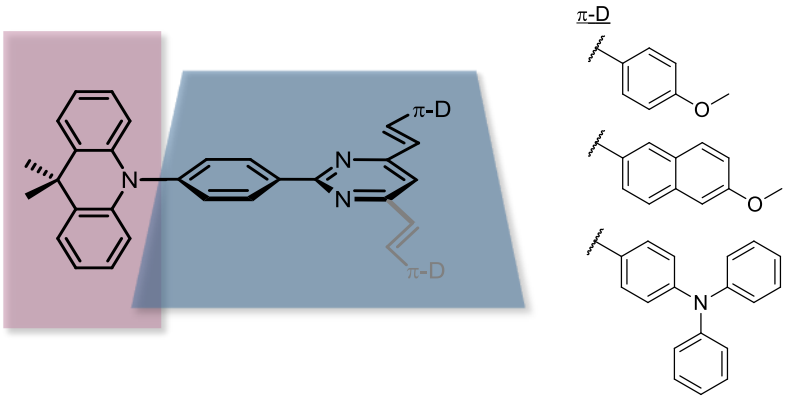

Figure R5. *Structure des chromophores étudiés*

La première étape de synthèse, permettant l'interconnexion des unités acridine et phénylène, s'est révélée difficile, même si les conditions de réaction appropriées ont été trouvées. Les dérivés finaux ont été obtenus par réaction Suzuki-Miyaura CC à partir des 2-chloro-4-méthyl et 2-chloro-4,6-diméthylpyrimidines et de l'ester boronique **238** suivie d'une réaction de Knoevenagel entre le(s) groupe(s) méthyle(s) de la pyrimidine et les benzaldéhydes correspondants avec des rendements satisfaisants (*Schème R2*).

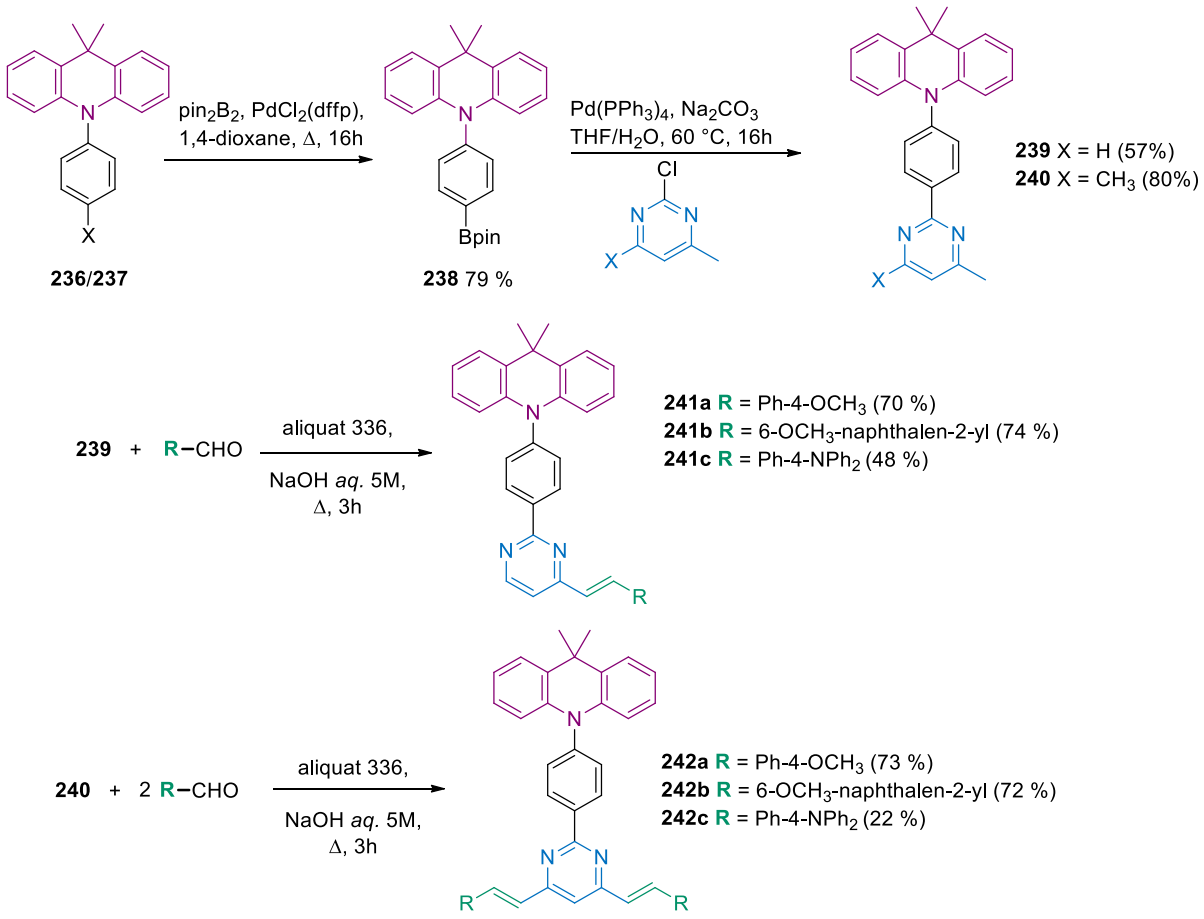

Schème R2. *Voie de synthèse des chromophores **241** and **242**.*

L'analyse DSC a montré que les unités donneuses d'électrons en position C4 / C6 n'affectaient que légèrement les propriétés thermiques, tandis que la présence de l'unité acridine entraînait une stabilité thermique élevée avec des températures de décomposition atteignant près de 400 ° C. Les structures cristallines obtenues par diffraction aux rayons X ont révélé une structure twistée avec des angles de torsion d'environ 85 ° entre le groupement acridine et le reste de la molécule et a également confirmé la configuration E des doubles liaisons C4 (C6).

Les résultats des mesures photophysiques ont montré des différences significatives dans le comportement photophysique des composés méthoxy (a et b) et diphénylamino (c). Une émission monobande, à la fois en solution et à l'état solide, un rendement quantique de fluorescence élevé dans CH_2Cl_2 et un solvatochromisme d'émission positif important ont été observés pour les dérivés de diphénylamino (*Figure R6*).

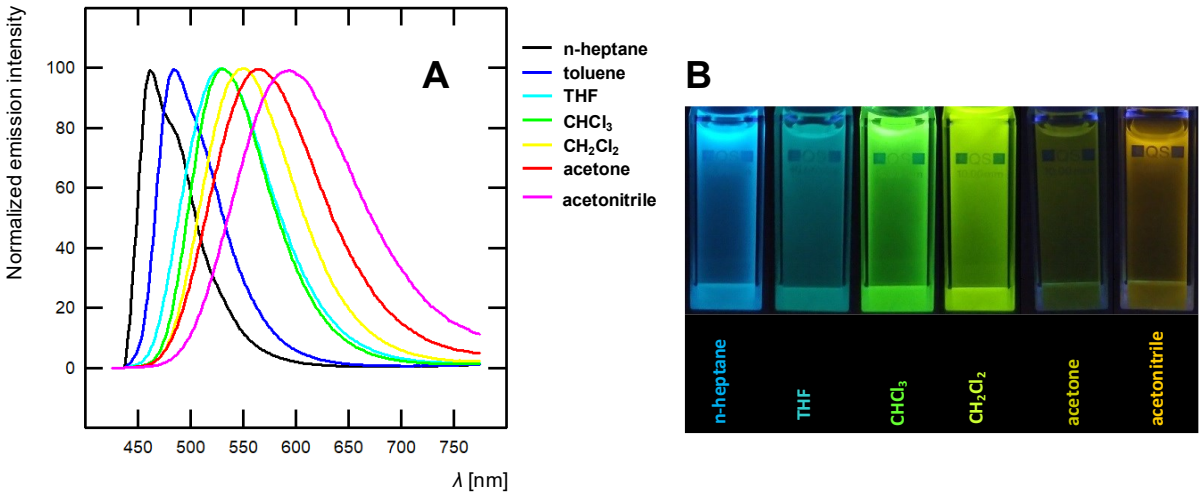

Figure R6. *A) Spectres d'émission normalisés du composé* ***242c*** *dans different solvants aprotiques, B) Photographie du composé* ***242c*** *en solution dans différents solvants sous irradiation UV (lampe portable λ = 254 nm).*

Les dérivés méthoxy présentent, quant à eux, une très faible fluorescence en solution dans CH_2Cl_2, augmentant dans le *n*-heptane non polaire et sensible à la présence d'oxygène. Les composés substitués par des groupements méthoxy présentent également une émission augmentant par agrégation (AIE) intense et une émission duale en solution de THF et à l'état solide (*Figure R7*).

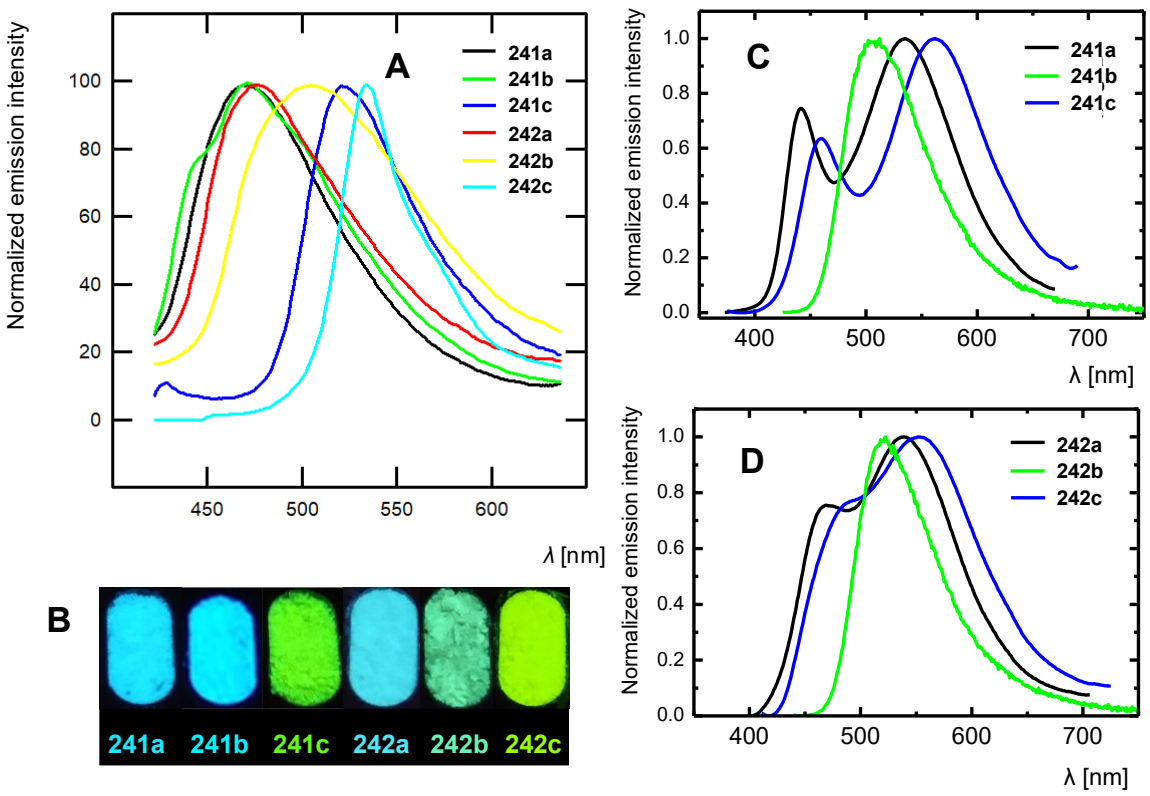

Figure R7. *(A) Spectres d'émission normalisés à l'état solide (poudre) des chromophores* ***241*** *et* ***242****. (B) Photographie des chromophores* ***241*** *et* ***242****. Sous irradiation UV (λ_{em} = 254 nm). Spectres d'émission des films fins des chromophores* ***241*** *(C) et* ***242*** *(D).*

La bande de longueur d'onde plus courte a été attribuée à l'émission de l'état LE et la bande de longueur d'onde plus longue a été attribuée à l'émission de l'état excité ICT / TICT avec une longue durée de vie. La couleur de la double émission dans les films minces est proche du blanc, ce qui fait de ces composés un matériau potentiel pour le développement de WOLED à émetteur unique. Le comportement TADF anticipé n'a pas été observé, probablement puisque la transition HOMO → LUMO ne possède aucune force d'oscillateur, néanmoins des propriétés photophysiques inattendues ont été obtenues pour les dérivés méthoxy (a et b). Le calcul DFT a montré que, bien que l'orbitale HOMO soit localisée sur l'unité acridine, elle était complètement isolé et n'affectait pas les propriétés d'absorption. Celles-ci sont uniquement affectées par les groupes donneurs d'électrons périphériques méthoxy ou diphénylamino portant l'orbitale HOMO–1.

Dans le chapitre 6, les travaux ont été orientés vers la chimie organométallique. Cinq nouveaux complexes de platine (II) cyclométallés à base de ligands phénylpyrimidine avec divers substituants ainsi que des ligands monodentates pyridine et chlore ont été préparés (*Figure R8*).

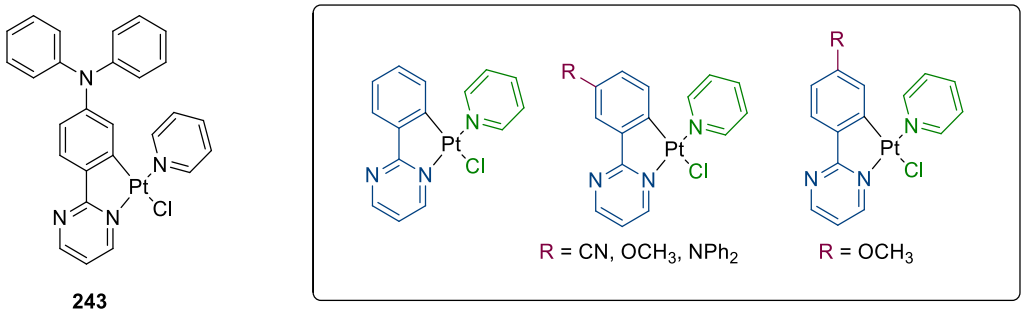

Figure R8. *Structures du complexe de référence* ***243*** *et des complexes* ***245*** *étudiés.*

Tous les complexes ont été obtenus avec des rendements modérés à bons. L'analyse par diffraction aux rayons X et les calculs DFT ont révélé une structure plan-carré de l'atome central de platine et une rotation possible de la pyridine le long de l'axe Pt-N. Cette rotation a conduit à une émission limitée en solution avec une amélioration spectaculaire de l'état solide, dans lequel la rotation est réduite. En ce qui concerne l'influence de la substitution, la présence d'un groupe donneur d'électrons en position conjuguée par rapport à l'atome de Pt entraîne une augmentation significative des rendements quantiques d'émission. Le rendement quantique dans le dichorométhane est de 0,4 pour le complexe **245c** avec un groupement méthoxy en position conjuguée par rapport au platine. Des durées de vie à l'état excité d'environ 10 µs et un déplacement bathochrome des spectres d'émission ont été enregistrés à l'état solide (*Figure R9*).

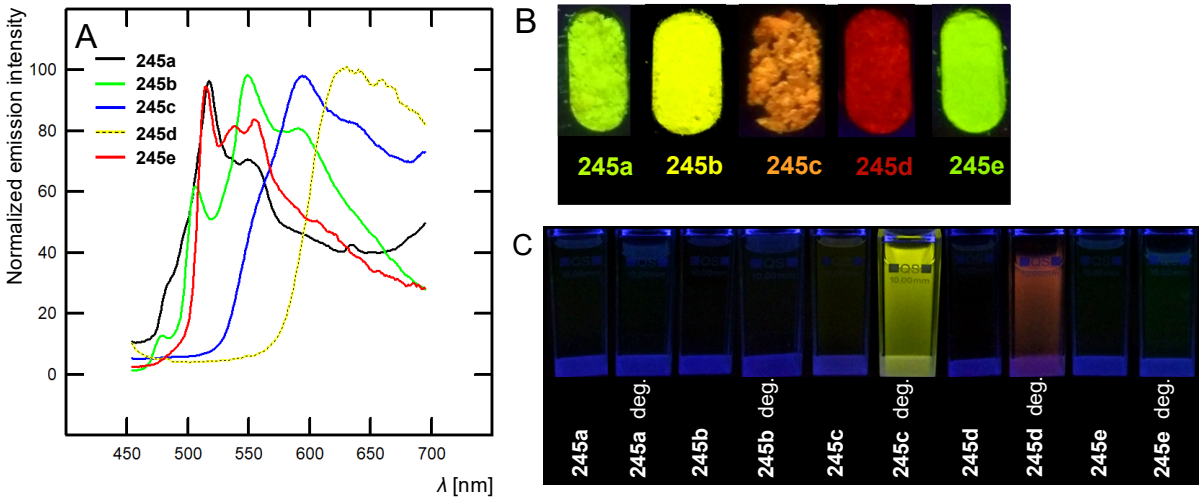

Figure R9. *(A) Spectres d'émission normalisés à l'état solide (poudres) des complexes* ***245****. Photographie (B) des poudres et (C) des solutions oxygénées et degasées dans le dichlorométhane des complexes* ***245*** *sous irradiation UV (*λ_{em} *= 254 nm).*

Une forte émission de ces complexes à l'état solide en fait des candidats prometteurs pour leur incorporation dans des dispositifs OLED.

TABLE OF CONTENT

LIST OF ABBREVIATION

1PA – one-photon absorption
1PE – one-photon excitation
2PA – two-photon absorption
2PE – two-photon excitation
acac – penta-2,4-dione
A – electron-acceptor
AcCz – 13,13-dimethyl-8-phenyl-8,13-dihydro-5*H*-indolo[3,2-*a*]acridinyl
AcDCz – 3,6-dicarbazole-9,9-dimethylacridinyl
ACN – acetonitrile
ACQ – aggregation-caused quenching
ACT – acetone
AIE – aggregation-induced emission
AH – adiabatic Hessian
B3LYP – Becke, 3-parameter, Lee-Yang-Parr exchange correlation functional
BFCz – benzofuro[3,2-*c*]carbazoyl
BLA – bond-length alternation
BTCz – benzothiopheno[3,2-c]carbazoyl
C-C – cross-coupling
CAM – Coulomb-attenuating method
CIE – Commission Internationale de l'Éclairage
Cz – carbazolyl
D – electron-donor
DCTB – *trans*-2-[3-(4-*tert*-butylphenyl)-2-methyl-2-propenylidene]malononitrile
DMAc – 9,9-dimethylacridinyl
DMSO – dimethyl sulfoxide
DNAN – 2,4-dinitroanisole
DPAc – 9,9-diphenylacridinyl
DPPICz1 – 12,12-dimethyl-11,12-dihydroindeno[2,1-*a*]carbazoyl
DPPICz2 – 11,11-dimethyl-5,11-dihydroindeno[1,2-*b*]carbazoyl
DSC – differential scanning calorimetry
EBL – electron-blocking layer
EGEE – 2-ethoxyethanol
EIL – electron-injection layer
EL – electroluminescence
EML – emitting layer
EQE – external quantum efficiency
ETL – electron-transport layer
EtOAc – ethyl acetate
fppr – 3,5-bis(trifluoromethyl)-2-(2′-pyridyl)pyrrole
fppz – 3-trifluoromethyl-5-(2-pyridyl)pyrazole
GM – Göppert-Mayer
HBL – hole-blocking layer
HEPT – *n*-heptane
HIL – hole-injection layer
HOMO – highest occupied molecular orbital
HR-MALDI-MS – high resolution-matrix-assisted laser desorption/ionization-mass spectrometry

HTL – hole-transport layer
IQE – internal quantum efficiency
IR (ATR) – infrared spectroscopy (attenuated total reflection)
ITO – indium tin oxide
IC – internal conversion
LE – locally excited (state)
LUMO – lowest unoccupied molecular orbital
MO-LCAO – molecular orbital – linear combination of atomic orbital
***n*-HEX** – *n*-hexane
NMR – nuclear magnetic resonance
OFET – organic field-effect transistor
(O)LED – (organic) light-emitting diode
OLET – organic light-emitting transistor
ORTEP – Oak Ridge Thermal Ellipsoid Plot
OTFT – organic thin-film transistor
PBE0 – Perdew-Burke-Ernzerhof/Hatree-Fock exchange energy correlation functional
PCM – polarizable continuum model
PhDEA – *N*,*N*-diethylaniline
PhDEEM– *N*,*N*-di(methoxyethoxyethyl)aniline
PhOLED – phosphorescent organic light-emitting diode
PhPrI – 2,6-diphenyl-4-benzylidene-4*H*-pyran
pic – 2-picolinic acid
PL – photoluminescence
pop – carbazolyl
ptzl – 1-pyridyl-3-trifluoromethyl-2,4,5-triazole
(R)ISC – (reverse) intersystem crossing
SpAc –spiro[acridine-9,9'-fluorene]
stpip – imidotetraphenyldithiodiphosphinic acid
TADF – thermally-activated delayed fluorescence
taz – 5-trifluoromethyl-3-(2′-pyridyl)-1,2,4-triazole
tBCz – 3,6-di(*tert*-butyl)-carbazoyl
TCSPC – time correlated single photon counting
(TD-)DFT – (time-dependent) density functional theory
TD-SCF – time-dependent self-consistent field
(T)ICT – (twisted) intramolecular charge transfer
THF – tetrahydrofuran
TOL – toluene
TPEF – two-photon excited fluorescence
tpip – imidotetraphenyldiphosphinic acid
WOLED – white organic light-emitting diode
XAc – spiro[acridan-9,9'-xanthene]

GENERAL INTRODUCTION

In the 1990s, especially in their late years, research of organic electronics started to growth exponentially.[1] Organic semiconductors, curtail part of organic electronics, were developed as an alternative to well-established silicon or gallium arsenide or metal-based inorganic semiconductors.[2] Mechanical properties such as high flexibility and toughness, fabrication at low temperature, in large areas and at low cost are among the main advantages of organic electronics.[3] These advantages and the fact that properties of organic material are easily tuneable by structural modifications largely contribute to the growth of organic electronics research and industry.

Examples of organic electronics are organic light-emitting diodes, which utilize luminescent organic or organometallic semiconductors to convert electrical power into the light.[4] Within a few decades, this technology has transformed from very simple single device, through small displays, into the extravagant light sources and large displays, which currently occupy a position among popular products in marketplace.[5–7] Even though these devices already reach a point of commercialisation, consumers' desire for better performance is a driving force for development of novel and improved materials.

This doctoral thesis consists of five main chapters. Chapter 1 focuses on theoretical background of luminescence, defines basic concepts and physical quantities. The second half of Chapter 1 briefly presents organic light-emitting diodes, their structure, working principles and their characterisation. Chapter 2 summarizes past and current development of pyrimidine-based luminescent materials, structure-luminescence relationships and their applications as fluorescent sensors and probes or semiconductors in organic light-emitting diodes. Chapters 3, 4 and 5 discuss three novel series of organic and organometallic luminophores with pyrimidine as an electron-withdrawing unit, their synthesis, thermal and photophysical properties. Besides experimental data, theoretical calculations are also provided to extend and support the discussion. Each series features different general structure, and consequently slightly different photophysical behaviour, and therefore the series are presented separately.

AIMS OF THE DISSERTATION

- Perform a literature search focusing on pyrimidine-based organic and organometallic luminophores and their applications in OLED devices.
- Synthesise novel luminophores with pyrimidine electron-withdrawing group and various electron-donating groups. Verify their structure and purity as well as all intermediates by standard analytical measurements.
- Elucidate structure-luminescence relationships based on experimental and theoretical photophysical data.

CHAPTER I. Luminescence and Organic Light Emitting Diodes

1.1 Luminescence

Luminescence is a term first introduced by German historian of science and physicist Eilhard E. G. Wiedemann in 1888 for description of "all those phenomena of light which are not solely conditioned by the rise in temperature".[8] The origin of the term *luminescence* comes from Latin (lumen = light), and nowadays is used to describe "spontaneous emission of infrared, visible or ultraviolet photons from an electronically or vibrationally excited material".[9] This term is also called a "cold light" for distinction from *incandescence* or "hot light" which refers to "an emission of visible light from material as a result of high temperature".

From ancient times, the humankind has been fascinated by the manifestations of luminescence. First documented mentions of fireflies, glow-worms, aurora polaris, luminous stones or sea light, can be found in sacred books of India and China, in the works of Aristotle and other philosophers (1500-100 B.C.).[10] Important milestones in the history of photoluminescence include research by physicists E. Becquerel and Sir G. G. Stoke, who independently published the statement that "wavelength of emitted light is always higher than that of absorbed light" and its mathematical description is still used today under the name *Stokes shift*.[11,12] In the same publication, Stoke also introduced the term of fluorescence *"I am almost inclined to coin a word, and call the appearance fluorescence, from fluorspar, as the analogous term opalescence is derived from the name of a mineral"*.[11] On the other hand, Becquerel had focused his later investigation more on phosphorescence and he carried out first time-resolved phosphorescence experiment on phosphoroscope on his own construction in 1858.[13] Last but not least, Aleksander Jabłoński, who is called the father of fluorescence spectroscopy, is probably the most known for his eponymous diagram. A description of concentration polarization and definition of the term fluorescence belongs among his achievements in the field of photoluminescence.[14]

Luminescence include dozens of subcategories that differ from each other in the way of inducing an excited state.[15] Examples of luminescence types and excitation modes are summarized in *Table 1*. For the purpose of this work, following chapter will only consider principles of photoluminescence (PL) and electroluminescence (EL).

Table 1. *Types of luminescence and their ways of excitation.*[16–26]

Types of luminescence	***Way of excitation***
Photoluminescence (fluorescence, phosphorescence, delayed fluorescence)	Absorption of UV-Vis radiation
Chemiluminescence	Chemical reaction
Bioluminescence	Chemical reaction in living entities
Thermoluminescence	Thermal activate ion recombination
Radioluminescence	Ionizing radiation
Crystalloluminescence	Crystallization
Electroluminescence	Electric field (injection of charge)
Cathodoluminescence	Electron beam
Mechanoluminescence	Mechanical force
Lyoluminescence	Dissolving of crystals
Sonoluminescence	Sound waves

1.1.1 Excited state

Outcomes of light-matter interaction depend on whether we consider matter as a bulk material or as a system of molecules or atoms.[27] Interaction of light with "bulk" matter results in (i) elastic light scattering from droplets, (ii) diffraction, (iii) reflection and (iv) refraction. From point of view of the influence of light on molecules (atoms), we distinguish (i) Raman or Rayleigh scattering and (ii) absorption of light energy. Subsequent processes of energy absorption are schematically summarized in *Figure 1* and those that include transition between electronic state will be discussed in the following paragraphs. For better understanding of their mutual relationship, it is necessary to consider a timescale in which they take place:

- absorption 10^{-15} s
- vibrational relaxation 10^{-13}–10^{-10} s
- internal conversion 10^{-11}–10^{-9} s
- fluorescence lifetime 10^{-10}–10^{-7} s
- intersystem crossing 10^{-10}–10^{-8} s
- phosphorescence lifetime 10^{-6}–10^{2} s.[28]

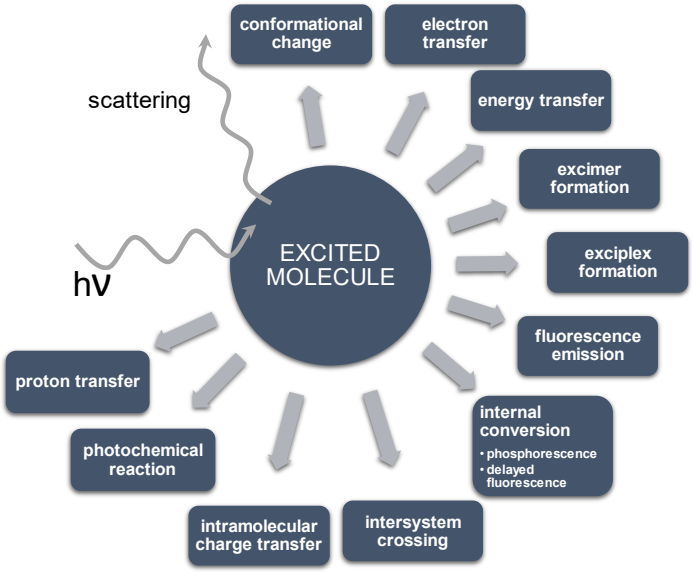

Figure 1. *Results of interaction between light and molecule.*

Figure 2 is a representation of Perrin-Jabłoński diagram, which is an energy diagram used for explanation of electronic transition within molecule during absorption of energy.[29] Energy raises from bottom to top and each column represents spin multiplicities. Bold grey horizontal lines are limits of electronic states that contain multiple vibrational (or vibronic) levels (pale grey horizontal lines). Multiple of rotational levels lie within each vibrational level, however they are not included in *Figure 2*.

As it was mentioned in previous paragraphs, photoluminescence occurs after the molecule absorbs ultraviolet or visible light (photon) and electron is promoted from a ground state orbital to an unoccupied orbital. Energy of an absorbed photon must match with energy difference between any vibronic level of ground electronic (S_0) and any vibronic level of excited electronic state (S_1, S_2…) for successful excitation of a molecule.[28] This case is called *one-photon excitation* (1PE) or *one-photon absorption* (1PA) and it is represented in Jabłoński diagram by green arrows (*Figure 2*).

Besides 1PE, promotion of molecule to the excited state is also possible by simultaneous absorption of multiple photons whose energy sum is sufficient for transition between ground and excited states.[30] The most common multi-photon excitation is *two-photon excitation* or *two-photon absorption* (2PE, 2PA, *Figure 2* orange arrow). Probability of 2PA is low, therefore use of a high light irradiation by laser is necessary.[31] Further details concerning 2PA will be discussed in *Chapter 1.1.4*.

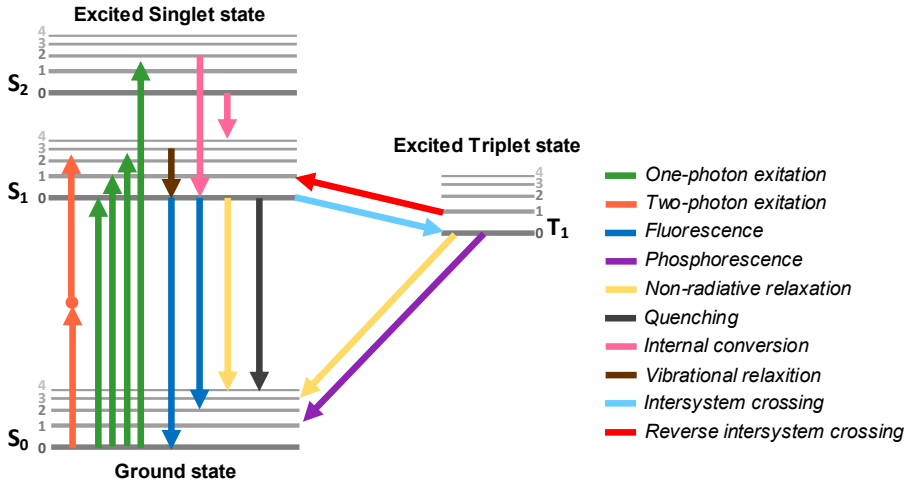

Figure 2. *Perrin-Jabłoński diagram.*

In solution, if the molecule is excited to upper vibrational level of higher S level, the molecule can rapidly lose any excess energy during collision with other molecule and diminish to the zero vibrational level of the same excited state.[32] This transition is called *vibrational relaxation* (*Figure 2* brown arrow). Molecule can also decrease its energy by relaxation from higher excited to the lower excited state with the same multiplicity. In this case it is *internal conversion* (*IC*, *Figure 2* pink arrows). Both processes are rapid and effective and in solution mostly take place before luminescence, which then starts from the lowest vibrational level of S_1.

Radiative relaxation from upper S exited levels, in most cases from S_1, to ground S_0 is called *fluorescence* (*Figure 2* blue arrows).[30] Photon with energy corresponding to the difference of electronics level is released with the same speed as absorption. Fluorescence is usually spontaneous, but it can be also trigger by e.g. dye laser. Competitive processes for fluorescence are *non-radiative deexcitation* or *quenching* (*Figure 2* yellow and black arrows), both are relaxation processes without light emission.

So far, all the transitions involve passage through state without change of an electron spin. These movements are spin-allowed and result in systems with antiparallel spins. Another possible transition from S_1 is *intersystem crossing (ISC),* which leads to triplet excited state T_1 (*Figure 2* pale blue arrow).[33] This happens with change of spin and final systems have parallel electron spins. This type of crossing is in principle spin-forbidden, but it is possible due to the spin-orbital coupling. Names singlet and triplet are based on multiplicities of electrons in ground and excited state from equation $M = 2S + 1$, where S is quantum number. This number is an absolute value a sum of spins, thus for singlet state ($s_i = -½$ and $s_i = +½$) is equal to zero

and for triplet state ($2 \times s_i = +½$ or $2 \times s_i = –½$) is equal to 1. Therefore, the multiplicity of singlet state is M = 1 and triplet state M = 3, three states with equal energy.

After intersystem crossing, molecule rapidly relax to the lowest vibrational level of T_1 and from this point, molecule may undergo radiative or non-radiative deexcitation to the S_0 ground state or go back to the excited singlet state.[34] Radiative deexcitation is called *phosphorescence* and it is possible even though is spin-forbidden transition (*Figure 2* purple arrow). When the T_1 and S_1 are energetically close, retrograde conversion, also known as *reverse intersystem crossing (RISC)*, can occur (*Figure 2* red arrow). Molecule is back in the singlet state and all previously mention processes are possible. When fluorescence occurs after reverse intersystem crossing this type of emission is called *delayed fluorescence*.

1.1.2 Characteristics of absorption and emission

Determination of absorption properties of an investigated molecule is first and crucial step in order to study molecular luminescence. Ultraviolet-visible (UV-Vis) absorption is defined as a transfer of energy to a molecular entity from electromagnetic field with range of wavelength between 190 and 800 nm.[35,36] Physical quantity of absorption is *absorbance (A)*, which is equal to a negative decadic logarithm of *transmittance (T)* according to *Equation 1*:

$$A = -\log T = \log\frac{P_0}{P} \tag{1}$$

where:

- P_0 … incident spectral radiant power [W nm^{-1}]
- P … transmitted spectral radiant power [W nm^{-1}].

For diluted solutions, absorbance of a sample is linearly related to concentration and absorption path length and obeys the *Beer-Lambert Law* given in *Equation 2*:

$$A(\lambda) = \varepsilon(\lambda)cl \tag{2}$$

where:

- $\varepsilon(\lambda)$ … molar (decadic) absorption coefficient [dm^3 mol^{-1} cm^{-1}]
- c … concentration [mol dm^{-3}]
- l … absorption pathlength [cm].

Division of absorbance by absorption path length gives *absorption coefficient* which can be *decadic* $a(\lambda)$ or *Napierian* $\alpha(\lambda)$ as described by *Equations 3* and *4*, respectively.

$$a(\lambda) = \frac{A(\lambda)}{l} = \left(\frac{1}{l}\right)\log\left(\frac{P_0}{P}\right) \tag{3}$$

$$\alpha(\lambda) = a(\lambda) \ln 10 = \left(\frac{1}{l}\right) \ln\left(\frac{P_0}{P}\right) \tag{4}$$

Photon-capture area of molecule, so-called *absorption cross-section* (given in *Equation 5*), is derived from Napierian absorption coefficient, divided by number of molecules in a volume of absorbing medium along a light path (C):

$$\sigma(\lambda) = \frac{a(\lambda)}{C} = \left(\frac{1}{Cl}\right) \ln\left(\frac{P_0}{P}\right) \tag{5}$$

Unit of the absorption cross-section varies depending on the number of simultaneously absorbed photons, for 1PE is cm^2 and for 2PE is given in [GM] (Göppert-Mayer), where 1 GM = 10^{-50} cm^4 s/photon.[30] In 2PE, a simultaneous interaction of two photons with a molecule is required, therefore the probability of 2PA is proportional to square of the intensity. Considering this, the unit of 2PE cross-section can be explained by a simple deliberation. The number of photons per second for 1PA is given in *Equation 6*:

$$NA_{1\mathrm{PE}} = \sigma_{1\mathrm{PE}} I \tag{6}$$

where:

- $NA_{1\mathrm{PE}}$ … [photon/s]
- $\sigma_{1\mathrm{PE}}$ … [cm^2]
- I … [photon/cm^2 s]

Similar equation can be drawn for 2PE with square of the intensity (*Equation 7*):

$$NA_{2\mathrm{PE}} = \sigma_{2\mathrm{PE}} I^2 \tag{7}$$

and if:

- $NA_{2\mathrm{PE}}$ … [photon/s]
- I … [photon/cm^2 s]

then unit of $\sigma_{2\mathrm{PE}}$ must be [cm^4 s/photon]. Similar deduction can be made for absorption cross-section of three- and higher-photon techniques.

For understanding of a relationship between the luminescence characteristics (lifetime, quantum yield etc.) is necessary to define rate constants of various processes as shown in *Figure 3*:

- k_{A} … rate constant of absorption,
- $k_{\mathrm{R}}(S)$ … rate constant for fluorescence (radiative transition $S_1 \rightarrow S_0$),
- $k_{\mathrm{IC}}(S)$ … internal conversion $S_1 \rightarrow S_0$ rate constant,
- k_{ISC} … rate constant of intersystem crossing $S_1 \rightarrow T_1$,
- $k_{\mathrm{NR}}(S)$ … rate constant for non-radiative deactivation; $k_{\mathrm{NR}}(S) = k_{\mathrm{IC}}(S) + k_{\mathrm{ISC}}(S)$,
- $k_{\mathrm{R}}(T)$ … rate constant for phosphorescence (radiative transition $T_1 \rightarrow S_0$),

- $k_{\mathrm{NR}}(T)$ … rate constant for non-radiative deactivation $T_1 \rightarrow S_0$.[33]

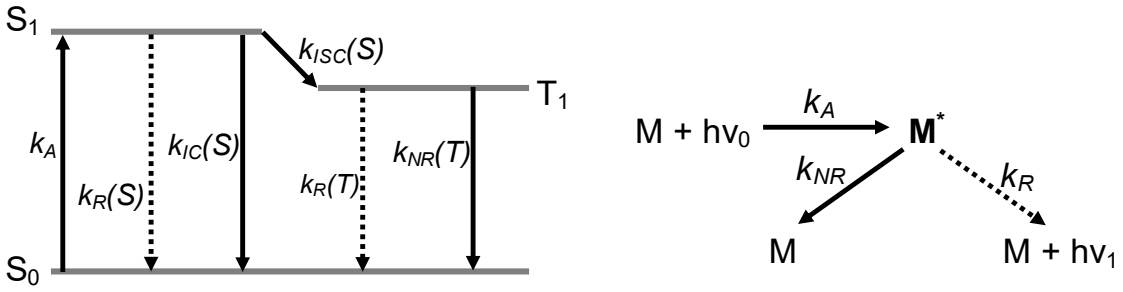

Figure 3. *Scheme of rate constants for various electronic transition.*

After excitation of a diluted solution of studied molecules M with very short pulse of light, excited molecules with initial concentration $[M^*]_0$ return to the ground state by radiative or non-radiative deexcitation or undergo intersystem crossing. These processes can be mathematically described by differential kinetics *Equation 8*:

$$-\frac{d[M^*]}{dt} = (k_{\mathrm{R}}(S) + k_{\mathrm{NR}}(S))[M^*] \tag{8}$$

After integration we get *Equation 9*:

$$[M^*] = [M^*]_0 exp\left(-\frac{1}{\tau_{\mathrm{S}}}\right) \tag{9}$$

where τ_{S} is a *lifetime of S_1 excited state* and is equal to reciprocal sum of rate constant of radiative and nonradiative deexcitation to the S_0 ground state by *Equation 10.*

$$\tau_{\mathrm{S}} = \frac{1}{k_{\mathrm{R}}(S) + k_{\mathrm{NR}}(S)} \tag{10}$$

The *lifetime of T_1 state* can be described in a similar manner (*Equation 11*). Both lifetimes are essential for dynamic measurements because they define the experimental window for measuring.

$$\tau_{\mathrm{T}} = \frac{1}{k_{\mathrm{R}}(T) + k_{\mathrm{NR}}(T)} \tag{11}$$

A ratio between molecules returning to the ground state with fluorescence emission and all excited molecules gives *fluorescence quantum yield* Φ_{F} (*Equation 12*).

$$\Phi_{\mathrm{F}} = \frac{k_{\mathrm{R}}(S)}{k_{\mathrm{R}}(S) + k_{\mathrm{NR}}(S)} = k_{\mathrm{R}}(S)\tau_{\mathrm{S}} \tag{12}$$

Phosphorescent quantum yield Φ_{P} is given in *Equation 13*:

$$\Phi_{\mathrm{F}} = \frac{k_{\mathrm{R}}(T)}{k_{\mathrm{R}}(T) + k_{\mathrm{NR}}(T)}\Phi_{\mathrm{ISC}} \tag{13}$$

where Φ_{ISC} is quantum yield of the intersystem crossing and is defined in *Equation 14*.

$$\Phi_{\mathrm{ISC}} = \frac{k_{\mathrm{ISC}}}{k_{\mathrm{R}}(S) + k_{\mathrm{NR}}(S)} = k_{\mathrm{ISC}}\tau_{\mathrm{S}} \tag{14}$$

So far, we have not considered deexcitation of excited molecule by an interaction with other molecules. These bimolecular processes compete with radiative relaxation of excited molecule and can decrease the PL intensity or its quantum yield. We distinguish two types of quenching mechanism: (i) static quenching, which inhibits creation of the excited state and (ii) dynamic quenching which interferes the excited state nature after its formation.[37,38] Examples of known ways of PL quenching includes collision between examined excited molecule and:

- heavy metals (e.g. Hg^{2+}, Co^{2+})
- paramagnetic species (e.g. O_2 or NO)
- identical molecule resulting in creation of *excimer* (excited state dimers)
- different molecule resulting in creation of *exciplex* (excited state complexes)
- another molecule with simultaneous *electron transfer* leading to creation of radical anion and radical cation
- another molecule with simultaneous *proton transfer*
- different molecule with simultaneous *energy transfer*.

During the years of atomic and molecular spectroscopy research scientists invented multiple rules and principles for description of electrons transition between energetic states, and therefore for explanation of spectrum characteristics. First of them are *selection rules* which determine allowed and forbidden electron transition from the perspective of symmetry or spins in initial and final states.[37,39] Spin-forbidden are transition between states with different multiplicities. Exceptions are possible due to the already mentioned spin-orbit coupling – interaction of magnetic moments of electron orbital motions and electron spin. Symmetry-forbidden transitions, according to a Laporte rule, are transitions without change in parity for molecule with inversion centre. Violation of this rule is caused by a vibronic coupling – interaction between electronic and vibrational motions in a molecular entity.

Second theorem is *Franck-Condon principle* of vertical transition during promotion of electron from ground to the excited state meaning that excitation occurs without change in atomic nuclei's position.[37,39,40] This is caused by difference in speed of electron excitation (10^{-15} s) and molecular vibration (10^{-10} – 10^{-12} s) and results in Franck-Condon state. The quantum mechanical approach to the Franck-Condon principle states that vibronic

transition (transition with change in both electronic and vibrational quantum numbers) is equal to square of overlap integral between ground and excited state included in the transition.

Third rule is *Kasha-Vavilov rule* declaring that luminescence quantum yield is independent of energy (wavelength) of excitation.[37,41] It is a result of *Kasha's rule* stating that luminescence of polyatomic molecules originates substantially from lowest energy state of a given multiplicity. Exception of this law is fluorescence from higher excited states (S_2) which is possible under specific circumstances, e.g. large energy gap between S_2 and S_1 causing IC from S_2 to S_1 less efficient than fluorescence ($S_2 \rightarrow S_0$) itself.[42]

Both previous rules lead to the *Stokes shift* that rates the frequency difference between the lowest energy absorption band (its Franck-Condon maxima) and the maxima of luminescence from this transition.[30,37] In other words, Stokes shift is a gap between absorption and emission maxima given in wavenumber (*Equation 15*). It is a mathematical expression of *Stokes rule,* which was formulated by G. G. Stokes and states that luminescence possesses longer wavelength than the wavelength of the initial excitation.

$$\Delta\bar{\nu} = \bar{\nu}_A - \bar{\nu}_E \qquad (15)$$

Opposite phenomenon, where emission wavelength is shorter than that of excitation, is called *anti-Stokes shift* and it can be caused by three processes.[43] The common feature of these processes is that energy of excitation (E_{EX}) is composed of energy of light source (E_1) and additional energy (E_2), and even though overall excitation energy is still higher than emitted energy (E_{EM}), energy of light source compare to energy of emitted photon is lower ($E_{EM} > E_1$). First process is *upconversion* where additional energy (E_2) is received from pre-existing excited molecule. We distinguish two mechanisms of upconversion: lanthanide-based and triplet-triplet annihilation-based upconversion. In second process called *hot band absorption*, the energy E_2 comes from heat. Parts of molecules according to heat-dependant Boltzmann distribution are located in higher vibrational level of ground state, also known as hot band. From this point, molecule can be excited and then emit photon with higher energy. Last process is *two-photon absorption* in which $E_{EX} = 2 \times E_1$ while $E_1 < E_{EM}$.

All the above-mentioned rules have a direct effect on the appearance of absorption, excitation and emission spectra (*Figure 4*). *Absorption spectrum* is a record of absorbance or absorption coefficient against photon energy (mostly wavenumber ν or wavelength λ). Plot of emission intensity (spectral radiant power or of the emitted spectral photon irradiance) against photon energy results in *emission spectrum*. Last commonly measure spectrum, in molecular UV-Vis spectroscopy, is *excitation spectrum*: a plot of emission intensity against excitation frequency at particular luminescence wavelength.[37]

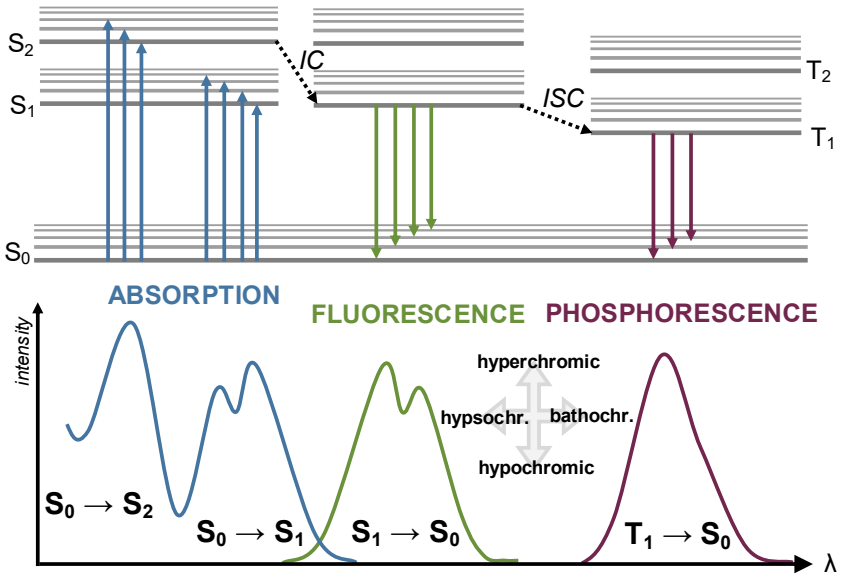

Figure 4. *Correlation between Perrin- Jabłoński diagram and absorption/emission spectra.*

For description of spectral bands, following terms are used:

- *hyperchromic shift* … increase in intensity,
- *hypochromic shift* … decrease in intensity,
- *bathochromic shift* … shift to higher wavelength (lower frequency), also called *red-shift,*
- *hypsochromic shift* … shift to lower wavelength, also called *blue-shift*.[37]

Reason why fluorescence spectra are mostly red-shifted as compared to absorption spectra, has been already explained (Kasha-Vavilov rule, Stokes shift). The excess energy is usually lost as heat. The bathochromic shift of phosphorescence band as compared to fluorescence one, is a consequence of Hund's rule: triplet state T_1 is less energetic than S_1 because parallel spins are further apart, and therefore show less mutual repulsion.[32]

1.1.3 Structure-luminescence relationship

Valence electrons in organic molecules allow to absorb electromagnetic radiation and jump from occupied bonding or lone pair to unoccupied antibonding orbital. These molecular orbitals arise from the fusion of atomic orbitals according to *MO-LCAO* (*Molecular Orbital – Linear Combination of Atomic Orbitals*) theory.[44] Let's consider simple ethane molecule, the single bond between two carbon atoms was created by merge of two sp^3 hybrid orbital and give rise to two molecular orbitals: bonding σ orbital with two electron and empty antibonding σ^* orbital (*Figure 5A*). Energy necessary for $\sigma \rightarrow \sigma^*$ transition is higher than energy of visible light, therefore the absorption bands of these transitions could be found in vacuum UV region.[36] In the case of ethene, double bond is created by overlapping of two sp^2 hybrid orbitals and two p

orbitals, resulting in two bonding (σ, π) and two antibonding orbitals (σ^*, π^*), see *Figure 5B*. The energy gap between π and π^* is lower and absorption band is localized in UV region (~170 nm).[45] An addition of heteroatom with a lone electron pair in the structure leads to presence of nonbonding orbital n, such as in ethanal (*Figure 5C*). Last example is the simplest conjugated π-system, buta-1,3-diene shown in *Figure 5D*. π-Electrons of double bond are delocalized over all four carbon atoms which leads to decrease of π- π^* gap. This reduction in energy gap increases with extending conjugated chain and it is even more important in large aromatic cycles.

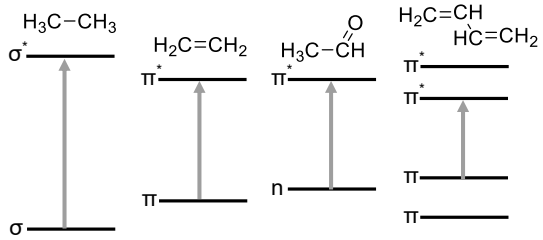

Figure 5. *Schematic representation of molecular orbitals in the structure of (A) ethane, (B) ethene, (C) ethanal and (D) buta-1,3-dien.*

The probability of photoluminescence after excitation with wavelength less than 200 nm is low.[32] Most PL occurs in the course of $\pi^* \rightarrow \pi$ and $\pi^* \rightarrow$ n transition, preferable the less energetic process. $\pi^* \rightarrow \pi$ Transitions are more common for fluorescence due to the fact that $\pi^* \rightarrow$ n transition is less populated as compared to $\pi^* \rightarrow \pi$ (the molar absorption coefficient is significantly lower), have smaller energetic difference between the S_1 and T_1, longer lifetime and higher rate constant for intersystem crossing than for fluorescence. Therefore, molecules with low lying n, π^* usually do not fluoresce on the other hand, they can emit light as phosphorescence. Although prediction of PL is mostly challenging due to the lack of general concept, several empirical leads can be taken into consideration.

Length of conjugated system: the majority of fluorophores are aromatic compounds. Dominant $\pi \rightarrow \pi^*$ transition gives high molar absorption coefficient. Gradual extension of π-system leads to increase in fluorescence quantum yield and bathochromic shift in both absorption and emission band. This phenomenon is displayed in two series of polycyclic aromatic compounds **1–3** and **4–7** in *Figure 6*.[46]

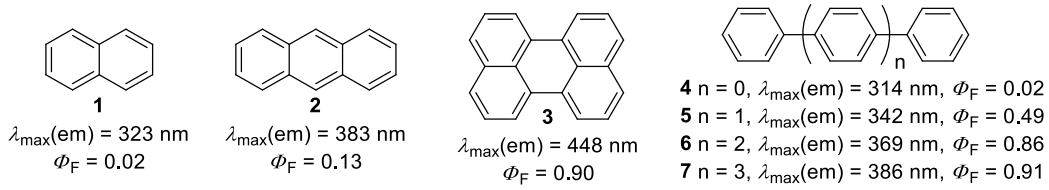

Figure 6. *Relationships between size of π -conjugated system and fluorescence properties. (Measurements parameters c = 10^{-6} mol.l^{-1}, $CHCl_3$, 295 K)*

Presence of heteroatom brings electron lone pair, and thus non-bonding orbital, into the molecular structure. It can affect PL in two ways depending on whether the lone electron pair is part of a conjugated system or not. If it is part of it, promotion of nonbonding electron shows similar properties as π → π* transition. If the lone pair is localized out of the conjugation, molecule possesses low lying n, π* transitions and fluorescence quantum yield becomes highly dependent on the solvent characteristics (see Chapter 1.1.4).[40]

Presence of heavy atom changes both fluorescence and phosphorescence nature. With increasing atomic mass fluorescence quenching occurs, the rate constant of intersystem crossing decreases and phosphorescence becomes more prominent, as a result of growing spin-orbit coupling. Example of heavy atom effect in the series of phenanthrenes **8–10** is given in *Figure 7* together with fluorescence and phosphorescence quantum yields.[47]

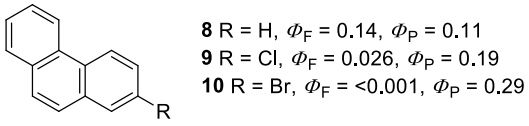

Figure 7. *Demonstration of heavy atom effect on series of phenanthrenes **8–10**.*

Electron-donors such as amino (-NH_2, -NHR, -NR_2), hydroxy (-OH) and alkyl(aryl)oxy (-OR) with lone pair of electrons effect PL in a different way than heteroatom in heterocyclic compounds because lone pairs of electron-donating groups are involved in the bonding with aromatic part of molecule.[28] This leads to increase in molar absorption coefficient, fluorescence intensity and bathochromic shift in absorption and emission spectra.

Presence of electron-withdrawing group, such as carbonyl, carboxylic acid or nitro, on aromatic skeleton generally leads to inhibition of fluorescence due to the predominant n → π* transition.[36,40] However, some aromatic carbonyl molecules have the π, π* energy gap smaller than n, π*, and thus they can fluoresce. If the n electronic state lies only slightly higher than π state, fluorescence can be induced by change of solvent polarity.

When a π -conjugated linker separates electron-donating and electron-withdrawing groups, electron interaction occurs between these groups and instantaneously induces large dipole moment across the molecule in the meaning of *photoinduced charge transfer*.[40] This highly

polarized excited Franck-Condon state, also called *locally excited state* (LE), is in a thermodynamic nonequilibrium with surrounding solvents molecules. During the excited lifetime, solvent molecules move around luminophore until the system reached equilibrium, so-called relaxed ICT (*intramolecular charge transfer*) state. Internal rotation inside the luminophore can take place during the solvent relaxation resulting in *twisted intramolecular charge transfer* (TICT) with total charge separation, which can be stabilized by polar solvents. Molecules undergoing this process show dual emission in polar solvents, where expected LE state is accompanied by red-shifted TICT state.

1.1.4 Two-photon absorption

The nonlinear optical properties of organic luminophores have attracted researchers' interest in past few decades due to application in fluorescent sensing and noninvasive biological imaging with low specimen photodamage and high penetration depth.[48,49] 2PA is only one of nonlinear optical processes and increase of 2PA cross-section (the intensity of 2PA) upon structural modifications will be subject of following paragraphs.

For π-conjugated organic molecules, the increase of nonlinear optical response can be mostly achieved by structural design.[31,50] First modification towards higher 2PA cross-section is an *elongation of π-conjugated system*. This can be demonstrated on a series of compounds **11–13** with increasing number of vinylene linkers (*Figure 8*).[51] Going from **11** with one vinylene to **12** with two vinylene linkers, the 2PA cross-section increase over two times. Addition of third vinylene bridge (**13**) results in 2PA cross-section 1.5 time higher than that of compound **12**.

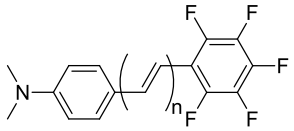

11 n = 1, λ_{max}(2PA) = 750 nm, δ_{max} = 120 GM[a]
12 n = 2, λ_{max}(2PA) = 825 nm, δ_{max} = 300 GM[a]
13 n = 3, λ_{max}(2PA) = 850 nm, δ_{max} = 500 GM[a]

[a]Measured by TPEF technique in toluene.

Figure 8. *2PA properties of compounds **11–13** with different numbers of vinylene linkers.*

2PA cross-section can be also enhanced by presence and strength of groups with electronic effect, i.e. electron-withdrawing and electron-donating groups.[52,53] Comparing compounds **14** and **15** (*Figure 9*), compound **14** with stronger electron-donating group exhibits higher 2PA cross-section.[54,55] Similarly, compound **16** with weaker electron-withdrawing CN group also shows lower 2PA response.

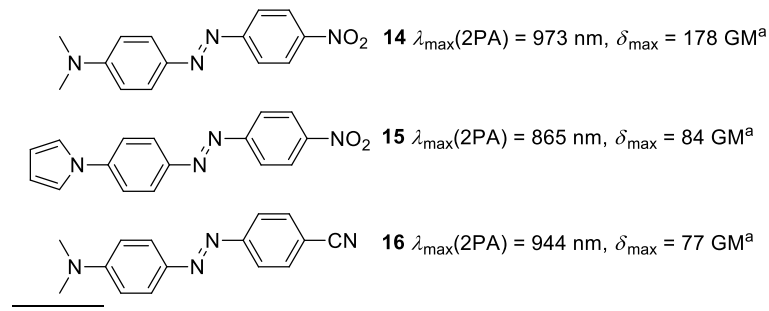

Figure 9. *2PA response of compounds* ***14–16****.*

Number of branches is another aspect which influences 2PA response, as it is demonstrated on a series of dipolar triphenylamine derivatives **17–19** with octylsulfonyl electron-withdrawing peripheral group, see *Figure 10*.[56] 2PA absorption cross-section increases in a sequence: dipolar **17** < quadrupolar **18** < octupolar **19**, in other words with increasing number of branches.

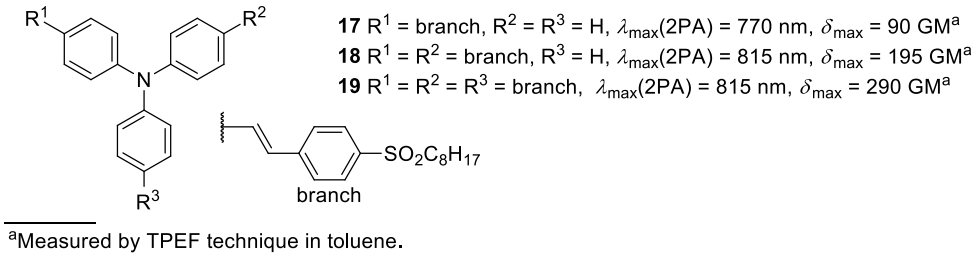

Figure 10. *2PA properties of multi-branched triphenylamine derivatives* ***17–19****.*

1.1.5 Environmental effect

Description of photoluminescence properties of given molecules in solution would be incomplete without taking into account surrounding microenvironment. PL is directly affected by solvent in many ways, which are schematically summarized in *Figure 11*.

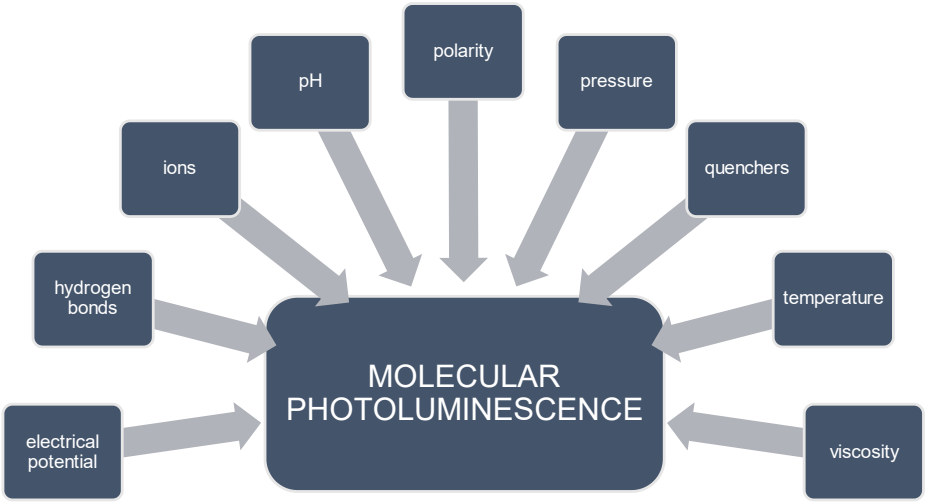

Figure 11. *Environmental effects on molecular photoluminescence.*

Generally, PL quantum yield decrease with raising temperature.[36] Energy in the system raises and induces more collisions between solvent molecules and the excited state, which leads to increase in nonradiative deexcitation. Probability of radiation-less transition is proportional to the excited lifetime duration, i.e. decrease in quantum yield is even more dramatic for phosphorescence. The viscosity of solvent has similar influence. When the viscosity is decreased, number of molecular collisions increases, and thus the quantum yield decreases.

If basic or acidic functional group is present in the luminophore's structure, its absorption and emission behaviour is pH dependent.[36,57] Generally speaking, the higher negative charge on electron-donor (or positive on electron-acceptor), the lower luminescence energy will be. For compounds with nonbonding electron pair, fluorescence quantum yield is usually low. However, if the electron lone pair is tied to proton, energy of the lowest n, π* excited level raised above the π, π^* excited singlet level. Emission from this level prevails, which results in increased fluorescence intensity.

Polarity of solvent affects luminescence in two ways depending on the dipole moment of molecule in the ground (μ_g) and in excited (μ_e) states.[30] The most of luminophores have larger dipole moment in excited state than in ground state. When a molecule reaches the excited states, dipole moments of the solvent start to orient themselves around the polarized molecule (solvent relaxation). The more polar solvent is, the lower the energy of the excited state. As a result, emission band shifts to higher wavelength with increase of solvent polarity, so-called *positive emission solvatochromic effect* or *solvatochromism*. On the contrary, larger dipole moment in ground state leads to a blue-shift in emission – *negative solvatochromism*.

1.1.6 Main classes of organic luminophores

Fluorescent analytical techniques are very sensitive measuring methods, therefore they are favourite choice for analyte detection in medicine, pharmacy, environmental science and cellular biology.[58] This chapter serves as an overview of the well-known types of fluorescent dyes.

Coumarin is a benzo-fused carbonyl heterocyclic compound, which possesses no luminescence; its structure is displayed in *Figure 12* (**20**). [40,59] Nevertheless, substitution in positions 7 with electron-donating and withdrawing groups in position 3 leads to a dramatic increase in fluorescence in blue-green region.

The general structure of cyanines is polymethine chain terminated with amino groups, see *Figure 12* structure **21**. Bathochromic shift about 100 nm in emission is observed with every additional vinylene group.

Boron dipyrromethene, also known under the shortcut BODIPY, is a group of very versatile fluorophores. They show large molar absorption coefficient, high quantum yield, good stability and solubility and emission wavelength mostly over 600 nm. General structure is provided in *Figure 12* under the number **22**.

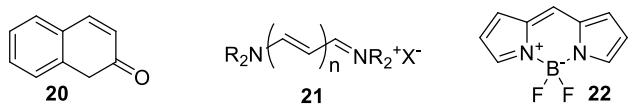

Figure 12. *General structure of coumarins **20**, cyanines **21** and BODIPY **22**.*

Another group, xanthene dyes, includes fluoresceins and rhodamines. Rhodamines have narrow both absorption and emission spectra with low Stokes shift. Fluorescein, its derivatives Eosin Y and erythrosine B are used as pH sensors due to their high pH sensitivity. General structure of rhodamines **23** among with fluorescein **24a** and its derivatives **24b–c** are shown in *Figure 13*.

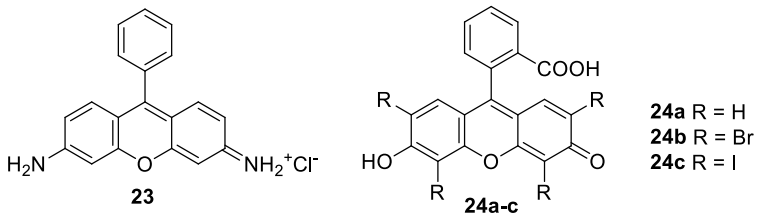

Figure 13. *General structure of rhodamines **23** and fluoresceins **24**.*

1.2 OLED technology

Organic light-emitting diode is a type of light-emitting diode (LED), which utilizes stacked thin layers of an organic material to convert electric energy to visible light.[60] The light

emission process after excitation by external electrical potential is called electroluminescence.[61,62] The first observation of EL phenomenon was done by H. J. Round (personal assistant of G. Marconi) in 1907 on silicon carbide.[63] Between 1950 and 1955, after almost fifty years, A. Bemanose and co-workers at the University of Nancy, France, applied a high alternating voltage on acridine orange spread over cellophane or cellulose surface and reported the first EL originating from organic material.[64] In 1987, C. W. Tang and S. Van Slyke at Eastman Kodak published a paper about first convenient OLED device with 8-hydroxyquinoline aluminium (Alq_3) **25** and diamine **26** layers (*Figure 14*).[65] Ten years after, Pioneer Corporation introduced on market the first commercial OLED for car audio screens. Since that time, a variety of OLED-based products, such as light for general-lighting application, smart watches, cell phones, and even large television displays, have conquered the world market.[6]

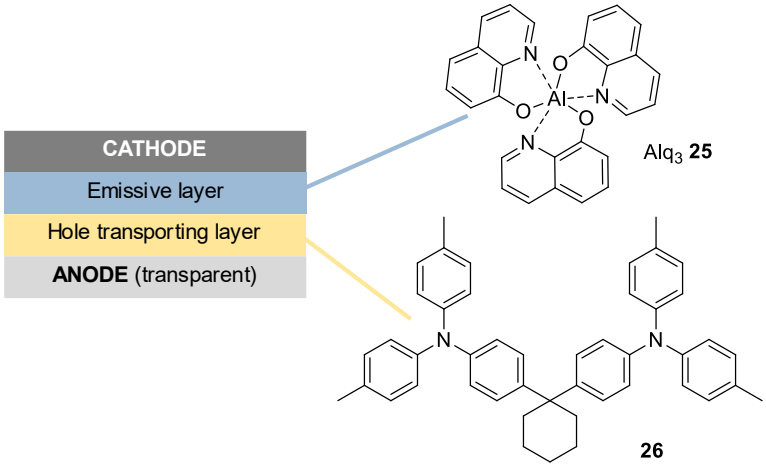

Figure 14. *Composition and structure of the very first OLED device by Tang and Van Slyke.*[65]

1.2.1 Organic semiconductors

Organic semiconductors represent significant part of large family of organic electronics. Whereas the inorganic semiconductors possess strong covalent bond between each atom and ideally obey the band theory, i.e. they possess almost-empty conductive band and almost-filled valence band,[66] the organic counterparts are mostly π-conjugated small molecules or polymers interacting through weak Van der Waals forces. They structure is built on sp^2 hybridized carbon atoms, while the electrons present in the remaining p-orbital are highly delocalized. An overlap of the delocalized π-electron in the solid state leads to conductivity.

Sharing of electrons and overlap of atomic orbitals within a molecule results in formation of a molecular orbital.[67] The HOMO (*Highest Occupied Molecular Orbital*) of organic semiconductors is responsible for hole transport similarly to the valence band in inorganic

semiconductors. On the other hand, the first empty quantum case – the LUMO (*Lowest Unoccupied Molecular Orbital*) transports electrons and is similar to the conduction band (*Figure 15*).[60]

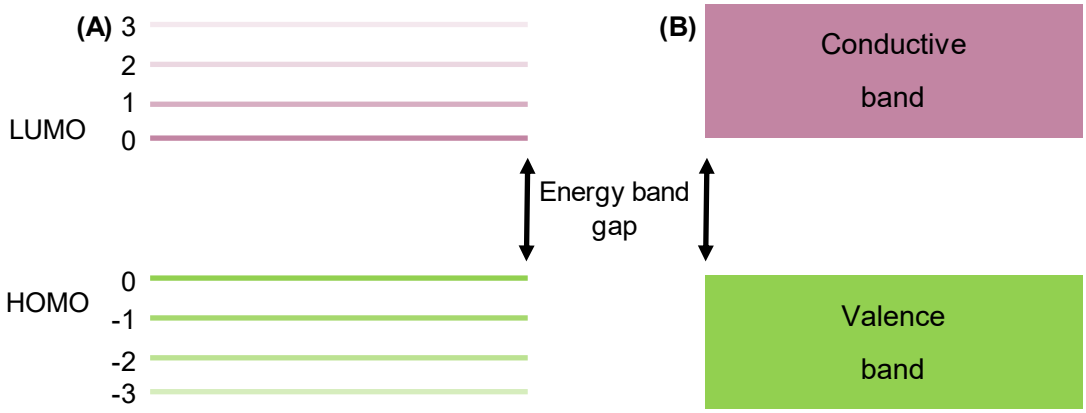

Figure 15. *Energy diagram of (**A**) molecular orbitals in organic semiconductor and (**B**) bands in inorganic semiconductor.*

Achieving efficient injection of charge carries (holes and electrons) from the metallic electrodes into the conductive layer represents major task of organic electronics.[68] Whereas the electrode contacts of inorganic semiconductors must be heavily doped to allow tunnelling of carriers through barriers, the hole injection in organic semiconductors is reached by matching the anode work-function and the conductive material's HOMO levels. Similarly, the cathode work-function and the organic semiconductor's LUMO levels must be close for a good electron injection.

The basic advantages of inorganic semiconductors (hardness, high conductivity and high melting points) are beaten by organic semiconductors in many aspects. For instance, they can be in a form of mechanically flexible and light-weight plastic and possess low-cost production.[69] Very attractive organic semiconductors' properties are fabrication of devices by simple solution processing techniques, e.g. ink-jet printing, which allows inexpensive manufacturing of organic electronics on various substrates. Organics semiconductors found applications across the organic electronics including organic light-emitting diodes (OLEDs), organic thin-film transistors (OTFTs), organic light-emitting transistors (OLETs), electrophotographic devices as well as organic field-effect transistors (OFETs).[70–73]

1.2.2 Structure of OLED

In OLEDs, stacked layers of different semiconducting materials are placed between two electrodes. Application of electrical potential on electrodes causes movement of electrons from the cathode and holes from the anode through the layers into the emitting layer where both

recombine to form exciton. The general structure of multilayer OLED is displayed in *Figure 16*. It consists of anode, following by *hole-injection layer* (HIL), *hole-transport layer* (HTL), *electron-blocking layer* (EBL), *emitting layer* (EML), *hole-blocking layer* (HBL), *electron-transport layer* (ETL), *electron-injection layer* (EIL) and ends with cathode. A real OLED device does not have to include all aforementioned layers but special requirements, such as good thermal stability, high conductivity, low power-on voltage etc., are necessary for the particular organic materials.

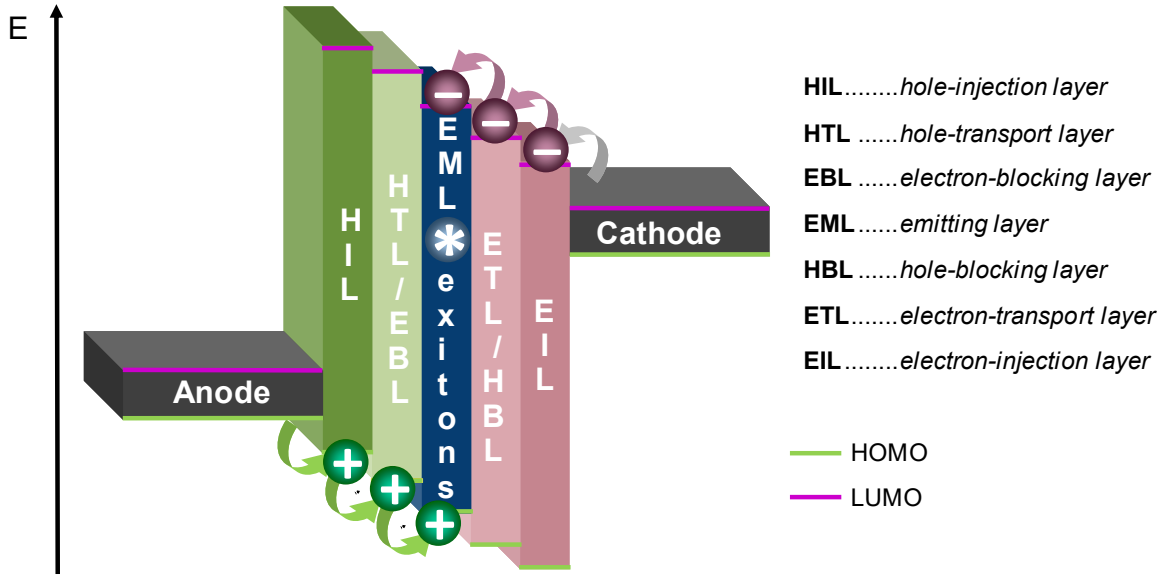

Figure 16. *General architecture of an OLED device.*

General requests for anode are high transparency, conductivity, good adhesion properties and high work-function to inject hole into the HOMO of organic material.[68] Indium tin oxide (ITO) is the most common choice of anode material. It has good conductivity, high chemical stability, high work function, good transparency (90%) to visible wavelength range and excellent adhesion to substrate. However, indium oxide can migrate into organic layer and devalue emitting properties of OLED. ITO also has high refractive index, which is resulting in 75% loss of the generated photons. Another material for anode is fluorine-doped tin oxide, aluminium-doped zinc oxide and transparent conductive oxides – $Ga_{0.08}In_{1.28}Sn_{0.64}O_3$, $Zn_{0.5}In_{1.5}O_3$ and $Zn_{0.46}In_{0.88}Sn_{0.66}O_3$.[74]

The hole-injection/electron-injection layer helps to reduce energy barrier between the anode/cathode work-function and the HOMO/LUMO level of the emissive layer.[75] Triphenylamine derivatives such as **27** or copper complex of phthalocyanine **28** are widely used as HIL. Selection of EIL can be complicated. Alkali metal halides and metal oxides or lithium quinolate **29** are often employed (*Figure 17*).[74]

The HTL and ETL transport charge carriers into emissive layer.[76] The HOMO level of HTL material should be slightly lower than that of EML for improving charge flow into to the EML with a minimum hole accumulation on their interface. The energy gap should be wide to block transfer of excitons and electrons towards anode. The HTL layer can be doped with electron-accepting *p*-dopant while conductivity of the ETL can be improved by adding *n*-dopants. The HTL is often used as electron-blocking layer and the ETL as hole-blocking layer. Typical HTL materials are aromatic amines, for example diamino compound **30**, derivative **31** with two carbazole units or spirobifluorene **32**. Lithium quinolate **29**, oxadiazole **33** or phenanthroline **34** are the most-widely used ETL materials (*Figure 17*).[74,77]

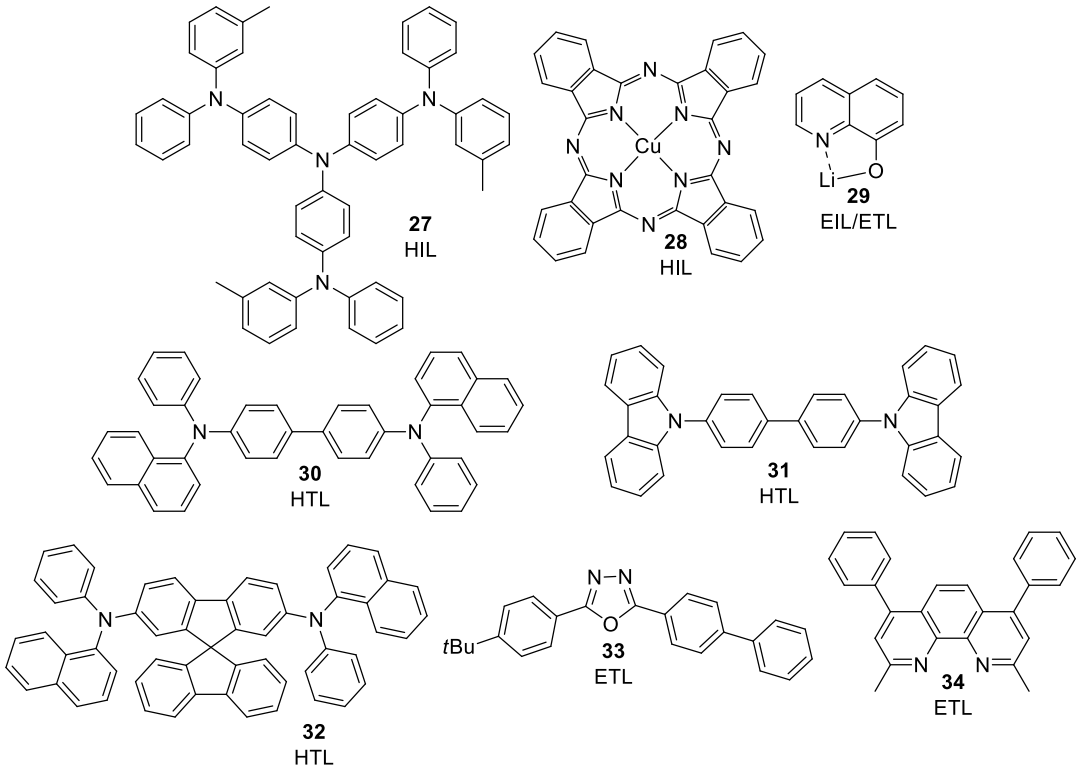

Figure 17. *Examples of organic compounds used in OLED devices.*

Mg:Ag (10:1), LiF and Mg:Al are favourite materials for cathode. This electrode should have low work-functions and efficient electron injection properties.[77]

Emissive layer in OLED is mostly composed of dopants and host. Dopants are emissive organic semiconductors; these can be generally divided into three categories: (i) small molecules, (ii) conjugated dendrimers and (iii) conjugated polymers. Host materials transport charge carriers, allow excitons formation and simplify radiative recombination. Requirements for the EML materials are high efficiency, lifetime and colour purity. The colour of the generated light depends on the choice of emissive dopant.[78]

1.2.3 Working principle of OLED

Organic material, as a semiconductor, shows high resistance at low electric field.[77] That creates high energy barrier at the interface of an electrode and organic layer. In order to cross this barrier, energy of injected charge carrier must overcome the potential energy barrier. This injection mechanism is called *Schottky or thermionic emission*. Carriers can also penetrate through the energy barrier, if it is thin enough, in the meaning of *tunnel or field emission*. A successful hole and electron injection through both processes (*Figure 18*) requires low energy of the barrier and high HOMO and low LUMO levels of the organic material.

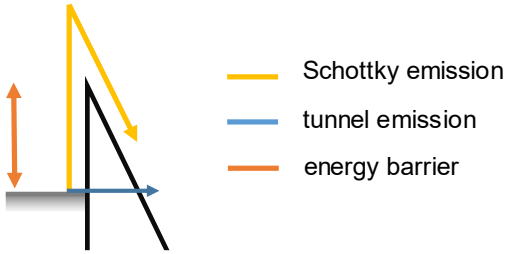

Figure 18. *Schottky and tunnel emission.*

The thin layer in OLED are in the most cases composed of amorphous organic material, therefore the charge transfer cannot be explained by the band-like transfer as in crystalline semiconductors. Thus, the *hoping transport* mechanism has been proposed to explain charge movement through the organic layers. In this scenario, charge is transferred by successive jumping from one molecule to the neighbour molecule. However, charge transfer in this manner is low 10^{-7}–10^{-2} $cm^2.V^{-1}.s^{-1}$).

When holes and electrons reach the emissive layer, they recombine in exciton.[66,75,77,79] It usually occurs as two-step process. Firstly, loosely bonded triplet or singlet polaron pairs (charge-transfer excitons) are formed. Subsequently, they turn into neutral singlet or triplet forms. In many cases, emissive material suffers from concentration quenching. As a solution, small amount of emitters (guests) can be doped into host matrix. It is a way how to increase *EQE* and also tune the light colour of emitted light. In this system, energy transfer takes place between the host (exciton donor) and the guest (exciton acceptor) by *Förster or Dexter mechanism*. Förster is long range dipole-dipole mechanism between singlet states typical for fluorescent emitters. On the other hand, Dexter one involves short range intramolecular electron exchange between triplets or singlets.

1.2.4 OLED characteristics

Before starting characterization of OLED, fundamental properties of the used emitting organic material must be evaluated by absorption and emission spectra, PL quantum yield

and lifetime, thermal stability and cyclic voltammetry. These measurements estimate if a given compound is suitable candidate for OLED fabrication based on its photoluminescence performance, thermal robustness and HOMO/LUMO energy levels. Examples are shown in *Figure 19* for compounds **26** and **27**.[80]

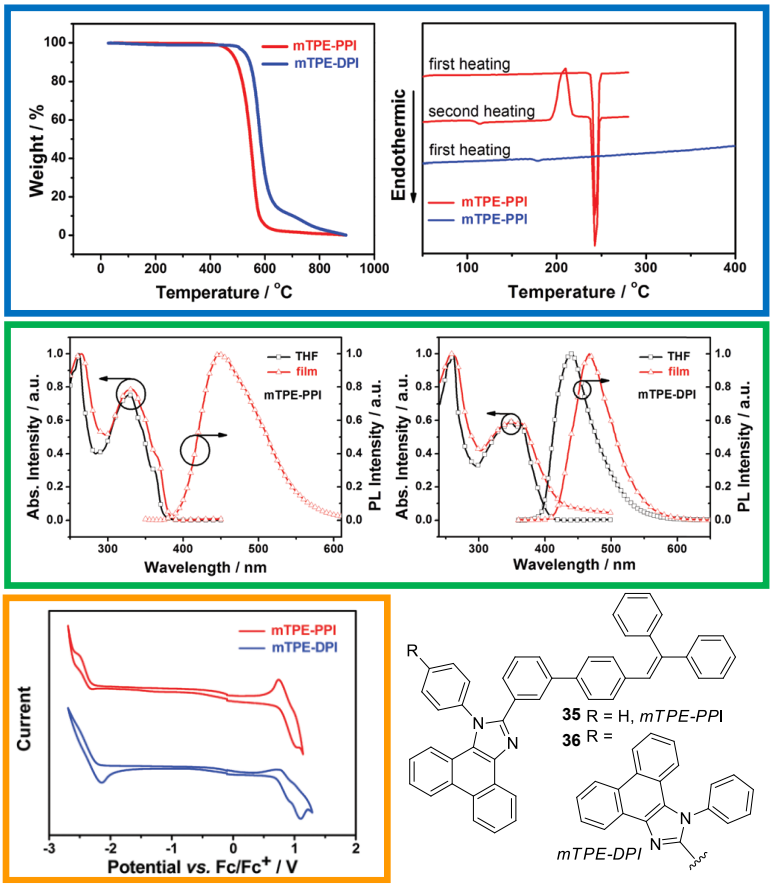

Figure 19. *TGA and DSC thermograms (blue), absorption and emission spectra (green) and cyclic voltammograms (orange) for compounds* ***35*** *and* ***36****.*[80]

The efficiency of light emission of an OLED device is usually assessed by *external quantum efficiency* (*EQE*; η_{ext} [%]). This value represents *internal quantum efficiency* (*IQE*; η_{int} [%]) reduced by light loss due to the absorption, refraction etc., the relationship is given in *Equation 16*. In other words, external quantum efficiency gives a ratio between the amount of injected charges and emitted photons.[79] The theoretical *EQE* for fluorescence from *Equation 16* is 5% and for phosphorescence 20%.[81] Example of *EQE* of compound **35** and **36** plotted versus current density is provided in *Figure 20C*.[80]

$$\eta_{\text{ext}} = \eta_r \times \Phi_{\text{PL}} \times \chi \times \eta_{\text{out}} = \eta_{\text{int}} \times \eta_{\text{out}} \qquad (16)$$

where

- η_{r} … probability of exciton formation,
- Φ_{PL} … PL quantum yield,

- χ … exciton generation efficiency,
- η_{out} … photon refraction ($\sim 1/(2n^2)$; n is refraction index).

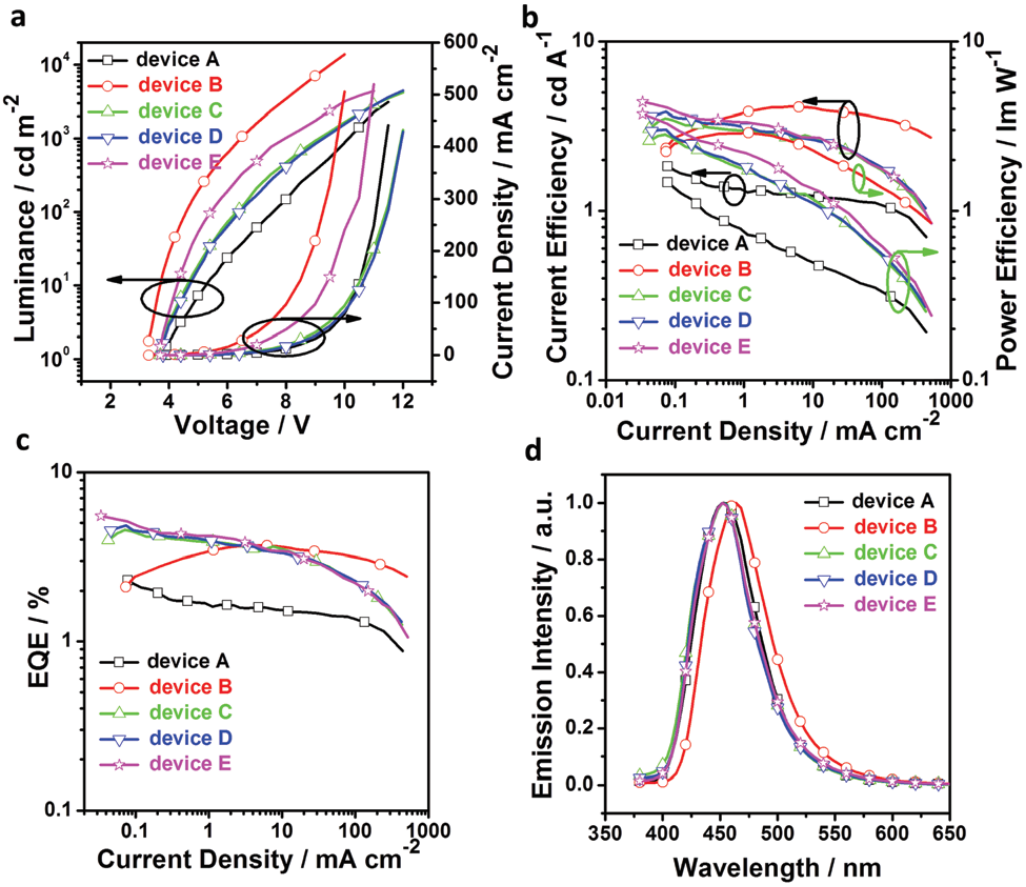

Figure 20. *J-V-L characteristics (a), power and current efficiency (b), EQE vs current density plot (c) and EL spectra (d) for OLEDs fabricated with compounds* ***35*** *and* ***36****.*[80]

A dependency of the emitted luminance [Cd.m^{-2}] on the current density [A.cm^{-2}] is *current efficiency*. Another OLED efficiency can be express as a ratio of the optical power [W or lm] to power taken by the device [W], which is called *power efficiency*.[82] Both efficiencies for **35** and **36** are shown in *Figure 20B*.

I-V characterization, also known as current-voltage characteristics, is a standard measuring technique to determine diode behaviour in an electrical circuit. During this measurement, direct current going through OLED is detected as a function of increasing applied voltage and creates curve with an important point. It is called cut-in voltage, a point when a barrier voltage is overcome. The cut-in voltage should be lower than 5V.[82,83]

J-V-L characteristics demonstrate relationship between current density, bias voltage and luminance, see *Figure 20A*. The current density is defined as current over area of OLED and both with luminance raise with increasing drive voltage.[83]

Electroluminescence spectrum is a plot of luminescence intensity of OLED device versus wavelength at specific current density. Example of EL spectra for compounds **35** and **36** are given in *Figure 20D*.

Chromaticity diagram, 2D colour space created based on human eyes perception, defines the emitted light colour as surface coordinates.[84] Usually, the chromaticity coordinates are given as CIE 1931 references (designed by *Commission Internationale de l'éclairage* in 1931).[85] *Figure 21* shows CIE diagram for OLED device fabricated with **35** and **36** compounds.

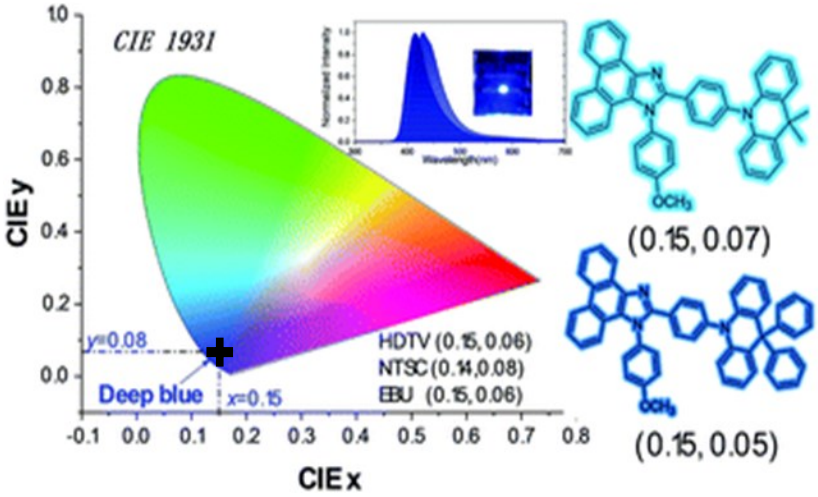

Figure 21. *Example of chromaticity diagram.*[80]

All figures in this subchapter were taken from article of *C. Li et al.* "*Efficient deep-blue OLEDs based on phenanthro[9,10-d]imidazole-containing emitters with AIE and bipolar transporting properties*", © Royal Society of Chemistry 2021.[80]

1.2.5 Types of OLEDs

There are many ways to categorize OLED devices. For the main purposes of this work, sorting OLEDs into three generations according to their emissive layer seems to be the most suitable way. This sorting is based on a mechanism of harvesting excitons by the emitting media, see *Figure 22*. Charge recombination in emissive layer corresponds to spin statistics in 25% of singlet and 75% triplet excitons.[86] The first-generation OLED is fabricated with purely organic fluorescent emitter, and therefore, can use only singlet excitons and achieve only 25% of internal quantum efficiency (*IQE*). The second-generation OLEDs utilize phosphorescent emitters with heavy metals, which can harvest triplet excitons and also remaining 25% of singlets by intersystem crossing. Third-generation OLEDs possesses so-called thermally-activated delayed fluorescent (TADF) material in their emissive layer,

which can be organic and also organometallic compound.[87] These materials are able to reach both singlets and triplets by reverse intersystem crossing, which is the mechanism converting triplet excitons to singlets by tapping into the thermal energy, without the need to use rare and expensive elements. So, the *IQE* for the second- and third-generation OLED can theoretically reach up to 100%.[88] A small energy gap between the *S* and *T* energy levels is crucial for both transferring mechanisms ISC and RISC.[68] The organic TADF emitters possess combined advantages of the first- and second-generation OLEDs, i.e., high stability and high luminance efficiency and metal-free composition with low-cost fabrication. In addition, these allow producing stable deep-blue light, which had always been problematic for the second-generation OLED devices.

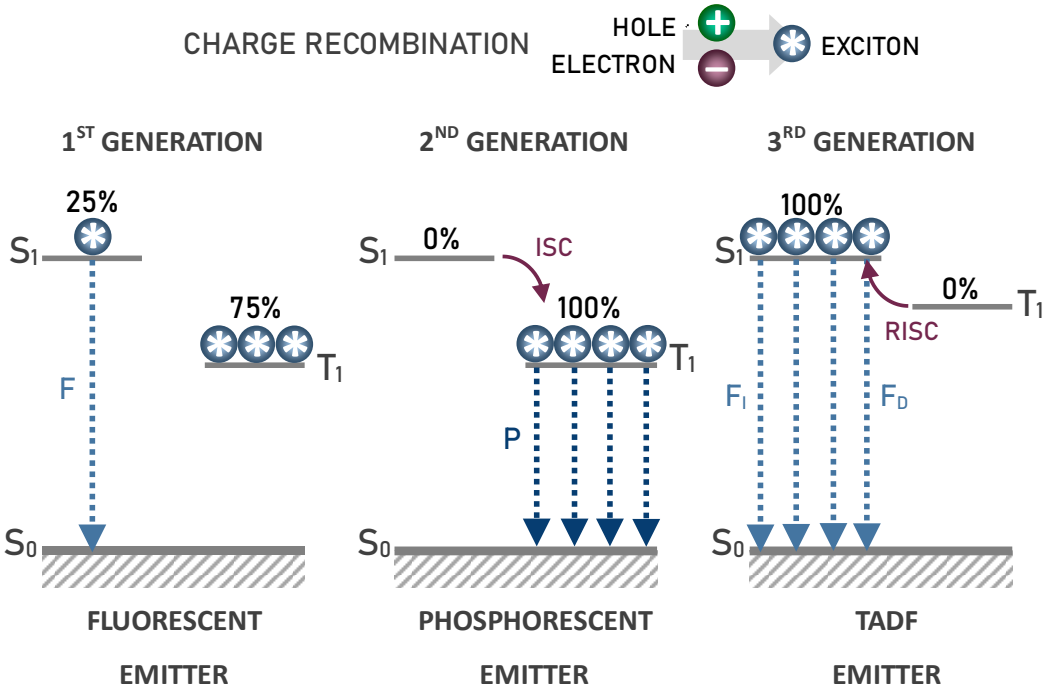

Figure 22. *Excitons harvesting mechanism in the 1st, 2nd and 3rd generation OLEDs.*

CHAPTER II. The use of pyrimidine core for the conception of luminescent materials

2.1 Description of pyrimidine

During the past few decades, five-membered and six-membered heterocycles have attracted considerable research interest due to their perspective application in organic electronics.[89] Five- and six-membered heterocycles stand for unsaturated organic compounds derived from benzene by replacing one or two methine groups by one up to six heteroatoms. These heterocycles include pyrimidine, which is six-membered ring with two nitrogen atoms in positions 1 and 3. Presence of two heteroatoms brings interesting properties that will be discussed in the following paragraphs as comparison with a few other common heterocycles shown in *Figure 23*.

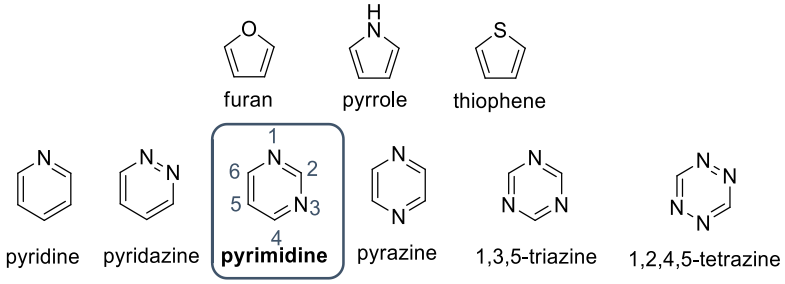

Figure 23. *Examples of common unsaturated five-membered (first row) and six-membered (second row) heterocycles.*

Unsaturated heterocycles are structurally related to benzene; thus, they possess high aromaticity. The unified aromaticity index (I_A), calculated from the experimental bond lengths, is a suitable quantity to compare their aromaticity (*Table 2*).[90] Nature of heteroatom increase the aromaticity in the sequence S~N>O. In the case of azines, the aromaticity is mostly affected by the positioning of the nitrogen atoms rather than their number. The aromaticity rises with increased symmetrical redistribution of the charge. This effect can be demonstrated on diazines (pyridazine < pyrimidine < pyrazine).

Electronic effects of six-membered nitrogen rings depend on the number of nitrogen atoms and their mutual localization within the heterocyclic ring.[91] One of the indicators of electronic properties is Hammett's substituent constant σ_p; the values for given heterocycles are summarized in *Table 2*.[91,92] Due to the presence of electronegative nitrogen atoms, azines are electron deficient heterocycles. The azinyl fragments may serve as electron-attracting scaffold, especially when the sidechain is connected to the azine's alternating position (compare pyridin-3-yl/pyridin-4-yl, pyrimidin-5-yl/pyrimidin-4-yl, etc.). Going from pyridine to diazines

and triazines, the Hammett's σ_p constants increase stepwise with additional nitrogen atom. Pyrrol-*N*-yl group acts as electron-withdrawing group as well.[93] On the other hand, thiophene and furan, as electron rich heterocycles, are considered weak electron-releasing moieties.

The lone electron pair present in azines plays a key role in their chemistry, especially for its capability to catch protons. Due to higher "s character" of the N(sp^2)–H bond are azines weaker bases than aliphatic amines. However, pyridine is often used as a basic solvent and neutralizing agent during various reactions.[94] Negative inductive and mesomeric effects of the second nitrogen atom in diazines destabilizes the monoprotonated species, and therefore, leads to lowering of their basicity as compared to parent pyridine. *Table 2* summarizes azine's pK_a values.[95] The second nitrogen atom in diazines has somewhat surprisingly affected their pK_a values: 2.2 for pyridazine, 1.2 for pyrimidine and 0.6 for pyrazine. The increased basicity of pyridazine is explained on the basis of removed lone pair–lone pair repulsion in cation species.[96] Similarly to diazines, addition of third and fourth nitrogen decreases the basicity.

Table 2. *Dissociation constants (pK_a),[95] Bird index (I_A),[90] and Hammett's substituent constants (σ_p)[92,97] of selected heterocycles.*

	pK_a	I_A	σ_p
furan	–	53	0.02 (2-yl)
pyrrole	–	85	0.37 (1-yl)
thiophene	–	81.5	0.05 (2-yl)
			–0.02 (3-yl)
pyridine	5.3[a]	85.7	0.17 (2-yl)
			0.25 (3-yl)
			0.44 (4-yl)
pyridazine	2.2[a]	78.9	0.48 (3-yl)
	(–7.1)[b]		0.59 (4-yl)
pyrimidine	1.2[a]	84.3	0.53 (2-yl)
	(–6.3)[b]		0.63 (4-yl)
			0.39 (5-yl)
pyrazine	0.6[a]	88.8	–
	(–6.6)[b]		
1,3,5-triazine	-1.7[a]	100	0.88 (2-yl)
1,2,4,5-tetrazine	-6[a]	97.8	–

[a]pK_A values of monoprotonation. [b]pK_A values of twofold *N*,*N*-protonation.[96]

Besides the protonation ability, the non-bonding electron pair of azines can also coordinate metal cations. Pyridine,[98,99] polyazines,[99–101] and their derivatives have been used as *N*-chelating or cyclometalating ligands in a broad spectrum of complexes with non-transition, transition and rare earth metals. Azines can also serve as coordination centres in inverse

coordination complexes, i.e. the core is formed by nitrogen heterocycle and surrounded by a number of metals ions.[102]

All aforementioned structural features influence the physical properties of pyrimidine, and therefore, its chemistry offers a wide range of possibilities to design target compounds with desired character.

2.2 Pyrimidines luminescent materials

This Chapter is dedicated to short evaluation of relationship between the structure of chromophore and its fluorescence and two-photon absorption properties. Even though prediction of structure-fluorescence relationship is quite complicated, a few general rules can be estimated based on properties of already existing fluorophores. In the end, short chapter discussing general reaction leading to pyrimidine-based chromophores is included.

2.2.1 Overview of structure-fluorescence relationship

Effect of electron-donors

The majority of pyrimidine-based fluorophores are push-pull compounds, in which pyrimidine acts as electron-withdrawing group, and their PL behaviour is influenced by the nature of electron-donating group.[103] It can be demonstrated on a series of compounds **37–41** (*Figure 24*) in which increasing strength of peripheral donating group causes red-shift of the emission λ_{max} within the order: H (**37**) < OCH_3 (**38**) < $OC_{10}H_{21}$ (**39**) < SCH_3(**40**) < $N(CH_3)_2$ (**41**).[104,105] Fluorescent quantum yield slightly increases in the same order as well. On the other hand, presence of electron donor OCH_3 (**43**) or SCH_3 (**44**) on pyrimidine core results in blue-shift in emission and decrease of quantum yield in the case of **43** as compared to non-substituted derivative **42**.[106] Electron-attracting groups, such as methylsulfonyl (**45**) or cyano (**46**), enhance fluorescence quantum yield and cause red-shift of the emission band.

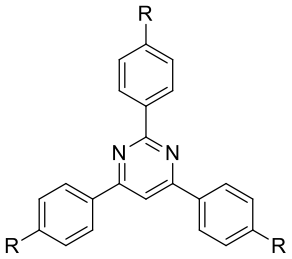

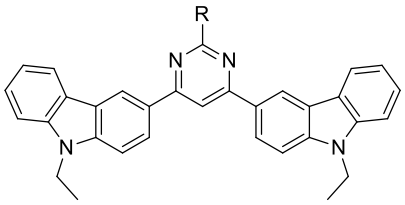

37 R = H, λ_{max}(em) = 381 nm, Φ_F = <0.01[a]
38 R = OCH_3, λ_{max}(em) = 372 nm, Φ_F = 0.04[a]
39 R = $OC_{10}H_{21}$, λ_{max}(em) = 387 nm, Φ_F = 0.04[a]
40 R = SCH_3, λ_{max}(em) = 398 nm, Φ_F = 0.14[a]
41 R = NCH_3, λ_{max}(em) = 427 nm, Φ_F = 0.14[a]

42 R = H, λ_{max}(em) = 395 nm, Φ_F = 0.44[b]
43 R = SCH_3, λ_{max}(em) = 394 nm, Φ_F = 0.23[b]
44 R = OCH_3, λ_{max}(em) = 388 nm, Φ_F = 0.48[b]
45 R = SO_2CH_3, λ_{max}(em) = 426 nm, Φ_F = 0.61[b]
46 R = CN, λ_{max}(em) = 427 nm, Φ_F = 0.63[b]

[a]Measured in $CHCl_3$. [b]Measured in THF.

Figure 24. *Impact of substituent electronic effect on photophysical properties of molecules* ***37–46****.*

Effect of π-conjugated system

Generally, fluorescence quantum yield and emission wavelength raise with extended π-conjugated system, as is the case of compounds **47** < **50** < **51** < **57** bearing methoxy group (*Figure 25*).[107–110] A series of dimethylamino- and diphenylamino-substituted fluorophores **48**, **52**, **58** and **49**, **53**, **59**, respectively, shows similar trend, except of lower fluorescence quantum yield for derivative **58** and **59** with ethynyl bridge as compared to **52** and **53**. However, diphenylamino compound **49** shows red-shifted emission with regards to its dimethylamino analogue **48**, despite the fact that dimethylamino group is stronger electron-acceptor. This behaviour is no longer observed in molecules with longer conjugated linker. Replacement of 1,4-phenylene by 2,5-thienylene unit (**54–56**) results in a red-shifted emission of methoxy (**54**) and a blue-shifted emission of amino derivatives (**55** and **56**).

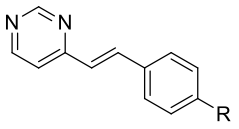

47 R = OCH_3, emission not detected
48 R = $N(CH_3)_2$, λ_{max}(em) = 488 nm, Φ_F = 0.15[a]
49 R = NPh_2, λ_{max}(em) = 526 nm, Φ_F = 0.45[a]

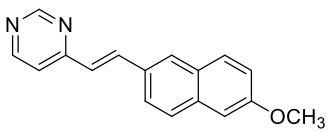

50 λ_{max}(em) = 436 nm, Φ_F = 0.03[a]

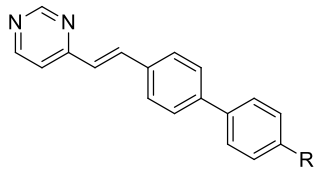

51 R = OCH_3, λ_{max}(em) = 447 nm, Φ_F = 0.14[a]
52 R = $N(CH_3)_2$, λ_{max}(em) = 570 nm, Φ_F = 0.66[a]
53 R = NPh_2, λ_{max}(em) = 563 nm, Φ_F = 0.52[a]

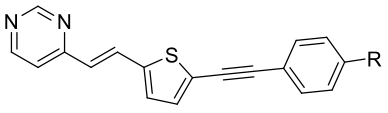

54 R = OCH_3, λ_{max}(em) = 489 nm, Φ_F = 0.04[a]
55 R = $N(CH_3)_2$, λ_{max}(em) = 607 nm, Φ_F = 0.80[a]
56 R = NPh_2, λ_{max}(em) = 583 nm, Φ_F = 0.79[a]

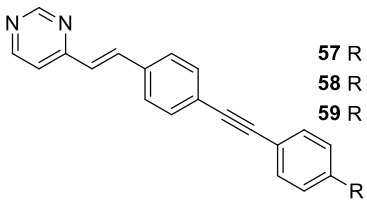

57 R = OCH_3, λ_{max}(em) = 460 nm, Φ_F = 0.51[a]
58 R = $N(CH_3)_2$, λ_{max}(em) = 612 nm, Φ_F = 0.54[a]
59 R = NPh_2, λ_{max}(em) = 590 nm, Φ_F = 0.41[a]

[a]Measured in CH_2Cl_2.

Figure 25. *PL properties of compounds* ***47–59*** *with gradually extended conjugated pathway.*

Influence of branching number

An addition of identical arm in C6 position of pyrimidine core results in substantial red-shift of the emission maxima in contrast to 4-substituted compounds: compare **47–50** and **52–53** with their disubstituted analogues **60–62**, **65**, **67–68** (*Figure 26*). Fluorescent quantum yield is also higher for bipodal compounds, except of compound **67**. Molecules **63**, **64** and **66**, analogues of **60**, **61** and **65** without the ethenylene bridge, showed blue-shift in emission maxima and higher fluorescence quantum yield. Concerning branching number, 4,6-disubtituted derivatives fluoresce at higher wavelength as compared to their 2,4,6-trisubstituted analogues (**64** vs **41**).

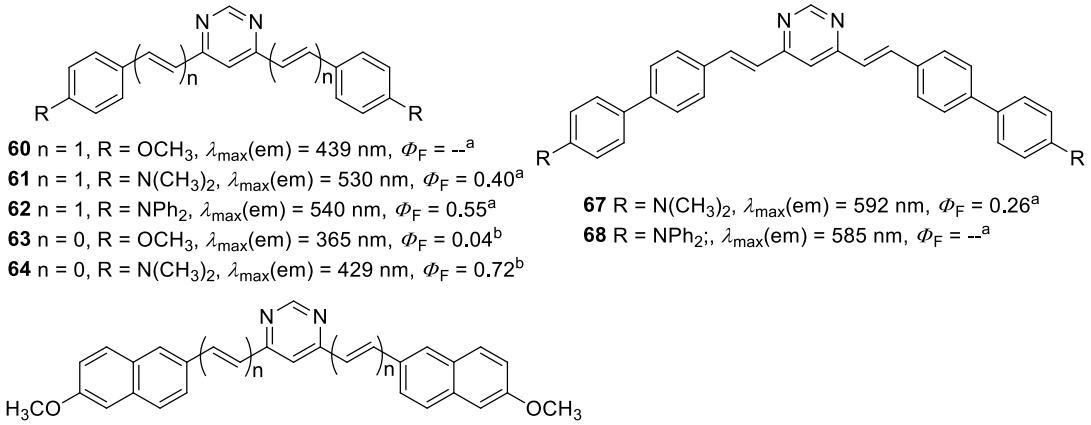

Figure 26. *Influence of additional vinylene linker and branching number on PL of pyrimidine fluorophores **60–68**.*

2.2.2 Overview of structure-2PA properties relationship

As already mentioned in *Chapter 1.1.4.*, nonlinear optically active organic materials have been subject of intensive research due to their interesting properties and application. In this context, research of pyrimidine-based chromophores for nonlinear optics started to growth during the last two decades.[113] Similar trends to those discussed in previous chapter can be concluded for pyrimidine 2PA chromophores.

Effect of electron-donors

When going from unsubstituted anthracene **69** and methoxy derivative **70** to amino derivatives **71** and **72** 2PA cross-section increases rapidly (*Figure 27*).[114] Among amino derivatives, 2PA cross-section raise within the following order: $N(CH_3)_2$ (**73**) < $N(CH_2CH_3)_2$ (**74**) < NPh_2 (**75**).[115] A replacement of alkyl groups in amino donors (**76** and **78**) with methoxyethoxyethyls (**77** and **79**) results in almost doubling of 2PA cross-section.[116–118]

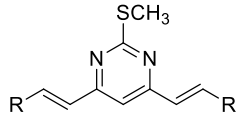

69 R = anthracen-9-yl, λ_{max}(2PA) = -- nm, δ_{max} = 21 GM[a]
70 R = 4-C_6H_4-OCH_3, λ_{max}(2PA) = -- nm, δ_{max} = 20 GM[a]
71 R = 4-C_6H_4-$N(CH_3)_2$, λ_{max}(2PA) = 800 nm, δ_{max} = 352 GM[a]
72 R = 4-C_6H_4-$N(CH_2CH_3)_2$, λ_{max}(2PA) = -- nm, δ_{max} = 901 GM[a]

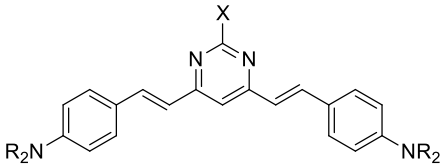

73 X = NH_2, R = CH_3, λ_{max}(2PA) = 840 nm, δ_{max} = 366 GM[a]
74 X = NH_2, R = CH_2CH_3, λ_{max}(2PA) = 840 nm, δ_{max} = 461 GM[a]
75 X = NH_2, R = Ph_2, λ_{max}(2PA) = 840 nm, δ_{max} = 625 GM[a]
76 X = Cl, R = C_6H_{13}, λ_{max}(2PA) = 850 nm, δ_{max} = 786 GM[a]
77 X = Cl, R = $(CH_2)_2O(CH_2)_2OCH_3$, λ_{max}(2PA) = 820 nm, δ_{max} = 1450 GM[a]
78 X = imidazol-1-yl, R = CH_2CH_3, λ_{max}(2PA) = 840 nm, δ_{max} = 1890 GM[b]
79 X = imidazol-1-yl, R = $(CH_2)_2O(CH_2)_2OCH_3$, λ_{max}(2PA) = 840 nm, δ_{max} = 2844 GM[b]

[a]Measured by TPEF technique in CH_3CN. [b]Measured by TPEF technique in benzene.

Figure 27. *Effect of donor on 2PA properties of compounds* ***69–79****.*

Effect of π-conjugated system

Concerning composition of π-conjugated linker, bridging with 2,5-thienylene unit is more efficient as compared to 1,4-phenylene analogue (**80** vs **81**), see *Figure 28*.[119] A replacement of 1,4-phenylene by fluorene moieties in **82** results in compound **83** with over two-times enhanced 2PA cross-section.[120] An addition of two ethynylene units in the conjugated linker decreases 2PA cross-section (**84** vs **85**).[121] Their exchange by triazole heterocycle, structurally closer to the pyrimidine ring, results in increased cross-section. However, a replacement of the other ethynylene units with triazole reduces the cross-section dramatically.

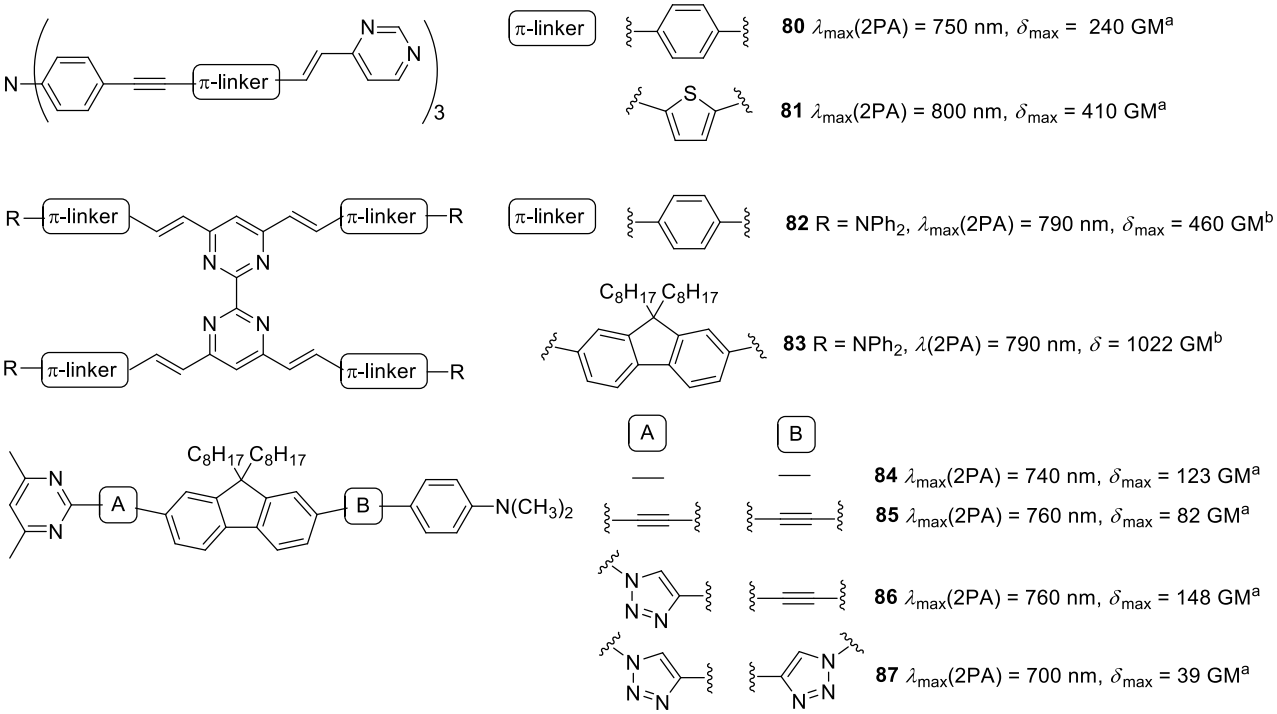

80 λ_{max}(2PA) = 750 nm, δ_{max} = 240 GM[a]
81 λ_{max}(2PA) = 800 nm, δ_{max} = 410 GM[a]
82 R = NPh_2, λ_{max}(2PA) = 790 nm, δ_{max} = 460 GM[b]
83 R = NPh_2, λ(2PA) = 790 nm, δ = 1022 GM[b]
84 λ_{max}(2PA) = 740 nm, δ_{max} = 123 GM[a]
85 λ_{max}(2PA) = 760 nm, δ_{max} = 82 GM[a]
86 λ_{max}(2PA) = 760 nm, δ_{max} = 148 GM[a]
87 λ_{max}(2PA) = 700 nm, δ_{max} = 39 GM[a]

[a]Measured by TPEF technique in CH_2Cl_2. [b]Measured by TPEF technique in $CHCl_3$.

Figure 28. *2PA properties of* ***80–87*** *with variable π-conjugated pathway.*

Effect of branching number

Electronic effect of C2 substituent directly influences 2PA properties. Donating groups reduce 2PA cross-section with increasing electron-realising strength as it is in a row **88** dimethylamino (340 GM) < **89** methoxy (390 GM) ~ **90** methyl (390 GM) < **91** none substituent (400 GM), see *Figure 29*.[122] On the contrary, chromophores with electron-withdrawing groups **92** and **93** show higher 2PA cross-section. Increased 2PA response with a higher number of branches is well-known trend as can be seen in pyrimidine derivatives, e.g. compare 4-pyranylidine molecule with 4,6-derivative (**94** vs **97**), diethylamino compounds (**95** vs **74**) and compounds **96** vs **79**.[114,116,123]

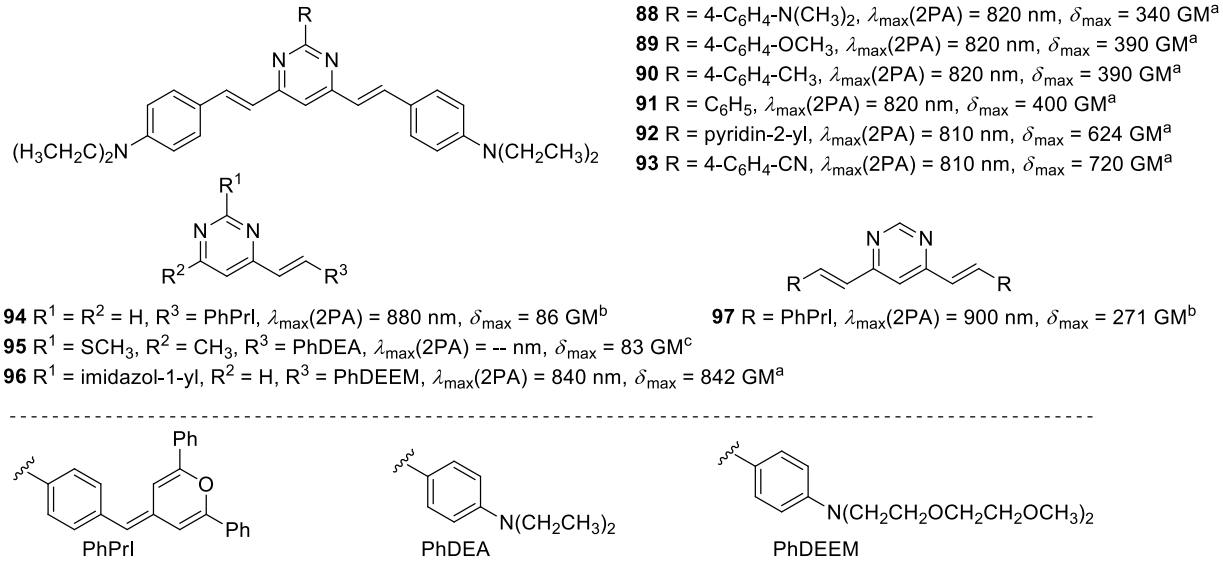

Figure 29. *Impact of C2 substituent and branching number on 2PA response of* ***88****–****97****.*

2.2.3 General synthetic approaches leading to pyrimidine-based fluorophores

Generally, pyrimidine derivatives can be prepared by a condensation reaction, in which the pyrimidine core is built during the reaction, or by decorating existing pyrimidine ring. The first synthetic approach is rather limited due to a low degree of substitution in final compound.[124] The second synthetic approach involves very versatile *cross-coupling* (C-C) reactions, Knoevenagel condensation, nucleophilic substitutions, *N*-alkylation etc. A large number of halogenated pyrimidine derivatives are commercially available. For example, Sigma Aldrich's catalogue contains 190 records of such compounds to date.[125] Two nitrogen atoms in pyrimidine nucleus attract electrons from cycle, lowers electron density in C2, C4 and C6 positions and facilitate nucleophilic substitution.[126] From the perspective of cross-coupling reaction feasibility, this electron-deficiency enables easier oxidative addition of a metal

into the carbon-halogen bond as compared to benzoid compounds. Hence, the reaction can be carried out under mild conditions without a need of sophisticated and expensive catalyst.[127,128] Manifold cross-coupling reactions with polyhalogenated pyrimidine occurs with high regioselectivity in the sequence C4, C6 and last C2 position.[129] Knoevenagel condensation, in the case of pyrimidine a reaction between activated methyl group of methylpyrimidine and aldehyde in acidic or basic condition, is simple and useful reaction for synthesis of vinylene-linked chromophores with exclusively *E* configuration.[130]

2.3 Influence of environment on the emission properties of pyrimidine chromophores

As it was mentioned in previous sections, microenvironment has a great impact on fluorescence performance. Together with easy tuning of fluorescence by structural changes, pyrimidine-based push-pull chromophores constitute a wide class of single- and two-photon fluorogenic probes for detection of solvent polarity, pH, cations, anions, organic compounds and cellular molecular structures in organic or aqueous solution as well as in living cells.

2.3.1 Pyrimidine fluorescent sensors

Probes for solvent polarity detection

Solvent polarity, beside other solvent's properties, plays a key rule during chemical reactions, and therefore its determination is crucial step in synthesis planning.[131] From the perspective of fluorescence, potential solvent polarity probe can exhibit negative or positive solvatochromism (for more details see *Chapter 1.1.5.*) based on different stabilisation of ground and excited state by surrounding solvent molecules. General approach towards pyrimidine-based solvent polarity probes is creation of push-pull structure with pyrimidine as an electron-withdrawing part connected through conjugated system of electrons with an electron-donating unit. This arrangement generally leads to polarization of molecule in ground and even more in excited state, and therefore to the positive solvatochromism. Three examples of such probes are displayed in *Figure 30* with their fluorescence spectra in various solvents as well as picture of their fluorescence.[110,132,133] For evaluation of their efficiency, shifts between emission maxima in toluene and CH_2Cl_2 were calculated as follows: **98** ($\Delta\upsilon$ = 2038 cm^{-1}), **99** ($\Delta\upsilon$ = 2124 cm^{-1}) and **55** ($\Delta\upsilon$ = 2537 cm^{-1}). These results indicates that the strength, and thus better distinguish of emission colour, raise in the row **98** < **99** < **55**.

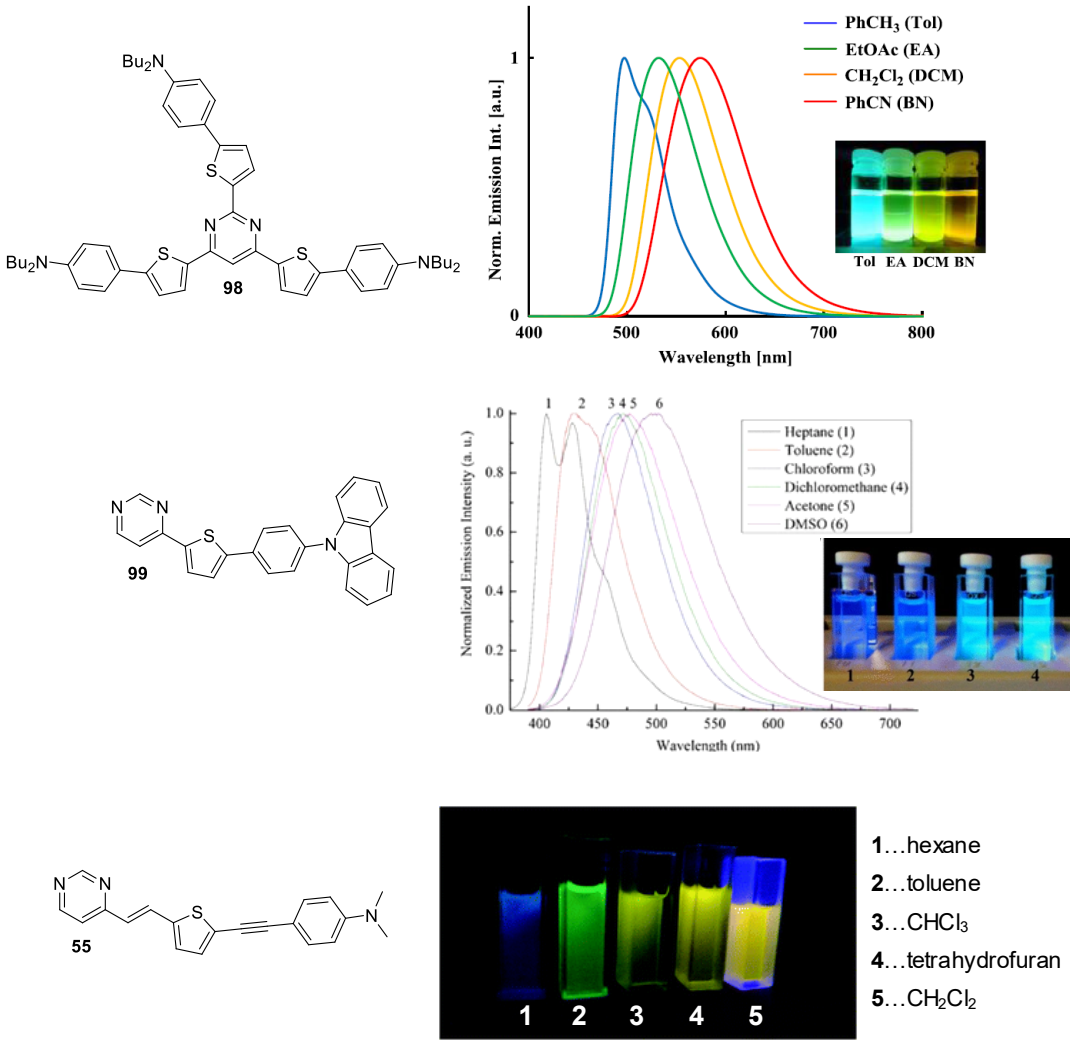

Figure 30. *Solvatochromic behaviour of* ***55****,* ***98*** *and* ***99*** *in solvents with various polarity.*[110,132,133]

Probes for ions detection

Pyrimidine-based chromophores found their application as cations probes due to their ability to provide electron lone pair into the complexation with cation. Suitable cation probe should exhibit high ion-selectivity and its complex with cation should have photophysical properties different enough (signal-selectivity) to allow to detect a colorimetric change (change in the colour of solution) or fluorometric change (change in the intensity or colour of emission) by naked eye or by measurement for qualitative and/or quantitative detection.[134]

Pyrene-based pyrimidine **100**, displayed in *Figure 31*, was designed as a selective Al^{3+} detector.[135] This compound fluoresces at 450 nm in the presence of Al^{3+} ion and has potential application as an intracellular sensor due to its ability crossing through the cell membrane. Fluorogenic compound **101** is another example of a selective "turn-on" probe for Al^{3+} ions detection.[136] Low cytotoxicity and chelation enhanced fluorescence upon exposing to Al^{3+}ions

in physiological medium make the compound **101** very promising intracellular probe. Intense green fluorescence is observed after addition of Al^{3+} salt into the solution of compound **102**.[137] Polyfluorene copolymer **103** with pyrimidine were prepared also as Al^{3+} probe, showing good metal ions selectivity and detection limit at approximately 2×10^{-8} M.[138]

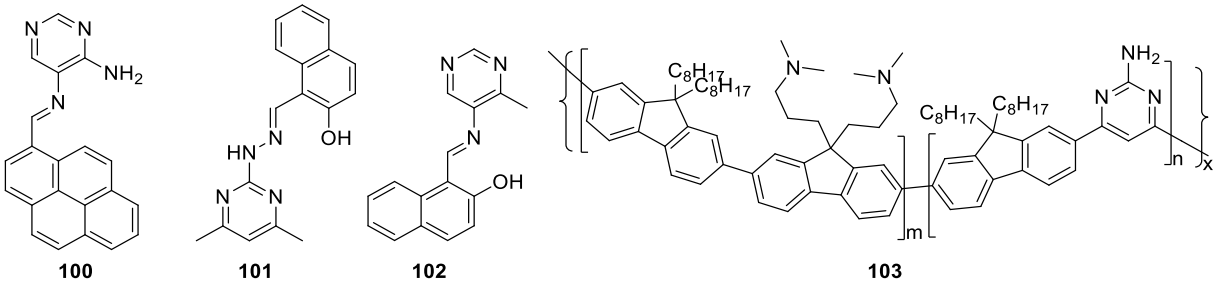

Figure 31. *Pyrimidine-based fluorogenic probes **100–103** for Al^{3+} ions detection.*

A blue to green colour switch of the emitted light was observed for compound **104** in the presence of Hg^{2+}, see *Figure 32*.[139] Advantages of this sensor are easy synthesis, ratiometric response and complete reversibility. *Goswami and co-workers* developed a test kit for detection of Hg^{2+} cations with filter paper coated with coumarin-based pyrimidine **105**.[140] Both colorimetric and fluorometric change can be easily seen by naked eye after dipping the test strip in studied aqueous solution. 2,4,6-Triaminopyrimidine **106** were employed in carbon dots, which fluorescence is selectively quenched by Hg^{2+} at pH 6 or by Ag^{+} under basic condition.[141] Pyrimidine derivative **107** possesses the ability to detect presence of Hg^{2+} and Cu^{2+} ions with both colorimetric and fluorometric change from yellow to red or orange, respectively.[142]

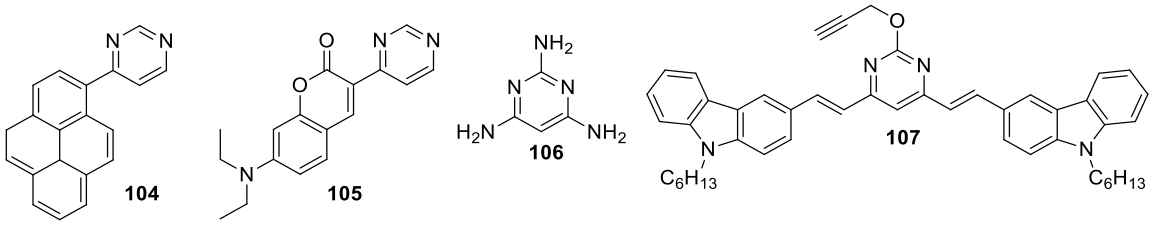

Figure 32. *Hg^{2+} selective pyrimidine-based fluorescent probes **104–107**.*

2,4-Dipyridyl-6-arylvinylpyrimidines **108–110** were developed as fluorogenic probes with moderate selectivity towards Zn^{2+} and Sn^{2+} cations in water (*Figure 33*).[143] Even though these probes were not soluble in water, they exhibited overall good performance towards studied analytes when the probes were impregnated in paper, see right part of *Figure 33*.

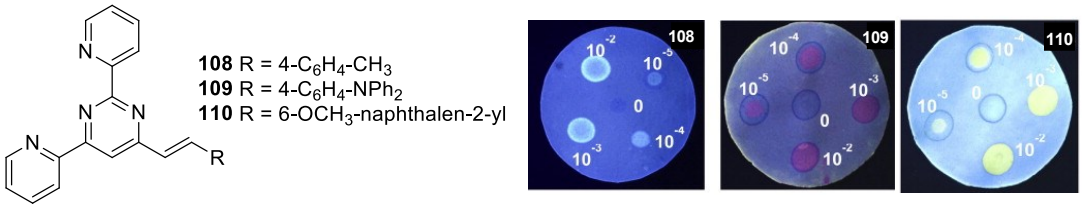

Figure 33. *Derivatives **108–110** as probes towards Zn^{2+} ions with picture of paper impregnated with these compounds and dotted with $ZnCl_2$ water solution taken under UV-lamp (λ_{em} = 254 nm).[143]*

Derivative **111** was tested as sensor for Fe^{2+}/Fe^{3+} cations, showing good fluorescence response in human prostate carcinoma cells (PC-3), see *Figure 34*.[144] Green light emitting compound **112** changes colour to orange in the presence of Cu^{2+} cations, other tested cations showed no influence on PL properties of this compound.[145] Pyrimidine-based fluorophores can be used as sensors for anions as well. An example of anion probe is compound **113**, which forms strong complexes selectively with F^- and HSO_4^- ions causing emission quenching.[146]

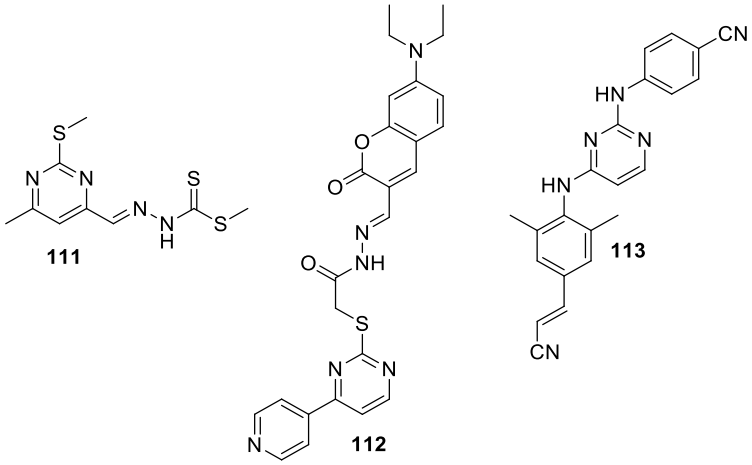

Figure 34. *Miscellaneous pyrimidine-based fluorescent probes **111–113**.*

Conventional fluorogenic probes for bioimaging

Fluorophores containing pyrimidine heterocycle show a great potential as probes for fluorescent imaging in living cells. Amino-substituted 4,6-distyryl derivatives **61** (*Figure 26*) and **114** (*Figure 35*) show high selectivity towards known Alzheimer's disease related alterations and high permeability through blood-brain barrier for **61**.[147] Fluorescence intensity of boron-ester **115** increases in the presence of H_2O_2, and thus this compound has a great potential for investigation of relationship between Parkinson's disease and H_2O_2 overexpression.[148] Pyrimidine compound **116** bears resorufin moiety (red part) in its C2 position and does not fluoresce.[149] However, biothioles (e.g. cysteine or glutathione), especially their thiolate anions, are strong nucleophiles which can trigger nucleophilic aromatic substitution on pyrimidine C2 position resulting in 2-biothiolepyrimidine and releasing

of fluorescent resorufin. Similar phenomenon is observed in compound **117**, but in this case, the S_NAr is triggered by thiophenol and released fluorescent unit is fluorescein (green part).

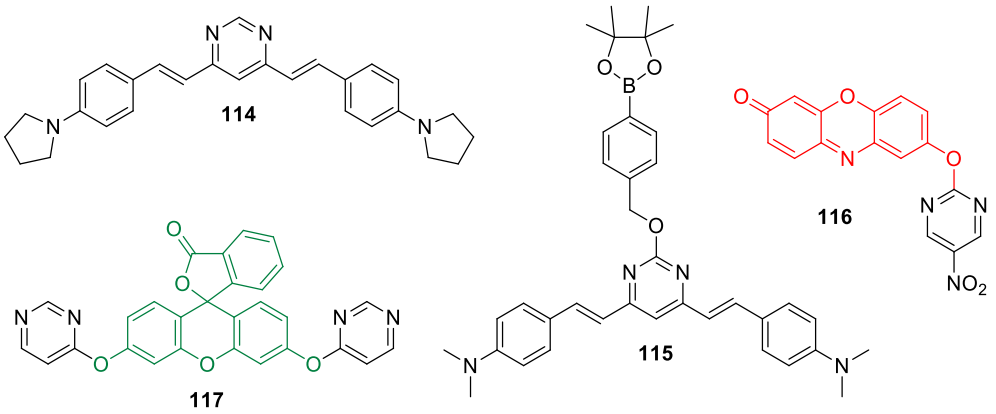

Figure 35. *Pyrimidine-based fluorophores **114–117** for bioimaging.*

Probes towards detection of nitroaromatic explosives

Verbistkiy and his group developed almost twenty push-pull molecules bearing pyrimidine electron-withdrawing unit as fluorescent sensors towards nitroaromatic explosives.[150] Generally, these compounds possess amino electron-donating group, such as triphenylamine, or carbazole or pyrene unit. Peripheral donating group is connected through 2,5-thienyle or 1,4-phenylene π-linkers with the pyrimidine ring in C2, C2/C4, C4/C5 or C4/C6 positions. These "turn-off" fluorescent probes show good selectivity and detection limit up to 7.4×10^{-7} M for 2,4-dintiroanisole (DNAN) explosive has been achieved for compound **118** (*Figure 36*). Compounds **62** (*Figure 26*) and **119** were tested as probes towards 2,4-dinitrotoluene vapours. The presence of alkoxy chain in C2 position of pyrimidine resulted in higher porous film of solid **119**, in which the diffusion, and therefore overall performance was improved in comparison to C2 unsubstituted **62**.

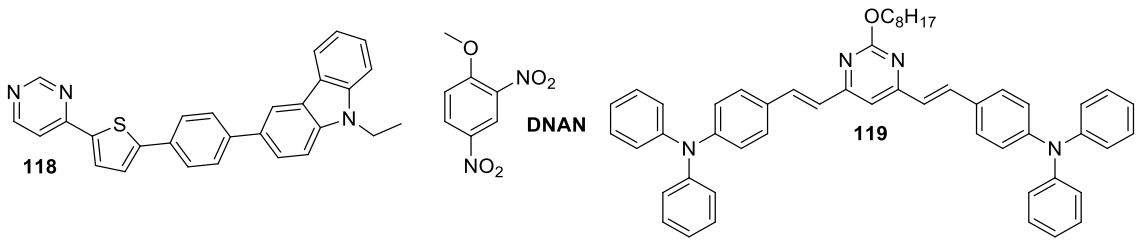

Figure 36. *Structure of sensor **118**, **119** and DNAN explosive.*

2PA fluorogenic probes for bioimaging

Figure 37 contains structure of pyrimidine derivatives with potential application as two-photon probes for bioimaging. Compounds **120** and **121** with peripheral piperazine donors were tested as probes for determination of bonding processes in DNA.[151] Their 2PA response

changes with molecular fluctuations during DNA bonding. Imidazole bearing molecules **96** (*Figure 29*) and **79** (*Figure 27*) were studied as fluorescent probes for cytoplasm imaging.[116] Compound **79** with D-π-A-π-D arrangement shows larger 2PA cross-section with brighter light response and low cytotoxicity. Derivatives **122** and **123** and their single-branched analogues **130** and **131** were tested as two-photon sensors in human HepG2 cancer cells in mice liver tissue.[152] All compounds showed moderate 2PA cross-section and as compared to *N*-ethoxy-substituted **123** and **131**, compounds **122** and **130** exhibit higher photostability in live cells and lower cytotoxicity. Fluorophores with imidazole (**78**, *Figure 27*) or pyrazole (**124**) C2 substituent were also studied as probes in human cancer cells showing good 2PA cross-section response.[118] Hexafluorophosphate derivatives **125** and **126** were tested as fluorogenic probes for imaging of organelles in living cells showing high selectivity towards mitochondria, good water solubility, high photostability, low cytotoxicity at concentration used for imaging and high signal ratio.[153] 2-Chloropyrimidine-based fluorophores **76** and **77** (*Figure 27*) were developed as two-photon probes for selective sensing of Fe^{3+} and Cu^{2+} in living cells with good 2PA cross-section.[117] Nitrobenzoxadiazole unit in non-fluorescent compound **127** can be selectively removed by biothiolates or sulfides resulting in fluorescent hydroxyphenylpyrimidine, which is measurable by 2PA.[154] This reaction was successfully used to detect presence of biothiolates in HeLa cells, mice brains and zebrafishes. Derivatives **128** and **129** show good properties as two-photon probes for cytoplasm staining, according to their good results from testing in Hep-G2 cells.[155]

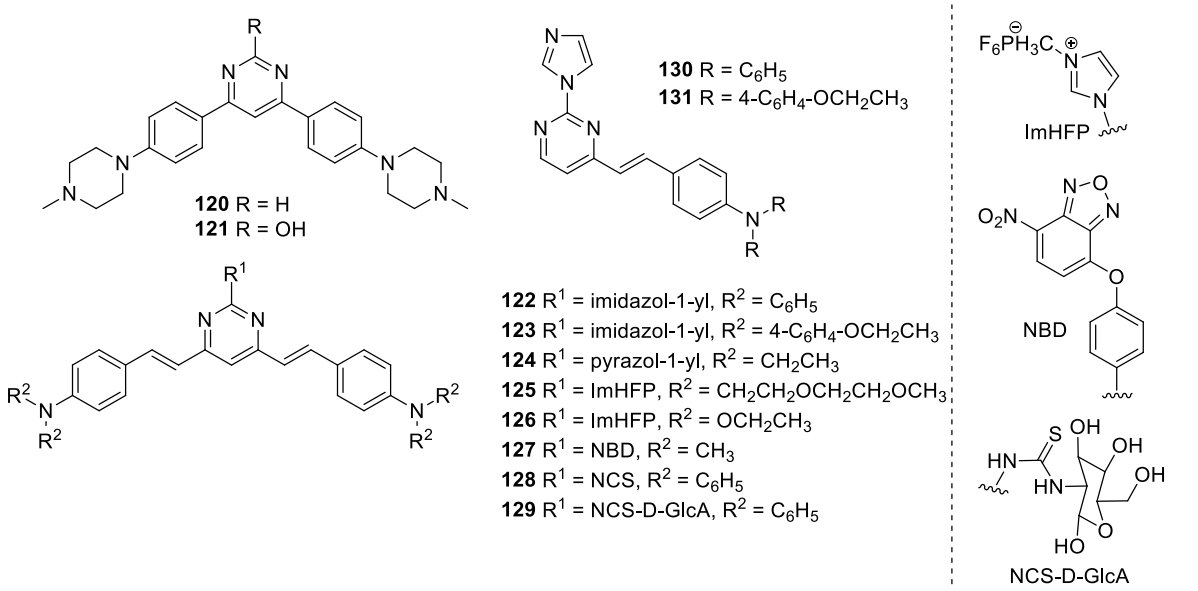

Figure 37. *Structures of 2PA probes* ***120–131*** *for bioimaging.*

2.3.2 White light emission by controlled protonation of pyrimidine chromophores

As discussed in Chapter 2.1., one of the pyrimidine's nitrogen can be easily protonated, see *Figure 38A*. This reversible reaction has great impact on photophysical properties of pyrimidine bearing chromophores.[109,156–158] In most cases, it leads to emission quenching, however in push-pull chromophores with long conjugated system and weak peripheral donor such as methoxy group or with limited π-conjugated system and slightly stronger donor such as carbazole, the protonation leads to creation of new red-shifted emission band. In certain point, when the solution with chromophore is only partially protonated, the "sum" of both neutral and protonated bands results in white light emission, see *Figure 38B*.

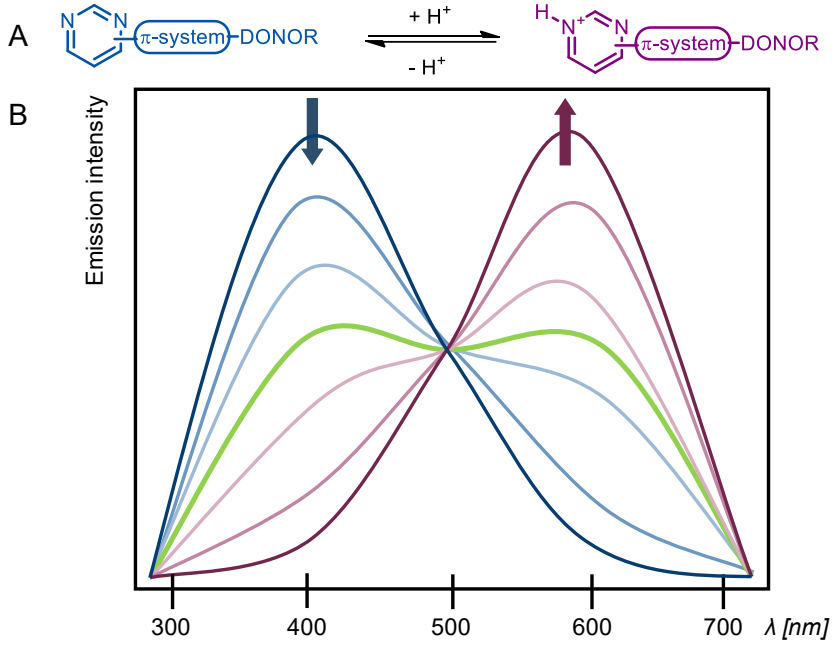

Figure 38. *(A) Protonation of pyrimidine chromophore and (B) schematical emission spectra of gradual protonation of pyrimidine chromophore.*

Achelle et al. have developed three pyrimidine-based fluorophores that provide white light by controlled protonation both in solution and solid state.[156,157] These compounds possess a great potential for fabrication of WOLED with only one emissive material.

First compound showing white emission from a mixture of its neutral and protonated species is **65** (*Figure 26*).[156] Progressive disappearance of emission maxima at 460 nm upon addition of trifluoroacetic acid is accompanied by appearance of red-shifted band of monoprotonated compound. Solution with 50 equivalents of acid shows dual emission of white light (*Figure 39A*). This trend was also observed in polystyrene films doped

with 1 wt% of **65** (*Figure 39B*) with CIE chromaticity coordinates (0.31, 0.30); compare to those of pure white light (0.33, 0.33).

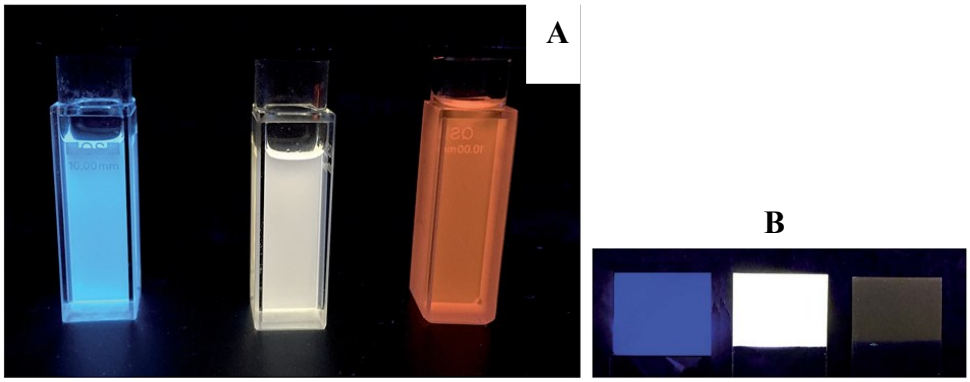

Figure 39. *(A) Photo of* ***65*** *with 0 equiv. (left), 50 equiv. (middle) and 1000 equiv. (right) of trifluoroacetic acid taken under UV lamp irradiation (λ = 366 nm) in (A) CH_2Cl_2 solution (B) polystyrene thin films. Reproduced with author permission (© The Royal Society of Chemistry 2015).*[156]

Second example is 4,6-diarylvinylpyrimdine **57** (*Figure 25*).[109] Its neutral form emits blue light in CH_2Cl_2 solution emission maxima at 460 nm with the fluorescence quantum yield $\Phi_F = 0.51$. During addition of trifluoroacetic acid, fluorescence of the emission band at 460 nm slowly decrease, whereas new red-shifted emission band, belonging to monoprotonated species, slowly appears (*Figure 40A*). White emission occurs when solution of **57** contains 100 equivalents of acid, see *Figure 40B*.

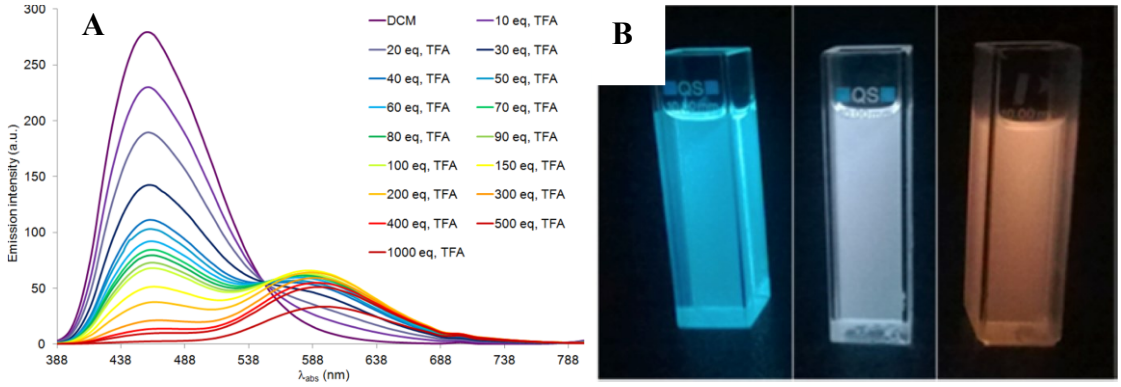

Figure 40. *(A)Fluorescence spectra of* ***57*** *with increasing concertation of trifluoroacetic acid in CH_2Cl_2. (B) Photos of neutral (left), partially protonated (middle) and fully protonated (right)* ***57*** *in CH_2Cl_2 solution taken under UV lamp irradiation (λ = 366 nm). Reproduced with author permission (© American Chemical Society 2016).*[109]

Last example is carbazole-substituted fluorophore **132** with the structure displayed in *Figure 40*. Its neutral form emits purple light in CH_2Cl_2 solution and fully protonated species by camphorsulfonic acid emits bright yellow light. White emission is observed after addition

of 45 equivalents of acid, see *Figure 41A*. Similar colour switch occurs in doped polystyrene thin film with CIE (0.30, 0.34) (*Figure 41B*).

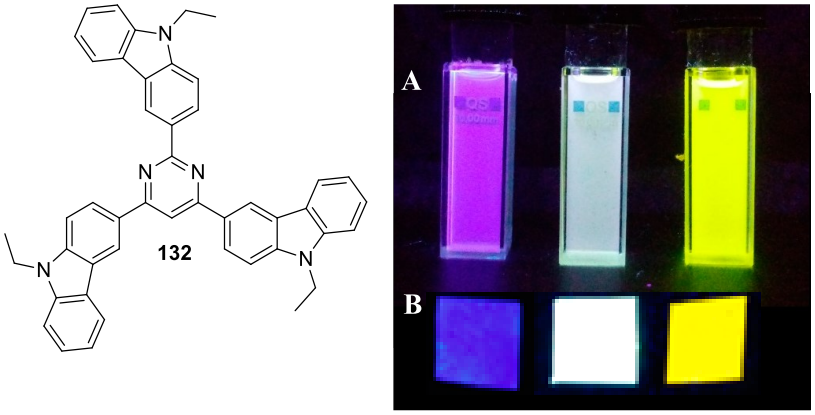

Figure 41. *Structure of fluorophore* ***132****. (A) Solution containing* ***132*** *and 0 equiv. (left), 45 equiv. (middle) and full protonation (right) under UV irradiation (hand-held lamp λ = 366 nm). (B)* ***132*** *doped into polystyrene thin films with 0 equiv., 0.1 equiv. and 80 equiv. of acid (from left to right). Reproduced with author permission.*[157]

2.4 Pyrimidine in OLEDs

Pyrimidine as an aromatic heterocycle with two nitrogen atoms, which cause electron-deficiency in the heterocycle, can provide electron lone pair for complexation or protonation, plays an important role as an organic semiconducting material.[87] Due to these properties, pyrimidine-based chromophores and transition metals complexes with pyrimidine ligands found their application among all three types of OLED emitters. In this point, it should be noted that devices discussed in following chapters will be compared to each other based on their EQE_{max} values, although these values are not the only characteristics of OLED devices. Reader is kindly asked to find more information about discussed devices in corresponding references.

2.4.1 First generation emitters

First generation OLED were developed with fluorescent material and due to their low efficiency, they have nowadays only limited application (for more details see *Chapter 1.2.5.*). Nevertheless, before invention of TADF emitters, fluorescence emitters attracted researchers interest due to the fact that often emitted blue light, which is in contrast to the second generation emitters[87] A few of pyrimidine-based devices can be found in literature such as compounds **133** and **134**, see *Figure 42*.[159,160] Both of these devices emitted blue light with EQE_{max} of 4% for **134**.

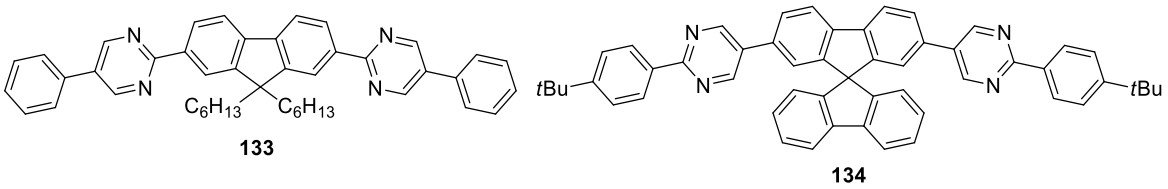

Figure 42. *Fluorene- and spirofluorene-based pyrimidines* ***133*** *and* ***134*** *as first generation emitters.*

2.4.2 Second generation emitters

The majority of second generation emitters bearing pyrimidine-based ligands found in literature are iridium(III) complexes connected to the nitrogen or carbon atom of pyrimidine and also similar platinum(II) complexes, however in a significantly lower number. Iridium (III) complexes bearing bidentate pyrimidine-based ligands show great potential for fabricating high performance PhOLEDs. Complex **135** derived from the simplest ligand 2-phenylpyrimidine shows EQE_{max} 13.9% as green light-emitting device with 10% doping (*Figure 43*).[161] Change of ancillary ligand and addition of two fluorine atoms results in rapid decrease of EQE_{max} to 2.2% for compound **136**.[162] Introduction of fluorine atom into C5 pyrimidine position of **137** leads to significant decrease of EQE_{max} to 5.3%. On the other hand, the OLED device based on dinuclear iridium complex with the same fluorinated ligand showed 17.9% EQE_{max}.[163] *Sarma et al.* published study about Ir complexes with fluorine atoms on the phenyl ring of 2-phenylpyrimidine ligands **138–140**.[164] All three complexes carry different ancillary ligands and emit sky-blue light. The corresponding OLEDs have the EQE_{max} within the outstanding range of 30.1 to 31.3 %. Compound **141** with bis(diphenylphorothioyl)amide (stpip) ancillary ligand also emits sky-blue light with EQE_{max} over 19%.[165] Green light emitting device was fabricated with 10% doping of **142** and EQE_{max} 14%.[166] Complex **143** containing stpip ancillary ligand incorporated in green OLED reveals 30.8 % EQE_{max}.[167] A series of bright-blue devices were fabricated with 7% doping of **144–146** revealing that fluorinated pyrimidine ligand **146** (EQE_{max} 21.23%) is more efficient than ligands with trifluoromethyl groups **144** and **145** (EQE_{max} around 18.6%).[168] Compounds **148–150** were prepared as dopants for bluish-green OLEDs showing small decrease in external quantum yield with introduction of fluorine in C5 position of pyrimidine; compare **147** (32.5%) and **148** (35.0%) with their fluorinated analogues **149** (31.1%) and **150** (33.7%).[169] Last example of phenyl-pyrimidine based cyclometallating ligands for iridium complexes is compound **151**. Using this emitter, a green light emitting OLED has been described with 6% doping of and EQE_{max} over 27%.[170] In the same article, complex **152** was tested as dopant for green OLED showing that exchange of phenyl with pyridyl leads to increase in quantum yield up to 32%. Three other green light-emitting diodes based

on 2-(pyrid-4-yl)pyrimidine complexes **153–155**, developed by *Han and co-workers*, have accomplished the 29.5–31.8% EQE_{max}.[171]

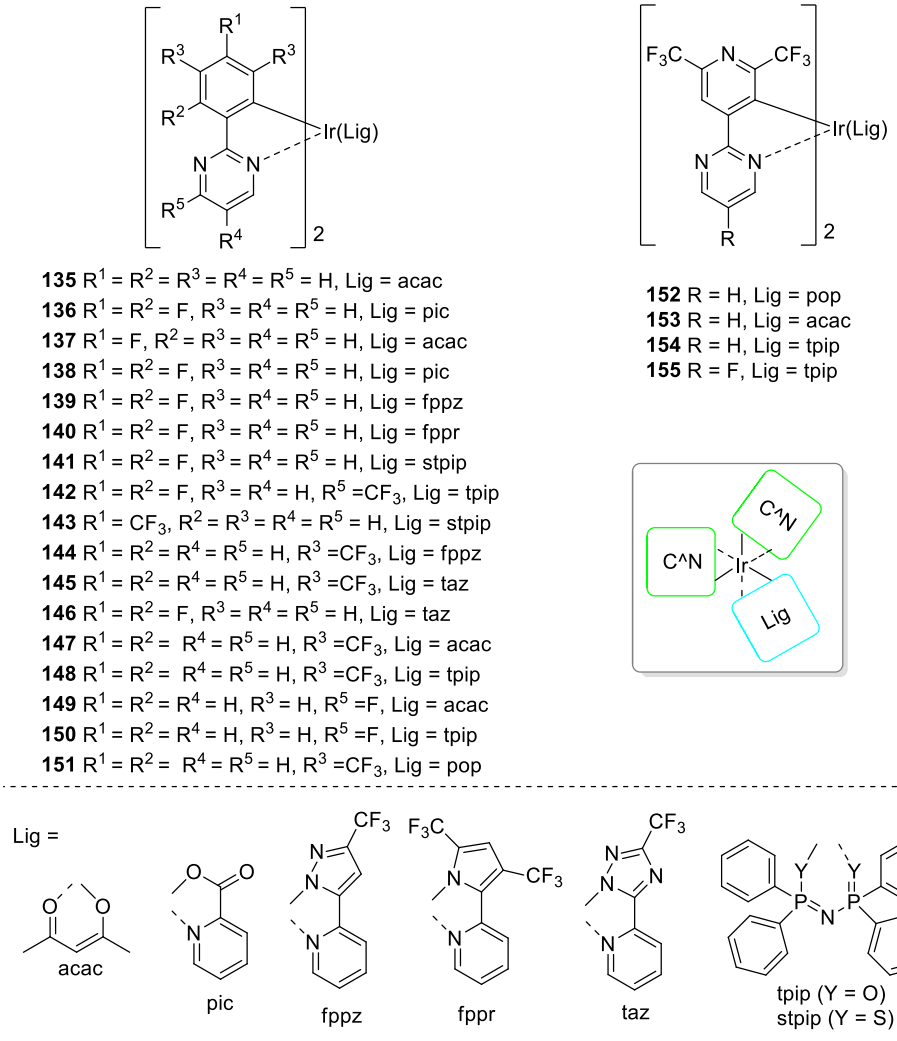

135 $R^1 = R^2 = R^3 = R^4 = R^5$ = H, Lig = acac
136 $R^1 = R^2$ = F, $R^3 = R^4 = R^5$ = H, Lig = pic
137 R^1 = F, $R^2 = R^3 = R^4 = R^5$ = H, Lig = acac
138 $R^1 = R^2$ = F, $R^3 = R^4 = R^5$ = H, Lig = pic
139 $R^1 = R^2$ = F, $R^3 = R^4 = R^5$ = H, Lig = fppz
140 $R^1 = R^2$ = F, $R^3 = R^4 = R^5$ = H, Lig = fppr
141 $R^1 = R^2$ = F, $R^3 = R^4 = R^5$ = H, Lig = stpip
142 $R^1 = R^2$ = F, $R^3 = R^4$ = H, $R^5 = CF_3$, Lig = tpip
143 $R^1 = CF_3$, $R^2 = R^3 = R^4 = R^5$ = H, Lig = stpip
144 $R^1 = R^2 = R^4 = R^5$ = H, $R^3 = CF_3$, Lig = fppz
145 $R^1 = R^2 = R^4 = R^5$ = H, $R^3 = CF_3$, Lig = taz
146 $R^1 = R^2$ = F, $R^3 = R^4 = R^5$ = H, Lig = taz
147 $R^1 = R^2 = R^4 = R^5$ = H, $R^3 = CF_3$, Lig = acac
148 $R^1 = R^2 = R^4 = R^5$ = H, $R^3 = CF_3$, Lig = tpip
149 $R^1 = R^2 = R^4$ = H, R^3 = H, R^5 = F, Lig = acac
150 $R^1 = R^2 = R^4$ = H, R^3 = H, R^5 = F, Lig = tpip
151 $R^1 = R^2 = R^4 = R^5$ = H, $R^3 = CF_3$, Lig = pop

152 R = H, Lig = pop
153 R = H, Lig = acac
154 R = H, Lig = tpip
155 R = F, Lig = tpip

Figure 43. *Heteroleptic iridium complexes bearing 2-phenylpyrimidine* ***135–151*** *and 2- pyridylpyrimidine* ***152–155*** *ligands.*

Figure 44 displays iridium(III) complexes with 5-pyridylpyrimidines, 4,6-diaryl- or 4,6 arylpyridylpyrimidines and also pyrimidine-based tridentate ligands. Complexes **156–161** with 4-pyridylpyrimidine ligands were employed as dopants in blue and bluish green OLEDs and showed external quantum efficiency between 11.5 and 13.7% (*Figure 44*).[172,173] Bipodal compounds **160–166** revealed to have versatile use as emitting dopants in phosphorescent OLEDs. *Tong and co-workers* prepared two green PhOLEDs with compounds **160** and **161** and performance between 10 and 17% EQE_{max}.[174] Compounds **162** and **163** were doped in emissive layer of orange and white devices with excellent performance over 26.8% of EQE_{max}.[175] Change of ancillary ligands in the compounds **164–166** allows variation of the colour from sky-blue to deep-blue with EQE_{max} 10–13 %.[176] Series of bis-tridentate iridium complexes **167–172** was prepared by *Chen et al.*.[177] All complexes exhibit blue

or green emission with EQE_{max} in the range of 14.5 to 18.7%. Overall, complexes with phenyl moiety in position C4 of pyrimidine are slightly more efficient than complexes with phenyl ring in position C2.

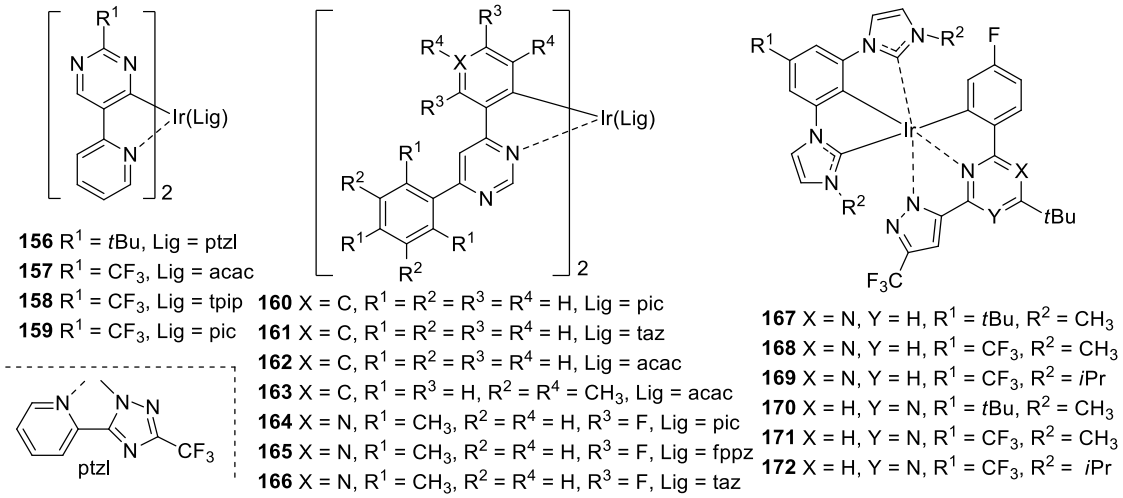

Figure 44. *Structure of iridium complexes with 4-pyridylpyrimidine ligands* ***156–159****, 4,6-substituted pyrimidines* ***160–166*** *and bis-tridentate ligands based on 2,4-substituted pyrimidines* ***167–172****.*

Platinum complexes with pyrimidine-based ligands have attracted researchers' interest in last few years (*Figure 45*). A series of homoleptic complexes **173–176** was prepared to study influence of nitrogen atom on photophysical properties of prepared OLED devices.[178] When changing orientation of nitrogen heterocycles, colour of emitted light is changing from yellow to red and external quantum efficiency varies between 19.7 and 27.5%. Non-doped OLED fabricated with complexes **177–180** prepared by *Wang and co-workers* achieved efficiency around 10% in NIR region.[179] *Shafikov et al*. have prepared two dinuclear Pt complexes **181** and **182** as emissive layer for NIR with EQE_{max} 9.9 and 3.6%, respectively.[180,181]

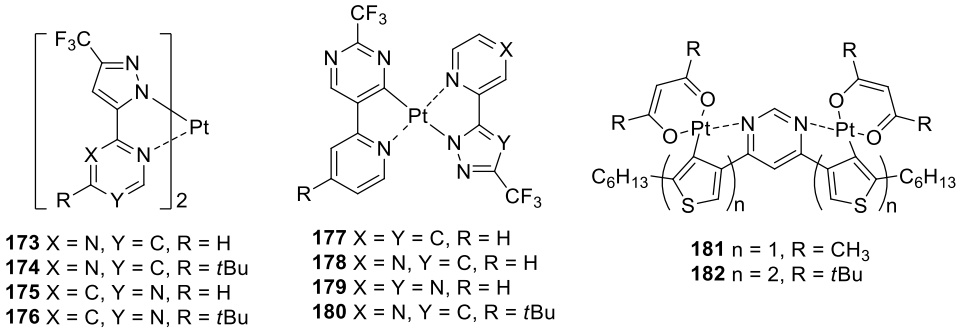

Figure 45. *Pyrimidine-based platinum(II) complexes.*

2.4.3 Third generation emitters

The use of TADF phenomena in OLED technology, done by *Adachi et al.* between the years 2009 and 2012, was a breaking point in development of highly efficient OLED

devices.[182–184] General advantages of TADF emitters was already discussed in *Chapter 1.2.5*. The crucial concept in these materials is creation of low energy difference between singlet and triplet excited, which can be achieved by spatial separation of frontier orbitals, by for example steric hindrance. One of the first pyrimidine-based TADF emitters were developed by *Komatsu and co-workers* in 2016 and since that pyrimidine chromophores with delayed fluorescence repeatedly proved their importance to this subject.[185]

Diphenylpyrimidines **183–185** were studied as TADF emitters for purely organic blue OLEDs (*Figure 46*).[186] The performance of OLEDs based on these materials judged by EQE_{max} was 6.72% for **183**, 10.9% for **184** and 8.50% **185**, respectively. Triphenylpyrimidines **186** and **187** are other examples of TADF emitters.[187] Despite their low EQE_{max}, i.e. 6.20% (**186**) and 5.80% (**187**), they exhibit excellent deep-blue light performance. *Serevičius et al*. synthesized two carbazole bearing TADF dopants **188** and **189** and fabricated deep-blue device with EQE_{max} 8.7% and blue OLED with EQE_{max} 19.7%, respectively.[188,189]

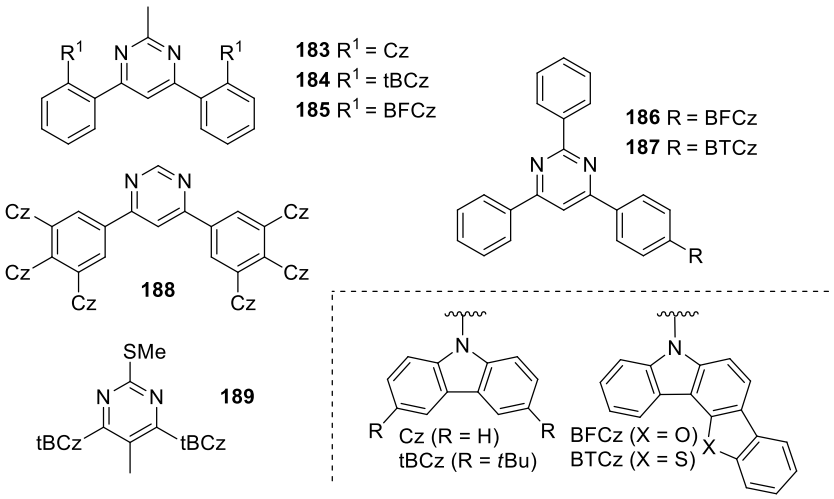

Figure 46. *Pyrimidine derivatives **183–189** bearing carbazole moiety as emitters in OLEDs.*

Beside carbazole unit, acridine moiety is also very popular donating group for designing TADF emitters, see *Figure 47*. *Nakao et al.* have synthesized and characterized a series of TADF emitters **190–192**.[190] Through changing the molecular structure they were able to control emission colour, TADF efficiency, and therefore, EQE_{max} which vary from 11.8% for blue **190**, 18.6% for bluish-green **191** to 22.8% for green **192**. Compounds **193–195** are very promising materials for displays and solid-state lighting application.[191] With their highly twisted structure they possess small ΔE_{ST}, hence, efficient TADF. They achieved excellent EQE_{max} as blue OLEDs 25.56, 24.34 and 31.45% for **193**, **194** and **195**, respectively. TADF luminophores **196** and **197** were chosen as interesting OLED emitters due to the pure blue emitting properties.[192] OLED devices fabricated from these materials exhibited EQE_{max}

around 20% for both compounds. AIE-TADF emitter **198** designed by *Zhang et al*. was prepared together with its triazine analogue.[193] EL performance of OLEDs doped with these luminophores demonstrated that pyrimidine central core is more convenient than the triazine one (EQE_{max} 22.0 vs. 13.2%). Compounds **199** and **200** were prepared as TADF dopants for green OLEDs showing excellent performance with *EQE* of 31.3 (**199**) and 30.6% (**200**).[194] Acridine-pyrimidine push-pull luminophores **201–205** were employed into the structure of deep-blue devices with external quantum efficiency in the range of 11.4–20.4%.[195]

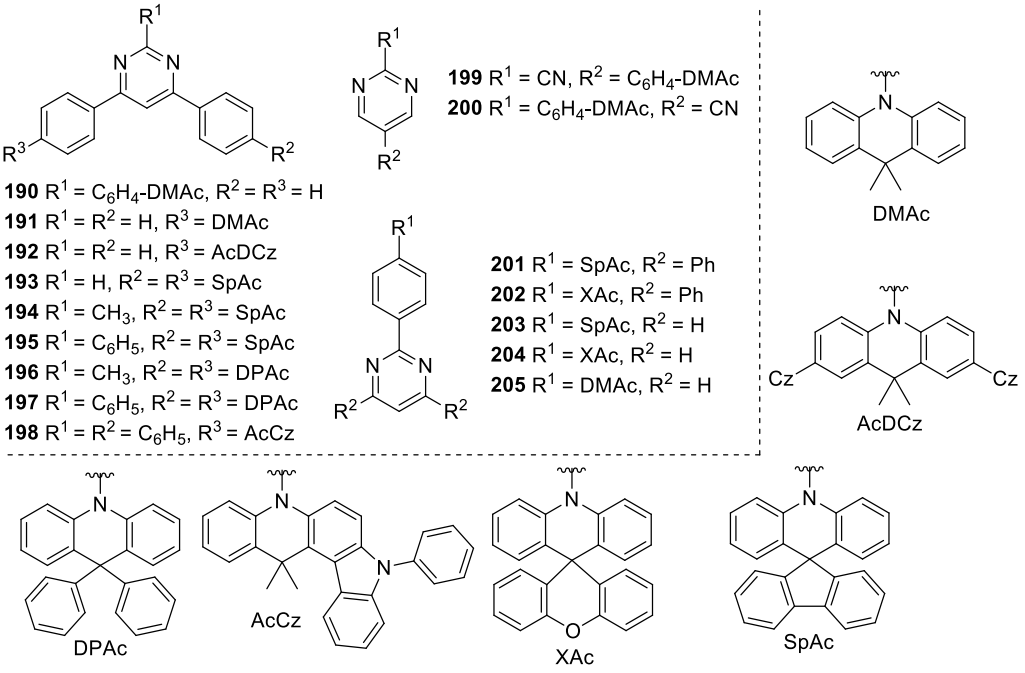

Figure 47. *Pyrimidines **190–205** with peripheral acridine units.*

Phenoxazine is also suitable donating unit for TADF luminophores, which brings a twisted butterfly-shaped structure (*Figure 48*). Compounds **206-208** were used as green dopants in highly efficient OLEDs.[196] EQE_{max} increases with increasing size of substituent in C2 position of pyrimidine core in the following order: H (**206**, 19.9%) < methyl (**207**, 22.2%) < phenyl (**208**, 24.6%). Changing the methyl position on 1,4-phenylene linker between pyrimidine and phenoxazine in compounds **209-211** improved the RISC and modified the light colour in the bluish green to green range, as well as EQE_{max}.[197]

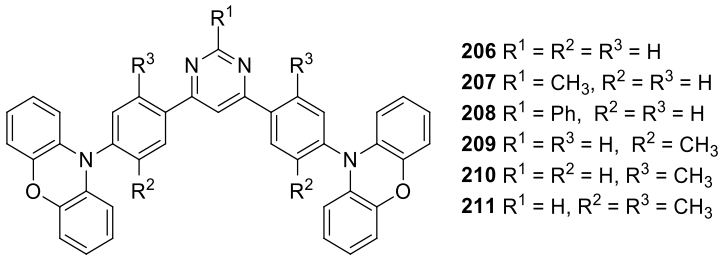

Figure 48. *TADF pyrimidine luminophores* ***206–211*** *featuring phenoxazine donor unit.*

2.4.4 Other application of pyrimidines in OLED

Electron deficiency of pyrimidine ring in comparison to benzene or pyridine ring brings a higher electronically negative character, and therefore enhanced electron-transporting and injection properties, which are crucial for host materials.[87] Especially a combination of pyrimidine with electron-donating group can lead to promising bipolar host materials.

Aizawa et al. have prepared pyrimidine-based host material **212** for solution-processed phosphorescent OLEDs which can lower the operating voltage (*Figure 49*).[198] Compound **213** provides a good host environment for red, green and also blue PhOLEDs.[199] Carbazole-based derivative **214** was tested together with **213** as host materials showing that both are suitable for red OLED with $Ir(piq)_3$ dopant.[200] Compounds **215–218** bearing indenocarbazole moiety were also synthesized as bipolar host materials for efficient green PhOLEDs with good electro-optical and thermal properties.[201] OLED devices with 5wt% of $Ir(ppy)_3$ dopant possess EQE_{max} within the range of 19.5–21.7%. Another carbazole-pyrimidine host materials **219** and **220** were developed by Li and co-workers.[202] These two isomeric bipolar molecules with weak TADF behaviour have shown to be useful hosts for highly efficient blue and green TADF-based OLEDs. When comparing the devices with asymmetric host **219**, the symmetric-hosted OLED gave higher EQE_{max} both in blue (20.4 vs. 15.0%) and green light-emitting diode (24.0 vs. 22.5%).

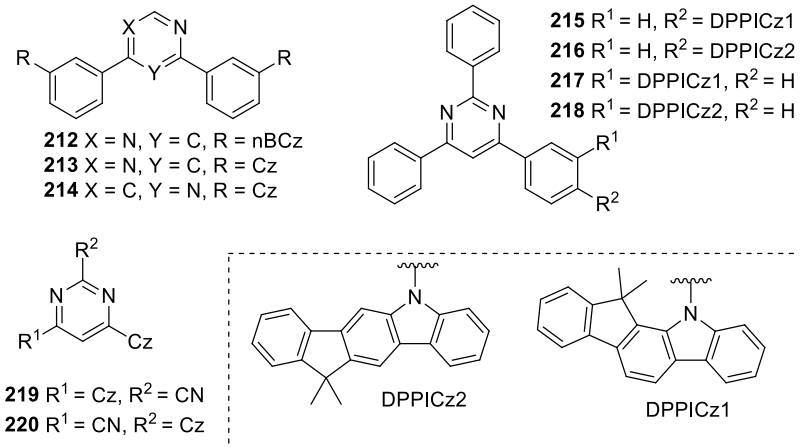

Figure 49. *Pyrimidine-carbazole host materials* ***212–220****.*

Spirobifluorene-based compound **221** and **134** (*Figures 50 and 42*) were developed as host materials for OLEDs. The bipolar material **221** was built into the scaffold of yellow phosphorescent organic light-emitting diode improving its maximum current, power and external quantum efficiencies.[203] Compound **134** was studied as emitting host in bright blue OLED showing high PLQY in neat film and good thermal stability.[160] Compound **222** has been employed as a host material in bluish-green OLED with EQE_{max} 13.0% and hybrid WOLED with EQE_{max} of 15.6%.[204]

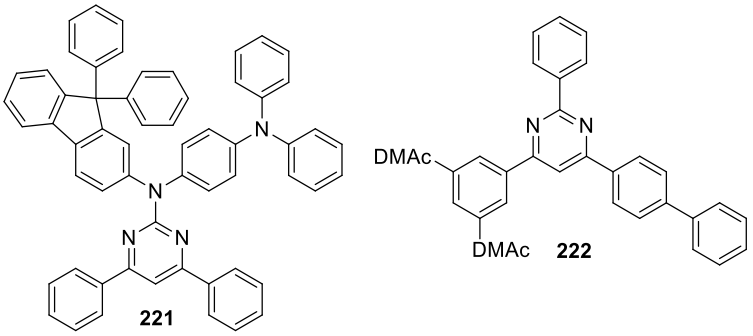

Figure 50. *Miscellaneous pyrimidine-based host materials* ***221*** *and* ***222****.*

Good electron injection properties are necessary for ETM, and thus the pyrimidine ring with its electron-deficiency is adequate candidate for application.[87] Bipodal compounds **223–225**, displayed in *Figure 51*, were prepared as ETM by *Sasabe et al.* for TADF OLEDs showing ultrahigh power efficiency over 130 $lm.W^{-1}$. Tripodal structures **226** and **227** have been designed as hole blocking material with deep HOMO level for high performance phosphorescent OLED devices.[205] Dibenzo[*b*,*d*]furan derivative **228** was designed as hole blocking material for blue phosphorescent OLED exhibiting improved performance in contrast to conventionally used HBL materials carrying heteroaromatic electron-attracting group.

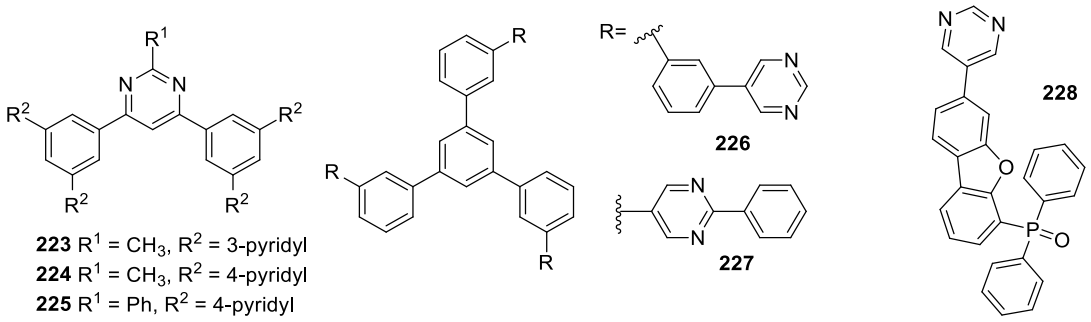

Figure 51. *Pyrimidine derivatives as electron-transporting material* ***223–225*** *and hole-blocking material* ***226–228****.*

CHAPTER III. The development of a new series of pyrimidine chromophores based on 2,4-di(arylvinyl)- and 2,4,6-tri(arylvinyl)-pyrimidines

3.1 Introduction

Whereas 4,6-distyrylpyrimidine chromophore have been extensively studied in the literature,[103] until now, only unsubstituted 2,4-distyryl and 2,4,6-tristyrylpyrimidines have been prepared.[206–208] Therefore, a new series of bipodal and tripodal arylvinyl-branched push-pull chromophores was designed to fill up an empty space among multipodal aryl-, arylvinyl- and arylethynylpyrimidines. As mentioned in the previous chapter and as can be found in the literature, multibranched pyrimidine compounds exhibits interesting fluorescence and 2PA properties.[103,113] Furthermore, star-shaped three-branched molecules with a $(D\text{-}\pi)_3\text{-}A$ topology are scarce, especially those without C_3 symmetry.[209–215] With this in mind, novel derivatives were prepared with 2,4-di(arylvinyl) or 2,4,6-tri(arylvinyl) substitution on pyrimidine central core with electron-donating and electron-withdrawing groups in alternating peripheral positions, see a schematic arrangement in *Figure 52*.

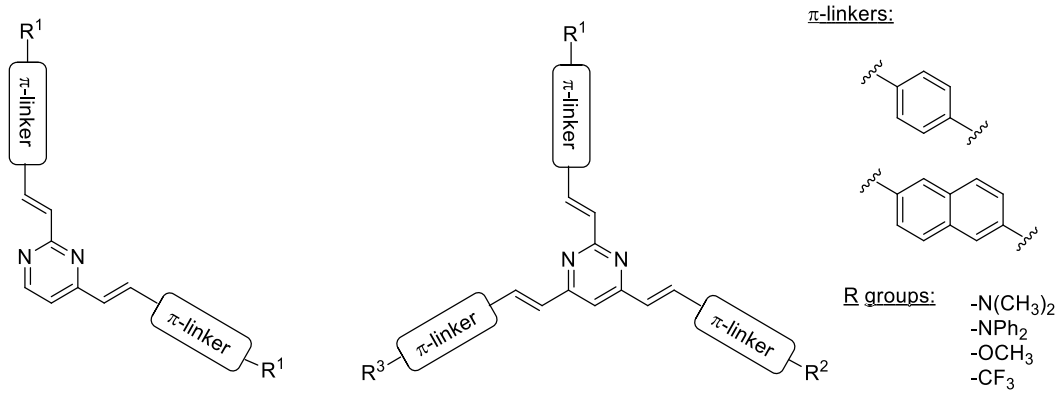

Figure 52. *Design of a novel series of 2,4-di(arylvinyl) and 2,4,6-tri(arylvinyl)pyrimidines.*

2,4-Di(arylvinyl)pyrimidines were prepared with identical donating groups on both arms ($(D\text{-}\pi)_2\text{-}A$). As far as 2,4,6-tri(arylvinyl)pyrimidines are concerned, derivatives can be sorted into three subgroups depending on the substituents: (i) similar donating groups on all three arms ($(D\text{-}\pi)_3\text{-}A$), (ii) C2 position substituted with electron-donating or electron-withdrawing groups and identical donating substituents on C4 and C6 arms ($(D^1\text{-}\pi)_2\text{-}A^1\text{-}(\pi\text{-}A^2/D^2)$) and (iii) different donor groups in all three positions ($(D^1\text{-}\pi)(D^2\text{-}\pi)\text{-}A(\pi\text{-}D^3)$). To evaluate the influence of C2 substituent, new chromophores and their properties will be compared to known compounds **51–53** (see *Figure 26* for their structure).[107,111] 2,4-Distyryl and 2,4,6-tristyrylpyrimidines were prepared as well for comparison.

Following chapters will be mostly dedicated to the novel series of 2,4-di(arylvinyl)- and 2,4,6-tri(arylvinyl)pyrimidines. Besides that, selected final chromophores were further studied along with their 4-arylvinyl- and 4,6-di(arylvinyl)pyrimidines analogues. Results of study focusing on effect of protonation on fluorescence dynamics are provided in *Chapter 3.4*. Furthermore, *Chapters 3.4, 3.5* and *3.6* are completed with outcomes from investigating (multi)branching effect on linear and nonlinear optical properties.

3.2 Synthesis

Palladium catalysed C-C reactions and Knoevenagel condensation are versatile reactions for construction of pyrimidine derivatives. Synthesis of final compound by multifold Knoevenagel condensation was considered, however, the methylated starting material is not commercially available, and its synthesis showed to be a very inconvenient. Nevertheless, 2-chloro-4-methylpyrimidine and 2-chloro-4,6-dimethylpyrimidine are commercially available products, in which the chlorine atom can be replaced by vinylene moiety by C-C reaction. For this purpose, palladium catalysed Suzuki-Miyaura reaction was employed.[128,216] Starting terminal alkyne underwent *in situ* hydroboration with catecholborane, while two portions of catecholborane were added over three hours under nitrogen atmosphere (*Scheme 1*). Without quenching the reaction, Suzuki-Miyaura cross-coupling was subsequently carried out with 2-chloropyrimidines providing 4-methylpyrimidines **229** or 4,6-dimethylpyrimidines **230** in moderate yields.

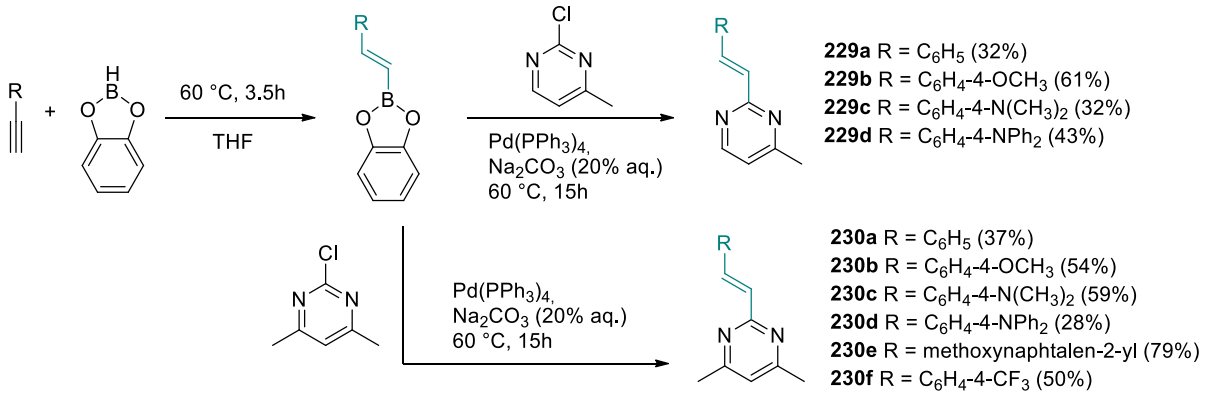

Scheme 1. *Two steps one-pot reaction leading to intermediates **229** and **230**.*

Starting from **229**, arylvinyl arm was introduced in position C4 by Knoevenagel condensation between activated methyl group of **229** and an aldehyde (*Scheme 2*).[111] The reaction was performed in boiling 5M aqueous solution of NaOH with Aliquat® 336 as phase-transfer catalyst. All final bipodal chromophores **231** were obtained in moderate to good yields. The reaction of intermediates **230** with C4 and C6 methyl groups was carried

out in similar manner with two equivalents of the corresponding aldehyde. Final tripodal derivatives **232** with identical substitution on all arms or with different substituent in C2 position were obtained with modest to good yields. Lower yields were observed for compounds **232a–d** with unsubstituted C2 styryl unit due to a complicated purifying process. Lower yields for diphenylamino compounds **232p** and **232s** resulted from multiple recrystallizations, which were necessary to remove Aliquat® 336 from final products.

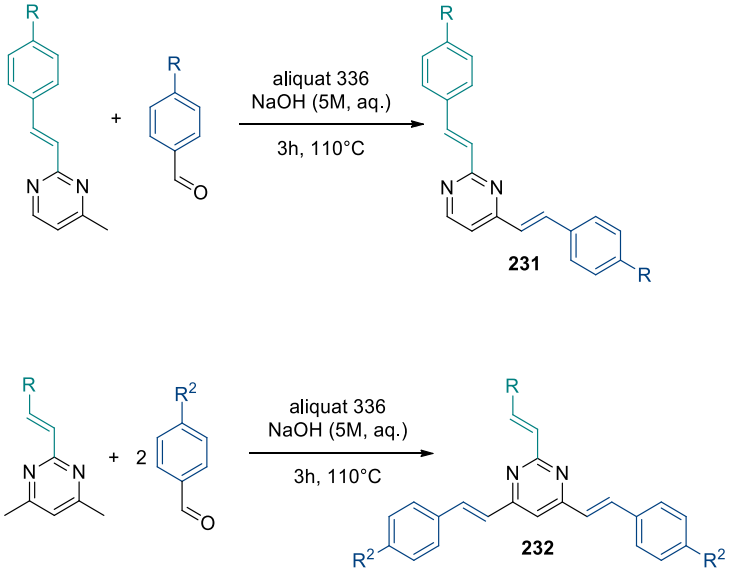

231a R = H (57%)
231b R = OCH_3 (84%)
231c R = $N(CH_3)_2$ (85%)
231d R = NPh_2 (41%)

232a R = Ph, R^2 = H (28%)
232b R = Ph, R^2 = OCH_3 (24%)
232c R = Ph, R^2 = $N(CH_3)_2$ (17%)
232d R = Ph, R^2 = NPh_2 (21%)
232e R = C_6H_4-4-OCH_3, R^2 = OCH_3, (79%)
232f R = C_6H_4-4-OCH_3, R^2 = $N(CH_3)_2$ (74%)
232g R = C_6H_4-4-OCH_3, R^2 = NPh_2 (80%)
232h R = C_6H_4-4-$N(CH_3)_2$, R^2 = OCH_3 (57%)
232i R = C_6H_4-4-$N(CH_3)_2$, R^2 = $N(CH_3)_2$ (65%)
232j R = C_6H_4-4-$N(CH_3)_2$, R^2 = NPh_2 (68%)
232k R = C_6H_4-4-NPh_2, R^2 = OCH_3 (73%)
232l R = C_6H_4-4-NPh_2, R^2 = $N(CH_3)_2$ (43%)
232m R = C_6H_4-4-NPh_2, R^2 = NPh_2 (57%)
232n R = 6-methoxynaphtalen-2-yl, R^2 = OCH_3 (77%)
232o R = 6-methoxynaphtalen-2-yl, R^2 = $N(CH_3)_2$ (70%)
232p R = 6-methoxynaphtalen-2-yl, R^2 = NPh_2 (30%)
232q R = C_6H_4-4-CF_3, R^2 = OCH_3 (42%)
232r R = C_6H_4-4-CF_3, R^2 = $N(CH_3)_2$ (40%)
232s R = C_6H_4-4-CF_3, R^2 = NPh_2 (28%)

Scheme 2. *Synthesis of final bipodal **231** and tripodal **232** compounds by Knoevenagel condensation.*

Final compounds **235a** and **235b** with three different arms in positions C2, C4 and C6 were synthesized in three steps from commercially available 2,4-dichloro-6-methylpyrimidine (*Scheme 3*). The first two steps involved one-pot hydroboration followed by Suzuki-Miyaura reaction, similarly as described for the synthesis of compounds **229** and **230**. It is known that all three chlorine atoms of 2,4,6-trichloropyrimidine can be regioselectively replaced in sequence 4, 6 and 2. This was utilized as synthetic strategy towards final derivatives with different substitution on each arm.[105,129] Knoevenagel condensation between C6 methyl and 4-diphenylaminobenzaldehyde was utilized as final step. Intermediates **233**, **234** and final compounds **235** were obtained with satisfying yields 33–75%.

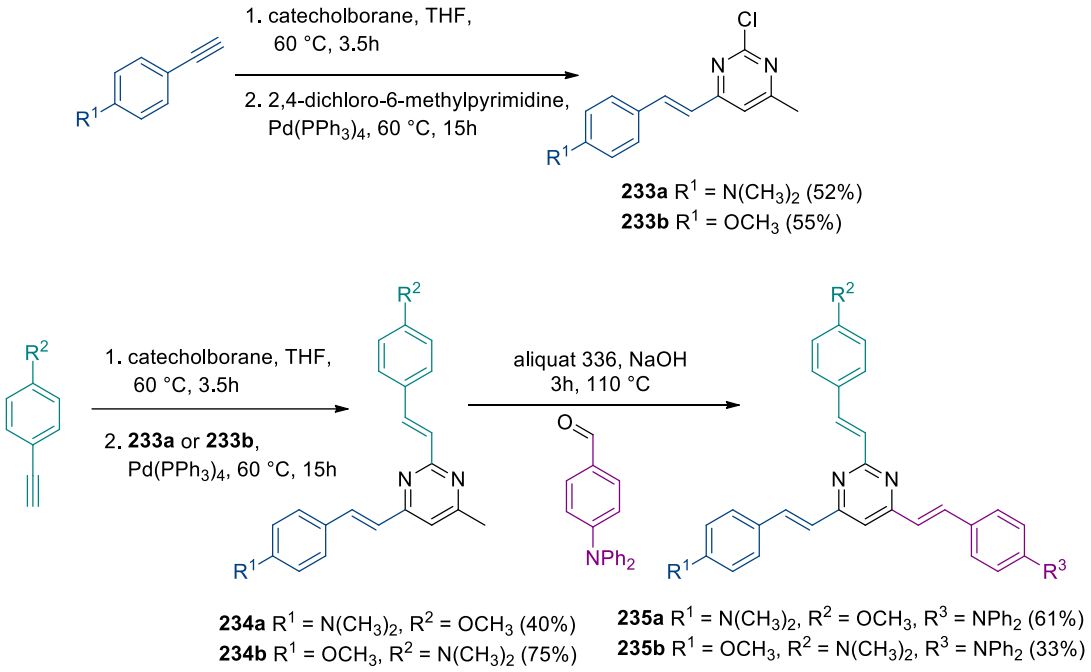

Scheme 3. *Three steps synthesis sequence for compounds **235**.*

Final compounds **231**, **232** and **235** along with intermediates **229**, **230**, **231** and **234** were analysed by ^{1}H and ^{13}C NMR spectroscopy and high-resolution MALDI mass spectrometry (HR-MALDI-MS). The *E* configuration of double bonds was unequivocally established on the basis of coupling constant the vinylene protons in the ^{1}H NMR spectra ($^{3}J_{H\text{-}H} \approx 16$ Hz). All prepared compounds showed good solubility and stability in chlorinated solvents such as dichloromethane and chloroform.

3.3 X-ray and thermal properties

X-Ray analysis

Attempts to growth crystals of vast majority of final compounds unfortunately did not lead to a single crystal suitable for X-ray analysis. Only final compound **232h** provided crystal suitable for X-ray analysis by slow evaporation of its CH_2Cl_2/EtOAc solution (1/1; v/v) in a dark at room temperature. Its RTG was performed and results analysed by Dr Thierry Roisnel, Université de Rennes 1 (France). Measurement of the crystal, a yellow transparent prism, confirmed proposed structure, especially the *E* configuration of all vinylene bridges (*Figure 53*). The X-ray analysis further revealed disorder on one of the C4/C6 arms, which was already observed for some 4,6-distyrylpyrimidines.[120] Molecular structure was not fully planar, torsion angle between the central pyrimidine core and the surrounding phenylene rings was less than 20°. It should be noted that the dihedral angle between the phenyl ring in C2 position and the pyrimidine core was the lowest (approximately 7°). Based on the calculated bond-length

alternation (BLA) values for each vinylene linkers, C2 arms imparted stronger ICT (BLA = 0.1185 Å) as compared to C4 and C6 arms (BLA = 0.1205, 0.1600 and 0.1775 Å). As far as supramolecular structure was concerned, molecules of final chromophore **232h** were organised in orthorhombic crystal order with a *Pna*2_1 space group.

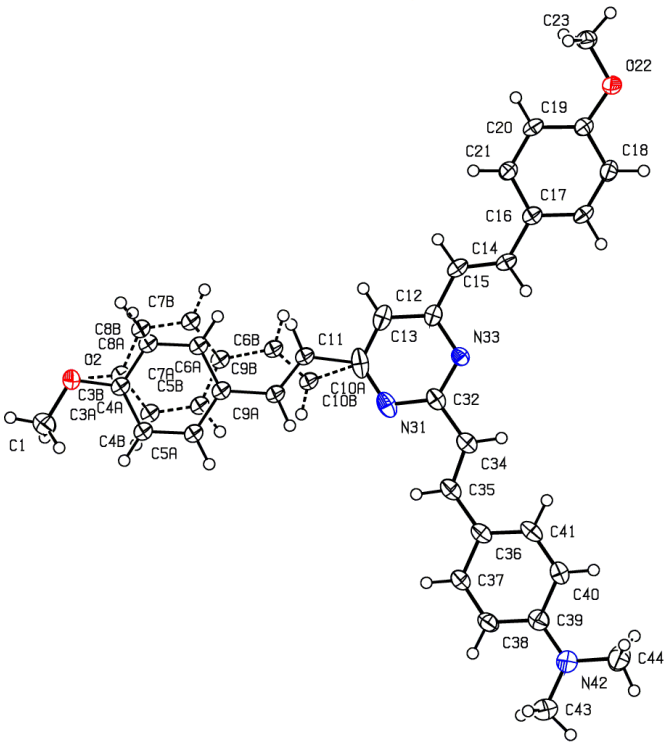

Figure 53. *Oak Ridge thermal ellipsoid plot (ORTEP) diagram of compound* ***232h*** *(thermal ellipsoids are shown at 50% probability).*

Thermal properties

Differential scanning calorimetry (DSC) was employed to study thermal behaviour of final compounds. *Table 3* provides melting points and thermal decomposition temperature of all final compounds together with compounds **61–62** for comparison. Measurements were performed by Ing. Milan Klikar, Ph.D., University of Pardubice (Czech Republic).

Table 3. *Results of DSC analysis for final chromophores **231**, **232**, **235** and compounds **61** and **62**.*

compd	T_m [°C]	T_d [°C]	*compd*	T_m [°C]	T_d [°C]	*compd*	T_m [°C]	T_d [°C]
61	191	260	***232d***	–	305	***232m***	–	310
62	205	320	***232e***	183	305	***232n***	–	290
231a	137	290	***232f***	–	250	***232o***	–	250
231b	185	305	***232g***	–	270	***232p***	–	220
231c	243	265	***232h***	200	295	***232q***	–	280
231d	–	250	***232i***	–	250	***232r***	210	265
232a	193	300	***232j***	–	240	***232s***	–	300
232b	128	290	***232k***	–	310	***235a***	–	240
232c	–	245	***232l***	–	195	***235b***	–	210

Final derivatives **231**, **232**, **235** and compounds **61–62** showed melting points within the range of 128–243 °C and temperature of decomposition between 195 and 320 °C.

For bipodal derivatives **231**, sharp peak of melting was observed in the range of 137–243 °C and gradual decomposition process with raising temperature between 250 and 305 °C. The only exception was compound **231d**, which did not melt and directly decomposed at 250 °C. Bipodal chromophores with electron-donating units showed higher melting points with difference up to 100 °C as compared to unsubstituted derivative **231a**. Monotropic solid-solid transition of metastable crystals was found for compounds **231a** as doubled peak of melting.

Tripodal final chromophores **232** and **235** were generally solid glasses and amorphous solids with complex thermal behaviour. Only a few of them demonstrated distinguishable melting peak, namely compounds **232a** (193 °C), **232b** (128 °C), **232e** (183 °C), **232h** (200 °C) and **232r** (210 °C). Solid-solid transition peaks with 10–30 °C width were observed for compounds **232c,d,f,g,i,j,k,n,o** within the range of 100 to 245 °C. Chromophores **232l** and **232m** underwent glass transition at 170 °C. The rest of tripodal molecules directly decomposed with increasing temperature over 200 to 300 °C. None further structure-thermal behaviour relationships can be drawn from the DSC analysis.

4,6-Disubstituted compounds **61** and **62** with peripheral dimethylamino and diphenylamino groups showed peak of melting and gradual decompositions. The higher number of phenyl units in compound **62** caused increase in both melting point and temperature of decomposition as compared to compound **61** (205, 320 °C vs. 191, 260 °C). Temperature of decompositions for compounds **61**, **62** and their tripodal analogous **232i**,**m** revealed to be influenced by the attached donating groups. Their thermograms displayed in *Figure 54* show almost identical T_d values for dimethylamino derivatives **61** and **232i** (250 and 260 °C) and for diphenylamino derivatives **62** and **232m** (310 and 320 °C).

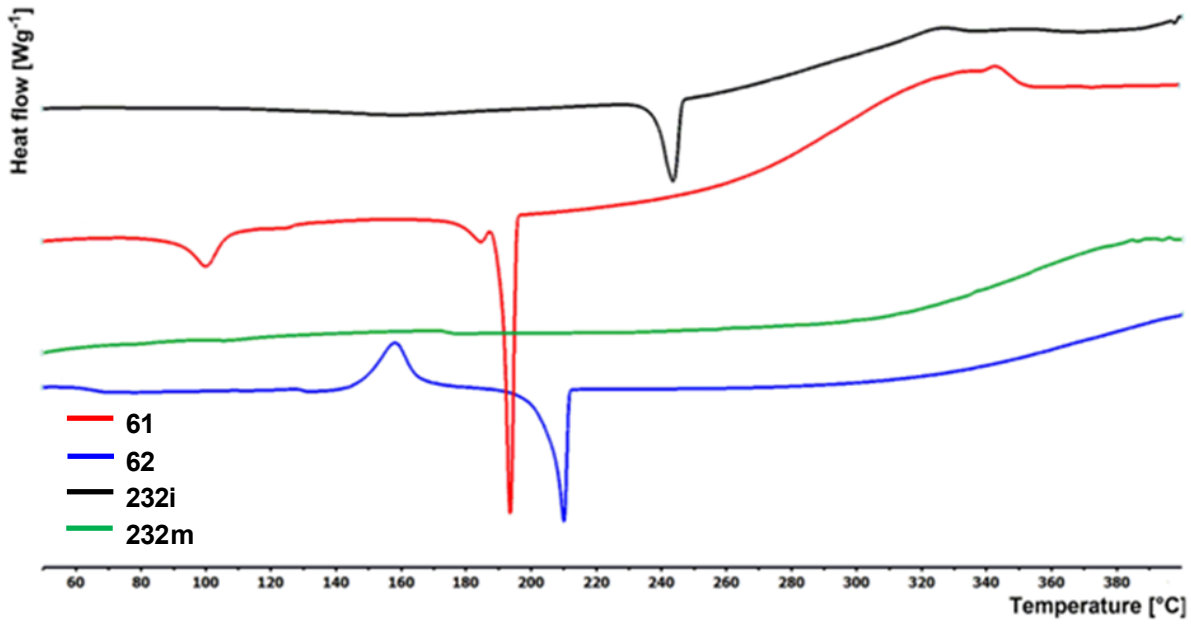

Figure 54. *DSC thermograms of compounds* ***61****,* ***62****,* ***232i*** *and* ***232m****.*

3.4 Photophysical properties

Absorption and emission in CH_2Cl_2: structure-property relationship

Results of UV/Vis absorption and photoluminescence analysis of final compounds **231**, **232** and **235** provided in *Table 4* were measured in CH_2Cl_2 with solute concentration $c = (1 \pm 0.5) \times 10^{-5}$ M. The longest-wavelength absorption band of all final compounds, ranging between 305 and 430 nm, belongs to charge-transfer. Peripheral substituents in C4/C6 positions caused red-shift of absorption band in the following order: H < OCH_3 < NPh_2 ~ $N(CH_3)_2$ as shown for compounds **232b,c,d** in *Figure 55A*. The effect of C2 substituent was more complicated. For tripodal compounds with amino groups in C4/C6 positions, methoxy and trifluoromethyl substituents on C2 arm (compounds **232f,g,o,p,r,s** and **235a**) did not substantially change wavelength of the absorption maxima but appending the amino group in C2 position resulted in slight blue-shift (compounds **232i,j,l,m**, *Figure 55B*). On the contrary, for compounds with methoxy C4/C6 substituents, the additional methoxy substitution on C2 arm caused blue-shift, while insignificant shifts were encountered for trifluoromethyl and amino substituents. Compared to 4,6-disubstituted analogues **60–62**, 2,4-disubstituted final compounds **231b–d** and 2,4,6-trisubstituted final compounds **232e,i,m** exhibited blue-shifted absorption maxima.

Table 4. *Photophysical properties of final chromophores* ***231****,* ***232****,* ***235*** *and compounds* ***60–62****.*

compd	λ_{max}(abs) (ε) [nm] ([$mM^{-1}\cdot cm^{-1}$])	λ_{max}(em) [nm]	Φ_F	*Stokes shift* [cm^{-1}]
60[107]	359 (36.0)	439	–	5076
61[111]	429 (42.1)	530	0.40	4442
62[111]	427 (47.6)	540	0.55	4901
231a	305 (41.3)	–	–	–
231b	331 (53.9)	–	–	–
231c	395 (67.2)	493	0.04	5032
231d	402 (45.5)	527	0.72	5900
232a	312 (74.3)	–	–	–
232b	369 (35.9)	442	0.10	4476
232c	423 (48.1)	537	0.72	5019
232d	430 (55.0)	551	0.78	5107
232e	339 (64.0)	439	0.15	6719
232f	423 (45.6)	533	0.53	4879
232g	424 (68.9)	543	0.91	5168
232h	370 (94.0)	–	–	–
232i	402 (97.3)	536	0.22	6219
232j	409 (112.9)	577	0.03	7118
232k	376 (61.7)	558	0.10	7799
232l	406 (42.4)	533	0.59	5869
232m	415 (86.2)	544	0.56	5714
232n	347 (61.6)	443	0.11	6245
232o	418 (52.5)	536	0.52	5266
232p	424 (69.7)	544	0.75	5202
232q	370 (26.8)	441	0.21	4351
232r	429 (49.1)	545	0.72	4961
232s	430 (60.4)	554	1.00	5205
235a	420 (40.4)	549	0.68	5595
235b	386 (58.1)	548	0.02	7659

All final chromophores showed significant emission, except of compounds **231a,b** and **232a,h**, which exhibited only negligible emission in *n*-heptane solution. The absence of emission of **232h** was probably caused by TICT excited state. Large Stokes shifts were observed for final chromophores, indicating extensive vibrational, electronic and geometric differences between the excited state and Franck-Condon state (see *Chapter 1.1.2*). For tripodal final compounds **232** and **235**, the emission wavelength maxima were mostly affected by substituents attached in C4/C6 positions. For compounds **232j** and **232k**, the emission properties were determined by C2 substituent, which is a stronger electron-donating group than C4/C6 substituents and caused substantial red-shift of the emission maxima in comparison

with their C2 unsubstituted analogues **232d** and **232b**. This phenomenon was probably caused by the transition of ICT from C4/C6 arms into the C2 arm. Addition of styryl unit into the C2 position in compounds **232b–d** (*Figure 55A*) led to slightly red-shifted emission and increase of quantum yields in comparison with 4,6-distyrylpyrimidines **60–62**. Decorating the C2 styryl branch with electron-donating groups (such as methoxy, dimethylamino and diphenylamino) caused a slight blue-shift of the emission, except of compounds **232j,k** that demonstrated opposite trend (*Figure 55B*). Derivatives with dimethylamino group in C2 position (**232i,j** and **235b**) exhibited the lowest fluorescence quantum yields among tripodal final compounds. The presence of electron-withdrawing trifluoromethyl unit in compounds **232q–s** resulted in an enhancement of the fluorescence quantum yield up to 1 (for compound **232s**). The emission spectra of 2,4-distyryl final chromophores are blue-shifted as opposed to their 4,6-distyryl and 2,4,6-tristyryl analogues.

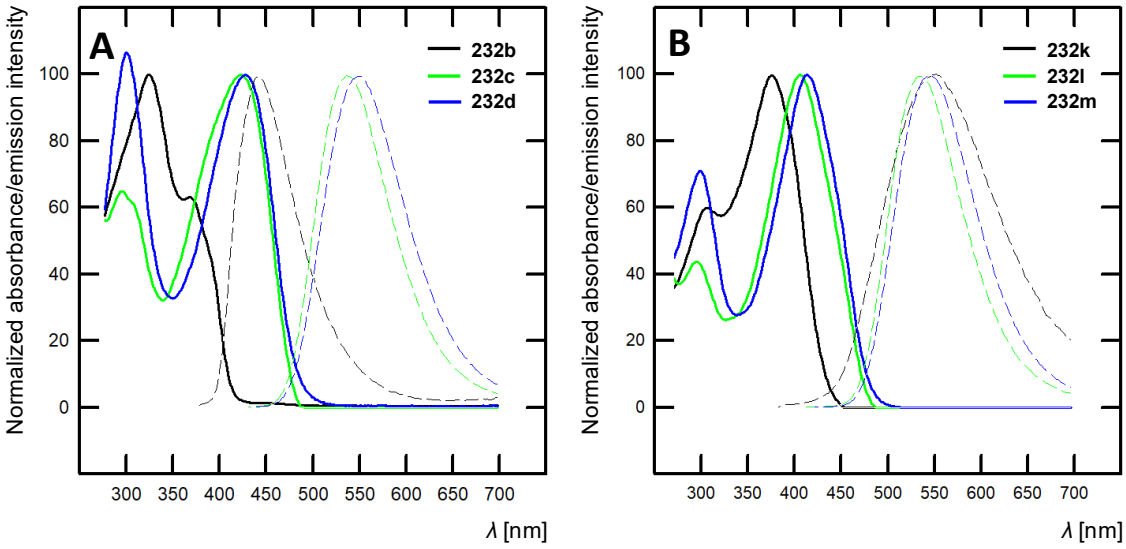

Figure 55. *Normalized absorption (solid lines) and emission (dashed lines) spectra of chromophores (A)* ***232b–d*** *and (B)* ***232k–m*** *measured in* CH_2Cl_2.

Emission solvatochromism

Solvatochromic effect of final compounds was studied in different aprotic solvents with increasing polarity as estimated by the Reichardt polarity parameter: *n*-heptane (HEPT), toluene (TOL), tetrahydrofuran (THF), dichloromethane (CH_2Cl_2), acetone (ACT), dimethyl sulfoxide (DMSO) and acetonitrile (ACN).[217] Whereas increasing the solvent polarity has diminished effect on the absorption maxima, the emission bands were red-shifted, a typical feature of positive emission solvatochromism. The emission spectra of compound **232k** are displayed in *Figure 56*. The ICT between the peripheral donor units and the central pyrimidine core enhanced dipole-dipole interaction between the given chromophore and solvent molecules,

which resulted in solvent relaxation and decreased energy of excited state. The emission maxima for all final fluorophores are summarized in *Table 5*. Difference between emission maxima in heptane and acetonitrile is up to 188 nm and the spectra became broader and structure-less with increasing solvent polarity.

Table 5. *Emission solvatochromism of final fluorophores in different aprotic solvents.*

	HEPT	*TOL*	*THF*	*CH_2Cl_2*	*ACT*	*DMSO*	*ACN*
$E_T(30)$	30.9	33.9	37.4	40.7	42.2	45.1	45.6
	λ_{max} [nm]	λ_{max} [nm]	λ_{max} [nm]	λ_{max} [nm]	λ_{max} [nm]	λ_{max} [nm]	λ_{max} [nm]
231c	433	455	484	493	523	527	513
231d	447	470	502	527	531	547	546
232b	397, 420	408, 429	432	442	450	471	470
232c	453	483	526	537	563	601	587
232d	464	482	520	551	563	596	591
232e	402, 421	410, 433	432	439	440	461	453
232f	450	480	522	533	559	598	581
232g	461	480	515	543	555	584	583
232i	450	479	521	536	558	601	577
232j	460	495	512	547	552	577	574
232k	439	466	511	558	572	622	627
232l	451	480	521	533	561	596	584
232m	460	479	514	544	555	586	589
232n	401, 422	411, 433	433	443	445	471	463
232o	449	480	520	536	565	597	586
232p	460	479	519	544	558	585	586
232q	398	411	436	441	452	475	463
232r	456	486	533	545	565	592	587
232s	467	486	526	554	567	599	600
235a	457	491	542	549	571	589	594
235b	398	411	436	441	452	475	463

These results were plotted versus Reichardt polarity parameters and a tight correlation was achieved. Slopes of the obtained linear functions can be used to quantify the emission solvatochromism. As for the absorption and emission properties, solvatochromic behaviour is mainly given by the nature of C4/C6 peripheral donor units, see the *Figure 57A*. Higher slopes were observed with increasing electron-donating ability of the attached substituents (OCH_3 < NPh_2 < $N(CH_3)_2$), except of compound **232k**. Both C4 and C6 arms play key role in emission solvatochromism, given the fact that slopes for 2,4,6-trisubstituted chromophores **232i,m** are higher than for their 2,4,-disubstituted derivatives **231c,d**. This trend is captured in *Figure 57B*.

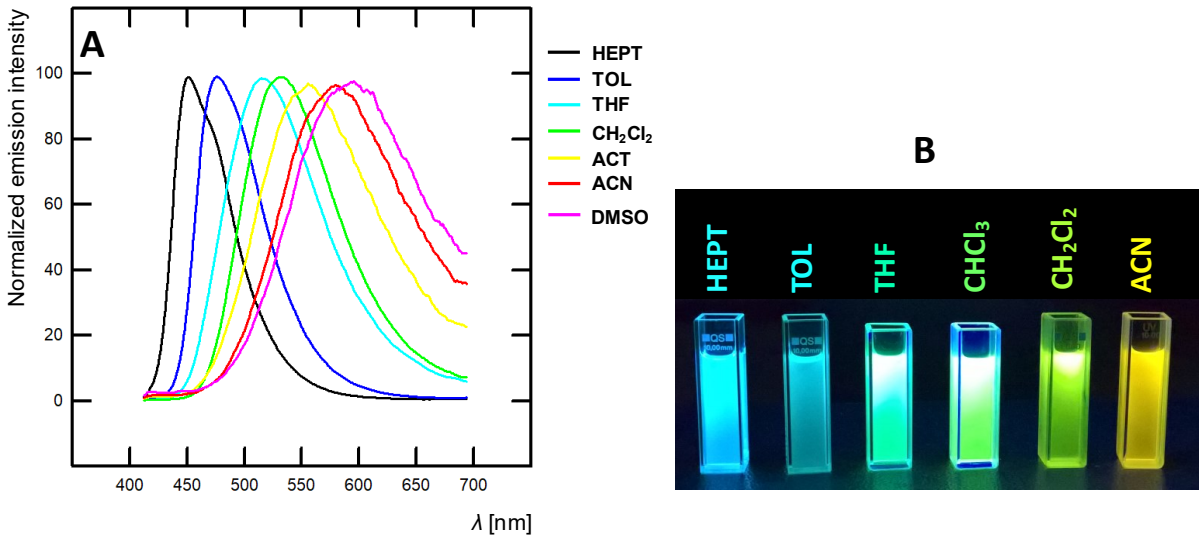

Figure 56. *(A) Normalized emission spectra of* ***232k*** *in different solvents. (B) Picture of* ***232k*** *colour change in different solvents taken under UV irradiation (hand-held lamp λ = 254 nm).*

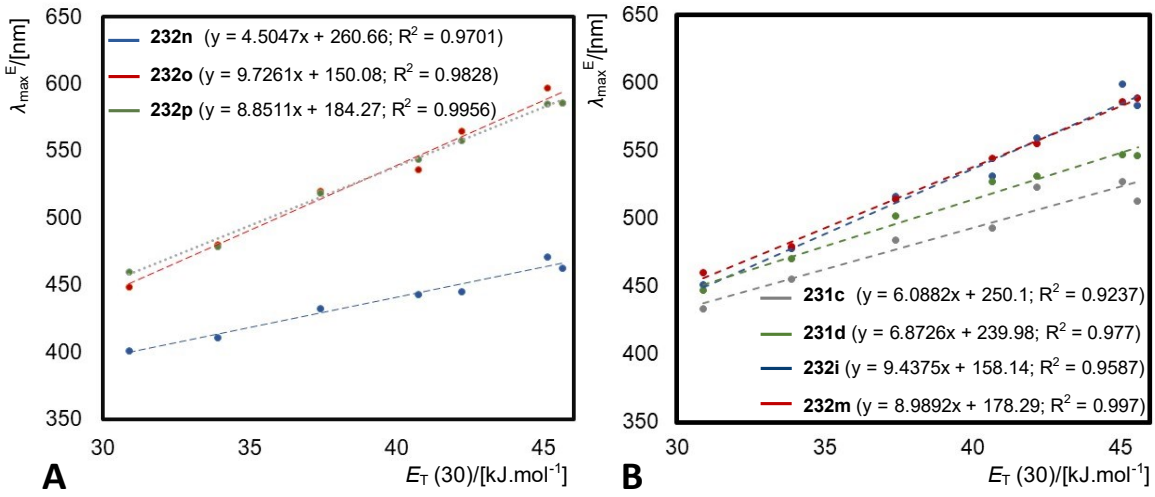

Figure 57. *Emission maxima as a function of the Dimroth-Reichardt polarity parameter for compounds (A)* ***232n–p*** *and (B)* ***231c,d*** *and* ***232i,m****.*

Effect of protonation

As it was mentioned in the beginning of *Chapter 2*, one of the nitrogen atoms in pyrimidine ring can be easily protonated by a moderately strong acid. Hence, the absorption and emission spectra of final chromophores were recorded in presence of (1*S*)-(+)-10-camphorsulfonic acid to obtain dual emissive mixture. In all absorption spectra, presence of a new red-shifted absorption band was observed. It is attributed to enhanced electron-accepting properties of the protonated pyrimidine, and therefore, stronger ICT. However, addition of acid led to dramatic decrease of fluorescence for most of the final compounds, except of methoxy derivative **232q**. According to other studies, protonation of amino-substituted pyrimidines generally led to

dramatic quenching of emission, while protonated methoxy pyrimidines exhibited significant emission (see *Chapter 2.3.2*).[109,156] In the case of compound **232q**, the emission spectra were recorded with increasing amount of acid (0, 0.2, 0.4, 0.6, 0.8, 1, 2, 4 and 50 equivalent, *Figure 58A*). Upon addition of the acid, the emission maxima recorded with excitation wavelength (λ(exc) = 380 nm) of originally neutral chromophore at 441 nm slowly decreased and a new band, red-shifted by 100 nm, slowly appeared. It belongs to monoprotonated chromophore. Isoemissive point is observed at 491 nm. Equivalency of neutral and protonated species was reached at approximately 0.8 equivalent of the acid producing sky blue light (*Figure 58B,C*). Neutral and monoprotonated species themselves emitted blue and yellowish-green light, respectively (*Figure 58B,C*).

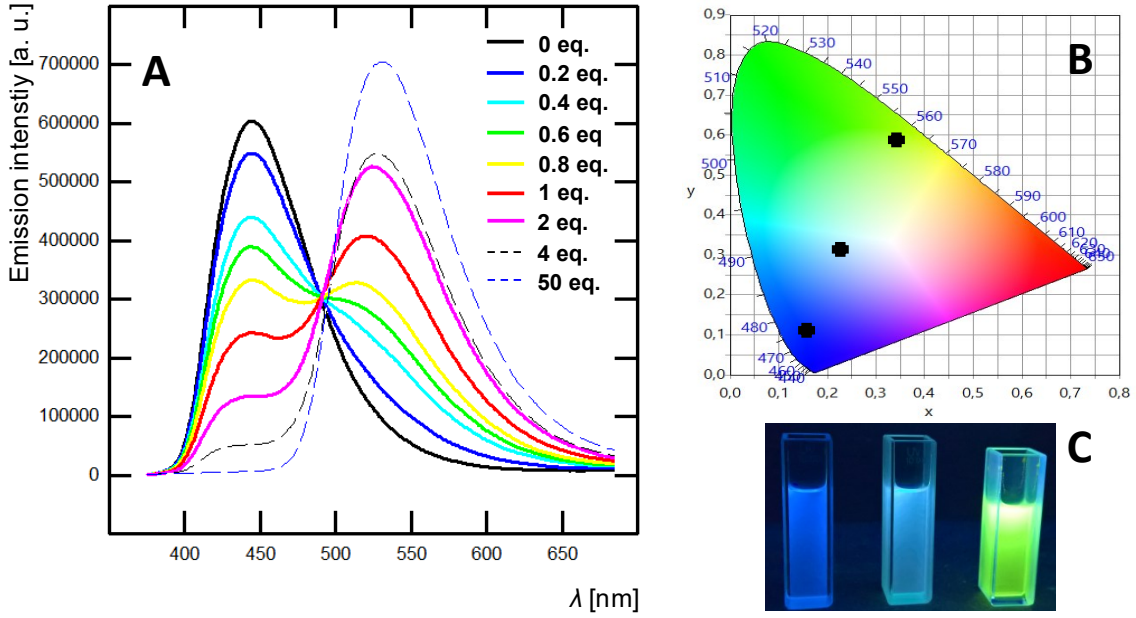

Figure 58. *(A) Emission spectra of chromophore **232q** with progressively increasing amount of acid in CH_2Cl_2 (λ(exc) = 380 nm). (B) 1931 CIE diagram of neutral, partially protonated and fully protonated **232q**. (C) Picture of CH_2Cl_2 solution of neutral (left), equilibrium (middle) and protonated (right) **232q** taken un UV irradiation (hand-held lamp λ = 254 nm).*

Additionally, for determination of protonation effects on the photophysical properties of pyrimidine-based chromophores, final tripodal derivative **232m** and bipodal compound **62** were further studied by steady state and time resolved spectroscopy. This work was performed in collaboration with Prof. Mihalis Fakis, University of Patras Greece. For these experiments, camphorsulphonic acid (pK_a = 1.2), trifluoracetic acid (pK_a = 0.3) and acetic acid (pK_a = 4.8) were tested. Spectra were recorded in $CHCl_3$ with solute concentration within the scale of 10^{-5} M and they are shown in *Figure 59*. The absorption spectrum of neutral form of **62** contained two bands at 300 and 436 nm. During addition of camphorsulfonic acid, two new bands gradually appeared at 350 and 566 nm at the expense of neutral form bands (300 and 436

nm). Three distinct isosbestic points at 325, 370 and 470 nm indicate the coexistence of both neutral and protonated species. Similar observation was made for protonation with trifluoracetic acid. However, effect of acetic acid turned out to be different. Due to its higher pK_a value, larger amounts of acid were necessary for pyrimidine protonation. Absorption peak at 350 nm was not observed and newly raising band of protonated form at 560 nm possesses considerably lower intensity as compared to bands of the protonated form created by camphorsulfonic and trifluoracetic acid. Chromophore **232m** exhibited similar behaviour with absorption band of the neutral and protonated forms at 414 and 530 nm, respectively. However, changes in the spectra were more pronounced and required lower amounts of acids. The gradual disappearance of the original band and appearance of new red-shifted band of protonated species with low intensity were also observed in emission, namely at 540/700 nm for **62** and at 530/670 nm for **232m**. It should be noted that intensities of emission peak of protonated species **232m** were significantly lower than for compound **62**.

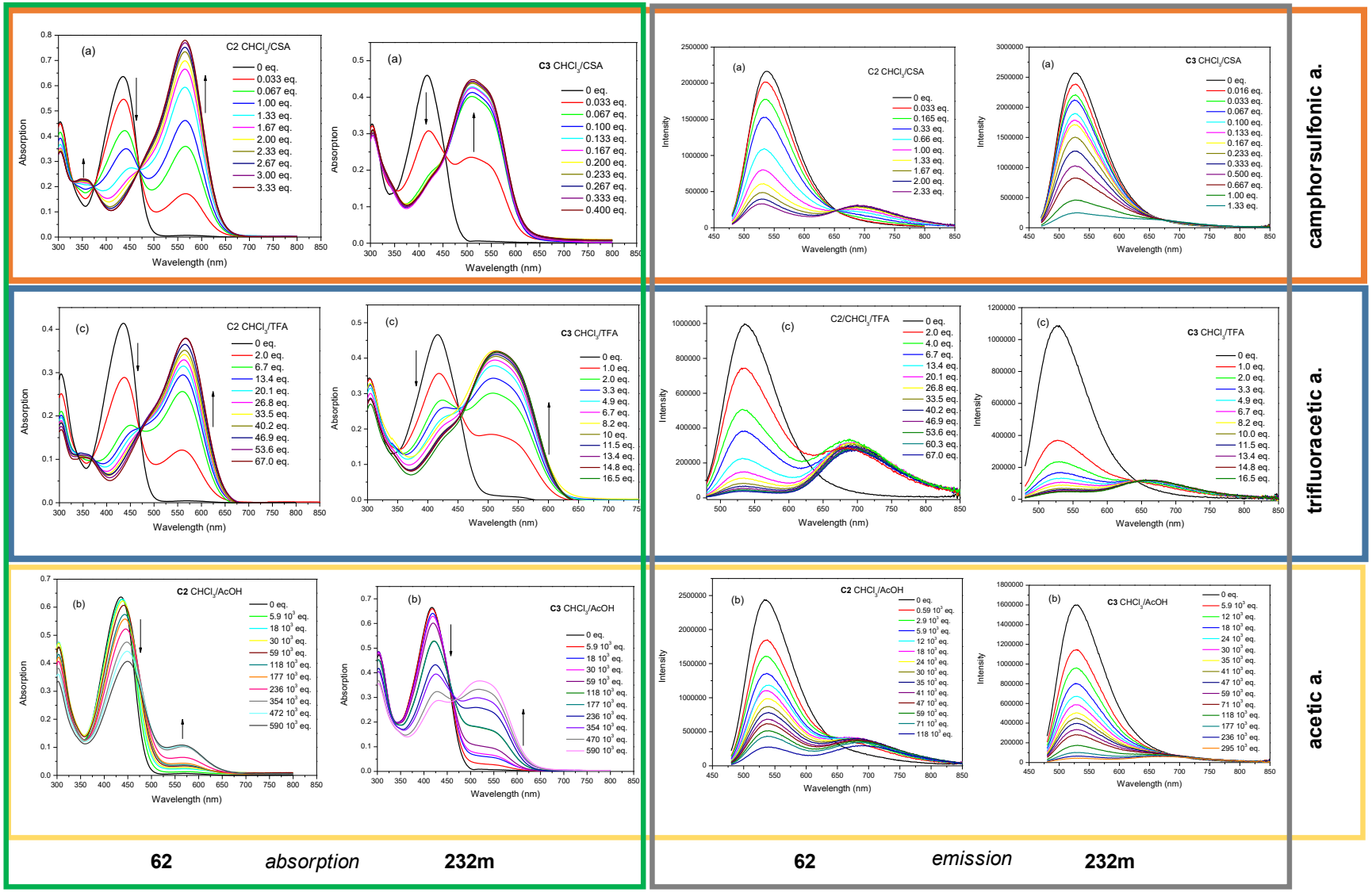

Figure 59. *Absorption and emission spectra of* ***62*** *and* ***232m*** *in $CHCl_3$ with progressive addition of camphorsulfonic, trifluoracetic and acetic acid.*

Results, which can be found in Ref.[218], of time resolved measurement can be briefly summarized as flows:

(i) quenching of neutral solute by camphorsulfonic and trifluoracetic acid takes place at the ground state, i.e. static quenching,

(ii) interaction of solute and acetic acid operates in both ground and excited state by the means of both static and dynamic quenching,

(iii) previous phenomena were observed for both bipodal derivative **62** and tripodal **232m**.

Branching effect: comparison with 4-stryl- and 4,6-distyrylpyrimidine

In order to gain further understanding how branching affects photophysical properties of styrylpyrimidines, final three-branched 2,4,6-tristyrylpyrimidines **232i,m** were studied by UV/Vis absorption, steady-state and time-resolved flourescence measurements together with two-branched 4,6-distyrylpyrimidines **61,62** and one-branched 4-styrylpyrimidines **48** and **49** (*Figure 60*).

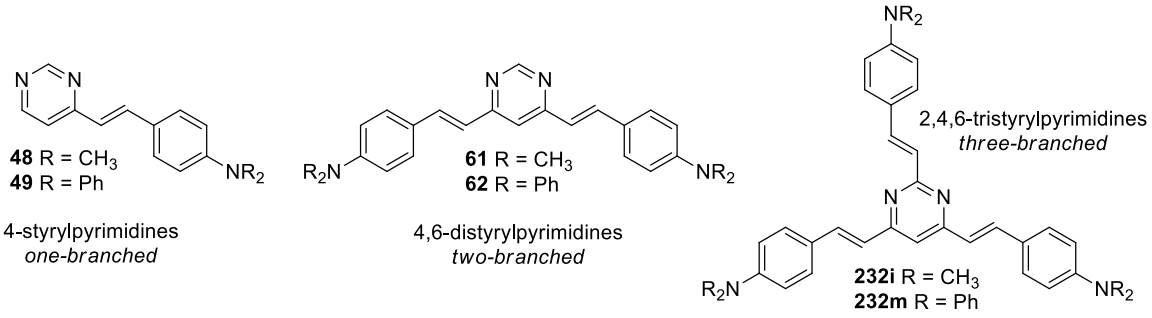

Figure 60. *Structures of compounds **48**, **49**, **61**, **62**, **232i** and **232m**.*

Absorption and emission properties were determined in various aprotic solvents, namely: *n*-hexane (*n*-HEX), toluene, tetrahydrofuran, chloroform, dichloromethane, acetone and acetonitrile. As it was already observed for multi-branched chromophores, increasing number of branches led to a red-shift of the longest wavelength absorption band.[56,219] This behaviour is predicted by Frenkel exciton model which assumes an intermolecular electrostatic coupling between monomers, in this case, between branches.[220] For two-branched V-shaped compounds, interaction among branches results in splitting of the excited state into two states, one is higher and the second lower in energy than the original excited state and both are one-photon allowed. This leads to broader and red-shifted absorption band. For three-branched chromophores with C_3 symmetry, Frenkel exciton model predicts splitting into three states, two degenerated states with lower energy and one with higher energy and vanishing oscillator strength. As a consequence, the longest wavelength absorption band is red-shifted and without

broadening corresponds to the absorption band of two-branched analogue. In our series, red-shift of the absorption maxima was observed in a sequence one-branched < three-branched < two-branched derivatives (*Figure 61*). The red-shift of absorption bands of two-branched compounds can be explained by splitting of excited state. This theory was supported by a presence of longer-wavelength shoulder visible in nonpolar solvents, such as *n*-Hex, see *Figure 61* compound **61**. On the other hand, lack of the three-fold (C_3) symmetry of the pyrimidine core, and therefore no splitting of the excited state, caused the blue-shifted absorption spectra of three-branched derivatives as compared to two-branched ones (**232i,m** vs. **61,62**). It should be also noted that absorption maxima of all dimethylamino derivatives were blue-shifted as compared to diphenylamino ones (**48**, **61**, **232i** vs. **49**, **62**, **232m**).

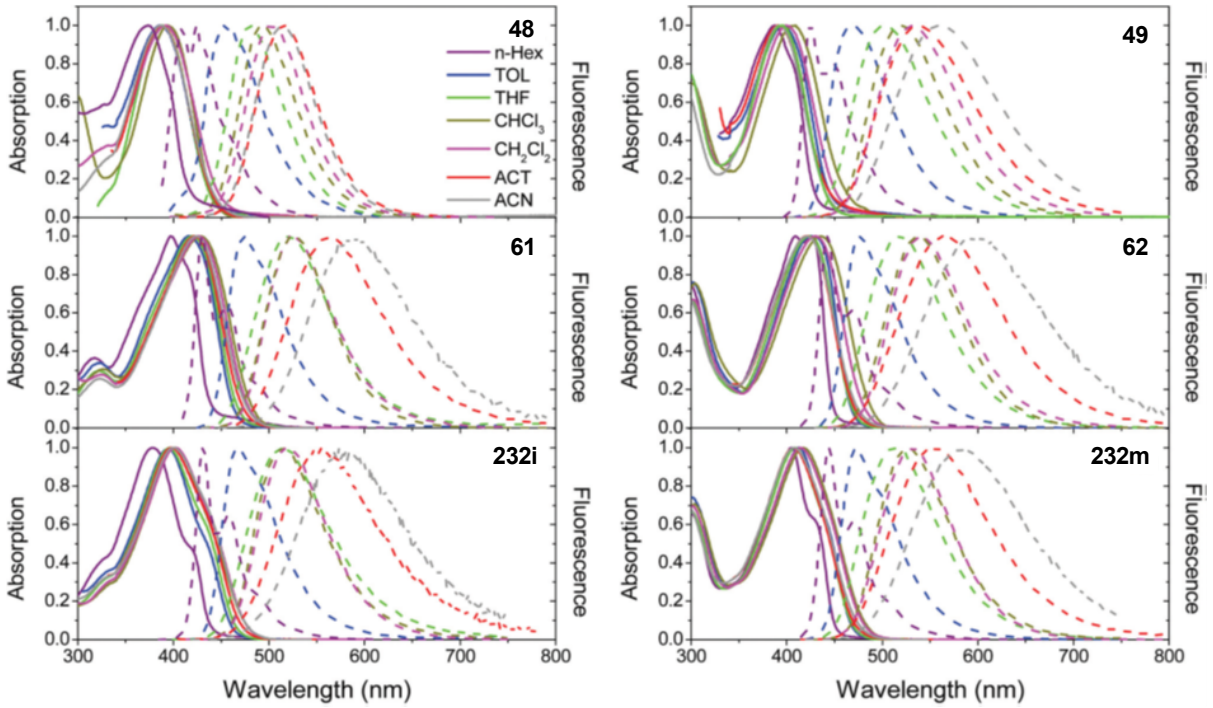

Figure 61. *Normalized absorption (solid) and emission (dashed) spectra of studied compounds* ***48****,* ***49****,* ***61****,* ***62****,* ***232i*** *and* ***232m*** *in various aprotic solvents with increasing polarity.*

Compared to their diphenylamino counterparts, a blue-shifted spectra of dimethylamino derivatives were observed for emission in all solvents, spectra are provided in *Figure 53*. The red-shifted spectra were obtained with increasing number of branches (**48** < **61** < **232i** and **49** < **62** < **232m**), suggesting interactions within the branches. All studied compounds exhibited significant positive emission solvatochromism. In the case of 4-styrylpyrimidines **48** and **49**, positive solvatochromism raised from their D-π-A structure, which increased polarization in the excited state. However, in the case of two- and three-branched compounds

61,**62** and **232i,m**, positive solvatochromism implied symmetry breaking in excited state with localization of excitation on a single chromophoric unit preceding the emission.

In collaboration with Prof. Mihalis Fakis, University of Patras (Greece) fluorescence dynamics of compounds **48**, **49**, **61**, **62**, **232i** and **232m** in a ns timescale were examined to determine solvent and branching effects on a fluorescence lifetime (*Figure 62*). The obtained spectral curves were fitted by single- or multi-exponential functions and their average lifetimes are provided in *Table 6*. Comparing to the dimethylamino derivatives **48**, **61** and **232i**, diphenylamino substituted chromophores **49**, **62** and **232m** exhibited longer dynamics with longer average fluorescence lifetimes as a consequence of higher fluorescence quantum yields. Average fluorescence lifetime of all studied compounds increased with raising solvent polarity. This indicated a stabilization of excited states. However, a deviation from this trend was observed for lifetime in ACN. Only slight reduction of lifetime was obtained for one-branched compounds **48** and **49**, however, with each additional branch the decrease became even more prominent. Similar phenomenon was already observed and thoroughly studied by *Ishow et al.* on a series of triphenylamines.[221] They suggest a relaxation from excited ICT state into the lower energy non-emissive ICT state with higher rate constant for nonradiative decay in highly polar solvents.

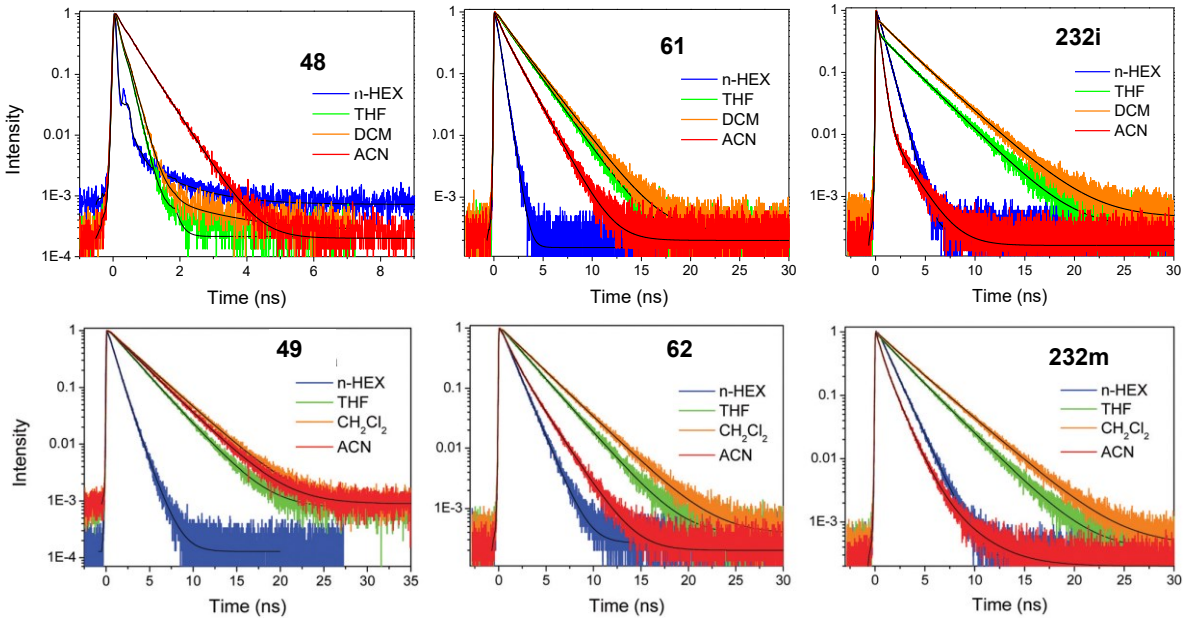

Figure 62. *Nanosecond scale fluorescence dynamics of compounds **48**, **49**, **61**, **62**, **232i** and **232m** in different aprotic solvents.*

Table 6. *Average fluorescence lifetime τ [ns] for studied compounds in various solvents.*

	48	***49***	***61***	***62***	***232i***	***232m***
n-Hex	0.03	0.86	0.41	1.14	0.71	1.26
TOL	0.07	1.36	0.79	1.40	0.99	1.46
THF	0.15	2.54	1.79	2.43	0.75	2.18
$CHCl_3$	0.11	2.39	1.37	2.10	1.58	2.10
CH_2Cl_2	0.16	3.11	1.95	2.87	2.68	3.04
ACT	0.31	3.18	1.78	2.53	0.36	1.27
ACN	0.41	2.88	1.14	1.35	0.33	0.80

3.5 DFT calculation

For investigation of the spatial and electronic properties of final chromophores **232g,j,k,m** and compound **62**, the Gaussian16 software package was employed at the DFT level of theory.[222] Their optimized geometries, energy of their frontier molecular orbitals (HOMO, LUMO) and ground state dipole moments were calculated by the DFT B3LYP/6-311+g(2d,p) method. All results are summarized in *Table 7* and visualization of the HOMO and the LUMO are provided in *Figure 63A*. The calculations were performed and evaluated by Prof. Ing. Oldřich Pytela, DrSc. and Prof. Ing. Filip Bureš, Ph.D.

Table 7. *Results of DFT calculation for final compounds* ***232g,j,k,m*** *and compound* ***62****.*

compd	E_{HOMO} *[eV]*	E_{LUMO} *[eV]*	ΔE *[eV]*	λ_{max} *[nm/eV]*
62	–5.26	–2.27	2.99	475/2.61
232g	–5.21	–2.19	3.02	468/2.65
232j	–5.09	–2.12	2.97	458/2.71
232k	–5.14	–2.13	3.01	403/3.08
232m	–5.14	–2.21	2.94	464/2.67

Energy difference between the HOMO and the LUMO range between 2.97–3.02 eV and are considered almost identical for all studied compounds (*Figure 63B*). However, a small energy difference was observed in HOMO/LUMO energy levels. Raising of both HOMO and LUMO levels was seen with addition of third branch (compare two-branched **62** with three-branched chromophores) and with replacing C2 methoxy group with amino group (**232g** vs. **232j,k,m**). Such steady HOMO/LUMO energy gap during expansion of chromophore by additional branches was already observed for multi-branched chromophores.[223–225] In all studied chromophores, the LUMO was localized on central pyrimidine core and adjacent double bonds in C4 and C6 positions. This spread over surrounding π-linker indicated lower charge separation. The HOMO localization was affected by attached substituent in C2 position. For compound **62** without any C2 substitution, the LUMO was spread over both peripheral

diphenylamino units and partially mixed with the HOMO in middle of the molecule. The HOMO distribution in compound **232g** resembled that of **62** with the HOMO situated on one of the C4/C6 diphenylamino groups and the HOMO–1 on the other one. However, different situation was seen for chromophores **232j,k,m** with amino donors on C2 branch. Replacement of weak methoxy group by stronger amino group resulted in a complete transfer and isolation of the HOMO on the peripheral amino donor in C2 position. This transfer was observed for all three chromophores regardless the substituent at C4/C6 (compare **232j,m** with **232k**).

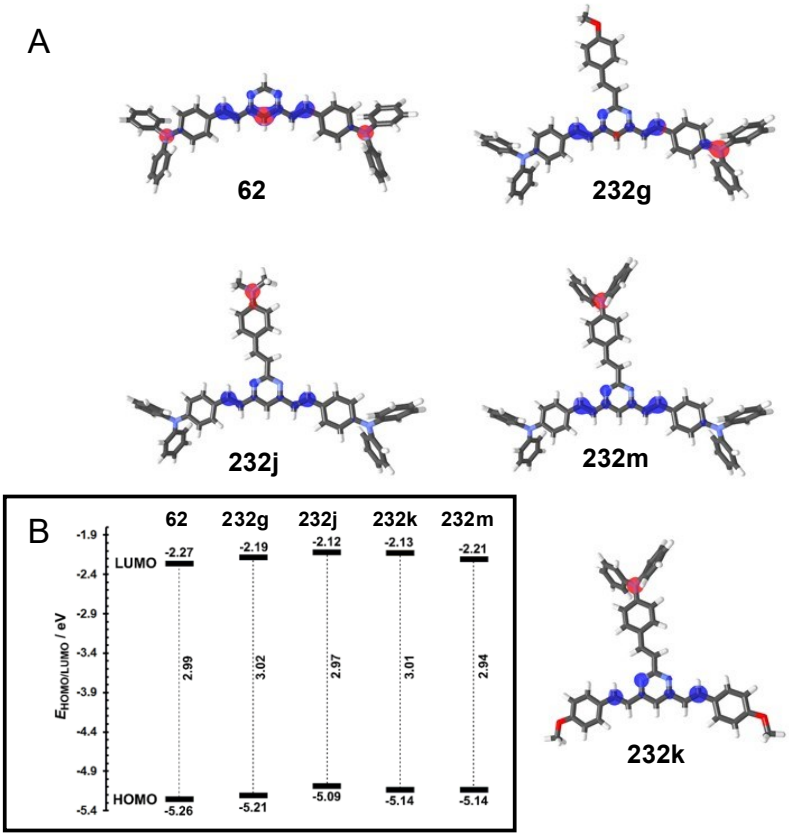

Figure 63. *(A) DFT-optimized geometries and (B) energy-level diagram of DFT-derived HOMO(red)/LUMO(blue) energies for* ***232g,j,k,m*** *and* ***62****.*

Time-dependent self-consistent field B3LYP/6-311+g(2d,p) method (TD-SCF, nstates = 10) was employed to determine electronic absorption spectra of final compounds **232g,j,k.m** and derivative **62**. The calculated longest wavelength absorption maxima are given in *Table 6* and the calculated spectra are displayed in *Figure 64* together with the corresponding experimental spectra. In general, the calculated data were red-shifted (approximately about 40 nm) but the features in both experimental and calculated spectra were consistent, and therefore are considered as useful for description of absorption trends within the studied series.

The calculated longest wavelength absorption bands, corresponding to charge transfer, appeared within the range of 403 and 475 nm. For two-branched compound **62**, this band is predominantly generated by the HOMO → LUMO transition. Similar result was obtained for three-branched compound **232g** with methoxy group in C2 position. On the other hand, the CT band of derivatives with amino group in C2 position (**232j,m**) consists of the HOMO → LUMO, HOMO–1 → LUMO and HOMO → LUMO+1 transitions. Presence of methoxy groups in C4/C6 positions (compound **232k**) led to a dramatic decrease of oscillator strength of the HOMO → LUMO transition and CT is generated by the HOMO–1 → LUMO and the HOMO → LUMO+1 transitions.

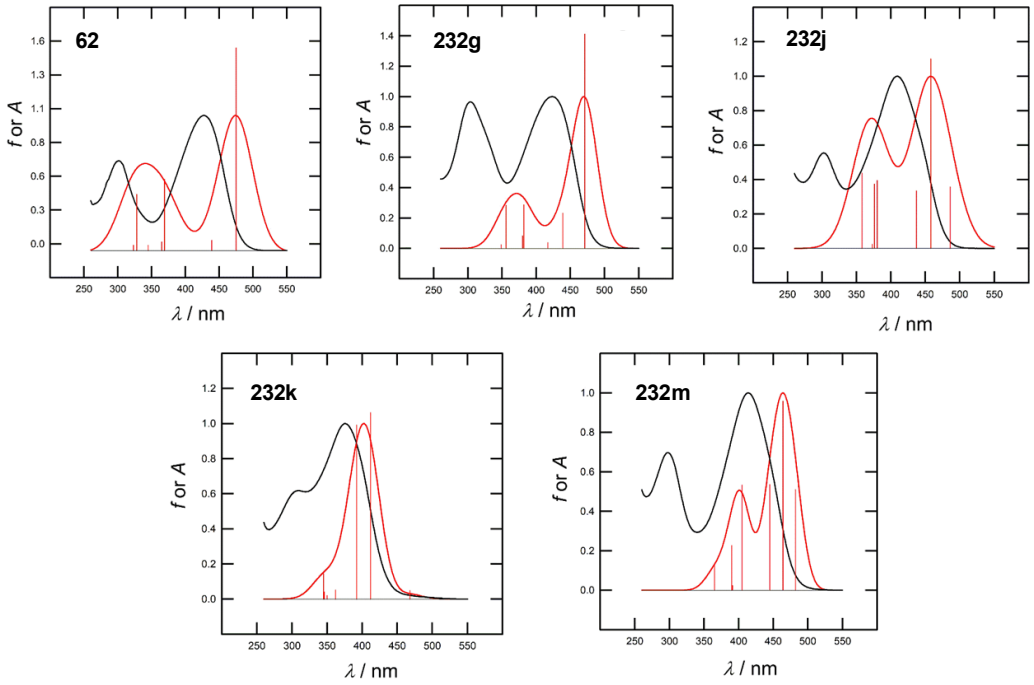

Figure 64. *TD-SCF (nstates = 10) B3LYP/6-311+g(2df,p) calculated (red) UV-Vis spectra of representative chromophores **232g,j,k,m** and **62**. Red vertical lines represent oscillator strengths (f); the black curves are experimentally obtained UV-Vis spectra in CH_2Cl_2. Both spectra were normalized to have maximal absorbance (A) of 1.*

Photophysical results for a series of one-branched **48**, **49**, two-branched **61**, **62** and three-branched **232i**,**m** (see their structures in *Figure 65*) were also extended and supported by computed data performed by Dr. Arnaud Fihey and Dr. Claudine Katan, University of Rennes 1 (France). For all following calculation, the DFT and TD-DFT levels implemented in Gaussian 16 software package were used.[222] For determination of optimized molecular structure, the PBE0 hybrid function was used together with the 6-31G(d,p) basis set, followed by frequency calculations to identify the nature of the energy minimum as a global minimum.[226] Planar molecular structures were obtained from ground and excited state

geometry optimizations, which were performed in a vacuum. The only deviation from planarity was observed for peripheral diphenylamino units with well-known propeller-like arrangement (dihedral angle ~ 40°). Two and three conformers were calculated for two- and three-branched derivatives, respectively, see *Figure 65*. Based on the calculated Gibbs free energies, conformers (*Figure 65* label Confo1) with C4/C6 arms parallel to N-N axis of pyrimidine core were a few kcal.mol^{-1} more stable with Boltzmann population ratio over 80%. BLA values of ground and excited states were calculated for vinylene units of conformers of all studied compounds (Confo1). Going from ground to excited states in one-branched derivatives **48** and **49**, a reduction in BLA values was observed indicating higher charge separation in the excited state. For two-branched derivatives **61** and **62**, the BLA values decreased equally for both branches with preserved geometry of ground state in excited state. However, different structural relaxation, and therefore symmetry breaking in excited state was observed for three-branched derivatives **232i**,**m** with slightly lower difference in BLA values for one of the C4/C6 branches and positive value for C2 arm. The differences of BLA values in ground and excited state are provided in *Figure 66*.

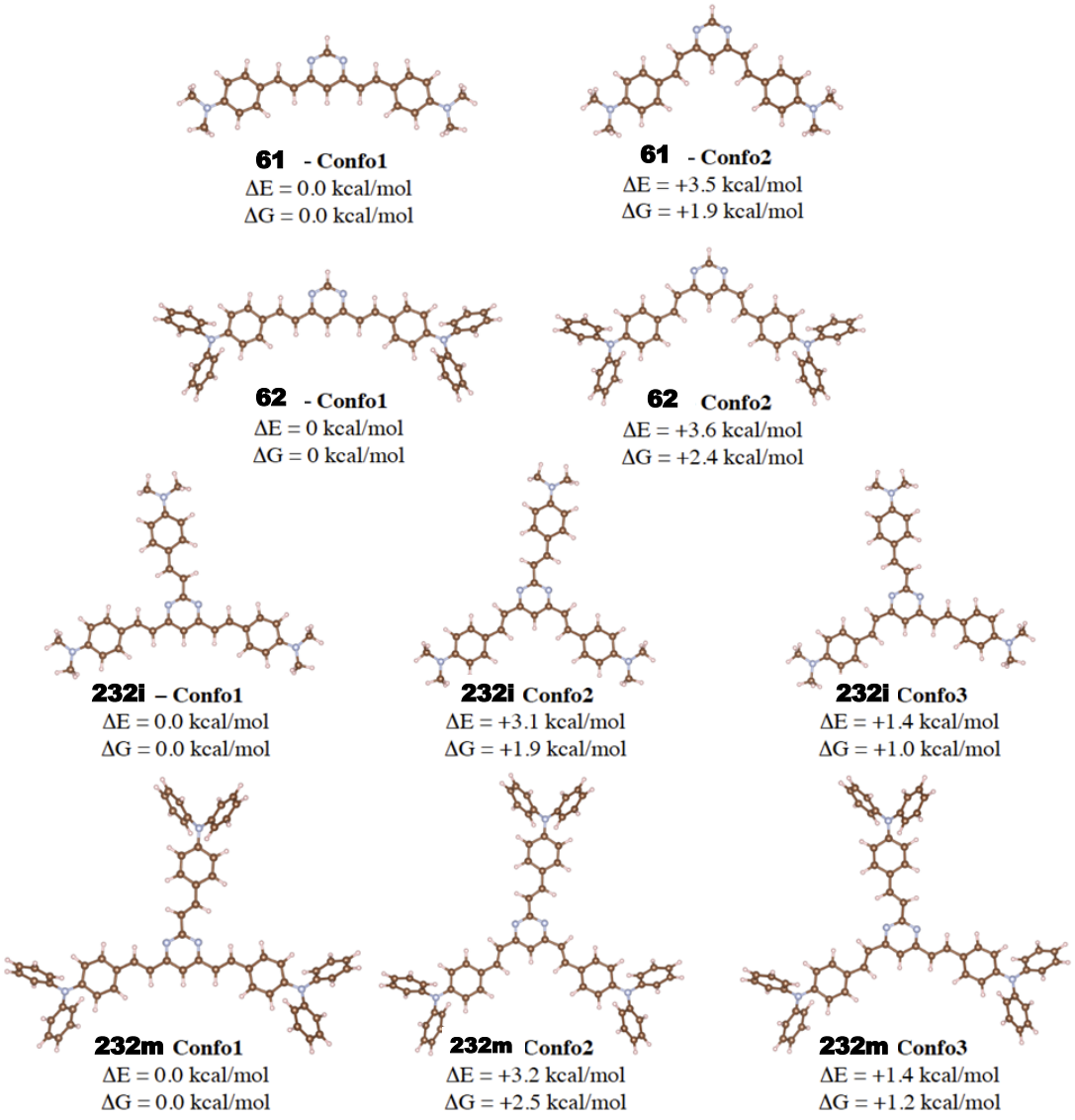

Figure 65. *Differences in electronic energies (ΔE) and free energies (ΔG) and Boltzmann population ratio (in parenthesis) for computed conformers of compounds* ***61****,* ***62*** *and* ***232i,m****. Provided values are related to conformers Confo1.*

The calculated absorption spectra of studied compounds in vacuum, displayed in *Figure 66*, revealed to be consistent with the experimental data. The red-shift in absorption was observed for diphenylamino derivatives as compared to the dimethylamino ones. Also, similar trend of the longest wavelength absorption maxima was found in calculated spectra in the meaning of red-shift within the order: one-branched < three-branched < two-branched. The lowest energy transitions (HOMO → LUMO) of two- and three-branched derivatives were almost identical with similar energy distribution over the C4 and C6 branches, based on the calculated transition energies (*Annexes 1*) and transition densities (*Figure 66*). However, absorptions of three-branched compounds were blue-shifted as compared to two-branched compounds, which was caused by contribution of the HOMO–1 → LUMO transition with high

oscillator strength to the longest wavelength absorption band. The second transition for two-branched and third transition for three-branched compound showed lower oscillator strength, however, they played a key role in two-photon absorption.

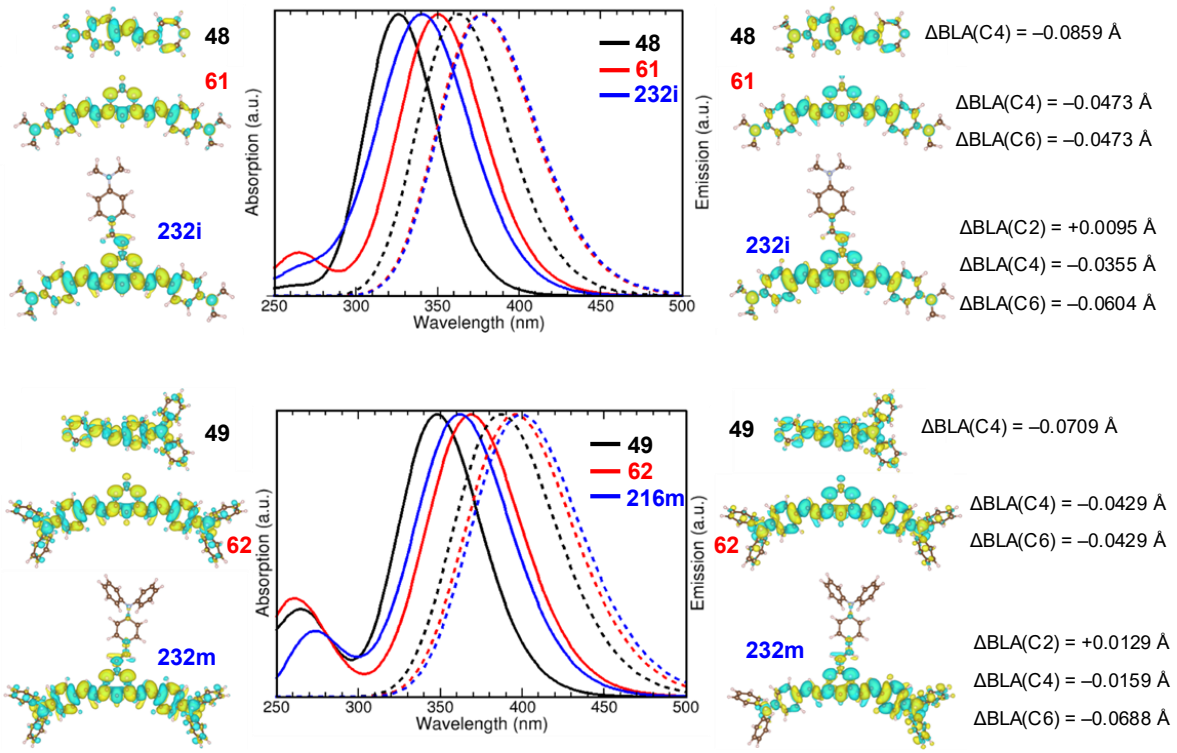

Figure 66. *Calculated absorption (solid) and emission (dashed) spectra of dimethylamino derivatives **48**, **61** and **232i** (up) and diphenylamino **49**, **62** and **232m** (down), their transition densities of the lowest lying excited state relevant to absorption (left) and emission (right) and differences in BLA values (right column).*

The calculated emission data were also in accordance with experimental data in nonpolar *n*-hexane. Red-shift in emission bands were observed for two- and three branched compounds as compared to one-branched. Due to the similar energy distribution over C4/C6 branches in dimethylamino compound **61** and its three-branched analogue **232i**, their spectra were similar to each other. On the other hand, symmetry breaking in three-branched **232m** resulted in slightly red-shifted emission spectra as compared to two-branched **62** (see *Figure 66*).

3.6 Two-photon absorption

In addition to their luminescence properties, the branching effect on two-photon absorption was studied for one-branched **48**, **49**, two-branched **61**, **62** and three-branched **232i**,**m** pyrimidine derivatives. Two-photon absorption measurements were performed by Dr. Jean-Pierre Malval and Dr. Arnaud Spangenberg, Université de Haute Alsace (France) using a two photon excitation fluorescence (TPEF) method in CH_2Cl_2 within the range of 700 to 1000

nm.[227] Results (spectra, 2PA absorption maxima and cross-sections) are provided in *Figure 67* together with superimposed one-photon absorption spectra for comparison.

Concerning one-branched chromophores **48** and **49**, their 2PA spectra matched the one-photon absorption spectra. This implies that both 1PA and 2PA originate from the HOMO → LUMO transition, also known as the first or $S_0 \rightarrow S_1$ transition. On the other hand, blue-shift in 2PA spectra was observed for two-branched derivatives as compared to their 1PA spectra. For two-branched derivatives **61** and **62**, 2PA originated from the second transition ($S_0 \rightarrow S_2$ transition), which had a higher energy (see *Annexe 1*), causing blue-shift as compared to 1PA as well as 2PA of one-branched derivatives. Even more prominent blue-shift was observed in 2PA spectra of three-branched compounds **232i** and **232m** with regards to their 1PA spectra and 2PA spectra of one- and two-branched counterparts. This shift was attributed to high energy third transition, which, even though exhibited low oscillator strength, was still the most active in 2PA response. Although, the lower energy transitions for two- and three-branched compounds were theoretically two-photon forbidden, they were still slightly active in 2PA showing small bands around 920 nm because of low molecular symmetry. For branched chromophores with C_3 symmetry, addition of third branch caused a change in the shape of 2PA spectra as compared to their two-branched derivatives.[56,228] However, in the case of this series (**61**/**62** vs **232i**/**m**) no changes in 2PA spectral shape were observed as a result of the lack of C_3 symmetry caused by the central pyrimidine core.

As far as the intensity of cross-section is concerned, approximately 1.5 times increase was observed in diphenylamino compounds **49**, **62** and **232m** as compared to dimethylamino derivatives (**48**, **61** and **232i**). Addition of aminostyryl branch in C6 position resulted in over 3 times increase in 2PA cross-section as compared to one-branched derivatives. Further raising of the cross-section was observed when going from two-branched to three-branched derivatives with the highest 2PA cross-section up to 500 GM for compound **232m** without change in position or shape of the spectra.

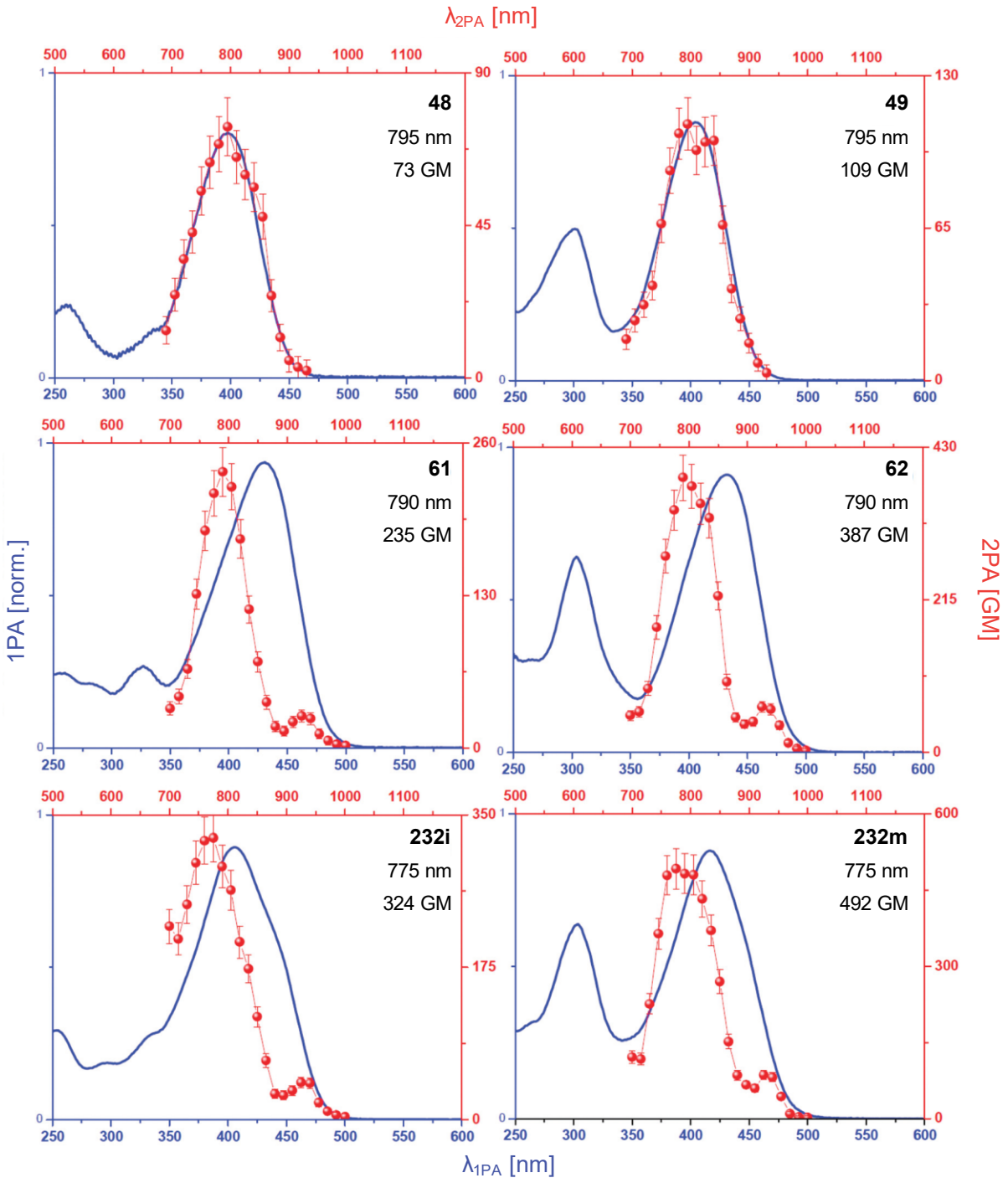

Figure 67. *One-photon (solid) and two-photon (dots) absorption spectra for compounds* ***48****,* ***49****,* ***61****,* ***62****,* ***232i*** *and* ***232m*** *and their 2PA maxima wavelength with corresponding 2PA cross-sections.*

3.7 Conclusions

A versatile and simple synthetic route to identically or differently substituted 2,4-distyryl and 2,4,6-tristyrylpyrimidines was described with overall good yields. A large series of two- and three-branched chromophores, which included 23 new compounds, was prepared based on this procedure. Electron-deficient pyrimidine ring was employed as central electron-

accepting unit and was connected to peripheral (mostly) electron-donating moieties via arylvinyl π-conjugated linker.

Pyrimidine ring does not show three-fold symmetry and this fact brings interesting and uncommon optical properties compared to multi-branched common chromophores with C_3 symmetry. Generally, the photophysical behaviour is given by peripheral substituent(s) attached in C4/C6 positions. However, when the C2 substituent was stronger electron-donating group than substituents in C4/C6 positions, the ICT dominates from the C2 position, and photophysical properties were mainly dependent on the substituent attached on C2 arm. Moderate to high fluorescence quantum yields were observed for most of the final compounds. Absorption and emission properties were studied during addition of an acid. For amino-substituted derivatives, protonation led to a dramatic quenching of the emission. However, in the case of final derivatives with peripheral methoxy groups, protonation resulted in formation of a new red-shifted emission band. An example of the emission light tuning upon addition of acid was provided. 2PA study of one-, two- and three-branched pyrimidine chromophores with peripheral amino substitution showed significant increase in 2PA cross-section with each additional branch within the same spectral region.

Results discussed in this chapter were published in three articles:

[1] M. Fecková, P. le Poul, F. Robin-le Guen, T. Roisnel, O. Pytela, M. Klikar, F. Bureš and S. Achelle: 2,4-Distyryl- and 2,4,6-tristyrylpyrimidines: Synthesis and Photophysical Properties, Journal of Organic Chemistry, **2018**, *83*, 11712–11726. 10.1021/acs.joc.8b01653

[2] F. Kournoutas, I. O. Kalis, M. Fecková, S. Achelle, M. Fakis: The effect of protonation on the excited state dynamics of pyrimidine chromophores, Journal of Photochemistry & Photobiology A: Chemistry, **2020**, *391*, 112398. 10.1016/j.jphotochem.2020.112398

[3] F. Kournoutas, A. Fihey, J.-P. Malval, A. Spangenberg, M. Fecková, P. le Poul, C. Katan, F. Robin-le Guen, F. Bureš, S. Achelle, M. Fakis: Branching effect on the linear and nonlinear optical properties of styrylpyrimidines, Physical Chemistry Chemical Physics, **2020**, *22*, 4165–4176. 10.1039/c9cp06476a

CHAPTER IV. 9,9-Dimethylacridan-substituted phenyl(arylvinyl)-pyrimidines as potential emitter for WOLED

4.1 Introduction

During the past two decades, exploring of utilization of TADF emitters in OLED devices, so-called 3rd generation OLEDs, has attracted great interest among researchers.[229–234] As discussed in the Chapter 2, in TADF emitters both singlet and triplet excitons can be harvested to produce light via the RISC mechanism. This exciton up-conversion process allows to reach up to 100% of internal quantum efficiency. For successful RISC, small energy difference between singlet and triplet excited state is required. This can be achieved by creating a spatial separation between frontier molecular orbitals. Typical TADF emitter molecule consists of electron-donating unit (bearing the HOMO) and electron-withdrawing unit (LUMO) with steric hindrance between them resulting in required HOMO and LUMO separation. In this context, bulky electron-donors, such as carbazoyl,[235,236] acridan,[87] phenoxazine,[197,237] phenothiazine,[238,239] benzazasiline[240] and heterocyclic spiro-compounds,[241–244] are usually used with connecting to the acceptor through short π-linker (phenylene, heterocycles or double bond).[245]

Another crucial property of potential OLED emitter is solid-state emission. Generally, organic chromophores lose their emission during aggregation due to the strong intermolecular π-π stacking of their planar molecular backbones.[246] This phenomenon is known as aggregation-caused quenching (ACQ). In 2001, opposite process was described by *Tang et al*., nowadays known as aggregation-induced emission (AIE).[247] AIE is generally observed for molecules with highly twisted structure, which is believed to be the reason why these compounds do not fluoresce in solution but become highly emissive upon aggregation.[246] Their twisted structure should prevent the intermolecular π-π stacking and intramolecular motion, which are both processes supporting non-radiative decay of an excited state.

Based on this, a novel series of pyrimidine-based chromophores was designed. Their general structure, presented in *Figure 68*, consist of pyrimidine central ring, serving as electron-withdrawing unit, connected in C2 position through 1,4-phenylene linker to acridan moiety. Positions C4 and/or C6 of pyrimidine were further decorated with arylvinyl units bearing peripheral electron-donating methoxy or diphenylamino groups.

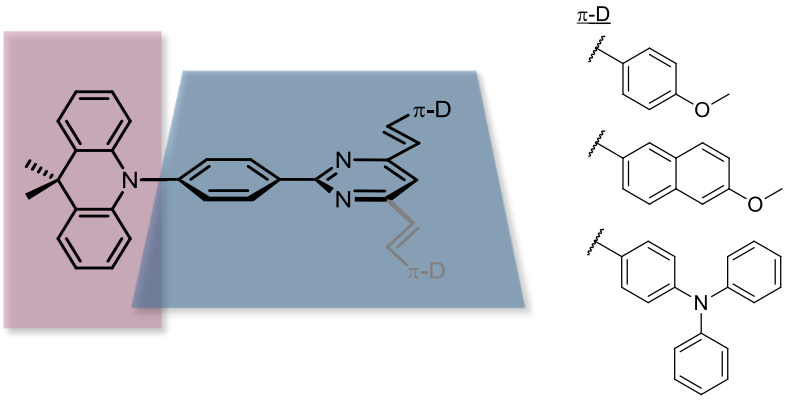

Figure 68. *Spatial arrangement of novel acridan-pyrimidine chromophores.*

4.2 Synthesis

The first step in synthesis leading to desired products was a reaction between 9,9-dimethyl-9,10-dihydroacridane and 4-bromo-1-iodobenezene, see *Scheme 4*. First attempt was carried out under conditions of Buchwald-Hartwig C-N cross-coupling reaction as described in a patent of LG Display Company.[248] However, no product was obtained. Reaction conditions of the second attempt were similar to the first one, except of replacing organic base (*t*-BuOK) with inorganic one (K_2CO_3), according to the literature.[249] In the same patent, researchers also reported Cs_2CO_3 as a base with higher solubility in organic solvents. Still, experiments with inorganic bases did not lead to compound **236**. Hence, Ullmann reaction was employed instead. The first tested conditions were similar to the conditions we used for preparation of *N* phenyl-substituted carbazoles, but only traces of **236** were observed.[250] Subsequently, different conditions were tested with changes in copper catalyst (CuI, CuBr), base (Cs_2CO_3, K_3PO_4, *t*-BuOK) and solvent (dimethylformamide, *i*-propylalcohol, 1,4-dioxane, *N*-methyl-2-pyrrolidone).[251–253] Finally, combination of elemental copper with K_2CO_3 as base in dimethylformamide led to desired product **236** with 56% conversion.[254] Along with bromo-derivative **236**, its iodo-derivative **237** was obtained with a ratio of 87:13 (based on ^{1}H NMR signals of hydrogens in *ortho* positions to halogens).

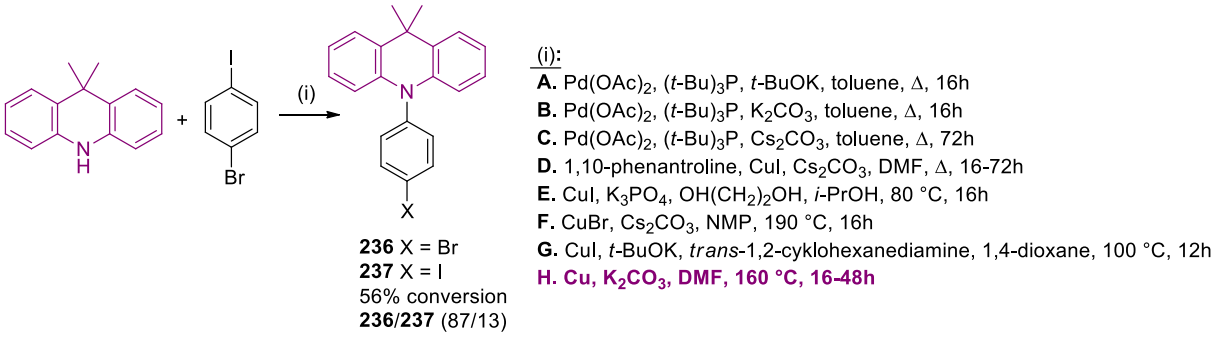

Scheme 4. *Preparation of compounds **236/237**.*

The following step was a preparation of boron-derivative **238** suitable for Suzuki-Miyaura C-C by replacing of halogen with boronic acid pinacol ester using common bis(pinacolato)diboron and Pd(dppf)Cl_2 catalyst (*Scheme 5*).[254,255] Compound **238**, prepared in 79% yield, was used for preparation of intermediates **239** and **240** by Suzuki-Miyaura reaction with 2-chloro-4-methyl- and 2-chloro-4,6-dimethylpyrimidines.[122,128] .[122,128] Finally, methyl group(s) underwent Knoevenagel condensation with corresponding aldehydes providing final chromophores **241** and **242**.[111]

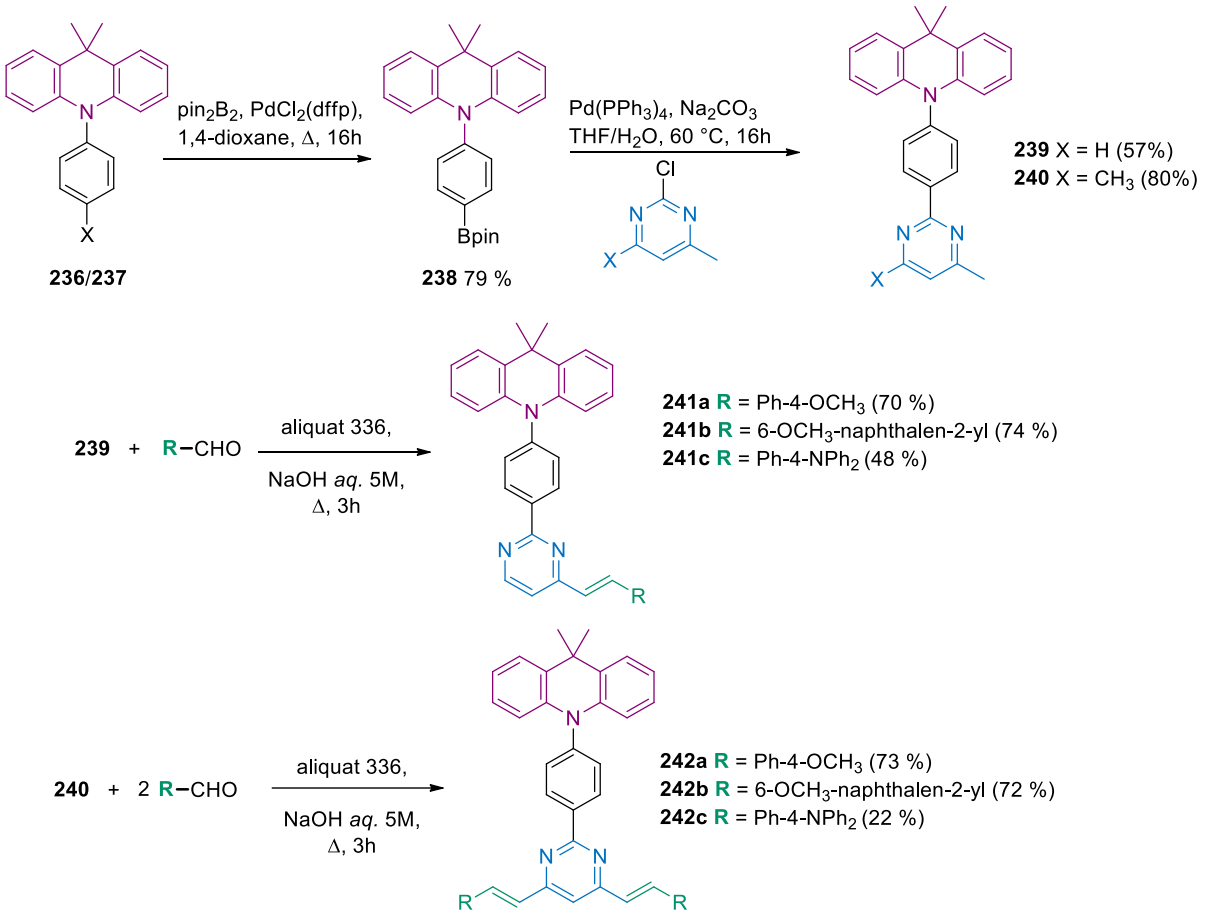

Scheme 5. *Synthetic route leading to final chromophores **241** and **242**.*

Lower yields were observed for compounds **241c** and **242c** with peripheral diphenylamino donor units as compared to their methoxy analogues (**a** and **b**) due to their more complicated purification process. Compounds **239–242** were characterized by standard analytical measurements (^{1}H/^{13}C NMR spectroscopy and HR-MALDI mass spectrometry) and results are provided in Chapter 6. *E* configuration of double bonds was determined by coupling constant of the ^{1}H NMR spectra ($^3J_{H\text{-}H} \approx 16$ Hz).

4.3 Thermal properties

Thermal behaviour of final chromophores **241** and **242** was studied by DSC analysis. Results of measurement are summarized in *Table 8* and thermograms of compounds **241** are displayed in *Figure 69*. Measurements were performed by Ing. Milan Klikar, Ph.D., University of Pardubice (Czech Republic).

Table 8. *Results of thermal properties studied by DSC analysis for final compound **241** and **242**.*

compd	T_m [°C]	T_d [°C]	*compd*	T_m [°C]	T_d [°C]
241a	204	380	***242a***	201	370
241b	199	375	***242b***	271	380
241c	–	375	***242c***	233	380

Measured melting points ranged from 199 to 271 °C and temperatures of decompositions from 370 to 380 °C. All studied final derivatives were crystalline solids, except of compounds **241c**, which was amorphous solid, and this fact was reflected in its thermal behaviour. Its thermogram consists of glass transition at 70 °C followed by decomposition at 375 °C without any melting process, as a contrast to the rest of compounds, which showed sharp melting peaks. During the heating of chromophore **242a**, polymorphous enantiotropic transition around 140–150 °C was recorded. Monotropic solid-solid transition of metastable crystals at 253 °C was observed for compound **242b**. For compounds **242**, position of melting peaks was determined by the nature of C4/C6 branches. On the other hand, temperature of decomposition showed to be independent on number of branches, their length or type of peripheral donor unit. The high thermal robustness of studied compounds was given by the parent acridan-pyrimidine scaffold.

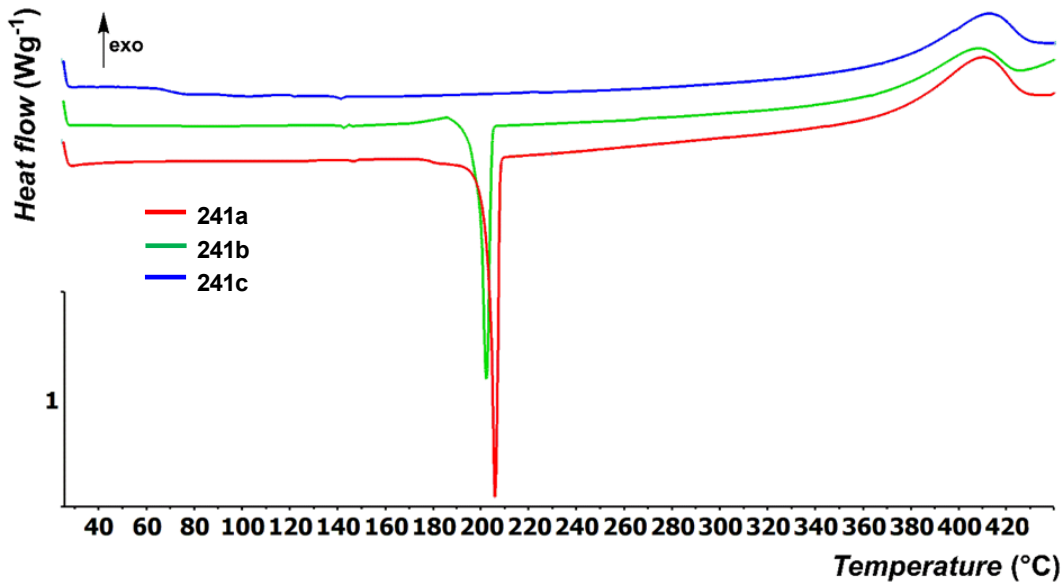

Figure 69. *DSC curves of final compounds* ***241****.*

4.4 X-Ray analysis

Slow evaporation of ethyl acetate/dichloromethane solutions of final compounds **241a**, **242a** and **242c** resulted in suitable crystals, colourless or yellow prisms, for X-ray analysis performed by Dr. Thierry Roisnel, Université de Rennes 1 (France). Proposed structures with *E* configuration on double bonds were confirmed, see *Figure 70*. Concerning space groups, $P2_1/c$ was revealed for monoclinic crystals of **241a** and **242a** and $P1$ for triclinic crystal of **242c**. A molecule of ethyl acetate was found in the asymmetric unit of two **242a** molecules. Similarities between structures of studied compounds and their structural analogues were found, such as dihedral angles between pyrimidine central core and C2 phenyl ring (<17.5°) and between phenylene units in styryl moiety and pyrimidine (<22°).[105,118,256] The anticipated twisted molecular structure was also confirmed for all studied derivatives. Torsion angles between peripheral acridan moiety and phenylene bridge were 82.3, 81.1 and 85.0° for **241a**, **242a** and **242c** and between acridan and central pyrimidine ring were established as 87.6, 88.3 and 83.3°, respectively. This structural arrangement would indicate an important spatial separation of the frontier molecular orbitals, which is one of the necessary aspects to afford small ΔE_{ST} values. BLA values were calculated for vinylene linkers attached to pyrimidine ring. These values ranged between 0.1265 and 0.1316 Å for compounds **241a** and **242a**. As a contrast to the methoxy derivatives, a significantly lower BLA value (0.107 Å) was obtained for one of the C4/C6 vinylene linker of compound **242c**. This implied a stronger ICT in one of the C4/C6 branches for diphenylamino derivative as compared to the methoxy-substituted derivates.

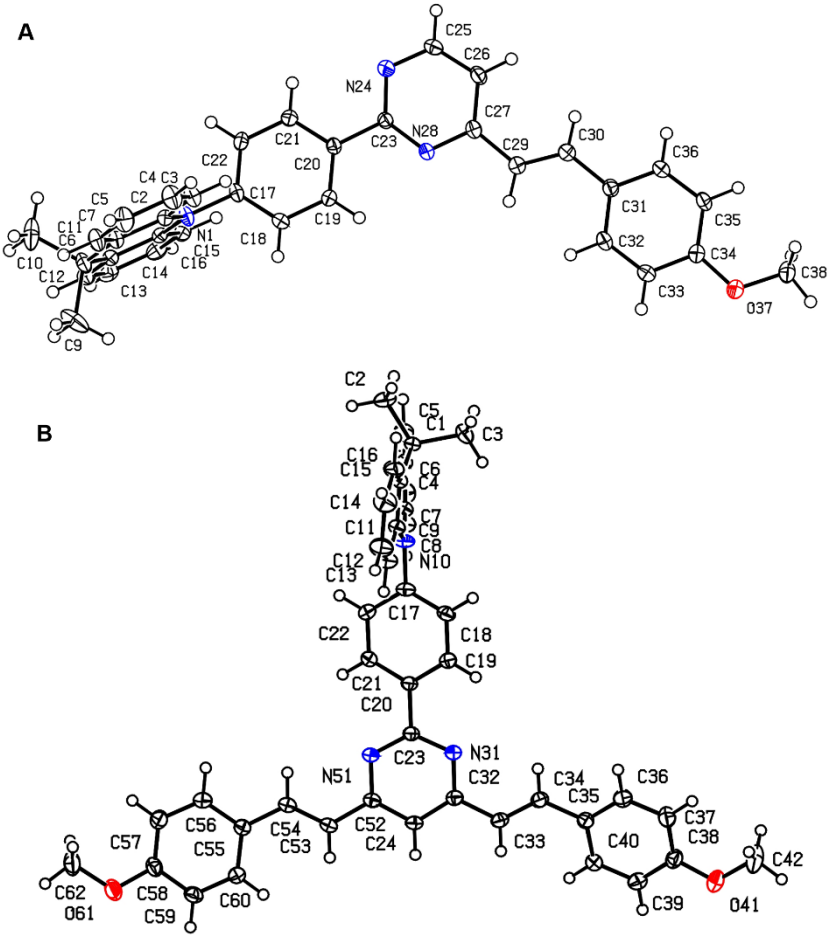

Figure 70. *ORTEP diagrams of compounds (A)* ***241a*** *and (B)* ***242a*** *obtained at 150 K (R = 0.05) with thermal ellipsoid at the 50% probability level.*

4.5 Photophysical properties

Absorption and emission in CH_2Cl_2

Initially, photophysical properties of final chromophores **241** and **242** were studied in CH_2Cl_2 solution with solute concentration $c = (1 \pm 0.1) \times 10^{-5}$ M. Results are provided in *Table 9*. The longest-wavelength absorption maxima were comparable to similar derivatives without C2 substitution with increasing red-shift in an order of methoxyphenyl (**a**) < methoxynaphthyl (**b**) < diphenylaminophenyl (**c**).[108,111] Red-shift in the absorption maxima (~ 20–30 nm) and increase in the molar absorption coefficient were recorded for compounds **242** bearing two arylvinyl branches as compared to their mono-arylvinyl-branched counterparts **241**. However, surprisingly final chromophores with peripheral methoxy groups (**a** and **b**) exhibited almost no emission, whereas diphenylamino-substituted compounds **c** were highly luminescent ($\Phi_F = 0.75$ for **241c** and $\Phi_F = 0.94$ for **242c**).

Table 9. *Absorption and emission data of compounds* ***241*** *and* ***242*** *in CH_2Cl_2, n-heptane and solid-state.*

	CH_2Cl_2				*n-heptane*				*Solid-state*	
Compd[a]	λ_{max}(abs) (ε) [nm] ([$mM^{-1}\cdot cm^{-1}$])	λ_{max}(em) [nm]	Φ_F[b]	Stokes shift [cm^{-1}]	λ_{max}(abs) (ε) [nm] ([$mM^{-1}\cdot cm^{-1}$])	λ_{max}(em) [nm]	Φ_F[b,c]	Stokes shift [cm^{-1}]	λ_{max}(em)[d] [nm]	CIE coordinates[e]
241a	340 (29.7)	–	–	–	337 (29.4)	432	0.11/0.15	6525	471	(0.28, 0.40)
241b	351 (35.4)	–	–	–	368 (24.5)	429	0.09/0.13	3864	471	(0.35, 0.41)
241c	406 (31.3)	531	0.75	5798	396 (30.7)	444	0.37/0.40	2730	521	(0.27, 0.54)
242a	369 (37.9)	–	–	–	383 (24.3)	426	0.06/0.08	2635	474	(0.29, 0.42)
242b	381 (57.5)	–	–	–	395 (48.8)	435	0.22/0.29	2328	508	(0.35, 0.45)
242c	431 (58.0)	552	0.94	5086	432 (53.6)	460	0.63(0.74	1409	535	(0.32, 0.60)

[a]All spectra were recorded at room temperature with solute concentration c = (1 ± 0.1) × 10^{-5} M. [b] Fluorescence quantum yield (±10%) determined relative to that of 9,10-bisphenylethynylanthracene in cyclohexane (Φ_F = 1.00).[257] [c]Before/after bubbling the solution with N_2. [d]Emission maxima of powdered samples. [e]CIE chromaticity coordinated (x,y) for thin layers.

Absorption and emission in n-heptane

Absorption and emission measurements were also performed in *n*-heptane, as a non-polar solvent (see *Figure 71* and *Table 9*). Similar trends to those in CH_2Cl_2 were observed for absorption, such as increasing red-shift with extended π-system and increasing electron-donating strength of peripheral donors. Nevertheless, photoluminescence of methoxy derivatives **a** and **b** enhanced significantly, while reduction was observed for diphenylamino compounds **c**. The increased fluorescence quantum yields (chromophores **a** and **b**) suggested aggregation-induced emission (AIE) phenomenon. It should be also noted that recorded emission spectra of methoxyphenyl derivatives (**a**) were almost identical to those of methoxynaphthyl (**b**). Deoxygenation of measured samples resulted in slight increase in fluorescence quantum yield for all studied compounds.

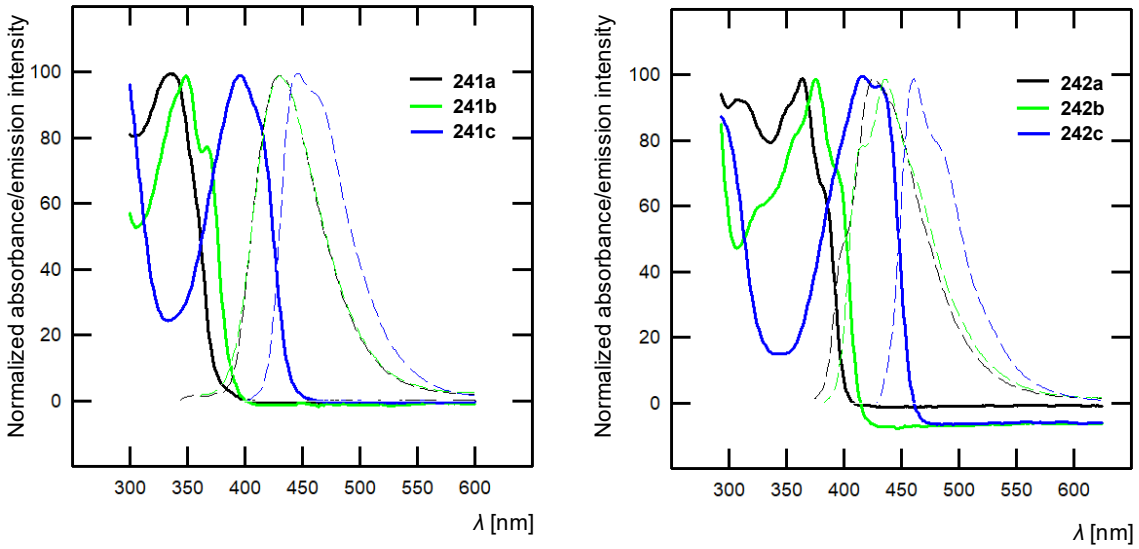

Figure 71. *Normalized absorption (solid) and emission (dashed)spectra of final chromophores **241** (left) and **242** (right) measured in n-heptane.*

Emission solvatochromism

Emission behaviour of final derivatives was also studied in various aprotic solvents. For diphenylamino-substituted chromophores **241c** and **242c**, red-shift in emission spectra was observed with raising solvent polarity, see *Figure 72*. This positive solvatochromism, typical feature of push-pull chromophores, was also described for tri(arylvinyl)pyrimidines in previous chapter. However, methoxy derivatives **241a,b** and **242a,b** did not show such solvatochromic behaviour. When going from *n*-heptane to toluene, the emission spectra became red-shifted and broader indicating emission from the ICT excited state. Nevertheless, dual emission was observed with further increase in solvent polarity for compounds **a** in acetone and for compounds **b** in THF. The red-shifted and broader band of dual emission accounted

for emission from ICT/TICT excited state, which respected the solvatochromic red-shift progression, while the blue-shifted band originated from locally excited (LE) state, which became more prominent due to a very low intensity of the ICT/TICT emission. Shorter-wavelength shoulder was recorded for compound **242a** even in THF but with lower intensity as compared to that in acetone. As it was already mentioned, dual emission was obtained in THF for methoxynaphthyl derivatives **b**. Their emission spectra in acetone composed predominantly of a single emission peak, which was blue-shifted with regard to that in toluene, with the origin in LE state. Based on these results, there are significant differences in the fundamental photophysics of methoxy and diphenylamino compounds, which is based on participation of these electron-donating groups in the ICT (and not the acridan).

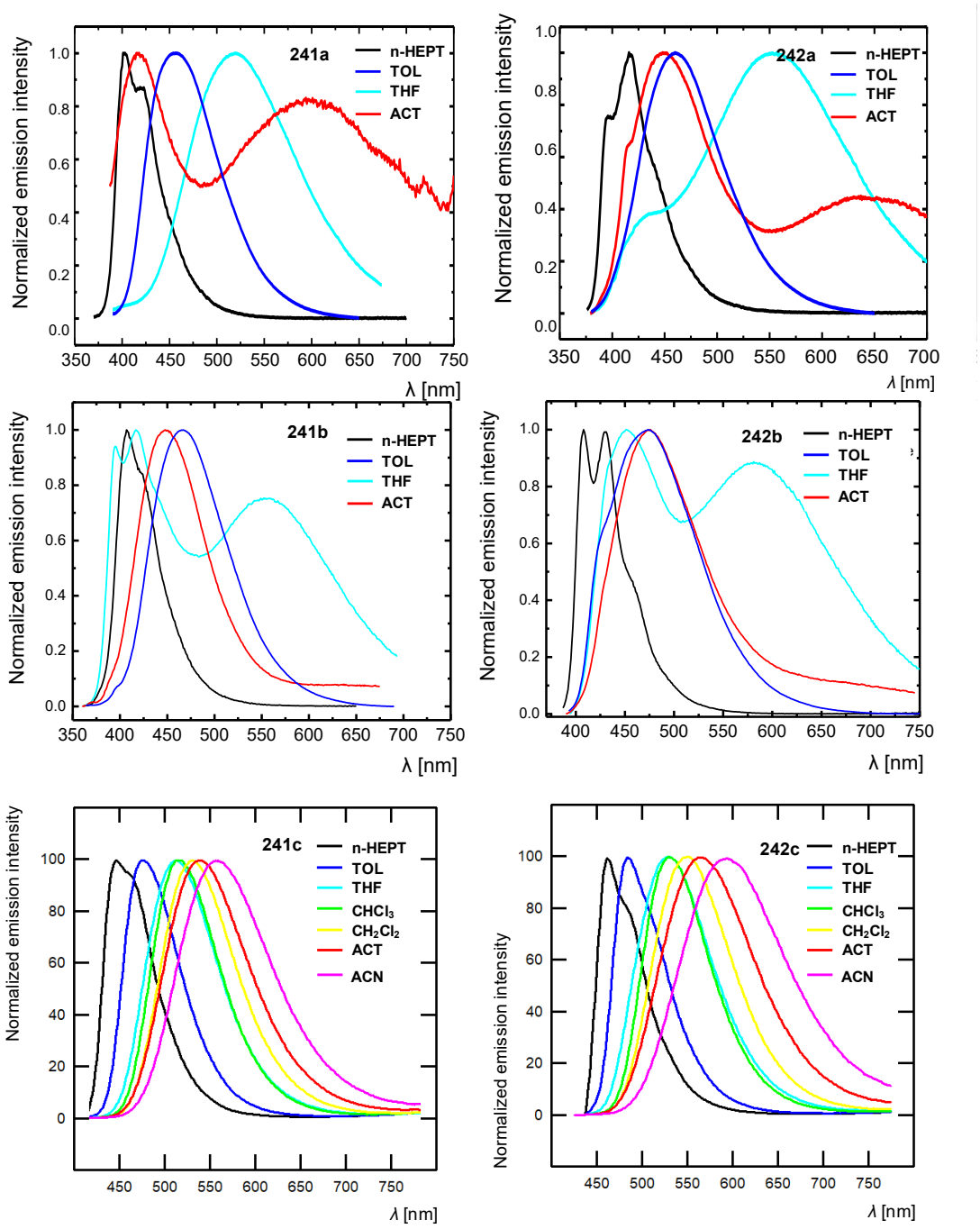

Figure 72. *Normalized emission spectra of final chromophores **241** and **242** in various aprotic solvents.*

Emission spectra of final compounds in THF were also measured after deoxygenation by bubbling N_2 through the solution (*Figure 73*). For methoxy derivatives **a** and **b**, the longer-wavelength band increased almost two-times, which suggested that this emission band is quenched by oxygen. On the other hand, shorter-wavelength emission band stayed almost unchanged upon bubbling. Oxygen is a common fluorescence quencher, which can impact both LE and ICT states, but affects the longer-lived state more dramatically. This indicated that

the ICT state of the methoxy derivatives was highly and long-life stabilized. On the contrary to diphenylamino chromophores **c**, emission spectra underwent only slightly increase during bubbling. This pointed to differences in the nature of the emitting state of methoxy and diphenylamino derivatives.

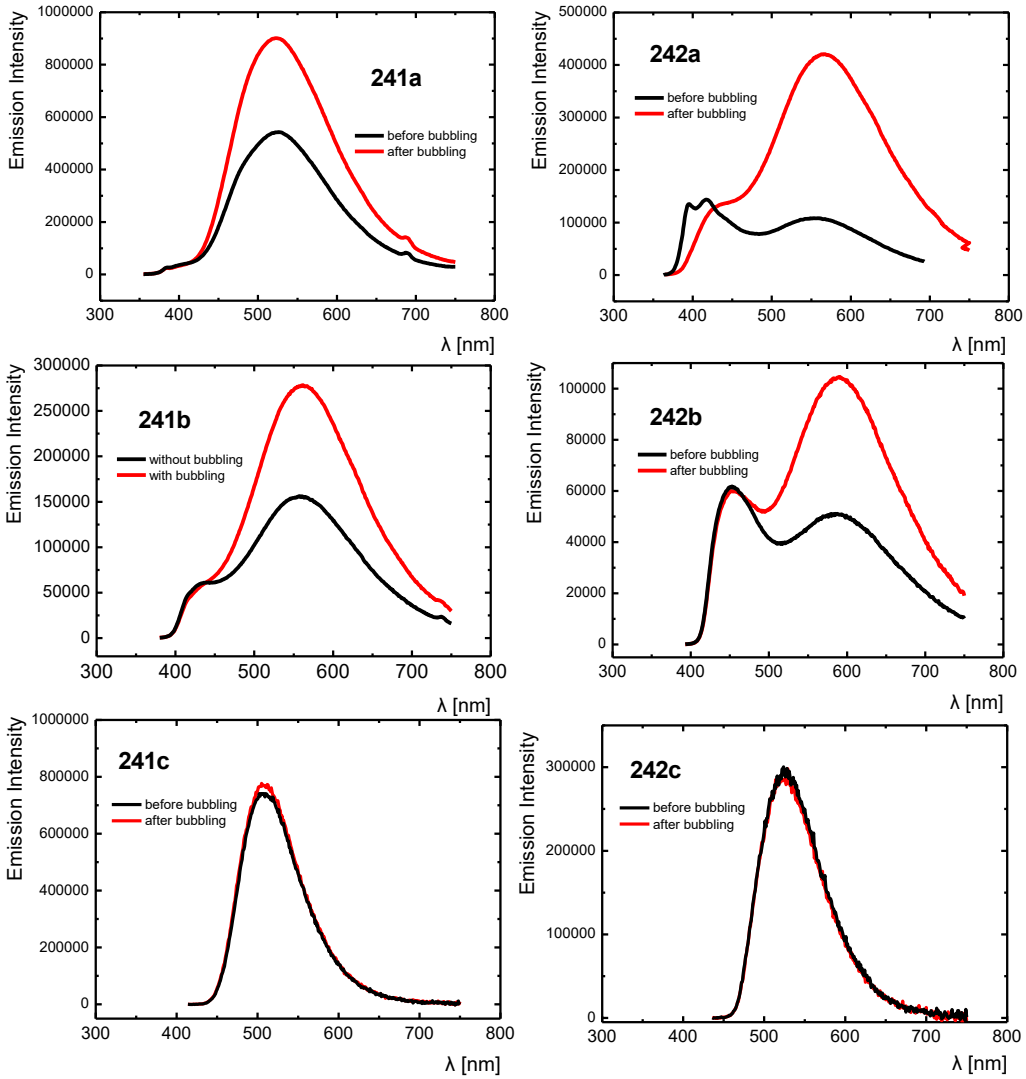

Figure 73. *Emission spectra of final compound **241** and **242** recorded in THF before (black) and after bubbling with N_2 (red).*

Excited-state dynamics

In order to shed more light into the fluorescence properties, emission dynamics of all final chromophores were measured by Prof. Mihalis Fakis, University of Patras (Greece). Spectra were detected in THF for both emission bands with or without bubbling and are shown in *Figure 74*. The decay of diphenylamino compound **c** differed from the decay of methoxy derivatives **a** and **b**. Compounds **241c** and **242c** exhibited average lifetimes of 2.45 ns, which is typical for molecules emitting from an ICT state. Deoxygenation of these solution affected lifetimes

only slightly (lifetimes of compounds **241c** and **242c** increased to 2.75 ns after bubbling with N_2). On the other hand, decay of methoxy derivatives were more complicated, varied for both shorter- and longer-wavelength bands and could not be explained by a typical ICT emitting state. Analysing fluorescence dynamics of compounds **242b** at the shorter-wavelength band, as an example, very fast dynamics with the lifetime within the instrument response function (<80 ps) were observed. This decay dynamics are typical for a molecule with a very low quantum yield in moderately polar solvents. Nonetheless, decay at the longer-wavelength contained two components: (i) a very fast (<80 ps, ≈ 90% amplitude) and (ii) longer one (within the order of 10 ns, ≈ 10% amplitude). After bubbling, the longer component prolonged up to 30 ns and returned to 10 ns after exposure to air. These observations implied that methoxy derivatives disponed with two contributions from emissions of different origin. The shorter-wavelength emission originated from fluorescence of the LE with small quantum yield independently on the oxygen in solution. The longer-wavelength emission band consisted of LE fluorescence and long-lived fluorescence from a highly stabilized ICT state strongly dependent on deoxygenation.

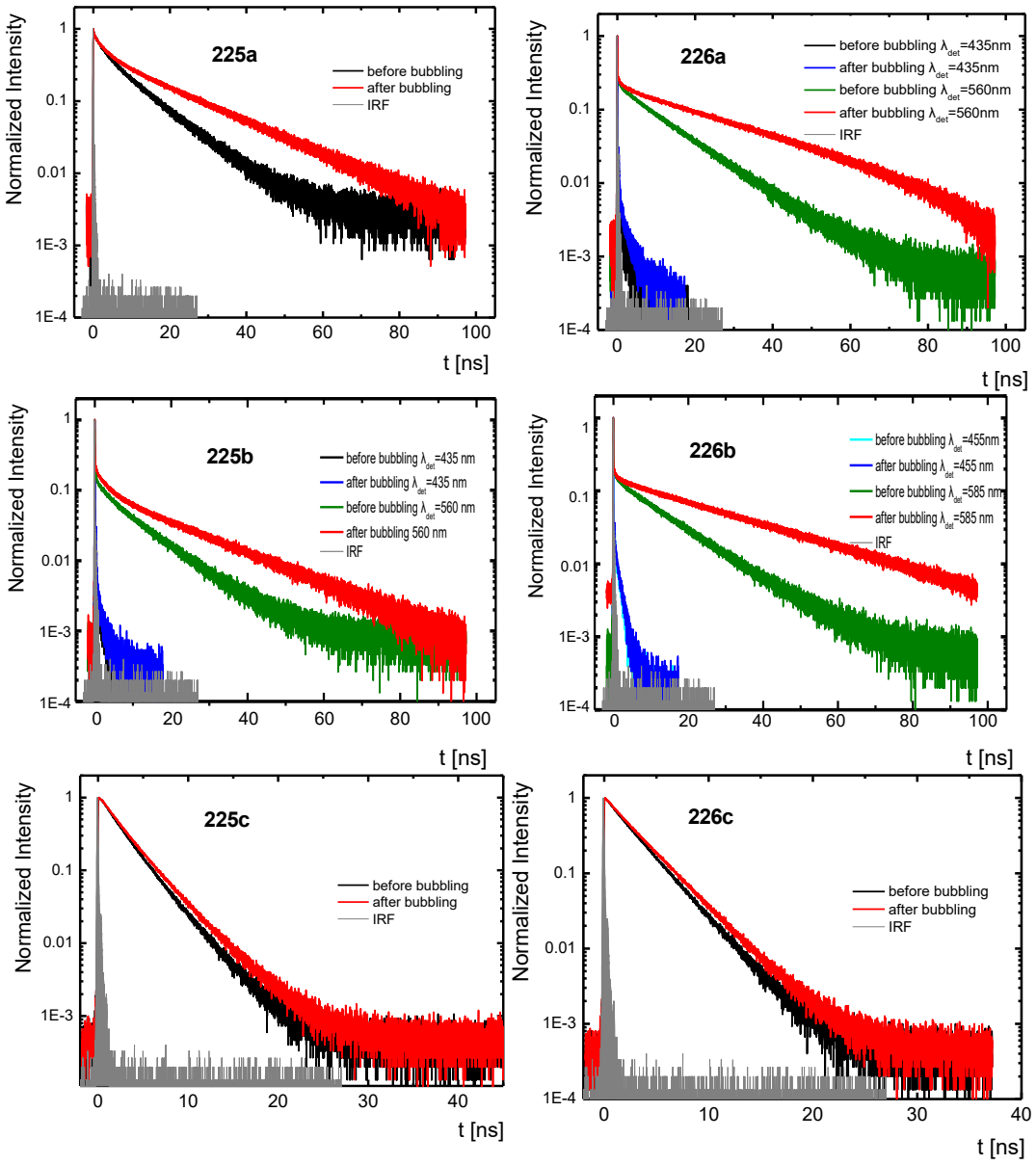

Figure 74. *Excited state dynamics of **241** and **242** in THF before and after bubbling with N_2. For compounds **241b**, **242a** and **242b** dynamics were detected at both shorter- and longer-wavelength emission bands.*

AIE properties

For investigation of an AIE properties, fluorescence spectra were measured in THF/water solutions with different ratios. Recorded spectra of all final compounds are displayed in *Figure 75*. The longer-wavelength emission band of methoxy derivatives **a** and **b** vanished after addition of 10% of water with remaining emission from the LE state. This emission band underwent a slight red-shift with increasing amount of water as a result of increasing polarity of solvents mixture. Emission intensities remained unchanged up to 60 % of water ratio. Further addition of water resulted in increase of emission intensity. Small blue-shift in emission maxima occurred at 90 and 97% of water content. For diphenylamino derivatives **c**, a slow decrease

in fluorescence intensity and red-shift of emission maxima were observed by up to ~50% of water. Additional water increased emission intensity, followed by a second gradual decrease and blue-shift in the emission maxima.

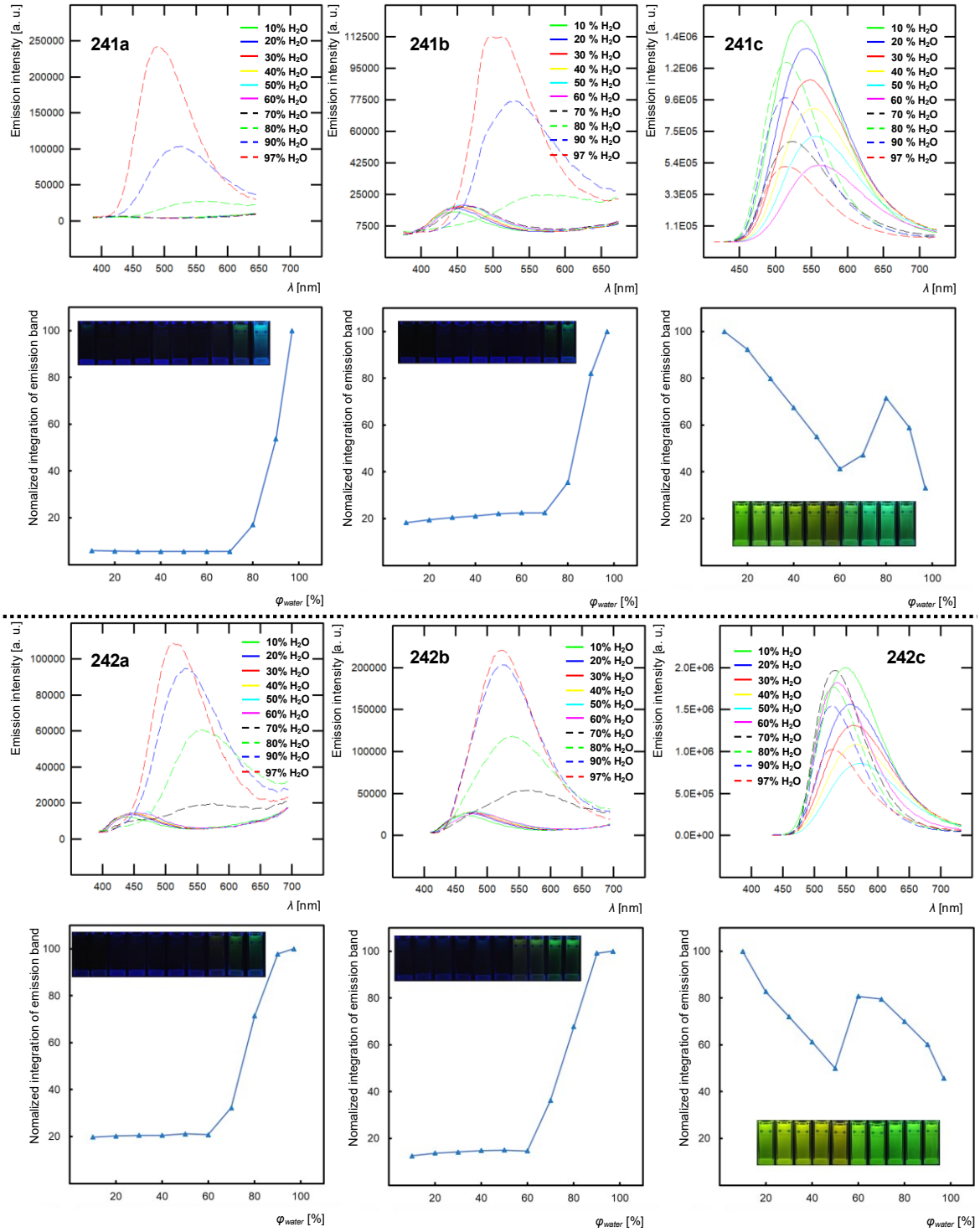

Figure 75. *Emission spectra of compounds* ***241*** *and* ***242*** *(c = 1 × 10^{-5} M) in THF/water mixture. Integration of emission band vs. water volume percent in mixture. Inserted pictures were taken upon irradiation with UV lamp (λ_{em} = 254 nm).*

Excited state dynamics of final compounds **241b** and **242b** were studied under the same conditions as described in previous paragraph; obtained spectra are shown in *Figure 76*. Increase in fluorescence lifetime was expected due the suppressing of nonradiative decays during aggregation. The out-of-plane rotation of acridan unit is expected to lower the luminescence intensity due to its energy consumption. However, aggregation is considered to hinder this process. Indeed, time resolved measurements revealed an increase of the average lifetime for compounds **241b** and **242b** upon increasing water ratio. In more details, the average lifetime of **241b** enhanced from <0.050 to 2.7 ns when going from 20% to 95% water solution. For compound **242b**, average lifetime increased from <0.050 ns up to 3.6 ns.

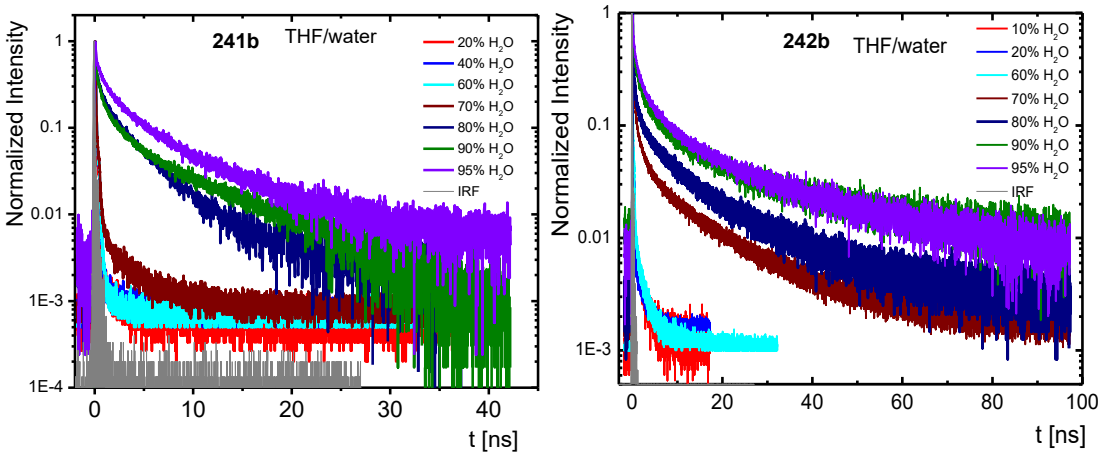

Figure 76. *Emission dynamics of **241b** and **242b** ($c = 1 \times 10^{-5}$ M) in THF/water mixture.*

Solid-state emission

Powdered samples of final compounds **241** and **242** were measured to obtaining their solid-state emission spectra. Results of this measurement, i.e. emission maxima are provided in *Table 10* and spectra are displayed in *Figure 77A*. Almost identical spectra were obtained for methoxy derivatives **241a**, **241b** and **242a**, which emitted green light with emission maxima around 470 nm. Red-shift in emission maxima to 508 nm was observed for turquoise light emitting compound **226b**. Both diphenylamino derivatives **c** showed emission maxima of their narrow emission bands in the range of 520–530 nm with green emission.

Spin-coating method was utilized to prepare thin films of final chromophores. Emission spectra of these neat films are provided in *Figure 77C* and *D*. Dual emission covering the vast majority of visible region was observed for chromophores **a** and **b** with peripheral methoxy group. Two distinguishable peaks could be seen in emission spectra of derivatives **225a,b**, whereas for compound **226a,b**, the LE state band appeared as pronounced shoulder superimposed on an emission band of the ICT state. The two emission bands clearly have a different origin, similarly to those obtained in THF. The longer-wavelength fluorescence band

involves a long-lived ICT state, as revealed by emission decays with long dynamics (see *Annex 4*). On the contrary, diphenylamino derivatives **c** exhibited narrow single peak emission with the maxima appearing slightly over 500 nm. Chromaticity coordinates, which are close to those of pure white light, are also provided in *Table 9*.

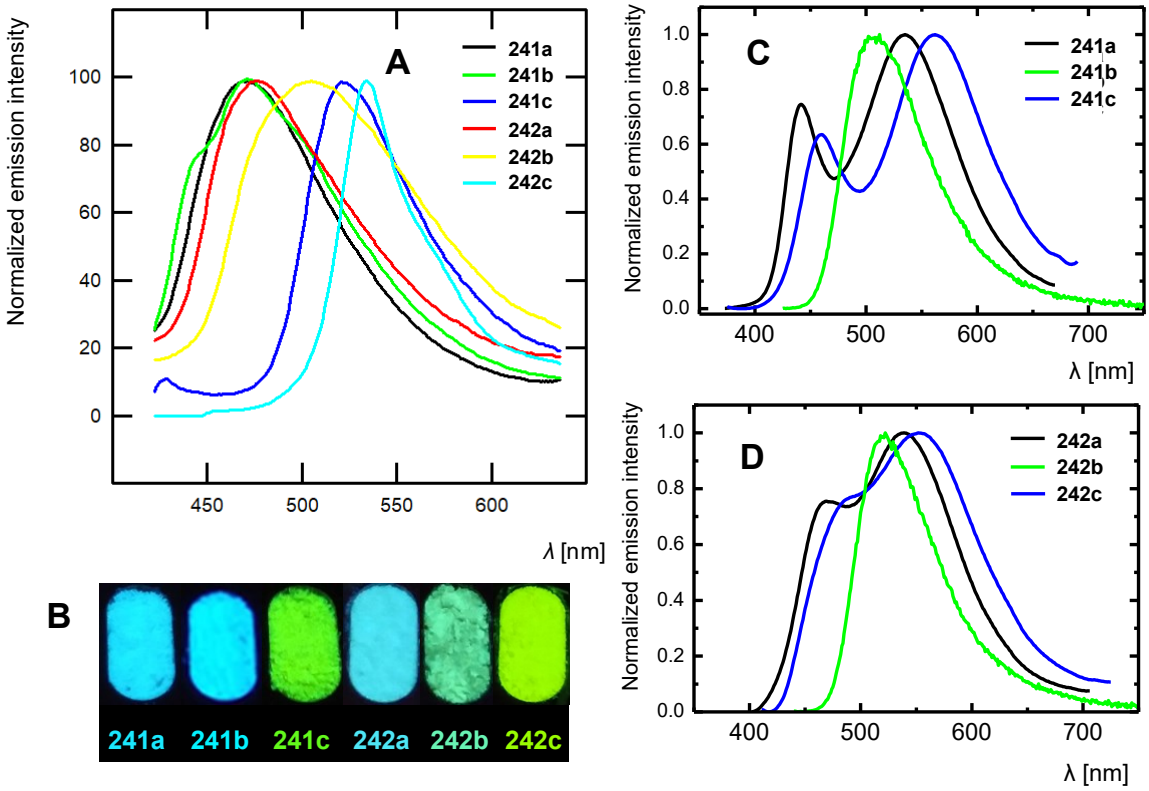

Figure 77. *(A) Normalized emission spectra of solid-state chromophores* ***241*** *and* ***242****. (B) Picture of powdered final compounds under UV lamp (λ_{em} = 254 nm). Emission spectra of neat film of compounds* ***241*** *(C) and* ***242*** *(D).*

4.6 DFT calculation

Gaussian 16W software was employed to establish the spatial and electronic properties of final compounds **241** and **242**. The initial geometries of studied molecules, HOMO and LUMO energies and ground state dipole moments were calculated at the B3LYP/6-311++G(3d.f.2p) level in vacuum. The electronic absorption spectra were calculated by the TD-DFT (*n* states = 8) B3LYP/6-311++G(3d,f.2p) method. Results are provided in *Table 10*. The calculations were performed and evaluated by Prof. Ing. Oldřich Pytela, DrSc. and Prof. Ing. Filip Bureš, Ph.D.

Table 10. *Results of DFT calculation for compounds **241** and **242**.*

compd	E_{HOMO-1} *[eV]*	E_{HOMO} *[eV]*	E_{LUMO} *[eV]*	E_{LUMO+1} *[eV]*	ΔE^a *[eV]*	λ_{max} *[nm/eV]*	*GoS*[b]
241a	–5.98	–5.10	–2.35	–2.35	2.75/3.63	352(3.52)	C_s
241b	–5.89	–5.06	–2.45	–2.45	2.61/3.44	381(3.25)	C_s
241c	–5.48	–5.08	–2.31	–2.31	2.77/3.17	434(2.86)	None
242a	–5.87	–5.13	–2.42	–2.42	2.71/3.45	393(3.16)	C_{2v}
242b	–5.66	–5.10	–2.46	–2.46	2.64/3.20	433(2.86)	C_{2v}
242c	–5.31	–5.16	–2.36	–2.36	2.80/2.95	474(2.62)	None

[a]HOMO–LUMO/HOMO–1–LUMO. [b]Group of symmetry.

The calculated optimized structures were in accordance with results drawn from X-ray analysis and side to side comparison of X-ray and DFT structures of **241a** and **242a** is displayed in *Figure 78*. Torsion angle between acridan moiety and rest of the molecule was found to be 86 and 90° for **241a** and **242a**, respectively. An inspection of the calculated molecular geometries also revealed that diphenylamino-substituted derivatives **c** possessed no symmetry, which is in contrast to methoxy derivatives **a** and **b**. No significant fluctuations in HOMO and LUMO levels, and therefore steady HOMO-LUMO gap, were observed when going from weaker donors **a,b** to the stronger diphenylamino **c**, indicating that these frontier molecular orbitals did not contributed to the ICT.

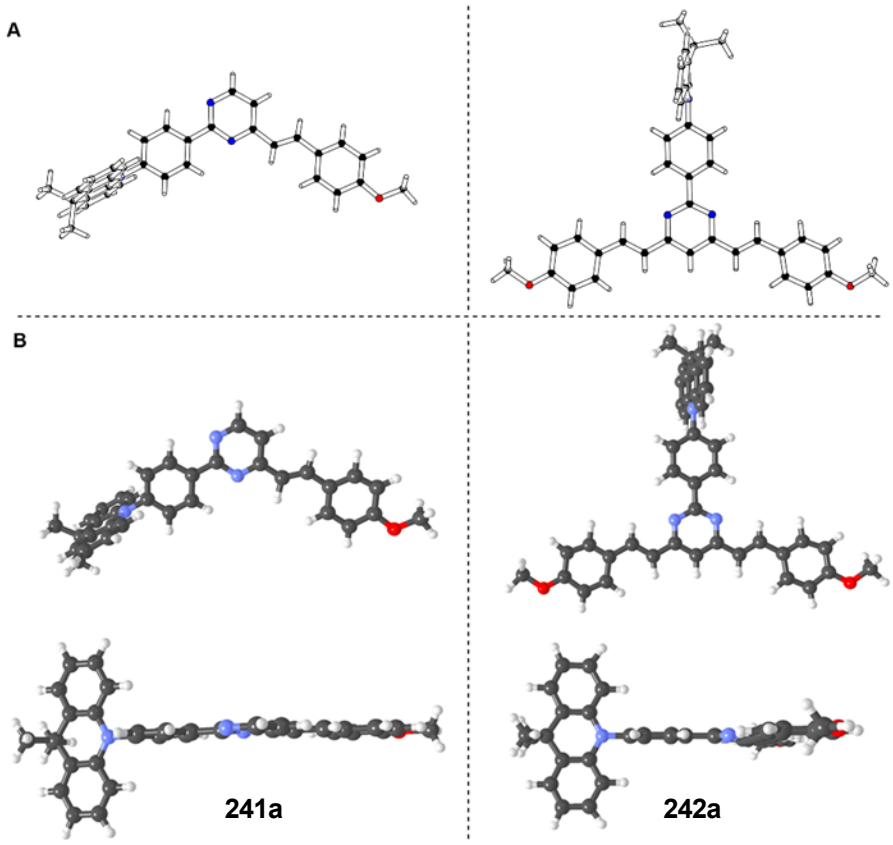

Figure 78. *(A) X-Ray and (B) DFT-optimized geometries of final derivatives* ***241a*** *and* ***242a****.*

Localization of molecular orbital is displayed in *Figure 79*. Similarly to tris(arylvinyl)pyrimidines, the LUMO was spread over the central pyrimidine ring and attached vinylene linkers. The HOMO was localized on nitrogen atom of acridan units for all final chromophores **241** and **242**. On the other hand, the HOMO–1 occupied peripheral methoxy or diphenylamino electron-donating groups. Position of the HOMO–2 varied depending on the number of C4/C6 branches. For derivatives **241** with one branch, the HOMO–2 was localized again on phenylacridan moiety, whereas for compounds **242** it remained localized like the HOMO–1. The LUMO+1 and LUMO+2 were found localized over the pyrimidine ring or the acridan unit.

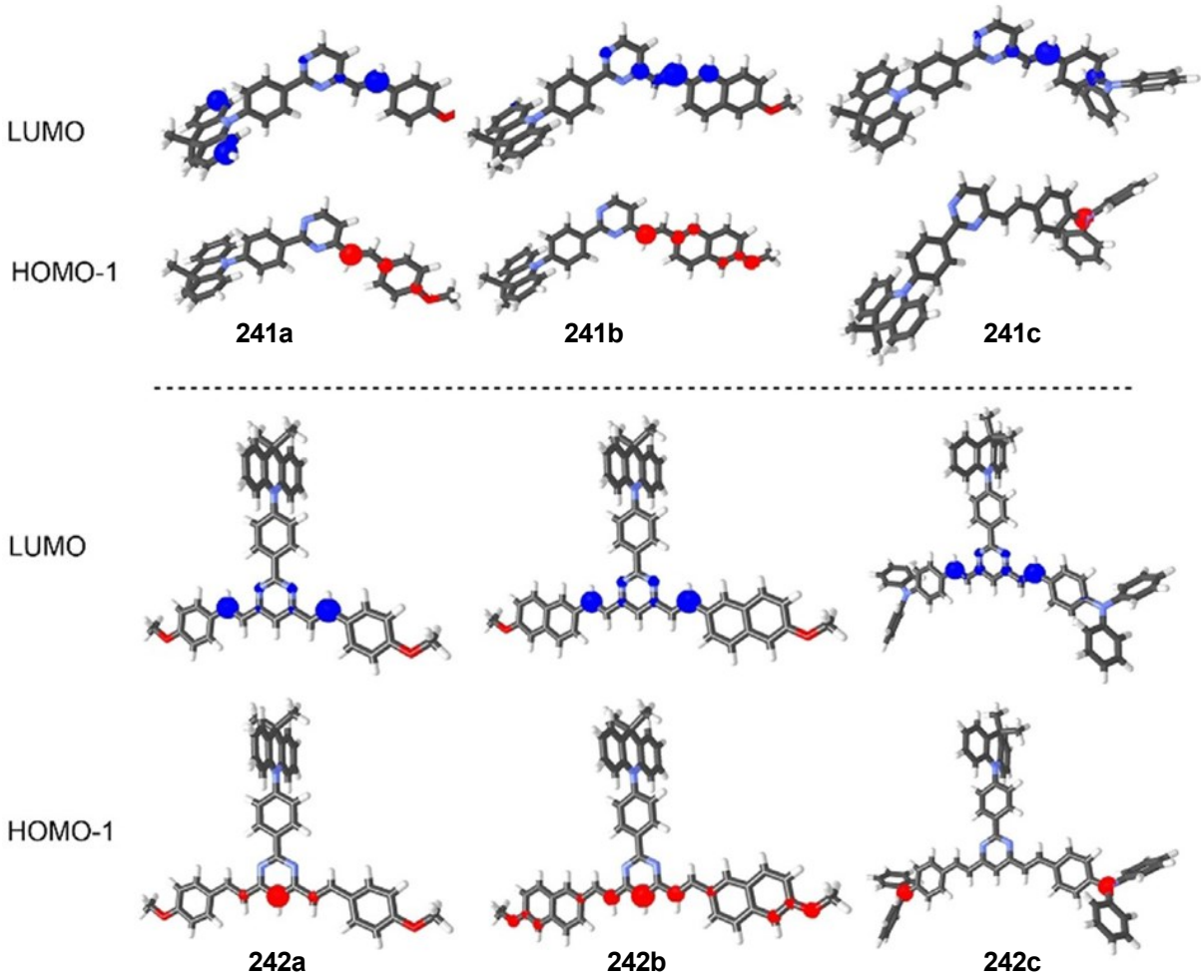

Figure 79. *Localization of HOMO–1 (red) and LUMO (blue) in compounds* ***241*** *and* ***242****.*

Calculated absorption spectra are provided in *Annex 2* and the longest-wavelength absorption maxima are summarized in *Table 10*. A small red-shift was found as compared to corresponding experimental data. However, trends and features of the spectra correspond to the experimental ones recorded in CH_2Cl_2. Contributions of different transitions to each band and their oscillator strength are summarized in *Annex 3*. In the case of compounds **241** and **242**, the HOMO → LUMO transition possessed zero oscillator strength and the longest wavelength band were dominated by the HOMO–1 → LUMO transitions. Considering the HOMO–1 localization over the C4/C6 peripheral donors, their donor-acceptor interaction with the central pyrimidine acceptor (LUMO) accounted for the ICT and explained the observed bathochromic shift of the longest-wavelength maxima when going from methoxy to diphenylamino derivatives (**a** → **c**). Besides the HOMO–1 → LUMO transition, transitions with significantly lower oscillator strengths were also detected by the DFT calculations, these include the HOMO–1 → LUMO+1 for **241** and the HOMO–2 → LUMO for compounds **242**.

4.7 Conclusions

A series of six new chromophores with pyrimidine heterocycle as central electron-withdrawing unit was prepared. Acridan moiety was connected to the C2 pyrimidine position via 1,4-phenylene linker and C4(C6) positions were extended by arylvinyl π-conjugated system with peripheral methoxy or diphenylamino donors. The first synthetic step, an interconnection of the acridine and phenylene unit, revealed to be challenging, however appropriate reaction conditions were found. The remaining synthesis was straightforward. Final derivatives were obtained by Suzuki-Miyaura C-C reaction of 2-chloro-4-methyl or 2-chloro-4,6-dimethylpyrimidine and ester of 4-acridanphenyl boronic acid followed by Knoevenagel reaction between pyrimidine methyl group(s) and corresponding aromatic aldehyde, with satisfying yields.

DSC analysis showed that peripheral C4/C6 electron-donating units affected the thermal properties only slightly, while the presence of acridan unit caused high thermal stability with temperatures of decomposition reaching almost 400 °C. The X-ray analysis revealed twisted acridan structure with torsion angles around 85° and also confirmed the *E* configuration of C4(C6) double bonds.

Results of photophysical measurements showed significant differences in photophysical behaviour of methoxy (**a** and **b**) and diphenylamino compounds (**c**). Single-band emission, both in solution and solid-state, high fluorescence quantum yield in CH_2Cl_2 and strong positive emission solvatochromism were observed for diphenylamino derivates. Meanwhile, methoxy derivatives exhibited very poor fluorescence in CH_2Cl_2 solution, which enhanced in nonpolar *n*-heptane and further slightly increased after deoxygenation. Methoxy-substituted compounds also exhibited intense AIE and dual emission in THF solution and solid state. The shorter-wavelength band was attributed to emission from the LE state and the longer-wavelength band was assigned to emission from the ICT/TICT excited state with long lifetime. The colour of the dual emission in thin films was close to white, which makes these compounds potential material for development of single emitter WOLEDs. The anticipated TADF behaviour was not observed, probably due to none oscillator strength of the HOMO → LUMO transition did not possess any oscillator strength, nevertheless unexpected photophysical properties were obtained for methoxy derivatives (**a** and **b**).

DFT calculation showed that, despite the HOMO is being localized on the acridan unit, it was completely isolated and did not affect the fundamental absorption properties. These are fully controlled by the peripheral methoxy or diphenylamino electron-donating groups bearing HOMO–1.

Results discussed in this chapter were published in one article:

[4] M. Fecková, I. K. Kalis, T. Roisnel, P. le Poul, O. Pytela, M. Klikar, F. Robin-le Guen, F. Bureš M. Fakis and S. Achelle: Photophysics of 9,9-dimethylacridan-substituted phenylstyrylpyrimidines exhibiting long-lived intramolecular charge-transfer fluorescence and aggregation induced emission characteristics, Chemistry- A European Journal, **2021**, *27*, 1145–1159. 10.1002/chem.202004328

CHAPTER V. Solid state emitting phenylpyrimidine platinum complexes

5.1 Introduction

As it was discussed in *Chapter 2*, platinum(II) complexes with pyrimidine-based ligands attracted researchers' interest in past few years for their potential application in PhOLEDs.[178–181] In this type of OLEDs, also known as 2nd generation OLEDs, phosphorescent emitters are used due to their ability to harvest both singlet and triplet excitons for light production.

Inspiration for design of new platinum complexes was drawn from work of *Zhao and co-workers*.[258] They recently published a study of complex **243** (*Figure 80*) with strong emission in solid-state and promising electroluminescent properties. It has also been demonstrated that electron-donating groups in para position of phenylpyridine ligand relative to central metal atom enhances the emission properties.[259] With this in mind, five platinum(II) complexes with phenylpyrimidine as cyclometalated ligand, pyridine and Cl^- as monodentate ancillary ligands were designed, see *Figure 80*. Structure of phenylpyrimidine was decorated with electron-donating and electron-withdrawing substituents in conjugated and non-conjugated positions (relative to Pt) to establish structure-photophysical properties relationships.

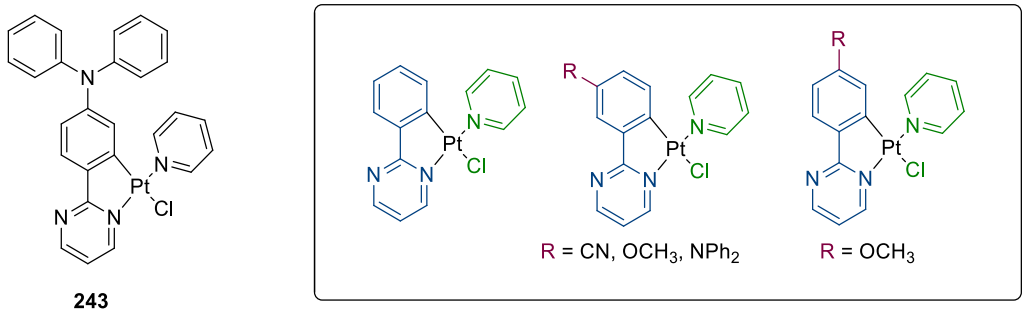

Figure 80. *Structures of compound **243** and designed Pt complexes.*

5.2 Synthesis

Ligands **244** for Pt(II) complexes were prepared by Suzuki-Miyaura C-C reaction between 2-chloropyrimidine and corresponding phenylboronic acid (*Scheme 6*).[128,129] All ligands were obtained in moderate to good yields. Subsequently, ligands underwent a complexation with K_2PtCl_4 in a mixture of ethoxyethanol (EGEE) and water (3/1, v/v) under nitrogen atmosphere. After 18 hours, the reaction mixture was cooled to room temperature and water was added until a precipitate was formed, which was collected and dried under vacuum. Without any further purification, μ-chloro bridged intermediate (the precipitate) was dissolved in $CHCl_3$ and underwent so-called "bridge splitting" reaction in the presence of pyridine.[258,260,261] Final Pt-complexes **245** were prepared in satisfying yields.

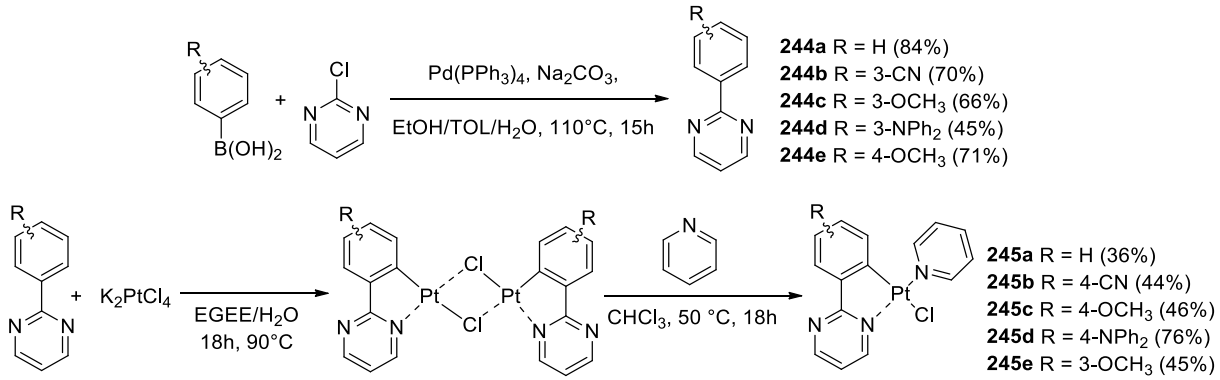

Scheme 6. *Synthesis of ligands **244** and Pt(II) complexes **245**. Substituents position for **245** are given with regards to platinum atom.*

All ligands **244** and final complexes **245** were characterized by $^{1}H/^{13}C$ NMR spectroscopy and HR-MALDI mass spectrometry.

5.3 X-ray analysis

An appropriate crystal of **245a** suitable for X-ray analysis was obtained by slow evaporation of its ethyl acetate/*n*-hexane solution. ORTEP diagram of this yellow prism with orthorhombic symmetry and P*bca* space group is presented in *Figure 81*. X-ray analysis was performed by Dr. Thierry Roisnel, Université de Rennes 1 (France).

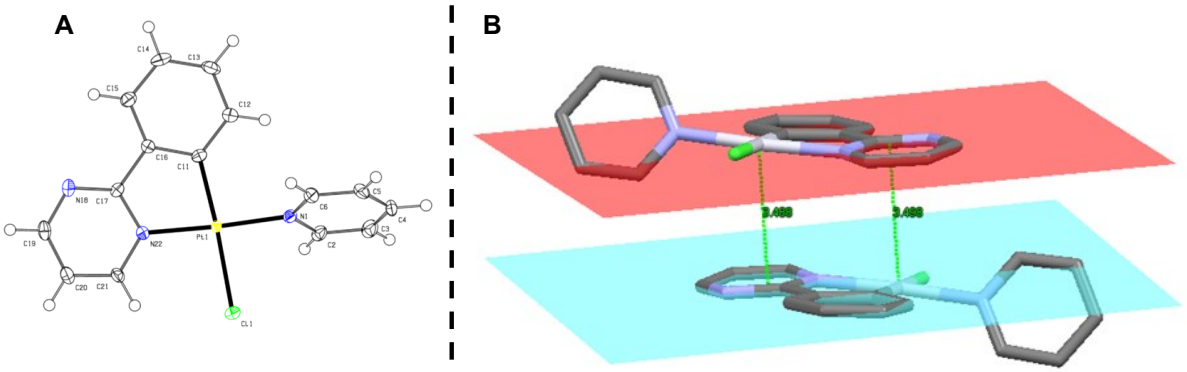

Figure 81. *(A) ORTEP diagram of complex **245a** with thermal ellipsoid at 50% probability. (B) Pt-π interaction in the crystal structure of **245a**.*

Square-planar geometry was observed with *trans* N,N *trans* C,Cl organisations of chelating positions. Values of bond lengths between central Pt atom and surrounding ligands were close to similar *trans* N,N *trans* C,Cl Pt complexes found in literature.[258,260,262] The square-planar geometry is slightly distorted with smaller angles between C11-Pt1-N22 (87.13(16)°) and Cl1-Pt1-N1 (87.48(9)°). Torsion angle of 67.66° was observed between the plane of pyridine ring and square-plane of the remaining molecule, indicating a possible rotation along the Pt-N atom of pyridine axis, which could be responsible for low luminescence in solution at room

temperature by reducing decay from T_1 or ISC, and high luminescence in solid-state, in which this rotational movements is limited.[258] Concerning the supramolecular arrangement in the solid state, possible interaction between molecules in inverted positions was found with the lowest distance between Pt and pyrimidine ligand of 3.49 Å, see *Figure 81B*. Similar value was already reported for electroluminescent Pt complexes that proved to form a stacked dimers by the Pt-π interaction.[263]

5.4 Photophysical properties

Absorption and emission in CH_2Cl_2

Photophysical behaviour of final derivatives **245** was measured in CH_2Cl_2 solutions with analyte concentration $c = (0.9 – 1.02) \times 10^{-5}$ M. Results are summarized in *Table 11*. Deoxygenated solutions were prepared by bubbling with N_2.

Table 11. *Absorption and emission data of **229** complexes in CH_2Cl_2 and solid state (powdered).*

	CH_2Cl_2[a]					*solid state*	
Compd	λ_{max}(abs) (ε) [nm] ([$mM^{-1}\cdot cm^{-1}$])	λ_{max}(em) [nm]	τ [μs]	Φ_{PL}[b]	Stokes shift [cm^{-1}]	λ_{max}, nm	τ [μs]
245a	249 (38.8), 286 (13.9)sh, 338 (6.1), 386 (2.0)	–	–	–	–	517, 535, 549	0.51, 2.72
245b	256 (43.4), 270 (36.2), 335 (4.5), 382 (2.1)	–	–	–	–	478, 505, 549, 590sh	0.30, 2.58
245c	251 (44.4), 283 (14.7)sh, 346 (5.5), 414 (2.6)	570	12.9	0.40	6610	591, 630sh	0.47, 2.05
245d	285 (27.0), 292 (35.2), 438 (2.3)	628	8.86	0.05	6907	629	0.40, 2.13
245e	264 (24.1), 314 (14.2), 384 (1.8)	–	–	–	–	515, 539, 556	0.34, 1.32

[a] All spectra were recorded at room temperature at $c = (0.9 – 1.02) \times 10^{-5}$ M with deoxygenated solutions prepared by bubbling N_2 through the solutions. [b] Photoluminescence quantum yield (±10%) determined relative to 9,10-bisphenylethynylanthracene in cyclohexane (Φ_{PL} = 1.00).[257]

Absorption spectra (*Figure 82A*) contained various bands with the most intense appearing around 250–300 nm attributed to the intramolecular π-π* transition. Position of these bands for complexes **245a–c** lay within the range of a few nm, whereas slight red-shift was found

for compound **245e** (over 10 nm relative to its analogue **245c** with methoxy group outside the conjugated position towards pyrimidine acceptor) and more significant (>30 nm) for compound **245d** with larger π-system.

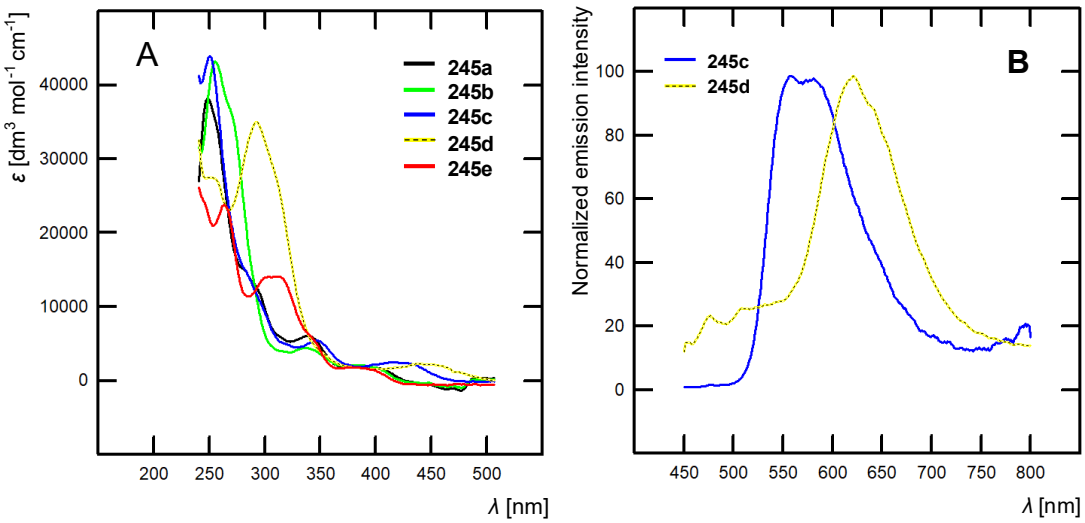

Figure 82. *(A) Experimental absorption spectra of complexes **245** measured in CH_2Cl_2 and (B) experimental emission spectra of complexes **245c,d** in CH_2Cl_2.*

No emission was observed for complexes in their oxygenated solutions. However, deoxygenation of solutions resulted in appearance of emission for derivatives **245c** and **245d** with donating group in *para* position towards central Pt atom (*Figure 82B*). Photoluminescence quantum yields were established as 0.40 and 0.05 for **245c** and **245d**, respectively, with long excited state lifetimes around 10 μs, typical for phosphorescence. This relatively low or none emission of other complexes could be ascribed to possible pyridine ring rotation, which allows non-radiative decay.[258]

Solid-state emission

Nevertheless, in the solid state (powder) all complexes exhibited bright emission with a structured spectrum. As mentioned in previous paragraphs, the appearance of emission in the solid-state is caused by restriction of pyridine ring rotation.[258] Concerning the colour of emitted light, complexes **245a** and **245e** without substitution in para position (against Pt) produced green light with the most blue-shifted emission bands (see *Figure 83*). Appending cyano group into the para position (**245b**) resulted in red-shift of spectra with yellow light emission. Further red-shift was observed for derivatives **245c** and **245d**, which emitted orange and red light, respectively.

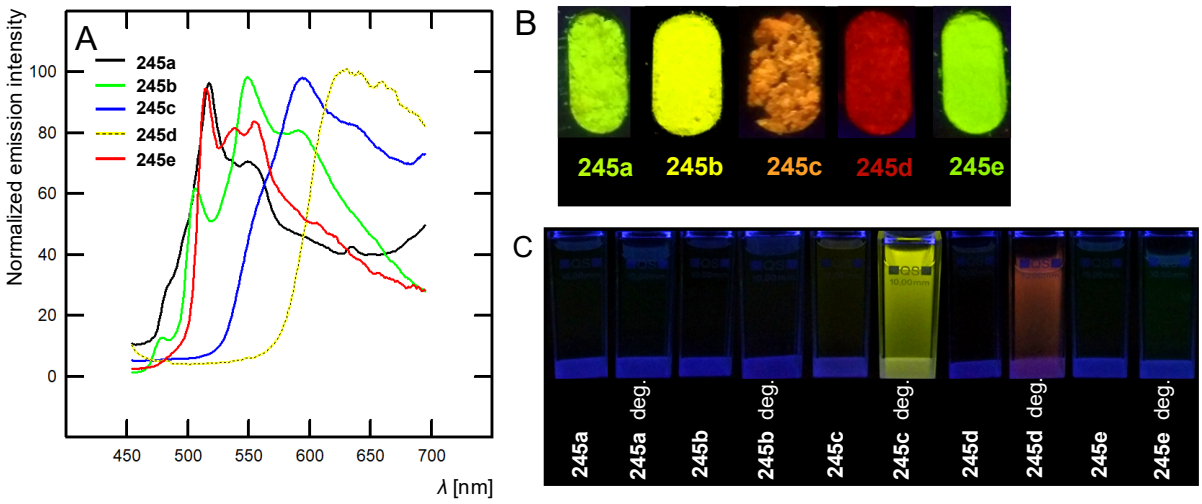

Figure 83. *(A) Solid state normalized emission spectra of powdered **245**. Pictures of (B) powdered and (C) oxygenated and deoxygenated CH_2Cl_2 solutions of **245** taken under UV-lamp (λ_{em} = 254 nm).*

5.5 DFT calculation

Figure 84 presents optimized structures of complexes **229**. (TD)-DFT calculations at the PBE0/LANL2DZ level of theory were performed by Prof. Jean-Yves Saillard and Dr. Samia Kahlal, Université de Rennes 1 (France). Relevant data are provided in *Annex 5* and for computational details see *Chapter 6*. The calculated structures are in agreement to X-ray structure of **245a**, with slightly longer metal-ligands bonds, which are usually found for DFT-optimized structures. Torsion angles between pyridine and plane of the molecule were determined in the range of 65–67°, which were comparable to the experimental angle found in crystal structure of **245a** (67.7°). The shortest calculated intermolecular H…H distance was found within the range of 2.7–2.8 Å. This value implied that pyridine rotated between planar structure with effective conjugation and twisted structure with reduced H...H steric repulsion. The energy difference between these two structures is only 0.01 eV indicating that, in solution, pyridine could rotate along the N-Pt axis a several tenths of degrees.

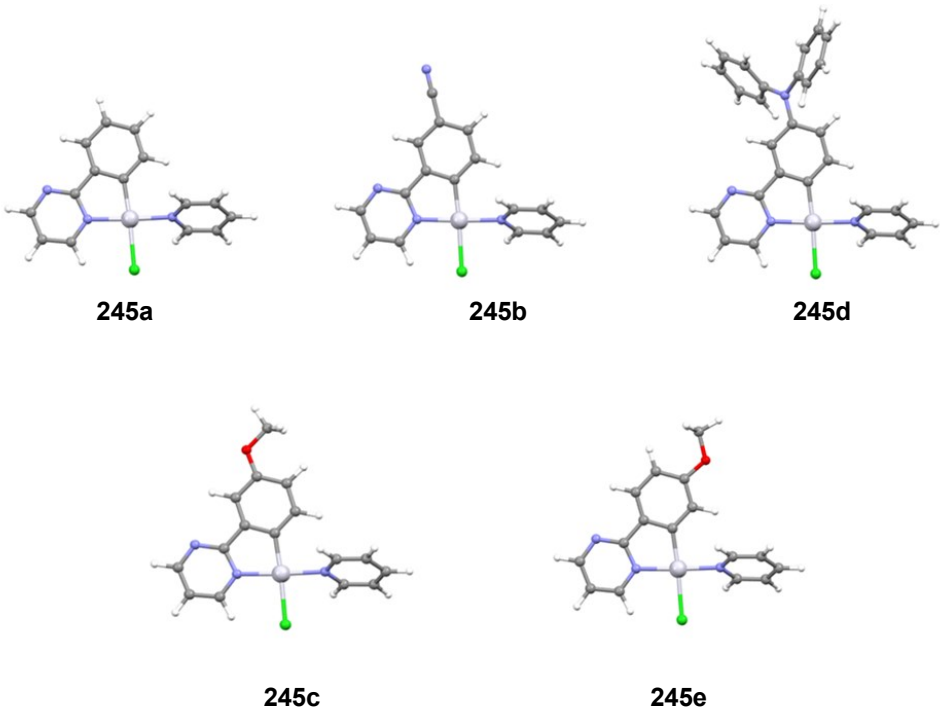

Figure 84. *DFT-optimized geometries of complexes* ***245****.*

The Natural Atomic Orbital (NAO) charges and the metal-ligand Wiberg bond indices of the five complexes were very close. The largest difference in atomic charge variation was observed for carbon atom attached to Pt, influenced by electronic effect of substituent in para position. The largest number was found for complexes **245c** and **245d** with electron-donating groups, which favored a more negative polarization of the C-atom. In the case of derivative **245b** with cyano group in alternating position, slightly stronger Pt-Cl bond was observed relative to the remaining complexes. It should be noticed that changes in these values are rather small. However, more substantial differences could be seen in HOMO-LUMO gaps that are in agreement with the experimental spectroscopic data. The smallest gaps were observed for derivatives **245c** and **d** with donating groups in conjugation with central metal. A further insight into the electronic structures was drawn from Kohn-Sham diagrams (*Figure 85A*) and localization of frontier orbitals (*Figure 85B*) of final complexes **245**. The results imply that studied complexes behave in three different ways based on the substituent in para position. Firstly, for complexes **245c** and **245d** substituted with electron-donating groups, destabilized HOMO by donors' electron lone pair with significant phenylpyrimidine character was found. Secondly, derivatives **245a** and **245d** without substitution in para position, and therefore without mesomeric effect, exhibited the HOMO with lower, but still substantial, phenylpyrimidine character. And last, complex **245b** with cyano group possessed the HOMO

with stabilization by electron-withdrawing nature of cyano group. The HOMO-LUMO gap of this derivative was not the lowest within the series since the LUMO level was also slightly stabilized.

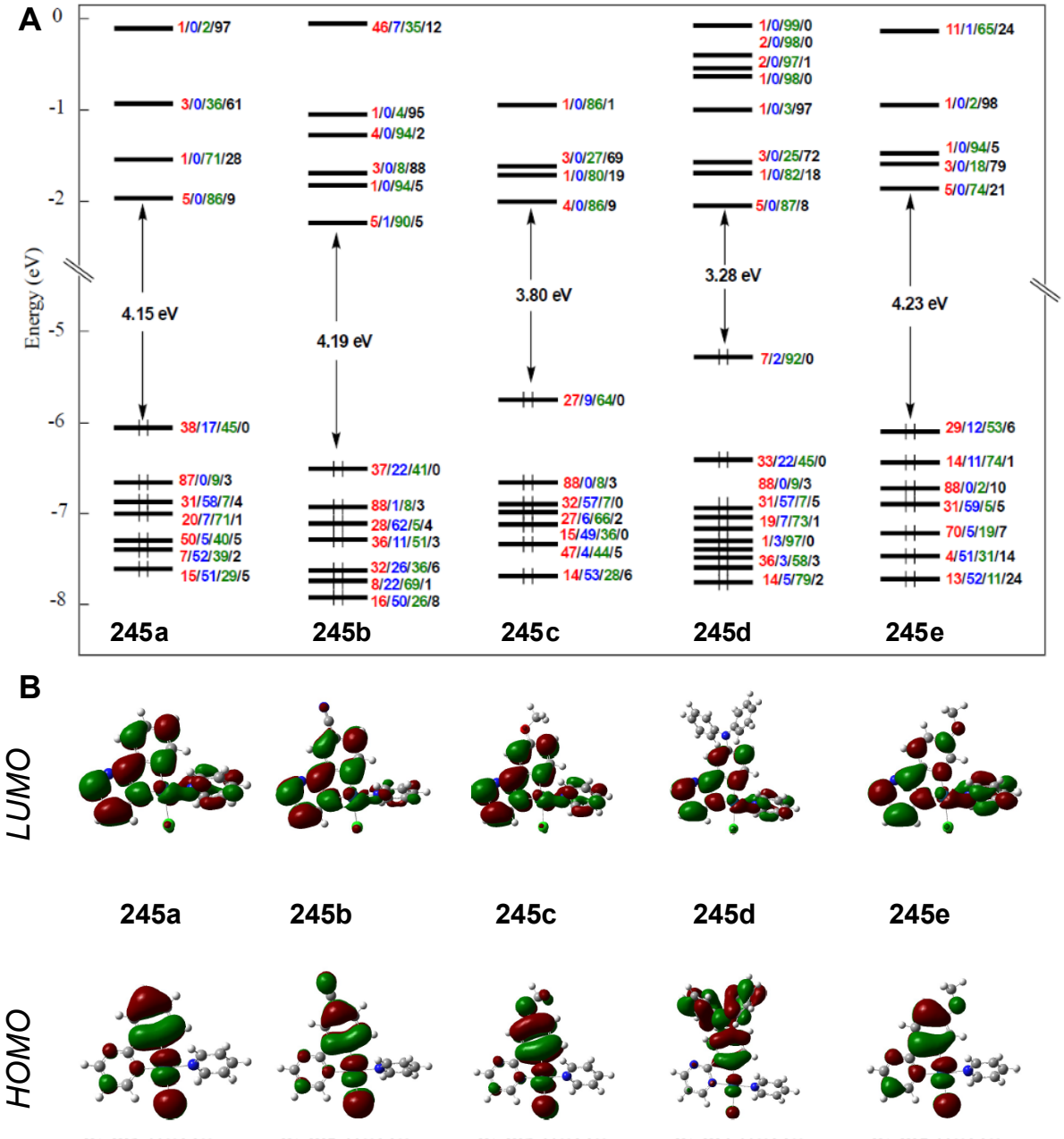

Figure 85. *(A) Kohn-Sham orbital diagrams of compounds* ***245*** *The MO localizations (in %) are given in the following order: Pt/Cl/phenylpyrimidine/pyridine. (B) Frontier orbitals of complexes* ***245****.*

Good agreement was found between the experimental and the TD-DFT calculated absorption spectra of **245**, see *Figure 86A* and *Table 12*. Nature of transition of each absorption bands are also provided in the same table. The longest-wavelength bands corresponded to the HOMO → LUMO transition. *Figure 85* revealed a mixed electron-transfer character, with a dominant intra phenylpyrimidine character. The other bands did not exhibit important

long-range transfers neither significant metal participation. Emission spectra in the solution were also calculated by using the Adiabatic Hessian (AH) method developed by *Barone et al.*, which was recently proven to be efficient for platinum complexes.[264–266] The calculated emission spectra are presented in *Figure 86B* and the corresponding emission maxima are provided in *Table 12*. A good agreement was found between the experimental and the calculated data and the transition was found to originate from the excited $(HOMO)^1(LUMO)^1$ triplet state.

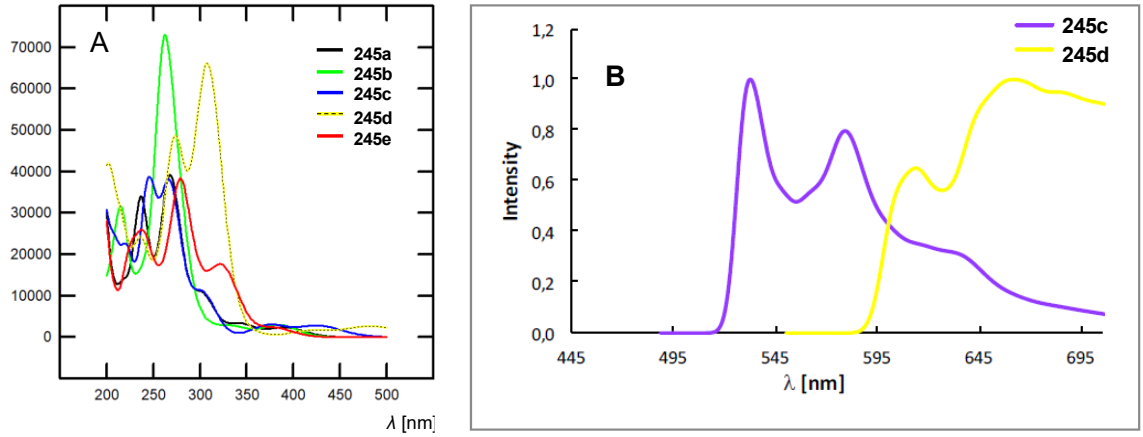

Figure 86. *Calculated (A) absorption spectra of complexes* ***245*** *and (B) calculated emission spectra of complexes* ***245c,d****.*

Table 12. *Experimental and calculated photophysical data of complexes* ***245****.*

	Absorption			*Emission*	
Compd.	λ_{max} (ε) exp [nm] ([$mM^{-1}\cdot cm^{-1}$])	λ_{max} (ε) calc [nm] ([$mM^{-1}\cdot cm^{-1}$])	Nature of the transition	Exp. λ_{max} [nm]	Comp. λ_{max} [nm]
245a	386 (2.0)	392 (0.03)	$ILCT^a + MLCT^b + LLCT^c$	–	–
	338 (6.1)	303 (0.11)	$ILCT^a + MLCT^b$		
	286 (13.9)sh				
	249 (38.8)	277 (0.10)	$ILCT^a + LLCT^d$		
245b	382 (2.1)	385 (0.04)	$ILCT^a + MLCT^b + LLCT^c$	–	–
	335 (4.5)	304 (0.11)	$ILCT^a + MLCT^b$		
	270 (36.2)				
	256 (43.4)	282 (0.17)	$ILCT^a + LLCT^d$		
245c	414 (2.6)	428 (0.04)	$ILCT^a + MLCT^b + LLCT^c$	570	578
	346 (5.5)	304 (0.12)	$ILCT^a + MLCT^b$		**532**
	283 (14.7)sh				
	251 (44.4)	277 (0.13)	$ILCT^a + LLCT^d$		
245d	438 (2.3)	485 (0.04)	$ILCT^a + LLCT^c$	628	**662**
	292 (35.2)	316 (0.19)	$LLCT^d + MLCT^b$		614
	285 (27.0)	275 (0.26)	$ILCT^a + LLCT^d$		
245e	384 (1.8)	380 (0.03)	$ILCT^a + MLCT^b + LLCT^c$	–	–
	314 (14.2)	299 (0.12)	$LLCT^d + MLCT^b$		
	264 (24.1)	280 (0.40)	$ILCT^a + LLCT^d$		

5.6 Conclusions

Five new platinum(II) complexes bearing phenylpyrimidine cyclometalated ligands with various substituents as well as pyridine and chlorine monodentate ligands were prepared. All complexes were obtained in moderate to good yields. X-ray analysis and DFT calculations revealed square-planar structure of the central platinum atom and possible rotation of pyridine along Pt-N axis. This rotation caused low or non-existing emission in the solution with a dramatic enhancement in the solid-state, in which the rotation was restricted. As far as the influence of substitution is concerned, presence of electron-donating group in alternating position towards Pt atom resulted in significant increase in the emission quantum yields. The yield in the solution was found up to 0.4 for complex **245c** and excited state lifetimes around 10 μs and red-shift of the emission spectra was recorded in the solid-state. Strong emission of these complexes in the solid-state makes them promising candidates for their incorporation in OLED devices.

Results discussed in this chapter were published in one article:

[5] M. Fecková, S. Kahlal, T. Roisnel, J.-Y. Saillard, J. Boixel, M. Hruzd, P. Le Poul, S. Gauthier, F. Robin-le Guen, F. Bureš and S. Achelle: Cyclometallated 2-phenylpyrimidine derived platinum complexes: synthesis and photophysical properties, European Journal of Inorganic Chemistry, **2021**, in press. 10.1002/ejic.202100155

GENERAL CONCLUSIONS AND PERSPECTIVES

This dissertation describes results of work concerning pyrimidine-based organic and organometallic luminescent materials suitable for application in OLED technology. The first chapter was dedicated to definition of general concepts and terms, physical quantities and phenomena used for description of luminescence. Basic relationships between structure and luminescence of organic compounds as well as an effect of environment on luminescence were also discussed. Second half of the first chapter contains description of organic semiconductors in the context of OLED technology. The general structure of OLED devices, working principle and ways of OLED's characterisation are also included. In the end, three types of OLED were distinguished based on mechanism how emitters harvest light.

Second chapter began with description of pyrimidine heterocycle and its role in organic materials. Subsequently, fluorescent push-pull chromophores were introduced in context of influence of structural changes on photophysical properties. Short overview of basic synthetic approaches towards building pyrimidine-based chromophores concluded the first part of the second chapter. The main purpose of the second part was to present wide use of pyrimidine containing luminescent materials. Fluorescent probes for detection of solvent polarity, cations, nitrogen explosive and bioimaging were presented. A few examples to achieve white light emission by partial protonation of pyrimidine chromophore were also included. Finally, the end of the second chapter was dedicated to highlight use of pyrimidine organic and organometallic luminophores in OLED devices.

Results of this doctoral work were summarized in three chapters, which were sorted based on the main structural motive, and consequently different photophysical features, of each series. The unified organisation of each chapter starts with the synthesis of target molecules following by results of DSC and X-ray measurements. Subsequent focus was put on photophysical properties of final derivatives and each chapter ended with results of theoretical calculations.

The first series of final derivatives included 2,4-di(arylvinyl)- and 2,4,6-tri(arylvinyl)pyrimidines, from which 23 derivatives were novel structures. Pyrimidine ring was used as a central electron-withdrawing group connected through arylvinylene bridges with mostly electron-donating groups at periphery. Synthesis of these molecules involved Suzuki-Miyaura C-C reaction and Knoevenagel condensation, which allowed preparing derivatives with identical or different substitution on each branch. Vast majority of final molecules exhibited measurable emission and their photophysical properties were mostly affected by electronic nature of C4 and C6 substituents. However, when comparing stronger electron-donor

appended in C2 or C4 and C6, both position and intensity of emission spectra were dictated by the C2 substitution. For all emissive derivative, significant positive emission solvatochromism was observed. Modulation of emission colour between dark blue and yellowish green of one final chromophore was achieved by gradual protonation of its solutions. In collaboration with research group of Prof. Mihalis Fakis, University of Patras (Greece), influence of type of acid on absorption, emission and excited state dynamics were studied for diphenylamino-substituted 4,6-distyryl and 2,4,6-tristyrylpyrimidines. In collaboration with Dr. Claudine Katan and Dr. Arnaud Fihey, Université de Rennes 1 as well as Dr. Jean-Pierre Malval and Dr. Arnaud Spangenberg, Université de Haute Alsace (France), influence of branching number of styrylpyrimidines on their photophysical properties was studied. It should be highlighted that the low symmetry given by the pyrimidine ring resulted in increase of 2PA cross-section up to 500 GM within the same spectral region with each additional branch. Concerning the perspectives of multibranched arylvinylpyrimidines, two series of novel derivatives are proposed, see *Figure 87*. Based on the fact, that derivatives with the electron-withdrawing CF_3 group in C2 position exhibited the most intense emission and also dual emission during protonation, studying the effect of different electron-withdrawing group in C2 position could potentially lead to interesting results. As a second series styrylpyrimidine-based dendrimers are proposed. The higher number of branches could potentially further increase the 2PA response.

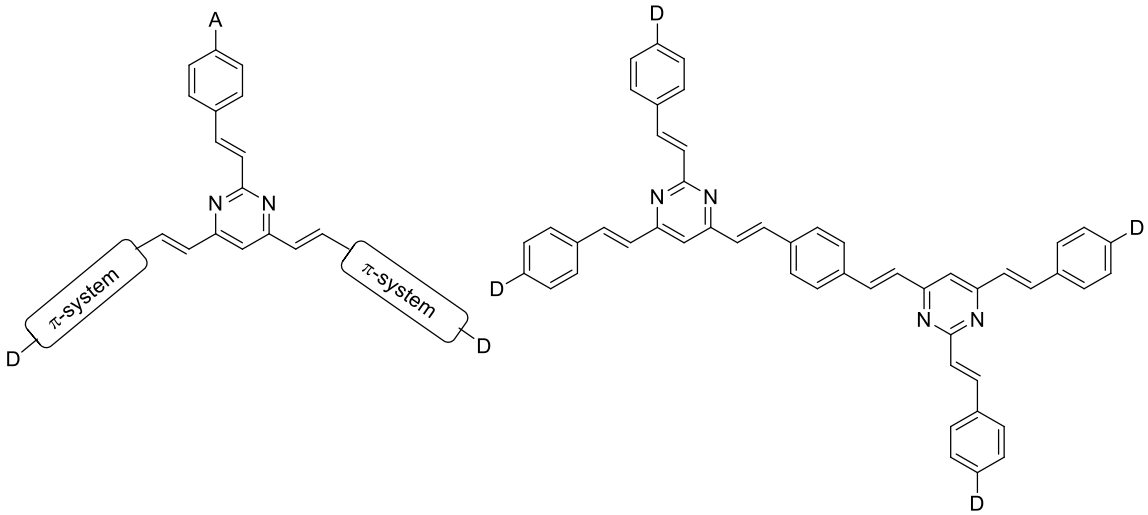

Figure 87. *Proposed structures of novel styrylpyrimidines.*

Second project concerned 4-arylvinyl- and 4,6-di(arylvinyl)pyrimidines with phenylacridan structure in C2 position of pyrimidine as potential TADF emitters. Six novel chromophores were prepared and fully characterized. The presence of phenylacridan moiety brought a high thermal robustness into these structures. Final derivatives can be divided into

two groups with different photophysical properties. Firstly, derivatives with diphenylamino electron-donors in C4/C6 positions exhibited similar properties to those of previously discussed styrylpyrimidines such as high fluorescence quantum yield in moderately polar solvent (CH_2Cl_2), strong positive emission solvatochromism, lower fluorescence quantum yield in low polar solvent (*n*-heptane) and no change in emission intensity after deoxygenation of their solution. On the other hand, derivatives with methoxy group showed significant emission in *n*-heptane solution with increase upon deoxygenation, aggregation-induced emission and dual emission of white light in both thin films and solution (THF or acetone). Although, their anticipated TADF behaviour was not observed, above mention emission phenomena makes them a very promising materials for fabrication of WOLED device based on single emitter.

Last project included synthesis and study of photophysical properties of platinum complexes with ancillary Cl^- and pyridine ligand and cyclometaled 2-phenylpyrimidine ligands with substituents both in alternating and non-alternating position towards platinum atom. All complexes showed luminescence in solid-state, however, derivatives with electron-donating groups in alternating position exhibited the most interesting photophysical properties, which makes them promising candidates for utilization as phosphorescent emitters in OLED. Replacement of chlorine atom by different ligands, substitution of the pyrimidine ring and study of their influence on luminescent properties is currently under investigation by Mariia Hruzd, Université de Rennes 1 (France).

Results discussed in this dissertation work were reported in five articles:

[1] M. Fecková, P. le Poul, F. Robin-le Guen, T. Roisnel, O. Pytela, M. Klikar, F. Bureš and S. Achelle: 2,4-Distyryl- and 2,4,6-tristyrylpyrimidines: Synthesis and Photophysical Properties, Journal of Organic Chemistry, **2018**, *83*, 11712–11726. 10.1021/acs.joc.8b01653

[2] F. Kournoutas, I. K. Kalis, M. Fecková, S. Achelle, M. Fakis: The effect of protonation on the excited state dynamics of pyrimidine chromophores, Journal of Photochemistry & Photobiology A: Chemistry, **2020**, *391*, 112398. 10.1016/j.jphotochem.2020.112398

[3] F. Kournoutas, A. Fihey, J.-P. Malval, A. Spangenberg, M. Fecková, P. le Poul, C. Katan, F. Robin-le Guen, F. Bureš, S. Achelle, M. Fakis: Branching effect on the linear and nonlinear optical properties of styrylpyrimidines, Physical Chemistry Chemical Physics, **2020**, *22*, 4165–4176. 10.1039/c9cp06476a

[4] M. Fecková, I. K. Kalis, T. Roisnel, P. le Poul, O. Pytela, M. Klikar, F. Robin-le Guen, F. Bureš, M. Fakis, S. Achelle: Photophysics of 9,9-Dimethylacridan-Substituted Phenylstyrylpyrimidines Exhibiting Long-Lived Intramolecular Charge-Transfer Fluorescence and Aggregation-Induced Emission Characteristics, Chemistry – A Eurupean Journal, **2021**, *27*, 1145–1159. 10.1002/chem.202004328

[5] M. Fecková, S. Kahlal, T. Roisnel, J.-Y. Saillard, J. Boixel, M. Hruzd, P. le Poul, S. Gauthier, F. Robin-le Guen, F. Bureš, S. Achelle: Cyclometallated 2-phenylpyrimidine derived platinum complexes: Synthesis and photophysical properties, European Journal of Inorganic Chemistry, 10.1002/ejic.202100155 Accepted Article

During my doctoral study I also participated on publication of the following articles and review:

[6] J. Tydlitát, M. Fecková, P. le Poul, O Pytela, M. Klikar, J. Rodriguez-Lopez, F. Robin-le Guen, S. Achelle: Influence of Donor-Substituents on Triphenylamine Chromophores Bearing Pyridine Fragments, European Journal of Organic Chemistry, **2019**, *9*, 1921–1930. 10.1002/ejoc.201900026.

[7] M. Fecková, P. le Poul, F. Bureš, F. Robin-le Guen, S. Achelle: Nonlinear optical properties of pyrimidine chromophores, Dyes and Pigments, 182, 108659. 10.1016/j.dyepig.2020.108659

[8] S. Achelle, E. V. Verbitskiy, M. Fecková, F. Bureš, A. Barsella, F. Robin-le Guen: V-shaped methylpyrimidinium chromophores for nonlinear optics, Submited to ChemPlusChem

CHAPTER VI. Experimental section

General methods

Starting materials for reactions were purchased from Acros, Alfa-Aesar, Fluka, Penta, Sigma-Aldrich and TCI companies and were used without any further purification. Dry THF was distilled over Na or Na/K alloy and benzophenone under inert atmosphere of nitrogen or argon. Solvents were evaporated on rotary evaporator Heidolph Laboratora 4000 or Büchi R-200 Rotavapor. Cross-coupling reactions and complexations were carried out in vacuum-dried Schlenk flask under nitrogen or argon atmosphere. The remaining reactions and following workups were performed on air. Column chromatography was carried out on silica gel 60; particle size 0.20–0.50 mm, 60–200 mesh ASTM (Acros) or particle size 0.040–0.063 mm, 230–400 mesh ASTM (Merk). Thin-layer chromatography was performed on EMD Silica Gel 60 F254 (Merck) aluminium plates with visualization by UV lamp (254 or 365 nm). ^{1}H and ^{13}C NMR spectra were recorded in $CDCl_3$ at 20 °C on a Bruker AC-300 (frequencies 300/75 MHz), a Bruker AVANCE III (frequencies 400/100 MHz) and a Bruker Ascend^{TM} (frequencies 500/125 MHz) spectrometers. Chemical shifts (δ) are provided in parts per million compare to signal of $(CH_3)_4Si$. Signals of (residual) solvents were used as internal standards [$CHCl_3$ in $CDCl_3$ 7.25 ppm (^{1}H) and $CDCl_3$ 77.16 ppm (^{13}C)]. Interaction constants (*J*) are given in Hz. Observed signals are described with the following abbreviations: s (singlet), d (doublet) and m (multiplet). Acidic impurities in $CDCl_3$ were removed by its treatment with anhydrous K_2CO_3. IR spectra were recorded on a Perkin-Elmer spectrum 100 spectrometer with an ATR sampling accessory. Mass spectra were measured on a GC/EI-mass spectrometer, which consists of a gas chromatograph Agilent Technologies 6890N (HP-5MS, column length 30 m, I.D. 0.25 mm, film 0.25 μm) and a Network MS detector 5973 (EI 70 eV, range 33–550 Da). High resolution MALDI mass spectra were measured by "dried droplet" method on a LTQ Orbitrap XL MALDI mass spectrometer (Thermo Fisher Scientic, Bremen, Germany) equipped with a nitrogen UV laser (337 nm, 60 Hz) and quadrupole analyser; positive-ion mode over a normal mass range (*m/z* 50–2000) with a resolution of 100 000 at *m/z* = 400. *trans*-2-[3-(4-*tert*-Butylphenyl)-2-methyl-2-propenylidene]malononitrile (DCTB) was used as a matrix.

DSC

The thermal properties of final derivatives were studied through DSC measurements with a Mettler-Toledo STARe system DSC 2/700 equipped with a FRS 6 ceramic sensor and HUBER TC100-MT RC 23 cooling system. The thermal behaviour of target compounds

was measured in open aluminous crucible under an inert atmosphere of nitrogen. DSC curve were determined at a scanning rate of 3 °C×min^{-1} within the range 25–500 °C.

X-Ray structural analysis

Single-crystal X-ray-diffraction data were obtained from a D8 VENTURE Bruker AXS diffractometer equipped with a (CMOS) PHOTON 100 detector, using Mo-Kα radiation (λ = 0.71073 Å, multilayer monochromator) at T = 150 K. Crystal structure was solved by dual-space algorithm using the SHELXT program,[267] and then refined with full-matrix least-squares methods based on F^2 (SHELXL program).[268] All non-hydrogen atoms were refined with anisotropic atomic displacement parameters. H atoms were finally included in their calculated positions and treated as riding on their parent atom with constrained thermal parameters. Drawing was produced using ORTEP-3. Deposition Numbers 1852296 (**232h**), 2004147 (**242a**), 2004148 (**241a**), 2004149 (**242a**) and 2039829 (**245a**). These data can be obtained free of charge from the Cambridge Crystallographic Data Centre via www.ccdc.cam.ac.uk/data_request/cif.

Steady state spectroscopy

UV-visible spectra were recorded on a Perkin-Elmer Lambda 25 spectrometer, a Spex Fluoromax-3 Jobin-Yvon Horiba spectrophotometer or a Jasco V-650 UV-Vis. Photoluminescence spectra were obtained using a Horiba Fluoromax spectrophotometer. Both UV-Vis and PL measurements in solution were carried out using standard 10 mm quartz cells. Compound were excited at their longest-wavelength absorption maxima. The Φ_{PL} values were calculated using a well-known procedure with 9,10-bis(phenylethynyl)anthracene (Φ_F = 1.00).[257] Stokes shifts were calculated by considering the longest-wavelength absorption band.

Time resolved spectroscopy

For time resolved fluorescence measurements in the ps-ns timescale, the Time Correlated Single Photon Counting (TCSPC) technique has been used based on a Fluotime 200 spectrometer (Picoquant).[269] The excitation source was a ps diode laser emitting 60 ps pulses at 400 nm and the IRF was ~80 ps. The samples for fluorescence dynamics measurements were dilute solutions with optical density (O.D.) at the excitation wavelength of ~0.1.

Two-photon absorption

The 2PA measurements were performed with femtosecond mode-locked laser pulses using a Ti: Sapphire laser (Coherent, Chameleon Ultra II: pulse duration: ~140 fs; repetition rate: 80 MHz; wavelength range: 680–1040 nm). A two-photon excited fluorescence method was employed to measure the 2PA cross-sections, δ.[227] The measurements of 2PA cross-sections were performed relative to reference molecules (*r*) such as fluorescein in water at pH = 11.[227,270] The samples used for the 2PA characterization were 10^{-5}–10^{-4}M solutions in CH_2Cl_2. The values of δ for a sample (*s*) is given by:

$$\delta_S = \frac{S_S \Phi_r \eta_r c_r}{S_r \Phi_S \eta_S c_S} . \delta_r$$

Where *S* is the detected two-photon excited fluorescence integral area, *c* is the concentration of the chromophores, Φ is the fluorescence quantum yield of the chromophores and η is the collection efficiency of the experimental set-up which accounts for the wavelength dependence of the detectors and optics as well as the difference in refractive indices between the solvents in which the reference and sample compounds are dissolved. The measurements were conducted in a regime where the fluorescence signal showed a quadratic dependence on the intensity of the excitation beam, as expected for two-photon induced emission. For the calibration of the 2PA spectra, the two-photon excited fluorescence signal of each compound was recorded at the same excitation wavelength as that used for standards (i.e. λ(exc) = 782 nm for fluorescein). The laser intensity was in the range of 0.2–2 x 10^9 W/cm^2. The experimental error on the reported cross section is 15 %.

Calculations

Compounds **62, 232g,j,k,m**: All calculations were carried out in Gaussian16,[222] at the DFT level of theory. The initial geometry optimizations were carried out by the PM3 method implemented in program ArgusLab[271] and subsequently by the DFT B3LYP method using the 6-311G++(2d,f,p) basic set. The energies of the HOMO and LUMO, their differences and ground-state dipole moments were calculated by the same method.

Compound **48**, **49**, **61**, **62** and **232i,m**: Density functional theory (DFT) and time-dependent (TD) DFT approaches, as implemented in the Gaussian 16 package,[222] were used to model all chromophores of interest. Calculations have been performed in vacuum (gas phase) to provide general insights regardless of the solvent used, and consist in:

- Molecular structure optimisations, using the PBE0 hybrid functional[226] combined with the 6-31G(d,p) basis set, followed by frequency calculations to identify the nature of the energy minimum as a global minimum.
- Linear optical properties computation, using the range-separated hybrid functional CAM-B3LYP alongside a 6-31G(d,p) basis set.[272] The absorption features are obtained through the first 15 vertical excitations, and the emission energies by optimizing the geometry of the first excited-state, which is then validated by an excited-state frequency calculation. The excitation and emission energies are convoluted into UV-Vis bands by applying Gaussian functions with a Half-width at Half-Height of 0.3 eV.

Compounds **241–242**: The spatial and electronic properties of the target chromophores were investigated using Gaussian®16W software[222] package at the DFT level. Initial geometries of molecules **241a-c** and **242a-c** as well as the energies of their frontier molecular orbitals and ground state dipole moments μ were calculated at DFT B3LYP/6-311++G(3d,f,2p) level in vacuum. Theoretical electronic absorption spectra were calculated at TD-DFT (nstates = 8) B3LYP/6-311++G(3d,f,2p) level in vacuum.

Complexes **245**: DFT and TD-DFT calculations were carried out using the Gaussian16 package,[222] employing the PBE0 functional,[226,273,274] together with the LanL2DZ basis set.[275–278] Solvent (chloroform) effects were included through the PCM approximation.[279,280] The optimized geometries were fully characterized as true minima by analytical frequency calculations (no imaginary values). The composition of the Kohn-Sham orbitals was calculated using the AOMix program.[281] The geometries obtained from DFT calculations were used to perform natural atomic charge analysis with the NBO 6.0 program.[282] Only singlet-singlet transitions were taken into account in the TD-DFT calculations. Only the transitions with-non-negligible oscillator strengths are discussed in the paper. The graphical GaussView interface[283] was used for simulating UV-vis spectra. The phosphorescence emission spectra were computed within the Franck-Condon principle by using the Adiabatic Hessian method[264,265] which takes into account vibrational mode mixing and a proper description of both optimized ground and excited (triplet) states potential energy surfaces. A class-based pre-screening[284–286] was applied in order to limit the number of terms involved in the vibronic calculation with the following settings: C1max = 70, C2max = 70, N1max = 100 × 108. The GaussView interface[283] was used for their simulation .

General method A – Suzuki-Miyaura cross-coupling reaction

The corresponding acetylene (1.57 equiv) was dissolved in THF (20 mL) and nitrogen was bubbled through the solution for 10 min. Catecholborane (1.9 equiv of 1 M solution in THF) was added and the reaction mixture was heated to reflux for 1.5 h. The second portion of catecholborane (0.7 equiv) was added and heating was continued for 2 h. The reaction mixture was cooled to room temperature and $Pd(PPh_3)_4$ (0.025 equiv) and corresponding pyrimidine (1 equiv) were added. The solution was stirred for 20 min whereupon 20% aqueous Na_2CO_3 (5 mL) was added and the mixture was stirred under nitrogen at reflux for 15 h. The reaction mixture was cooled and then diluted with CH_2Cl_2 (20 mL). The organic layer was washed with water (3x20 mL), brine (20 mL), separated, dried over $MgSO_4$ and the solvents were evaporated under reduced pressure. The crude product was purified by column chromatography (SiO_2, indicated solvents).

General method B – Knoevenagel condensation

Aldehyde (1 equiv) and corresponding 4-methylpyrimidine (1 equiv) or 4,6-dimethylpyrimidine (0.5 equiv) were added in 5 M aqueous NaOH (15 mL) containing Aliquat 336 (0.1 equiv). The solution was heated to reflux for 3 h and then cooled to room temperature. The precipitate was filtered off, washed with water and purified by recrystallization from CH_2Cl_2/*n*-heptane and/or by column chromatography (SiO_2, indicated solvents).

General method C – Suzuki-Miyaura cross-coupling reaction

Chloropyrimidine (1 equiv) and corresponding boronic acid or boronic acid pinacol ester (1.2 equiv) were dissolved in a mixture of toluene/EtOH (20:3, 23mL) or in THF (20 mL) and nitrogen was bubbled through the solution for 10 min. $Pd(PPh_3)_4$ (5 %) and 20% aqueous Na_2CO_3 were added and then the reaction was stirred at 110 °C for 15h. The reaction mixture was cooled to room temperature and diluted with CH_2Cl_2/aqueous NH_4Cl (1:1, 100 mL). The organic layer was separated and the aqueous one was extracted with CH_2Cl_2 (2 × 50 mL). The combined organic extracts were dried over anhydrous $MgSO_4$ or Na_2SO_4 and the solvent was evaporated under reduced pressure. The solid residue was purified by column chromatography (SiO_2; indicated solvents).

General method D – synthesis of Pt^{II} complexes

K_2PtCl_4 (1 equiv) and ligand **244** (1.2 equiv) were dissolved in a mixture of EGEE/H_2O (3:1, 20 mL). The mixture was bubbled with nitrogen for 10 min and then stirred at 90 °C for 15h. The solution was cooled to room temperature and diluted with H_2O, precipitate was filtrated off and dried under vacuum. μ-Chloro-bridged intermediate was dissolved in $CHCl_3$ and pyridine was added (2.5 equiv). The mixture was stirred at 50 °C for 15 h. The reaction mixture was cooled to room temperature and diluted with CH_2Cl_2/aqueous NH_4Cl (1:1, 100 mL). The organic layer was separated and the aqueous one was extracted with CH_2Cl_2 (2 × 50 mL). The combined organic extracts were dried over anhydrous $MgSO_4$ and the solvents were evaporated under reduced pressure. The solid residue was purified by column chromatography (SiO_2; 1:1, EtOAc/CH_2Cl_2).

229a (*E*)-2-styryl-4-methylpyrimidine

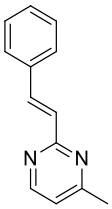

$C_{13}H_{13}N_2$

MW = 196.25

Compound **229a** was synthesized from phenylacetylene (176 mg, 1.72 mmol) and 2-chloro-4-methylpyrimidine (142 mg, 1.1 mmol) following the method A. The crude product was purified by column chromatography (SiO_2, petroleum ether:EtOAc, 8:2). Yield: 70 mg (32 %); white solid. R_f: 0.4 (SiO_2; petroleum ether:EtOAc, 8:2). Mp: 67.2–69.9 °C. ^{1}H NMR (300 MHz, $CDCl_3$): δ = 2.54 (s, 3H), 6.97 (d, $^3J_{H\text{-}H}$ = 4.8 Hz, 1H), 7.22 (d, $^3J_{H\text{-}H}$ = 15.9 Hz, 1H), 7.30–7.41 (m, 3H), 7.61–7.63 (m, 2H), 7.98 (d, $^3J_{H\text{-}H}$ = 15.9 Hz, 1H), 8.56 (d, $^3J_{H\text{-}H}$ = 4.8 Hz, 1H) ppm. ^{13}C NMR (75 MHz, $CDCl_3$): δ = 24.41, 118.27, 127.75, 128.90, 129.10, 136.27, 137.95, 156.76, 164.66, 167.14 ppm. Not all carbon atoms were observed. IR (ATR): ν = 2918, 1547, 1440, 1385, 978, 790, 747 cm^{-1}. HR-MALDI-MS (DCTB): *m/z* calculated for $C_{13}H_{13}N_2$ [$(M+H)^+$] 197.1073, found 197.1073. Data are in accordance with literature.[287]

229b (*E*)-2-(4-methoxystyryl)-4-methylpyrimidine

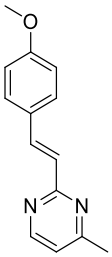

$C_{14}H_{14}N_2O$

MW = 226.27

Compound **229b** was synthesized from 4-ethynylanisole (311 mg, 2.35 mmol) and 2-chloro-4-methylpyrimidine (193 mg, 1.50 mmol) following the method A. The crude product was purified by column chromatography (SiO_2, petroleum ether:EtOAc, 7:3). Yield: 206 mg (61 %); brownish solid. R_f: 0.2 (SiO_2; petroleum ether:EtOAc, 7:3). Mp: 102.3–104.9 °C. ^{1}H NMR (300 MHz, $CDCl_3$): δ = 2.53 (s, 3H), 3.83 (s, 3H), 6.90–6.95 (m, 3H), 7.09 (d, $^3J_{H\text{-}H}$ = 15.9 Hz, 1H), 7.55–7.58 (m, 2H), 7.93 (d, $^3J_{H\text{-}H}$ = 15.9 Hz, 1H), 8.54 (d, $^3J_{H\text{-}H}$ = 5.1 Hz, 1H) ppm. ^{13}C NMR (75 MHz, $CDCl_3$): δ = 24.41, 55.47, 114.38, 117.92, 125.48, 129.06, 129.20, 137.60, 156.72, 160.55, 164.96, 167.08 ppm. IR (ATR): ν = 2937, 1566, 1509, 1249, 1178, 1028, 981, 821, 775 cm^{-1}. HR-MALDI-MS (DCTB): *m/z* calculated for $C_{14}H_{14}N_2O$ [M^+] 226.1101, found 226.1100.

229c (*E*)-2-(4-*N,N*-dimethylaminostyryl)-4-methylpyrimidine

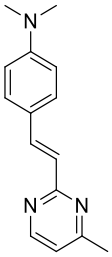

$C_{15}H_{17}N_3$

MW = 239.32

Compound **229c** was synthesized from 4-ethynyl-*N*,*N*-dimethylaniline (250 mg, 1.72 mmol) and 2-chloro-4-methylpyrimidine (142 mg, 1.1 mmol) following the method A. The crude product was purified by column chromatography (SiO_2, petroleum ether:EtOAc, 8:2). Yield: 85 mg (32 %); brown solid. R_f: 0.3 (SiO_2; petroleum ether:EtOAc, 8:2). Mp: 117.3–119.8 °C. ^{1}H NMR (300 MHz, $CDCl_3$): δ = 2.51 (s, 3H), 2.99 (s, 6H), 6.68–6.71 (m, 2H), 6.89 (d, $^3J_{H\text{-}H}$ = 5.1 Hz, 1H), 7.02 (d, $^3J_{H\text{-}H}$ = 15.9 Hz, 1H), 7.49–7.52 (m, 2H), 7.92 (d, $^3J_{H\text{-}H}$ = 15.9 Hz, 1H), 8.50 (d, $^3J_{H\text{-}H}$ = 5.1 Hz, 1H) ppm. ^{13}C NMR (75 MHz, $CDCl_3$): δ = 24.34, 40.33, 112.18, 117.34, 122.56, 124.26, 129.17, 138.55, 151.12, 156.55, 165.32, 166.94 ppm. IR (ATR): ν = 2912, 1602, 1523, 1435, 1363, 1167, 987, 805, 768, 750 cm^{-1}. HR-MALDI-MS (DCTB): *m/z* calculated for $C_{15}H_{17}N_3$ [M^+] 239.1417, found 239.1415.

229d (*E*)-2-(4-*N,N*-diphenylaminostyryl)-4-methylpyrimidine

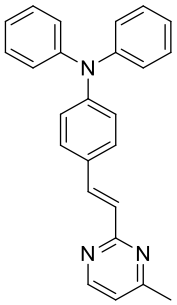

$C_{25}H_{21}N_3$

MW = 363.45

Compound **229d** was synthesized from 4-ethynyl-*N*,*N*-diphenylaniline (275 mg, 1.02 mmol) and 2-chloro-4-methylpyrimidine (84 mg, 0.65 mmol) following the method A. The crude product was purified by column chromatography (SiO_2, petroleum ether:EtOAc, 8:2). Yield: 102 mg (43 %); yellow solid. R_f: 0.2 (SiO_2; petroleum ether:EtOAc, 8:2). Mp: 120.9–123.5 °C. ^{1}H NMR (300 MHz, $CDCl_3$): δ = 2.53 (s, 3H), 6.94 (d, $^3J_{H\text{-}H}$ = 5.1 Hz, 1H), 7.02–7.15 (m, 10H), 7.25–7.31 (m, 3H), 7.46–7.49 (m, 2H), 7.92 (d, $^3J_{H\text{-}H}$ = 15.9 Hz, 1H), 8.54 (d, $^3J_{H\text{-}H}$ = 5.1 Hz, 1H) ppm. ^{13}C NMR (75 MHz, $CDCl_3$): δ = 24.41, 117.87, 122.62, 123.65, 125.18, 125.45, 128.75, 129.51, 129.80, 137.58, 147.40, 148.83, 156.70, 164.97, 167.06 ppm. IR (ATR): ν = 3036, 1572, 1487, 1266, 984, 831, 750, 695 cm^{-1}. HR-MALDI-MS (DCTB): *m/z* calculated for $C_{25}H_{21}N_3$ [M^+] 363.1730, found 363.1723.

230a (*E*)-2-styryl-4,6-dimethylpyrimidine

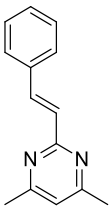

$C_{14}H_{14}N_2$

MW = 210.27

Compound **230a** was synthesized from phenylacetylene (161 mg, 1.57 mmol) and 2-chloro-4,6-dimethylpyrimidine (143 mg, 1 mmol) following the method A. The crude product was purified by column chromatography (SiO_2, petroleum ether:EtOAc, 7:3). Yield: 78 mg (37 %); white solid. R_f: 0.7 (SiO_2; petroleum ether:EtOAc, 7:3). Mp: 47.5–49.4 °C. ^{1}H NMR (300 MHz, $CDCl_3$): δ = 2.50 (s, 6H), 6.86 (s, 1H), 7.21 (d, $^3J_{H\text{-}H}$ = 15.9 Hz, 1H), 7.29–7.41 (m, 3H), 7.61–7.64 (m, 2H), 7.97 (d, $^3J_{H\text{-}H}$ = 15.9 Hz, 1H) ppm. ^{13}C NMR (75 MHz, $CDCl_3$): δ = 24.13, 117.74, 127.67, 127.91, 128.82, 128.91, 136.37, 137.60, 164.27, 166.60 ppm. IR (ATR): ν = 3057, 1533, 1367, 978, 747, 692 cm^{-1}. HR-MALDI-MS (DCTB): *m/z* calculated for $C_{14}H_{15}N_2$ [$(M+H)^+$] 211.1230, found 211.1227. Data are in accordance with literature.[288]

230b (*E*)-2-(4-methoxystyryl)-4,6-dimethylpyrimidine

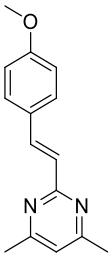

$C_{15}H_{16}N_2O$

MW = 240.30

Compound **230b** was synthesized from 4-ethynylanisole (415 mg, 3.14 mmol) and 2-chloro-4,6-dimethylpyrimidine (286 mg, 2 mmol) following the method A. The crude product was purified by column chromatography (SiO_2, petroleum ether:EtOAc, 7:3). Yield: 257 mg (54 %); brownish solid. R_f: 0.4 (SiO_2; petroleum ether:EtOAc, 7:3). Mp: 87.9–90.2 °C. ^{1}H NMR (300 MHz, $CDCl_3$): δ = 2.48 (s, 6H), 3.82 (s, 3H), 6.82 (s, 1H), 6.89–6.92 (m, 2H), 7.07 (d, $^3J_{H-H}$ = 15.9 Hz, 1H), 7.54–7.57 (m, 2H), 7.92 (d, $^3J_{H-H}$ = 15.9 Hz, 1H) ppm. ^{13}C NMR (75 MHz, $CDCl_3$): δ = 24.13, 55.44, 114.33, 117.43, 125.62, 129.14, 129.20, 137.35, 160.44, 164.61, 166.57 ppm. IR (ATR): ν = 3004, 1574, 1511, 1242, 1178, 1028, 981, 839, 818, 770 cm^{-1}. HR-MALDI-MS (DCTB): *m/z* calculated for $C_{15}H_{16}N_2O$ [M^+] 240.1257, found 240.1256.

230c (*E*)-2-(4-*N,N*-dimethylaminostyryl)-4,6-dimethylpyrimidine

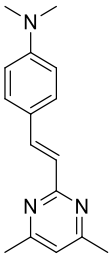

$C_{16}H_{19}N_3$

MW = 253.34

Compound **230c** was synthesized from 4-ethynyl-*N,N*-dimethylaniline (362 mg, 2.50 mmol) and 2-chloro-4,6-dimethylpyrimidine (230 mg, 1.61 mmol) following the method A. The crude product was purified by column chromatography (SiO_2, petroleum ether:EtOAc, 7:3). Yield: 244 mg (59 %); yellow solid. R_f: 0.6 (SiO_2; petroleum ether:EtOAc, 7:3). Mp: 112.8–115.2 °C. ^{1}H NMR (300 MHz, $CDCl_3$): δ = 2.47 (s, 6H), 3.00 (s, 6H), 6.69–6.72 (m, 2H), 6.78 (s, 1H), 7.01 (d, $^3J_{H-H}$ = 15.9 Hz, 1H), 7.51–7.54 (m, 2H), 7.91 (d, $^3J_{H-H}$ = 15.9 Hz, 1H) ppm. ^{13}C NMR (75 MHz, $CDCl_3$): δ = 24.21, 40.41, 112.23, 116.89, 123.16, 124.58, 129.12, 138.05, 151.04, 165.14, 166.45 ppm. IR (ATR): ν = 2919, 1580, 1443, 1356, 1165, 986, 820, 748 cm^{-1}. HR-MALDI-MS (DCTB): *m/z* calculated for $C_{16}H_{19}N_3$ [M^+] 253.1574, found 253.1562.

230d (*E*)-2-(4-*N,N*-diphenylaminostyryl)-4,6-dimethylpyrimidine

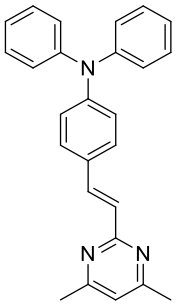

$C_{26}H_{23}N_3$

MW = 377.48

Compound **230d** was synthesized from 4-ethynyl-*N*,*N*-diphenylaniline (790 mg, 2.94 mmol) and 2-chloro-4,6-dimethylpyrimidine (267 mg, 1.87 mmol) following the method A. The crude product was purified by column chromatography (SiO_2, petroleum ether:EtOAc, 8:2). Yield: 200 mg (28 %); yellow solid. R_f: 0.4 (SiO_2; petroleum ether:EtOAc, 8:2). Mp: 132.7–135.7 °C. ^{1}H NMR (300 MHz, $CDCl_3$): δ = 2.49 (s, 6H), 6.83 (s, 1H), 7.02–7.14 (m, 9H), 7.25–7.30 (m, 4H), 7.46–7.49 (m, 2H), 7.91 (d, $^3J_{H\text{-}H}$ = 15.9 Hz, 1H) ppm. ^{13}C NMR (75 MHz, $CDCl_3$): δ = 24.09, 117.34, 122.61, 123.55, 125.09, 125.60, 128.65, 129.45, 129.95, 137.27, 147.39, 148.63, 164.57, 166.49 ppm. IR (ATR): ν = 3030, 1585, 1488, 1273, 749, 692 cm^{-1}. HR-MALDI-MS (DCTB): *m/z* calculated for $C_{26}H_{23}N_3$ [M^+] 377.1887, found 377.1888.

230e (*E*)-2-[(6-methoxynaphtalen-2-yl)ethenyl]-4,6-dimethylpyrimidine

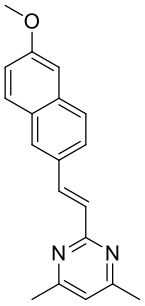

$C_{19}H_{18}N_2O$

MW = 290.36

Compound **230e** was synthesized from 2-ethynyl-6-methoxynaphtalene (286 mg, 1.57 mmol) and 2-chloro-4,6-dimethylpyrimidine (143 mg, 1 mmol) following the method A. The crude product was purified by column chromatography (SiO_2, petroleum ether:EtOAc, 7:3). Yield: 230 mg (79 %); yellowish solid. R_f: 0.3 (SiO_2; petroleum ether:EtOAc, 7:3). Mp: 133.5–134.9 °C. ^{1}H NMR (300 MHz, $CDCl_3$): δ = 2.45 (s, 6H), 3.86 (s, 3H), 6.75 (s, 1H), 7.06–7.13 (m, 2H), 7.26 (d, $^3J_{H\text{-}H}$ = 15.9 Hz, 1H), 7.66–7.77 (m, 3H), 7.88 (s, 1H), 8.09 (d, $^3J_{H\text{-}H}$ = 15.9 Hz, 1H) ppm. ^{13}C NMR (75 MHz, $CDCl_3$): δ = 24.00, 55.28, 105.93, 117.43, 119.08, 124.41, 126.98, 127.27, 128.44, 128.92, 129.86, 131.69, 134.93, 137.74, 158.25, 164.30, 166.42 ppm. IR (ATR): ν = 2931, 1582, 1364, 1163, 1027, 860, 803, 665 cm^{-1}. HR-MALDI-MS (DCTB): *m/z* calculated for $C_{19}H_{18}N_2O$ [M^+] 290.1414, found 290.1414.

230f (*E*)-2-(4-trifluoromethylstyryl)-4,6-dimethylpyrimidine

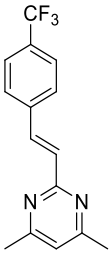

$C_{15}H_{13}F_3N_2$

MW = 278.27

Compound **230f** was synthesized from 4-trifluoromethylphenylacetylene (426 mg, 2.50 mmol) and 2-chloro-4,6-dimethylpyrimidine (228 mg, 1.59 mmol) following the method A. The crude product was purified by column chromatography (SiO_2, petroleum ether:EtOAc, 7:3). Yield: 222 mg (50 %); yellowish solid. R_f: 0.4 (SiO_2; petroleum ether:EtOAc, 7:3). Mp: 94.9–96.5 °C. ^{1}H NMR (300 MHz, $CDCl_3$): δ = 2.50 (s, 6H), 6.89 (s, 1H), 7.26 (d, $^3J_{H-H}$ = 15.9 Hz, 1H), 7.60–7.71 (m, 4H), 7.97 (d, $^3J_{H-H}$ = 15.9 Hz, 1H) ppm. ^{13}C NMR (75 MHz, $CDCl_3$): δ = 24.13, 118.23, 124.23 (q, $^1J_{C-F}$ = 270 Hz), 125.82 (q, $^3J_{C-F}$ = 4 Hz), 127.73, 130.41, 130.47 (q, $^2J_{C-F}$ = 32 Hz), 135.85, 139.86 (d, $^4J_{C-F}$ = 1 Hz), 163.72, 166.80 ppm. IR (ATR): ν = 2929, 1583, 1319, 1103, 1064, 831, 714 cm^{-1}. HR-MALDI-MS (DCTB): *m/z* calculated for $C_{15}H_{14}F_3N_2$ [(M+H)$^+$] 279.1104, found 279.1102.

231a (*E,E*)-2,4-distyrylpyrimidine

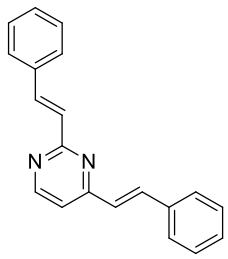

$C_{20}H_{16}N_2$

MW = 284.35

Compound **231a** was synthesized from **229a** (50 mg, 0.25 mmol) and benzaldehyde (28 mg, 0.25 mmol) following the method B. The crude product was purified by column chromatography (SiO_2; petroleum ether:EtOAc, 8:2). Yield: 41 mg (57 %); white solid. R_f: 0.4 (SiO_2; petroleum ether:EtOAc, 8:2). Mp: 137 °C. ^{1}H NMR (300 MHz, $CDCl_3$): δ = 7.08–7.15 (m, 2H), 7.32–7.41 (m, 7H), 7.63–7.68 (m, 4H), 7.92 (d, $^3J_{H-H}$ = 15.9 Hz, 1H), 8.05 (d, $^3J_{H-H}$ = 15.9 Hz, 1H), 8.67 (d, $^3J_{H-H}$ = 5.1 Hz, 1H) ppm. ^{13}C NMR (75 MHz, $CDCl_3$): δ = 115.91, 126.29, 127.82, 127.97, 128.93, 129.02, 129.14, 129.50, 135.92, 136.34, 137.25, 138.08, 157.56, 162.54, 164.87 ppm. Not all carbon atoms were observed. IR (ATR): ν = 3054, 3026, 1637, 1558, 1537, 1388, 975, 876, 738, 688 cm^{-1}. HR-MALDI-MS (DCTB): *m/z* calculated for $C_{20}H_{17}N_2$ [(M+H)$^+$] 285.1386, found 285.1385. Data are in accordance with literature.[206]

231b (*E,E*)-2,4-bis(4-methoxystyryl)pyrimidine

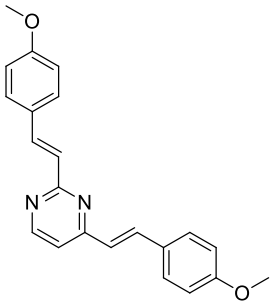

$C_{22}H_{20}N_2O_2$

MW = 344.41

Compound **231b** was synthesized from **229b** (170 mg, 0.75 mmol) and 4-methoxybenzaldehyde (103 mg, 0.75 mmol) following the method B. The crude product was purified by recrystallization from CH_2Cl_2/*n*-heptane. Yield: 218 mg (84 %); silver solid. R_f: 0.1 (SiO_2; petroleum ether:EtOAc, 7:3). Mp: 185 °C. ^{1}H NMR (300 MHz, $CDCl_3$): δ = 3.85 (s, 6H), 6.92–6.98 (m, 5H), 7.07 (d, $^3J_{H\text{-}H}$ = 5.1 Hz, 1H), 7.14 (d, $^3J_{H\text{-}H}$ = 15.9 Hz, 1H), 7.56–7.62 (m, 4H), 7.85 (d, $^3J_{H\text{-}H}$ = 15.9 Hz, 1H), 7.99 (d, $^3J_{H\text{-}H}$ = 15.9 Hz, 1H), 8.60 (d, $^3J_{H\text{-}H}$ = 5.1 Hz, 1H) ppm. ^{13}C NMR (75 MHz, $CDCl_3$): δ = 55.47, 55.49, 114.36, 114.45, 115.26, 124.08, 125.80, 128.69, 129.14, 129.21, 129.28, 136.71, 137.51, 157.28, 160.51, 160.79, 162.79, 165.05 ppm. IR (ATR): ν = 2964, 1560, 1250, 1177, 1028, 972, 826 cm^{-1}. HR-MALDI-MS (DCTB): *m/z* calculated for $C_{22}H_{21}N_2O_2$ [$(M+H)^+$] 345.1598, found 345.1592.

231c (*E,E*)-2,4-bis(4-*N,N*-dimethylaminostyryl)pyrimidine

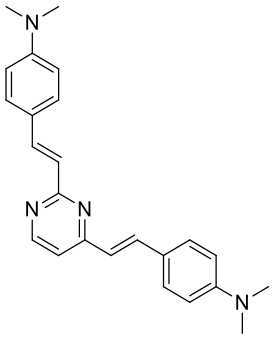

$C_{24}H_{26}N_4$

MW = 370.49

Compound **231c** was synthesized from **229c** (41 mg, 0.17 mmol) and 4-*N*,*N*-dimethylaminobenzaldehyde (26 mg, 0.17 mmol) following the method B. The crude product was purified by recrystallization from CH_2Cl_2/*n*-heptane. Yield: 55 mg (85 %); brown solid. R_f: 0.2 (SiO_2; petroleum ether:EtOAc, 8:2). Mp: 243 °C. ^{1}H NMR (300 MHz, $CDCl_3$): δ = 3.02–3.03 (m, 12H), 6.70–6.74 (m, 4H), 6.88 (d, $^3J_{H\text{-}H}$ = 15.9 Hz, 1H), 7.01–7.09 (m, 2H), 7.51–7.57 (m, 4H), 7.80 (d, $^3J_{H\text{-}H}$ = 15.9 Hz, 1H), 7.96 (d, $^3J_{H\text{-}H}$ = 15.9 Hz, 1H), 8.54 (d, $^3J_{H\text{-}H}$ = 5.1 Hz, 1H) ppm. ^{13}C NMR (75 MHz, $CDCl_3$): δ = 40.39, 40.45, 112.21, 112.27, 114.34, 121.69, 123.45, 124.06, 124.63, 129.18, 129.26, 137.31, 138.05, 151.07, 151.28, 156.91, 163.32,

165.46 ppm. IR (ATR): ν = 2920, 1602, 1550, 1520, 1359, 1163, 970, 810, 781 cm^{-1}. HR-MALDI-MS (DCTB): *m/z* calculated for $C_{24}H_{26}N_4$ [M^+] 370.2152, found 370.2150.

231d (*E,E*)-2,4-bis(4-*N,N*-diphenylaminostyryl)pyrimidine

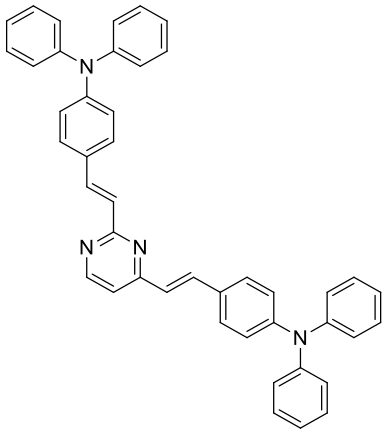

$C_{44}H_{34}N_4$

MW = 618.77

Compound **231d** was synthesized from **229d** (76 mg, 0.21 mmol) and 4-*N*,*N*-diphenylaminobenzaldehyde (58 mg, 0.21 mmol) following the method B. The crude product was purified by recrystallization from CH_2Cl_2/*n*-heptane. Yield: 51 mg (39 %); yellow solid. R_f: 0.3 (SiO_2; petroleum ether:EtOAc, 8:2). T_d: 250 °C. ^{1}H NMR (300 MHz, $CDCl_3$): δ = 6.92–6.97 (m, 2H), 7.04–7.15 (m, 19H), 7.29–7.32 (m, 6H), 7.46–7.52 (m, 4H), 7.82 (d, $^3J_{H\text{-}H}$ = 15.9 Hz, 1H), 7.97 (d, $^3J_{H\text{-}H}$ = 15.9 Hz, 1H), 8.59 (d, $^3J_{H\text{-}H}$ = 5.4 Hz, 1H) ppm. ^{13}C NMR (75 MHz, $CDCl_3$): δ = 115.13, 122.47, 122.71, 123.63, 123.84, 124.12, 125.17, 125.29, 125.90, 128.78, 128.82, 129.35, 129.52, 129.57, 129.98, 136.67, 137.46, 147.30, 147.45, 148.78, 149.14, 157.24, 162.87, 165.12 ppm. IR (ATR): ν = 3034, 2924, 1588, 1556, 1490, 1274, 1174, 972, 831, 751, 693 cm^{-1}. HR-MALDI-MS (DCTB): *m/z* calculated for $C_{44}H_{34}N_4$ [M^+] 618.2778, found 618.2779.

232a (*E,E,E*)-2,4,6-tristyrylpyrimidine

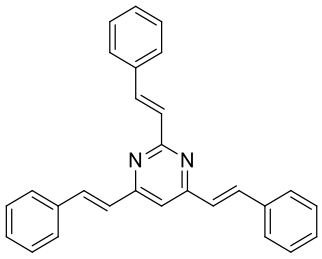

$C_{28}H_{22}N_2$

MW = 386.49

Compound **232a** was synthesized from **230a** (300 mg, 1.43 mmol) and benzaldehyde (303 mg, 2.85 mmol) following the method B. The crude product was purified by column chromatography (SiO_2, petroleum ether:EtOAc, 9:1) and then by recrystallization from

CH_2Cl_2/*n*-heptane. Yield: 155 mg (28 %); white solid. R_f: 0.4 (SiO_2; petroleum ether:EtOAc, 9:1). Mp: 193 °C. ^{1}H NMR (300 MHz, $CDCl_3$): δ = 7.08–7.16 (m, 3H), 7.28–7.43 (m, 10H), 7.62–7.69 (m, 6H), 7.93 (d, $^3J_{H\text{-}H}$ = 15.9 Hz, 2H), 8.11 (d, $^3J_{H\text{-}H}$ = 15.9 Hz, 1H) ppm. ^{13}C NMR (75 MHz, $CDCl_3$): δ = 113.68, 126.51, 127.73, 127.77, 128.29, 128.84, 128.95, 129.32, 136.03, 136.45, 136.72, 137.87, 162.94, 164.62 ppm. Not all carbon atoms were observed. IR (ATR): ν = 3025, 1635, 1564, 1514, 1368, 963, 739, 689 cm^{-1}. HR-MALDI-MS (DCTB): *m/z* calculated for $C_{28}H_{23}N_2$ [$(M+H)^+$] 387.1856, found 387.1855. Data are in accordance with literature.[208]

232b (*E*,*E*,*E*)-2-styryl-4,6-bis(4-methoxystyryl)pyrimidine

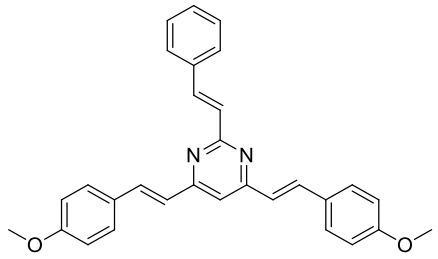

$C_{30}H_{26}N_2O_2$

MW = 446.54

Compound **232b** was synthesized from **230a** (78 mg, 0.37 mmol) and 4-methoxybenzaldehyde (102 mg, 0.74 mmol) following the method B. The crude product was purified by column chromatography (SiO_2, petroleum ether:EtOAc, 8:2) and then by recrystallization from CH_2Cl_2/*n*-heptane. Yield: 40 mg (24 %); yellowish solid. R_f: 0.4 (SiO_2; petroleum ether:EtOAc, 8:2). Mp: 128 °C. ^{1}H NMR (300 MHz, $CDCl_3$): δ = 3.86 (s, 6H), 6.93–7.01 (m, 6H), 7.11 (s, 1H), 7.29–7.44 (m, 4H), 7.58–7.61 (m, 4H), 7.68–7.70 (m, 2H), 7.89 (d, $^3J_{H\text{-}H}$ = 15.9 Hz, 2H), 8.11 (d, $^3J_{H\text{-}H}$ = 15.9 Hz, 1H) ppm. ^{13}C NMR (75 MHz, $CDCl_3$): δ = 55.51, 113.20, 114.46, 124.39, 127.80, 128.54, 128.86, 128.90, 128.91, 129.25, 136.25, 136.61, 137.65, 160.72, 163.15, 164.55 ppm. IR (ATR): ν = 2837, 1604, 1560, 1501, 1251, 1171, 1152, 967, 749 cm^{-1}. HR-MALDI-MS (DCTB): *m/z* calculated for $C_{30}H_{27}N_2O_2$ [$(M+H)^+$] 447.2067, found 447.2064.

232c (*E,E,E*)-2-styryl-4,6-bis(4-*N,N*-dimethylaminostyryl)pyrimidine

$C_{32}H_{32}N_4$

MW = 472.62

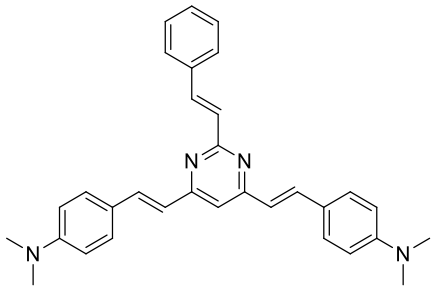

Compound **232c** was synthesized from **230a** (150 mg, 0.71 mmol) and 4-*N*,*N*-dimethylaminobenzaldehyde (213 mg, 1.43 mmol) following the method B. The crude product was purified by column chromatography (SiO_2, petroleum ether:EtOAc, 8:2) and then by recrystallization from CH_2Cl_2/*n*-heptane. Yield: 63 mg (17 %); black solid. R_f: 0.2 (SiO_2; petroleum ether:EtOAc, 8:2). T_d: 245 °C. ^{1}H NMR (300 MHz, $CDCl_3$): δ = 3.03 (s, 12 H), 6.71–6.74 (m, 4H), 6.91 (d, $^3J_{H\text{-}H}$ = 15.9 Hz, 2H), 7.08 (s, 1H), 7.28–7.35 (m, 4H), 7.53–7.56 (m, 4H), 7.68–7.70 (m, 2H), 7.86 (d, $^3J_{H\text{-}H}$ = 15.9 Hz, 2H), 8.10 (d, $^3J_{H\text{-}H}$ = 15.9 Hz, 1H) ppm. ^{13}C NMR (75 MHz, $CDCl_3$): δ = 40.39, 112.24, 112.41, 114.20, 114.74, 121.91, 124.28, 127.78, 128.73, 128.81, 129.21, 136.81, 137.25, 151.20, 163.36, 164.33 ppm. IR (ATR): ν = 2892, 1602, 1555, 1503, 1363, 1162, 965, 800, 746 cm^{-1}. HR-MALDI-MS (DCTB): *m/z* calculated for $C_{32}H_{32}N_4$ [M^+] 472.2622, found 472.2620.

232d (*E,E,E*)-2-styryl-4,6-bis(4-*N,N*-diphenylaminostyryl)pyrimidine

$C_{52}H_{40}N_4$

MW = 720.90

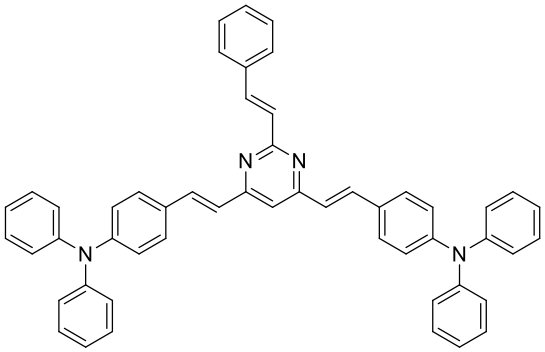

Compound **232d** was synthesized from **230a** (300 mg, 1.43 mmol) and 4-*N*,*N*-diphenylaminobenzaldehyde (780 mg, 2.85 mmol) following the method B. The crude product was purified by column chromatography (SiO_2, petroleum ether:EtOAc, 9:1) and then by recrystallization from CH_2Cl_2/*n*-heptane. Yield: 220 mg (21 %); yellow solid. R_f: 0.4 (SiO_2; petroleum ether:EtOAc, 9:1). T_d: 305 °C. ^{1}H NMR (300 MHz, $CDCl_3$): δ = 6.98 (d, $^3J_{H\text{-}H}$ = 15.9 Hz, 2H), 7.05–7.17 (m, 17H), 7.27–7.43 (m, 12H), 7.48–7.51 (m, 4H), 7.67–7.70 (m, 2H), 7.87 (d, $^3J_{H\text{-}H}$ = 15.9 Hz, 2H), 8.10 (d, $^3J_{H\text{-}H}$ = 15.9 Hz, 1H) ppm. ^{13}C NMR (75 MHz, $CDCl_3$): δ =

113.14, 122.54, 123.78, 124.41, 125.25, 127.79, 128.58, 128.77, 128.85, 128.88, 129.56, 129.59, 136.14, 136.61, 137.60, 147.34, 149.00, 163.11, 164.55 ppm. IR (ATR): ν = 3033, 1559, 1490, 1274, 969, 748, 693 cm^{-1}. HR-MALDI-MS (DCTB): *m/z* calculated for $C_{52}H_{40}N_4$ [M^+] 720.3248, found 720.3252.

232e (*E,E,E*)-2,4,6-tris(4-methoxystyryl)pyrimidine

$C_{31}H_{28}N_2O_3$

MW = 476.57

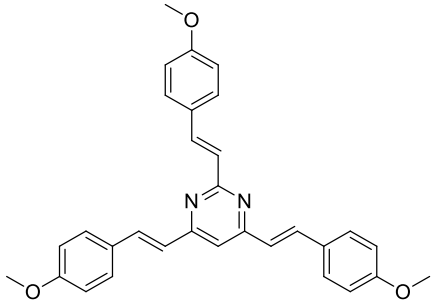

Compound **232e** was synthesized from **230b** (100 mg, 0.42 mmol) and 4-methoxybenzaldehyde (114 mg, 0.83 mmol) following the general procedure for Knoevenagel condensation. The crude product was purified by recrystallization from CH_2Cl_2/*n*-heptane. Yield: 156 mg (79 %); yellowish solid. R_f: 0.4 (SiO_2; petroleum ether:EtOAc, 8:2). Mp: 183 °C. ^{1}H NMR (300 MHz, $CDCl_3$): δ = 3.85 (s, 9H), 6.93–7.00 (m, 8H), 7.08 (s, 1H), 7.18 (d, $^3J_{H\text{-}H}$ = 15.9 Hz, 1H), 7.57–7.65 (m, 6H), 7.88 (d, $^3J_{H\text{-}H}$ = 15.9 Hz, 2H), 8.06 (d, $^3J_{H\text{-}H}$ = 15.9 Hz, 1H) ppm. ^{13}C NMR (75 MHz, $CDCl_3$): δ = 55.46, 55.49, 112.83, 114.34, 114.45, 124.50, 126.29, 128.96, 129.21, 129.40, 136.12, 137.30, 160.40, 160.68, 163.08, 164.84 ppm. Not all carbon atoms were observed. IR (ATR): ν = 2933, 1602, 1559, 1506, 1245, 1169, 1028, 959, 868, 810, 767 cm^{-1}. HR-MALDI-MS (DCTB): *m/z* calculated for $C_{31}H_{28}N_2O_3$ [M^+] 476.2094, found 476.2094.

232f (*E,E,E*)-2-(4-methoxystyryl)-4,6-bis(4-*N,N*-dimethylaminostyryl)pyrimidine

$C_{33}H_{34}N_4O$

MW = 502.65

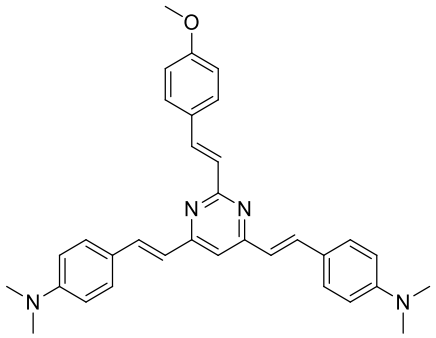

Compound **232f** was synthesized from **230b** (100 mg, 0.42 mmol) and 4-*N,N*-dimethylaminobenzaldehyde (125 mg, 0.83 mmol) following the method B. The crude product

was purified by recrystallization from CH_2Cl_2/*n*-heptane. Yield: 154 mg (74 %); red solid. R_f: 0.3 (SiO_2; petroleum ether:EtOAc, 8:2). T_d: 250 °C. ^{1}H NMR (300 MHz, $CDCl_3$): δ = 3.03 (s, 12H), 3.85 (s, 3H), 6.71–6.74 (m, 4H), 6.88–6.95 (m, 4H), 7.07 (s, 1H), 7.17 (d, $^3J_{H-H}$ = 15.9 Hz, 1H), 7.52–7.55 (m, 4H), 7.62–7.65 (m, 2H), 7.84 (d, $^3J_{H-H}$ = 15.9 Hz, 2H), 8.05 (d, $^3J_{H-H}$ = 15.9 Hz, 1H) ppm. ^{13}C NMR (75 MHz, $CDCl_3$): δ = 40.37, 55.44, 112.13, 112.22, 114.27, 122.04, 124.28, 126.65, 129.15, 129.57, 136.60, 136.80, 151.15, 160.25, 163.31, 164.66 ppm. Not all carbon atoms were observed. IR (ATR): ν = 2924, 1600, 1550, 1497, 1355, 1244, 1142, 971, 806 cm^{-1}. HR-MALDI-MS (DCTB): *m/z* calculated for $C_{33}H_{34}N_4O$ [M^+] 502.2727, found 502.2731.

232g (*E,E,E*)-2-(4-methoxystyryl)-4,6-bis(4-*N,N*-diphenylaminostyryl)pyrimidine

$C_{53}H_{42}N_4O$

MW = 750.93

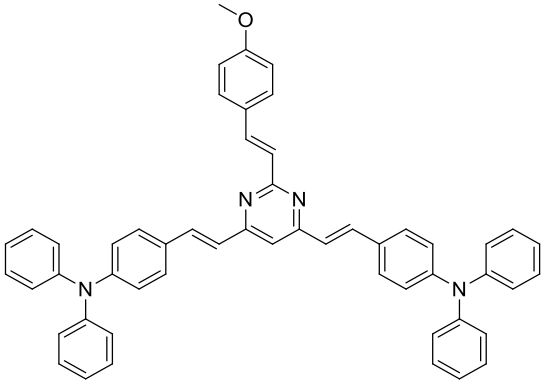

Compound **232g** was synthesized from **230b** (100 mg, 0.42 mmol) and 4-*N*,*N*-diphenylaminobenzaldehyde (228 mg, 0.83 mmol) following the method B. The crude product was purified by recrystallization from CH_2Cl_2/*n*-heptane. Yield: 225 mg (72 %); yellow solid. R_f: 0.7 (SiO_2; petroleum ether:EtOAc, 8:2). T_d: 270 °C. ^{1}H NMR (300 MHz, $CDCl_3$): δ = 3.85 (s, 3H), 6.92–7.21 (m, 24H), 7.27–7.32 (m, 6H), 7.48–7.50 (m, 4H), 7.61–7.64 (m, 2H), 7.86 (d, $^3J_{H-H}$ = 15.9 Hz, 2H), 8.06 (d, $^3J_{H-H}$ = 15.9 Hz, 1H) ppm. ^{13}C NMR (75 MHz, $CDCl_3$): δ = 55.46, 112.81, 114.33, 122.58, 123.75, 124.55, 125.24, 126.35, 128.74, 129.20, 129.42, 129.55, 129.67, 136.01, 137.25, 147.37, 148.97, 160.39, 163.05, 164.86 ppm. IR (ATR): ν = 3033, 1562, 1489, 1271, 1242, 1168, 972, 818, 749, 691 cm^{-1}. HR-MALDI-MS (DCTB): *m/z* calculated for $C_{53}H_{42}N_4O$ [M^+] 750.3353, found 750.3361.

232h (*E,E,E*)-2-(4-*N,N*-dimethylaminostyryl)-4,6-bis(4-methoxystyryl)pyrimidine

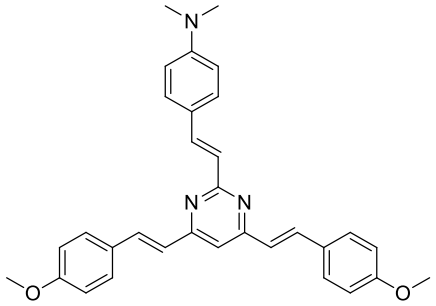

$C_{32}H_{31}N_3O_2$

MW = 489.61

Compound **232h** was synthesized from **230c** (110 mg, 0.43 mmol) and 4-methoxybenzaldehyde (119 mg, 0.87 mmol) following the method B The crude product was purified by recrystallization from CH_2Cl_2/*n*-heptane. Yield: 121 mg (57 %); brown solid. R_f: 0.3 (SiO_2; petroleum ether:EtOAc, 8:2). Mp: 200 °C. ^{1}H NMR (300 MHz, $CDCl_3$): δ = 3.02 (s, 6H), 3.85 (s, 6H), 6.72–6.75 (m, 2H), 6.93–7.00 (m, 6H), 7.05 (s, 1H), 7.12 (d, $^3J_{H\text{-}H}$ = 15.9 Hz, 1H), 7.57–7.61 (m, 6H), 7.87 (d, $^3J_{H\text{-}H}$ = 15.9 Hz, 2H), 8.05 (d, $^3J_{H\text{-}H}$ = 15.9 Hz, 1H) ppm. ^{13}C NMR (75 MHz, $CDCl_3$): δ = 40.43, 55.49, 112.25, 112.36, 114.42, 123.71, 124.70, 124.76, 129.03, 129.18, 135.89, 138.09, 151.02, 160.61, 163.00, 165.36 ppm. Not all carbon atoms were observed. IR (ATR): ν = 2924, 1603, 1558, 1502, 1357, 1249, 1168, 1028, 961, 810 cm^{-1}. HR-MALDI-MS (DCTB): *m/z* calculated for $C_{32}H_{31}N_3O_2$ [M^+] 489.2411, found 489.2414.

232i (*E,E,E*)-2,4,6-tris(4-*N,N*-dimethylaminostyryl)pyrimidine

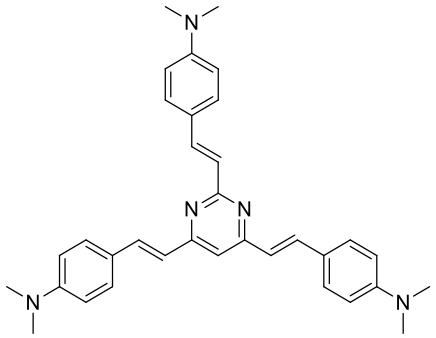

$C_{34}H_{37}N_5$

MW = 515.69

Compound **232i** was synthesized from **230c** (244 mg, 0.96 mmol) and 4-*N*,*N*-dimethylaminobenzaldehyde (287 mg, 1.92 mmol) following the method B. The crude product was purified by recrystallization from CH_2Cl_2/*n*-heptane. Yield: 212 mg (43 %); brown solid. R_f: 0.1 (SiO_2; petroleum ether:EtOAc, 8:2). T_d: 250 °C. ^{1}H NMR (300 MHz, $CDCl_3$): δ = 3.02–3.03 (m, 18H), 6.71–6.75 (m, 6H), 6.91 (d, $^3J_{H\text{-}H}$ = 15.9 Hz, 2H), 7.05 (s, 1H), 7.11 (d, $^3J_{H\text{-}H}$ = 15.6 Hz, 1H), 7.53–7.61 (m, 6H), 7.83 (d, $^3J_{H\text{-}H}$ = 15.9 Hz, 2H), 8.03 (d, $^3J_{H\text{-}H}$ = 15.9 Hz, 1H) ppm. ^{13}C NMR (75 MHz, $CDCl_3$): δ = 40.42, 40.47, 111.65, 112.28, 122.34, 124.16, 124.45, 125.03, 129.14, 136.42, 137.64, 150.92, 151.13, 163.25, 165.19 ppm. Not all carbon atoms

were observed. IR (ATR): ν = 2888, 1599, 1502, 1356, 1167, 965, 797 cm^{-1}. HR-MALDI-MS (DCTB): *m/z* calculated for $C_{34}H_{37}N_5$ [M$^+$] 515.3044, found 515.3044.

232j (*E,E,E*)-2-(4-*N,N*-dimethylaminostyryl)-4,6-bis(4-*N,N*-diphenylaminostyryl)pyrimidine

$C_{54}H_{45}N_5$

MW = 763.97

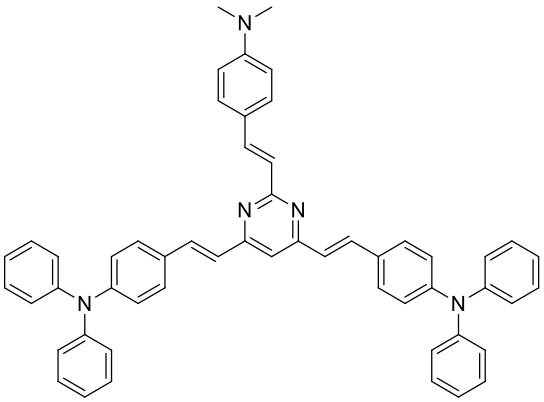

Compound **232j** was synthesized from **230c** (110 mg, 0.43 mmol) and 4-*N*,*N*-diphenylaminobenzaldehyde (238 mg, 0.87 mmol) following the method B. The crude product was purified by recrystallization from CH_2Cl_2/*n*-heptane. Yield: 225 mg (68 %); yellow solid. R_f: 0.6 (SiO_2; petroleum ether:EtOAc, 8:2). T_d: 240 °C. ^{1}H NMR (300 MHz, $CDCl_3$): δ = 3.02 (s, 6H), 6.72–6.75 (m, 2H), 6.99 (d, $^3J_{H\text{-}H}$ = 15.9 Hz, 2H), 7.05–7.16 (m, 18H), 7.27–7.32 (m, 8H), 7.48–7.50 (m, 4H), 7.57–7.60 (m, 2H), 7.85 (d, $^3J_{H\text{-}H}$ = 15.9 Hz, 2H), 8.04 (d, $^3J_{H\text{-}H}$ = 15.9 Hz, 1H) ppm. ^{13}C NMR (75 MHz, $CDCl_3$): δ = 40.43, 112.24, 112.30, 122.62, 123.70, 124.76, 124.78, 125.20, 128.71, 129.19, 129.53, 129.78, 135.79, 138.05, 147.38, 148.87, 150.99, 162.96, 165.36 ppm. Not all carbon atoms were observed. IR (ATR): ν = 3034, 1564, 1490, 1361, 1273, 1167, 971, 810, 749, 692 cm^{-1}. HR-MALDI-MS (DCTB): *m/z* calculated for $C_{54}H_{45}N_5$ [M$^+$] 763.3670, found 763.3673.

232k (*E,E,E*)-2-(4-*N,N*-diphenylaminostyryl)-4,6-bis(4-methoxystyryl)pyrimidine

$C_{42}H_{35}N_3O_2$

MW = 613.75

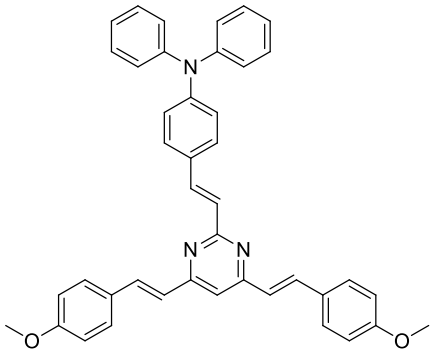

Compound **232k** was synthesized from **230d** (70 mg, 0.19 mmol) and 4-methoxybenzaldehyde (51 mg, 0.37 mmol) following the method B. The crude product was purified by column chromatography (SiO_2, petroleum ether:EtOAc, 8:2). Yield: 83 mg (73 %); yellow solid. R_f: 0.5 (SiO_2; petroleum ether:EtOAc, 8:2). T_d: 310 °C. ^{1}H NMR (300 MHz, $CDCl_3$): δ = 3.86 (s, 6H), 6.93–7.20 (m, 16H), 7.27–7.32 (m, 4H), 7.53–7.60 (m, 6H), 7.87 (d, $^3J_{H\text{-}H}$ = 15.9 Hz, 2H), 8.05 (d, $^3J_{H\text{-}H}$ = 15.9 Hz, 1H) ppm. ^{13}C NMR (75 MHz, $CDCl_3$): δ = 55.50, 112.77, 114.44, 122.76, 123.56, 124.53, 126.38, 128.76, 128.94, 129.21, 129.50, 130.27, 136.09, 137.23, 147.50, 148.60, 160.66, 163.07, 164.89 ppm. IR (ATR): ν = 3033, 1562, 1506, 1279, 1248, 1031, 972, 808, 752, 695 cm^{-1}. HR-MALDI-MS (DCTB): *m/z* calculated for $C_{42}H_{35}N_3O_2$ [M^+] 613.2724, found 613.2728.

232l (*E,E,E*)-2-(4-*N,N*-diphenylaminostyryl)-4,6-bis(4-*N,N*-dimethylaminostyryl)pyrimidine

$C_{44}H_{41}N_5$

MW = 639.83

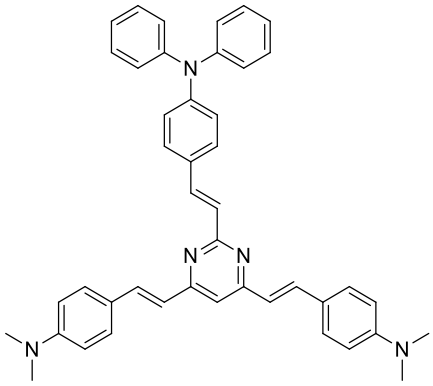

Compound **232l** was synthesized from **230d** (70 mg, 0.19 mmol) and 4-*N*,*N*-dimethylaminobenzaldehyde (56 mg, 0.37 mmol) following the method B. The crude product was purified by column chromatography (SiO_2, petroleum ether:EtOAc, 8:2) and then by recrystallization from CH_2Cl_2/*n*-heptane. Yield: 62 mg (52 %); yellow solid. R_f: 0.5 (SiO_2; petroleum ether:EtOAc, 8:2). T_d: 195 °C. ^{1}H NMR (300 MHz, $CDCl_3$): δ = 3.03 (s, 12H), 6.71–

6.74 (m, 4H), 6.90 (d, $^{3}J_{H\text{-}H}$ = 15.9 Hz, 2H), 7.03–7.08 (m, 5H), 7.13–7.19 (m, 5H), 7.28–7.31 (m, 4H), 7.52–7.55 (m, 6H), 7.83 (d, $^{3}J_{H\text{-}H}$ = 15.9 Hz, 2H), 8.03 (d, $^{3}J_{H\text{-}H}$ = 15.9 Hz, 1H) ppm. ^{13}C NMR (75 MHz, $CDCl_3$): δ = 40.41, 112.03, 112.24, 122.11, 122.86, 123.46, 124.31, 125.07, 126.79, 128.72, 129.17, 129.48, 130.53, 136.60, 136.77, 147.55, 148.41, 151.15, 163.31, 164.71 ppm. IR (ATR): ν = 2853, 1602, 1553, 1492, 1358, 1276, 974, 808, 751, 696 cm^{-1}. HR-MALDI-MS (DCTB): *m/z* calculated for $C_{44}H_{41}N_5$ [M^+] 639.3357, found 639.3359.

232m (*E,E,E*)-2,4,6-tris(4-*N,N*-diphenylaminostyryl)pyrimidine

$C_{64}H_{49}N_5$

MW = 888.11

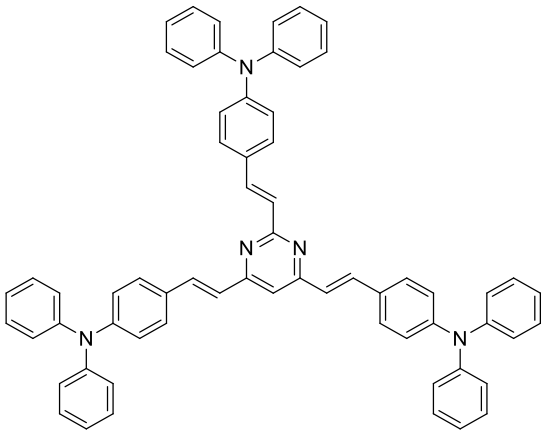

Compound **232m** was synthesized from **230d** (33 mg, 0.09 mmol) and 4-*N*,*N*-diphenylaminobenzaldehyde (48 mg, 0.17 mmol) following the method B. The crude product was purified by recrystallization from CH_2Cl_2/*n*-heptane. Yield: 44 mg (57 %); yellow solid. R_f: 0.8 (SiO_2; petroleum ether:EtOAc, 8:2). T_d: 310 °C. ^{1}H NMR (300 MHz, $CDCl_3$): δ = 6.97 (d, $^{3}J_{H\text{-}H}$ = 15.9 Hz, 2H), 7.04–7.20 (m, 26H), 7.27–7.32 (m, 12H), 7.47–7.55 (m, 6H), 7.85 (d, $^{3}J_{H\text{-}H}$ = 15.9 Hz, 2H), 8.04 (d, $^{3}J_{H\text{-}H}$ = 15.9 Hz, 1H) ppm. ^{13}C NMR (75 MHz, $CDCl_3$): δ = 112.70, 122.57, 122.76, 123.54, 123.75, 124.35, 124.57, 125.11, 125.23, 126.42, 128.74, 129.49, 129.54, 129.65, 130.28, 135.99, 137.20, 147.35, 147.49, 148.58, 148.95, 163.05, 164.90 ppm. IR (ATR): ν = 3034, 1588, 1558, 1489, 1273, 1174, 970, 750, 693 cm^{-1}. HR-MALDI-MS (DCTB): *m/z* calculated for $C_{64}H_{49}N_5$ [M^+] 887.3983, found 887.3982.

232n (*E,E,E*)-2-[(6-methoxynaphtalen-2-yl)ethenyl]-4,6-bis(4-methoxystyryl)pyrimidine

$C_{35}H_{30}N_2O_3$

MW = 526.62

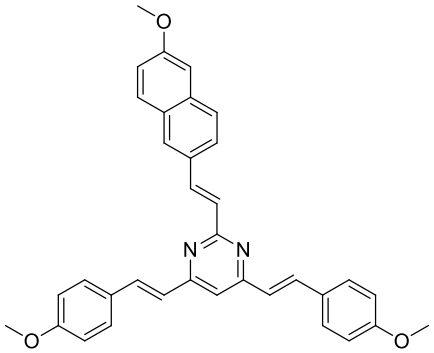

Compound **232n** was synthesized from **230e** (56 mg, 0.19 mmol) and 4-methoxybenzaldehyde (52 mg, 0.38 mmol) following the method B. The crude product was purified by recrystallization from CH_2Cl_2/*n*-heptane. Yield: 77 mg (77 %); yellowish solid. R_f: 0.3 (SiO_2; petroleum ether:EtOAc, 8:2). T_d: 290 °C. ^{1}H NMR (300 MHz, $CDCl_3$): δ = 3.86 (s, 6H), 3.94 (s, 3H), 6.94–7.19 (m, 9H), 7.38 (d, $^3J_{H\text{-}H}$ = 15.9 Hz, 1H), 7.59–7.61 (m, 4H), 7.74–7.98 (m, 6H), 8.24 (d, $^3J_{H\text{-}H}$ = 15.9 Hz, 1H) ppm. ^{13}C NMR (75 MHz, $CDCl_3$): δ = 55.51, 106.14, 113.09, 114.46, 119.23, 124.46, 124.78, 127.39, 127.80, 128.58, 128.95, 129.14, 129.24, 130.05, 132.07, 135.08, 136.18, 137.88, 158.40, 160.69, 163.12, 164.73 ppm. IR (ATR): ν = 2935, 1601, 1559, 1505, 1366, 1246, 1169, 1027, 959, 838, 809 cm^{-1}. HR-MALDI-MS (DCTB): *m/z* calculated for $C_{35}H_{30}N_2O_3$ [M^+] 526.2251, found 526.2252.

232o (*E,E,E*)-2-[(6-methoxynaphtalen-2-yl)ethenyl]-4,6-bis(4-*N,N*-dimethylaminostyryl)pyrimidine

$C_{37}H_{36}N_4O$

MW = 552.71

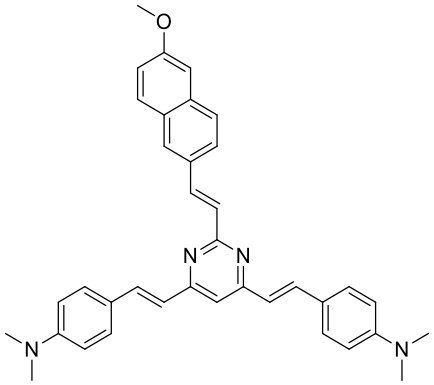

Compound **232o** was synthesized from **230e** (53 mg, 0.18 mmol) and 4-*N*,*N*-dimethylaminobenzaldehyde (54 mg, 0.36 mmol) following the method B. The crude product was purified by recrystallization from CH_2Cl_2/*n*-heptane. Yield: 70 mg (70 %); orange solid. R_f: 0.2 (SiO_2; petroleum ether:EtOAc, 8:2). T_d: 250 °C. ^{1}H NMR (300 MHz, $CDCl_3$): δ = 3.03 (s, 12H), 3.94 (s, 3H), 6.72–6.75 (m, 4H), 6.92 (d, $^3J_{H\text{-}H}$ = 15.9 Hz, 2H), 7.07–7.18 (m, 3H),

7.38 (d, $^{3}J_{H-H}$ = 15.9 Hz, 1H), 7.54–7.57 (m, 4H), 7.74–7.90 (m, 5H), 7.99 (s, 1H), 8.23 (d, $^{3}J_{H-H}$ = 15.9 Hz, 1H) ppm. ^{13}C NMR (75 MHz, $CDCl_3$): δ = 40.38, 55.49, 106.12, 112.24, 112.35, 119.13, 122.02, 124.30, 124.85, 127.32, 128.18, 128.44, 129.19, 130.03, 132.25, 134.97, 136.67, 137.39, 151.16, 158.30, 163.35, 164.54 ppm. Not all carbon atoms were observed. IR (ATR): ν = 2853, 1600, 1552, 1357, 1144, 969, 851, 804 cm^{-1}. HR-MALDI-MS (DCTB): *m/z* calculated for $C_{37}H_{36}N_4O$ [M^+] 552.2884, found 552.2889.

232p (*E,E,E*)-2-[(6-methoxynaphtalen-2-yl)ethenyl]-4,6-bis(4-*N,N*-diphenylaminostyryl)pyrimidine

$C_{57}H_{44}N_4O$

MW = 552.71

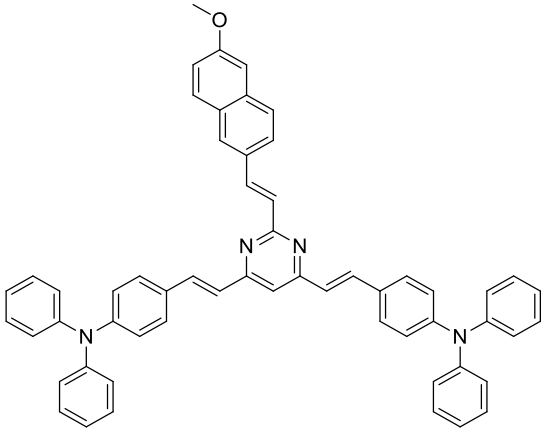

Compound **232p** was synthesized from **230e** (37 mg, 0.12 mmol) and 4-*N*,*N*-diphenylaminobenzaldehyde (69 mg, 0.25 mmol) following the method B. The crude product was purified by recrystallization from CH_2Cl_2/*n*-heptane. Yield: 30 mg (30 %); orange solid. R_f: 0.6 (SiO_2; petroleum ether:EtOAc, 8:2). T_d: 220 °C. ^{1}H NMR (300 MHz, $CDCl_3$): δ = 3.94 (s, 3H), 6.97–7.17 (m, 22H), 7.28–7.40 (m, 8H), 7.49–7.52 (m, 4H), 7.74–7.79 (m, 2H), 7.84–7.92 (m, 3H), 7.98 (s, 1H), 8.23 (d, $^{3}J_{H-H}$ = 15.9 Hz, 1H) ppm. ^{13}C NMR (75 MHz, $CDCl_3$): δ = 55.50, 106.12, 113.03, 119.21, 122.57, 123.76, 124.49, 124.78, 125.25, 127.37, 127.83, 128.57, 128.76, 129.13, 129.55, 129.64, 130.04, 132.07, 135.06, 136.07, 137.83, 147.38, 148.98, 158.39, 163.10, 164.76 ppm. IR (ATR): ν = 3034, 1588, 1558, 1490, 1268, 1174, 969, 849, 751, 694 cm^{-1}. HR-MALDI-MS (DCTB): *m/z* calculated for $C_{57}H_{44}N_4O$ [M^+] 800.3510, found 800.3518.

232q (*E,E,E*)-2-(4-trifluoromethylstyryl)-4,6-bis(4-methoxystyryl)pyrimidine

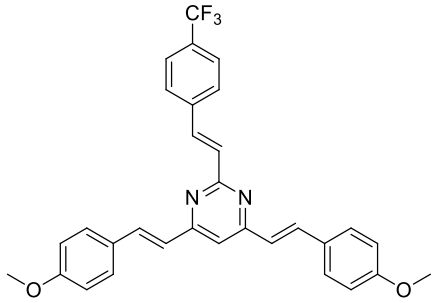

$C_{31}H_{25}F_3N_2O_2$

MW = 514.54

Compound **232q** was synthesized from **230f** (90 mg, 0.32 mmol) and 4-methoxybenzaldehyde (88 mg, 0.65 mmol) following the method B. The crude product was purified by column chromatography (SiO_2, petroleum ether:EtOAc, 7:3). Yield: 71 mg (43 %); yellowish solid. R_f: 0.7 (SiO_2; petroleum ether:EtOAc, 7:3). T_d: 280 °C. ^{1}H NMR (300 MHz, $CDCl_3$): δ = 3.86 (s, 6H), 6.94–7.02 (m, 6H), 7.13 (s, 1H), 7.38 (d, $^3J_{H\text{-}H}$ = 15.9 Hz, 1H), 7.58–7.61 (m, 4H), 7.65–7.68 (m, 2H), 7.76–7.79 (m, 2H), 7.91 (d, $^3J_{H\text{-}H}$ = 15.9 Hz, 2H), 8.11 (d, $^3J_{H\text{-}H}$ = 15.9 Hz, 1H) ppm. ^{13}C NMR (75 MHz, $CDCl_3$): δ = 55.51, 113.62, 114.50, 124.17, 124.29 (q, $^1J_{C\text{-}F}$ = 270 Hz), 125.83 (q, $^3J_{C\text{-}F}$ = 4 Hz), 127.82, 128.81, 129.28, 130.43 (q, $^2J_{C\text{-}F}$ = 32 Hz), 131.07, 135.81, 136.48, 140.07, 160.80, 163.24, 163.95 ppm. IR (ATR): ν = 2838, 1568, 1325, 1251, 1107, 976, 818 cm^{-1}. HR-MALDI-MS (DCTB): *m/z* calculated for $C_{31}H_{25}F_3N_2O_2$ [M^+] 514.1863, found 514.1861.

232r (*E,E,E*)-2-(4-trifluoromethylstyryl)-4,6-bis(4-*N,N*-dimethylaminostyryl)pyrimidine

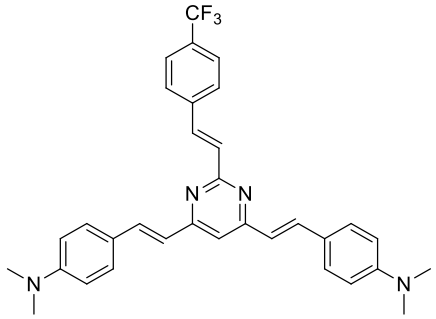

$C_{33}H_{31}F_3N_4$

MW = 540.62

Compound **232r** was synthesized from **230f** (90 mg, 0.32 mmol) and 4-*N*,*N*-dimethylaminobenzaldehyde (97 mg, 0.65 mmol) following the method B. The crude product was purified by column chromatography (SiO_2, petroleum ether:EtOAc, 8:2). Yield: 69 mg (40 %); orange solid. R_f: 0.3 (SiO_2; petroleum ether:EtOAc, 8:2). Mp: 210 °C. ^{1}H NMR (300 MHz, $CDCl_3$): δ = 3.04 (s, 12H), 6.72–6.75 (m, 4H), 6.91 (d, $^3J_{H\text{-}H}$ = 15.9 Hz, 2H), 7.10 (s, 1H), 7.37 (d, $^3J_{H\text{-}H}$ = 15.9 Hz, 1H), 7.53–7.56 (m, 4H), 7.64–7.67 (m, 2H), 7.76–7.79 (m, 2H), 7.86 (d, $^3J_{H\text{-}H}$ = 15.9 Hz, 2H), 8.09 (d, $^3J_{H\text{-}H}$ = 15.9 Hz, 1H) ppm. ^{13}C NMR (75 MHz, $CDCl_3$): δ = 40.39,

112.22, 112.88, 121.69, 124.14, 124.33 (q, $^{1}J_{C\text{-}F}$ = 270 Hz), 125.78 (q, $^{3}J_{C\text{-}F}$ = 4 Hz), 127.78, 129.24, 130.24 (q, $^{2}J_{C\text{-}F}$ = 32 Hz), 131.42, 135.37, 136.97, 140.24, 151.24, 163.46, 163.78 ppm. IR (ATR): ν = 2892, 1494, 1318, 1116, 1065, 974, 809 cm^{-1}. HR-MALDI-MS (DCTB): *m/z* calculated for $C_{33}H_{31}F_3N_4$ [M$^+$] 540.2495, found 540.2501.

232s (*E,E,E*)-2-(4-trifluoromethylstyryl)-4,6-bis(4-*N,N*-dimethylaminostyryl)pyrimidine

$C_{53}H_{39}F_3N_4$

MW = 788.90

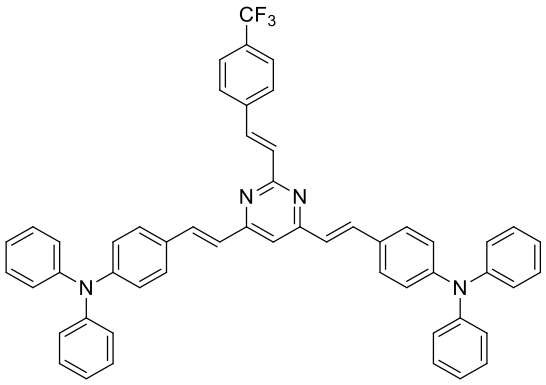

Compound **232s** was synthesized from **230f** (90 mg, 0.32 mmol) and 4-*N*,*N*-diphenylaminobenzaldehyde (177 mg, 0.65 mmol) following the method B. The crude product was purified by column chromatography (SiO_2, petroleum ether:EtOAc, 9:1). Yield: 70 mg (28 %); yellow solid. R_f: 0.7 (SiO_2; petroleum ether:EtOAc, 9:1). T_d: 300 °C. ^{1}H NMR (300 MHz, $CDCl_3$): δ = 7.00 (d, $^{3}J_{H\text{-}H}$ = 15.9 Hz, 2H), 7.08–7.19 (m, 18H), 7.30–7.43 (m, 8H), 7.50–7.53 (m, 4H), 7.66–7.69 (m, 2H), 7.78–7.80 (m, 2H), 7.90 (d, $^{3}J_{H\text{-}H}$ = 15.9 Hz, 2H), 8.12 (d, $^{3}J_{H\text{-}H}$ = 15.9 Hz, 1H) ppm. ^{13}C NMR (75 MHz, $CDCl_3$): δ = 113.57, 123.83, 124.03, 124.14, 124.50 (q, $^{1}J_{C\text{-}F}$ = 276 Hz), 125.28, 125.80 (q, $^{3}J_{C\text{-}F}$ = 4 Hz), 127.79, 128.79, 129.41, 129.56, 130.36 (q, $^{2}J_{C\text{-}F}$ = 32 Hz), 131.11, 135.72, 136.32, 140.05 (q, $^{4}J_{C\text{-}F}$ = 1 Hz), 147.29, 149.08, 163.16, 163.91 ppm. IR (ATR): ν = 3033, 1559, 1490, 1320, 1066, 968, 751 cm^{-1}. HR-MALDI-MS (DCTB): *m/z* calculated for $C_{53}H_{39}F_3N_4$ [M$^+$] 788.3121, found 788.3111.

233a (*E*)-2-chloro-4-(4-*N,N*-dimethylaminostyryl)-6-methylpyrimidine

$C_{15}H_{16}ClN_3$

MW = 273.76

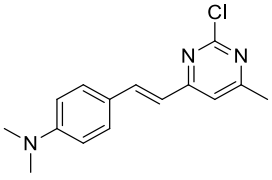

Compound **233a** was synthesized from 4-ethynyl-*N*,*N*-dimethylaniline (250 mg, 1.72 mmol) and 2,4-dichloro-6-methylpyrimidine (179 mg, 1.1 mmol) following the method A. The crude product was purified by column chromatography (SiO_2, petroleum ether:EtOAc, 8:2). Yield: 156 mg (52 %); brown solid. R_f: 0.4 (SiO_2; petroleum ether:EtOAc, 8:2). Mp: 163.4–

165.7 °C. ^{1}H NMR (300 MHz, $CDCl_3$): δ = 2.49 (s, 3H), 3.03 (s, 6H), 6.68–6.78 (m, 3H), 6.99 (s, 1H), 7.47–7.50 (m, 2H), 7.83 (d, $^{3}J_{H\text{-}H}$ = 15.9 Hz, 1H) ppm. ^{13}C NMR (75 MHz, $CDCl_3$): δ = 24.04, 40.30, 112.12, 115.63, 119.24, 123.31, 129.64, 139.55, 151.63, 161.09, 166.25, 169.95 ppm. IR (ATR): ν = 2913, 2193, 1566, 1258, 979, 809, 750, 765 cm^{-1}. HR-MALDI-MS (DCTB): *m/z* calculated for $C_{15}H_{16}ClN_3$ [M^+] 273.1027, found 273.1023.

233b (*E*)-2-chloro-4-(4-methoxystyryl)-6-methylpyrimidine

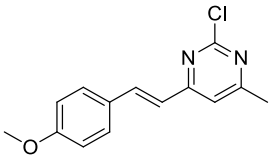

$C_{14}H_{13}ClN_2O$

MW = 260.72

Compound **233b** was synthesized from 4-ethynylanisole (311 mg, 2.35 mmol) and 2,4-dichloro-6-methylpyrimidine (245 mg, 1.5 mmol) following the method A. The crude product was purified by column chromatography (SiO_2, petroleum ether:EtOAc, 7:3). Yield: 215 mg (55 %); yellowish solid. R_f: 0.4 (SiO_2; petroleum ether:EtOAc, 7:3). Mp: 78.9–81.8 °C. ^{1}H NMR (300 MHz, $CDCl_3$): δ = 2.51 (s, 3H), 3.85 (s, 3H), 6.83 (d, $^{3}J_{H\text{-}H}$ = 15.9 Hz, 1H), 6.90–6.95 (m, 2H), 7.04 (s, 1H), 7.51–7.56 (m, 2H), 7.86 (d, $^{3}J_{H\text{-}H}$ = 15.9 Hz, 1H) ppm. ^{13}C NMR (75 MHz, $CDCl_3$): δ = 24.08, 55.53, 114.56, 116.24, 122.03, 128.17, 129.58, 138.70, 161.18, 161.21, 165.61, 170.54 ppm. IR (ATR): ν = 2924, 1570, 1512, 1256, 1178, 1020, 967, 819 cm^{-1}. HR-MALDI-MS (DCTB): *m/z* calculated for $C_{14}H_{13}ClN_2O$ [M^+] 260.0711, found 260.0710.

234a (*E,E*)-2-(4-methoxystyryl)-4-(4-*N,N*-dimethylaminostyryl)-6-methylpyrimidine

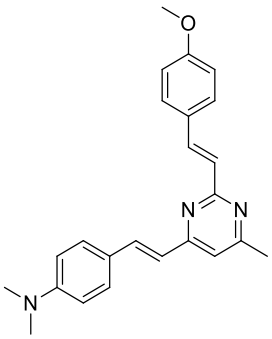

$C_{24}H_{25}N_3O$

MW = 371.47

Compound **234a** was synthesized from 4-ethynylanisole (91 mg, 0.69 mmol) and **233a** (120 mg, 0.44 mmol) following the method A. The crude product was purified by column chromatography (SiO_2, petroleum ether:EtOAc, 7:3). Yield: 65 mg (40 %); orange solid. R_f: 0.3 (SiO_2; petroleum ether:EtOAc, 7:3). Mp: 79.9–81.5 °C. ^{1}H NMR (300 MHz, $CDCl_3$): δ = 2.51 (s, 3H), 3.02 (s, 6H), 3.84 (s, 3H), 6.70–6.73 (m, 2H), 6.83–6.94 (m, 4H), 7.13 (d, $^{3}J_{H\text{-}H}$ = 15.9 Hz, 1H), 7.50–7.53 (m, 2H), 7.58–7.61 (m, 2H), 7.81 (d, $^{3}J_{H\text{-}H}$ = 15.9 Hz, 1H), 7.99 (d,

$^{3}J_{H\text{-}H}$ = 15.9 Hz, 1H) ppm. ^{13}C NMR (75 MHz, $CDCl_3$): δ = 24.34, 40.37, 55.45, 112.20, 114.30, 114.42, 121.59, 124.10, 126.10, 129.14, 129.18, 129.38, 137.08, 151.22, 160.35, 163.16, 164.61, 166.67 ppm. Not all carbon atoms were observed. IR (ATR): ν = 2922, 1602, 1509, 1352, 1242, 1169, 973, 809 cm^{-1}. HR-MALDI-MS (DCTB): *m/z* calculated for $C_{24}H_{25}N_3O$ [M^+] 371.1992, found 371.1988.

234b (*E,E*)-2-(4-*N,N*-dimethylaminostyryl)-4-(4-methoxystyryl)-6-methylpyrimidine

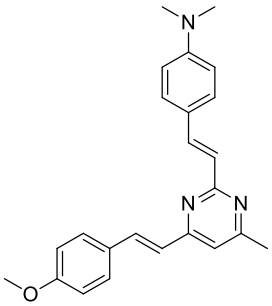

$C_{24}H_{25}N_3O$

MW = 371.47

Compound **234b** was synthesized from 4-ethynyl-*N*,*N*-dimethylaniline (155 mg, 1.06 mmol) and **233b** (177 mg, 0.68 mmol) following the method A. The crude product was purified by column chromatography (SiO_2, petroleum ether:EtOAc, 7:3). Yield: 190 mg (75 %); brown solid. R_f: 0.2 (SiO_2; petroleum ether:EtOAc, 7:3). Mp: 123.5–125.7 °C. ^{1}H NMR (300 MHz, $CDCl_3$): δ = 2.52 (s, 3H), 3.01 (s, 6H), 3.84 (s, 3H), 6.70–6.73 (m, 2H), 6.90–6.95 (m, 4H), 7.07 (d, $^{3}J_{H\text{-}H}$ = 15.9 Hz, 1H), 7.54–7.58 (m, 4H), 7.83 (d, $^{3}J_{H\text{-}H}$ = 15.9 Hz, 1H), 7.99 (d, $^{3}J_{H\text{-}H}$ = 15.9 Hz, 1H) ppm. ^{13}C NMR (75 MHz, $CDCl_3$): δ = 24.37, 40.40, 55.47, 112.22, 114.34, 114.40, 123.30, 124.45, 124.62, 128.94, 129.14, 136.03, 138.13, 151.01, 160.59, 162.46, 165.20, 166.94 ppm. Not all carbon atoms were observed. IR (ATR): ν = 2918, 1599, 1509, 1351, 1249, 1162, 970, 808 cm^{-1}. HR-MALDI-MS (DCTB): *m/z* calculated for $C_{24}H_{25}N_3O$ [M^+] 371.1992, found 371.1993.

235a (*E,E,E*)-2-(4-methoxystyryl)-4-(4-*N,N*-dimethylaminostyryl)-6-(4-*N,N*-diphenylaminostyryl)pyrimidine

$C_{43}H_{38}N_4O$

MW = 626.79

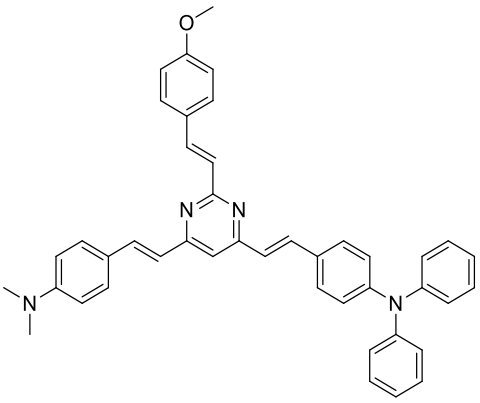

Compound **235a** was synthesized from **234a** (45 mg, 0.12 mmol) and 4-*N*,*N*-diphenylaminobenzaldehyde (33 mg, 0.12 mmol) following the method B. The crude product was purified by column chromatography (SiO_2, petroleum ether:EtOAc, 8:2). Yield: 46 mg (61 %); orange solid. R_f: 0.5 (SiO_2; petroleum ether:EtOAc, 8:2). T_d: 240 °C. ^{1}H NMR (300 MHz, $CDCl_3$): δ = 3.03 (s, 6H), 3.85 (s, 3H), 6.71–6.74 (m, 2H), 6.88–7.20 (m, 14H), 7.27–7.32 (m, 4H), 7.48–7.55 (m, 4H), 7.62–7.65 (m, 2H), 7.85 (d, $^3J_{H\text{-}H}$ = 15.9 Hz, 2H), 8.05 (d, $^3J_{H\text{-}H}$ = 15.9 Hz, 1H) ppm. ^{13}C NMR (75 MHz, $CDCl_3$): δ = 40.40, 55.47, 112.23, 112.49, 114.31, 121.88, 122.64, 123.71, 124.21, 124.74, 125.21, 126.51, 128.71, 129.18, 129.22, 129.50, 129.54, 129.80, 135.73, 136.92, 137.04, 147.40, 148.87, 151.22, 160.32, 162.75, 163.63, 164.77 ppm. IR (ATR): ν = 2925, 1561, 1490, 1247, 1170, 1144, 971, 694 cm^{-1}. HR-MALDI-MS (DCTB): *m/z* calculated for $C_{43}H_{38}N_4O$ [M^+] 626.3040, found 626.3038.

235b (E,E,E)-2-(4-*N,N*-dimethylaminostyryl)-4-(4-methoxystyryl)-6-(4-*N,N*-diphenylaminostyryl)pyrimidine

$C_{43}H_{38}N_4O$

MW = 626.79

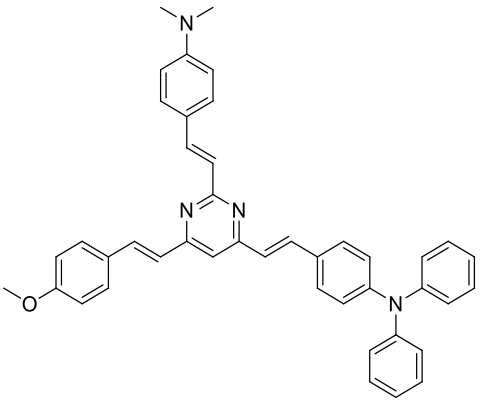

Compound **235b** was synthesized from **234b** (150 mg, 0.40 mmol) and 4-*N*,*N*-diphenylaminobenzaldehyde (110 mg, 0.40 mmol) following the method B. The crude product

was purified by column chromatography (SiO_2, petroleum ether:EtOAc, 7:3). Yield: 84 mg (33 %); orange solid. R_f: 0.5 (SiO_2; petroleum ether:EtOAc, 7:3). T_d: 210 °C. ^{1}H NMR (300 MHz, $CDCl_3$): δ = 3.02 (s, 6H), 3.85 (s, 3H), 6.72–6.75 (m, 2H), 6.93–7.16 (m, 14H), 7.27–7.32 (m, 4H), 7.48–7.51 (m, 2H), 7.57–7.60 (m, 4H), 7.82–7.90 (m, 2H), 8.05 (d, $^3J_{H-H}$ = 15.9 Hz, 1H) ppm. ^{13}C NMR (75 MHz, $CDCl_3$): δ = 40.44, 55.50, 112.26, 112.33, 114.43, 122.63, 123.72, 124.18, 124.36, 124.74, 124.78, 125.22, 128.40, 128.72, 129.05, 129.19, 129.37, 129.54, 129.77, 135.87, 138.09, 147.39, 148.90, 151.01, 160.60, 162.95, 163.03, 165.37 ppm. IR (ATR): ν = 2921, 1500, 1359, 1248, 1166, 971, 809, 693 cm^{-1}. HR-MALDI-MS (DCTB): *m/z* calculated for $C_{43}H_{38}N_4O$ [M^+] 626.3040, found 626.3058.

239 2-[4-(9,9-dimethyl-9,10-dihydroacridine)phenyl]-4-methypyrimidine

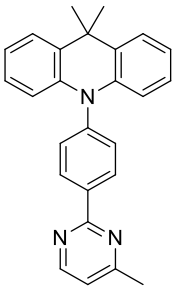

$C_{26}H_{23}N_3$

MW = 377.48

Compound **239** was synthesized from 2-chloro-4-methylpyrimidine (83 mg, 0.64 mmol) and boronic acid pinacol ester **238** (265 mg, 0.64 mmol) following the method C. Yield 138 mg (57 %); pale yellow solid; R_f = 0.2 (SiO_2; hexane/EtOAc 9:1); ^{1}H NMR (400 MHz, $CDCl_3$) δ = 8.71 (d, $^3J_{H-H}$ = 5 Hz, 1H), 8.69–8.67 (m, 2H), 7.48–7.46 (m, 4H), 7.13 (d, $^3J_{H-H}$ = 5 Hz, 1H), 6.99–6.91 (m, 4H), 6.36–6.34 (m, 2H), 2.64 (s, 3H), 1.71 (s, 6H) ppm. ^{13}C NMR (125 MHz, $CDCl_3$) δ = 167.69, 164.00, 157.13, 143.48, 140.82, 137.95, 131.63, 130.92, 130.11, 126.50, 125.40, 120.74, 119.04, 114.24, 36.11, 31.46, 24.62 ppm. HR-MALDI-MS (DCTB) *m/z* calcd for $C_{25}H_{20}N_3$ [M-CH_3^+] 362.1652, found 362.1640.

240 2-[4-(9,9-dimethyl-9,10-dihydroacridine)phenyl]-4,6-dimethypyrimidine

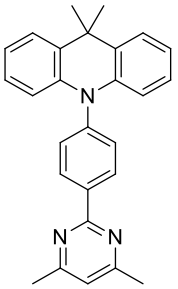

$C_{27}H_{25}N_3$

MW = 391.51

Compound **240** was synthesized from 2-chloro-4,6-dimethylpyrimidine (111 mg, 0.78 mmol) and boronic acid pinacol ester **238** (321 mg, 0.78 mmol) following the method C. Yield 166 mg (54 %); pale yellow solid; R_f = 0.3 (SiO_2; hexane/EtOAc 9:1); ^{1}H NMR (400 MHz, $CDCl_3$) δ = 8.73–8.71 (m, 2H), 7.54–7.51 (m, 4H), 7.07 (s, 1H), 7.04–6.97 (m, 4H), 6.42–6.40 (m, 2H), 2.66 (s, 6H), 1.78 (s, 6H) ppm. ^{13}C NMR (125 MHz, $CDCl_3$) δ = 167.21, 163.87, 143.22, 131.58, 130.99, 130.04, 126.49, 125.40, 120.69, 118.42, 114.26, 36.11, 31.52, 24.36 ppm. HR-MALDI-MS (DCTB) *m/z* calcd for $C_{26}H_{22}N_3$ [M-CH_3^+] 376.1808, found 376.1796.

241a (*E*)-2-[4-(9,9-dimethyl-9,10-dihydroacridine)phenyl]-4-[(4-methoxyphenyl)ethenyl]pyrimidine

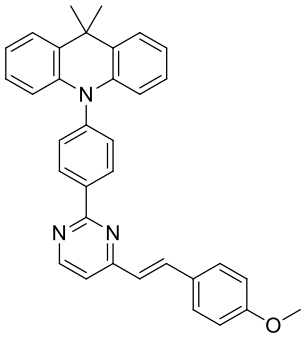

$C_{34}H_{29}N_3O$

MW = 495.61

Compound **241a** was synthesized from compound **239** (138 mg, 0.36 mmol) and 4-methoxybenzaldehyde (50 mg, 0.36 mmol) following the method B. The crude product was purified by recrystallization. Yield 126 mg (70 %); yellowish solid; R_f = 0.5 (SiO_2; CH_2Cl_2); mp: 204°C. ^{1}H NMR (500 MHz, $CDCl_3$) δ = 8.78–8.75 (m, 3H), 8.02 (d, $^3J_{H\text{-}H}$ = 16 Hz, 1H), 7.63–7.61 (m, 2H), 7.50–7.47 (m, 4H), 7.23–7.22 (m, 1H), 7.04 (d, $^3J_{H\text{-}H}$ = 16 Hz, 1H), 6.99–6.93 (m, 6H), 6.38–6.37 (m, 2H), 3.87 (s, 3H), 1.72 (s, 6H) ppm. ^{13}C NMR (125 MHz, $CDCl_3$) δ = 163.95, 163.09, 160.89, 157.81, 143.49, 140.85, 138.12, 137.14, 131.60, 130.99, 130.12, 129.41, 128.57, 126.53, 125.40, 123.79, 120.74, 116.53, 114.49, 114.27, 55.54, 36.13, 31.46 ppm. HR-MALDI-MS (DCTB) *m/z* calcd for $C_{33}H_{26}N_3O$ [M-CH_3^+] 480.2070, found 480.2058.

241b (*E*)-2-[4-(9,9-dimethyl-9,10-dihydroacridine)phenyl]-4-[(6-methoxynaphtalen-2-yl)ethenyl]pyrimidine

$C_{38}H_{31}N_3O$

MW = 545.67

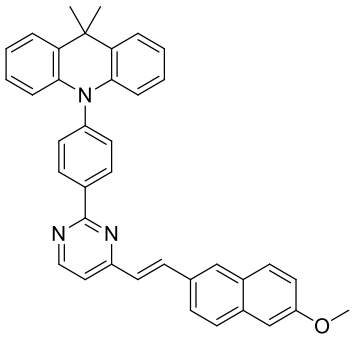

Compound **241b** was synthesized from compound **239** (102 mg, 0.27 mmol) and 6-methoxy-2-naphtalenaldehyde (51 mg, 0.27 mmol) following the method B. The crude product was purified by column chromatography (hexane/EtOAc 7:3). Yield 109 mg (74 %); yellowish solid; R_f = 0.5 (SiO_2; hexane/EtOAc 7:3); mp: 199 °C. ^{1}H NMR (400 MHz, $CDCl_3$) δ = 8.81–8.78 (m, 3H), 8.20 (d, $^3J_{H\text{-}H}$ = 16 Hz, 1H), 7.99 (br s, 1H), 7.83–7.77 (m, 3H), 7.52–7.47 (m, 4H), 7.28–7.16 (m, 4H), 7.01–6.93 (m, 4H), 6.41–6.38 (m, 2H), 3.95 (s, 3H), 1.73 (s, 6H) ppm. ^{13}C NMR (100 MHz, $CDCl_3$) δ = 164.02, 162.96, 158.72, 157.92, 143.60, 140.89, 138.11, 137.76, 135.40, 131.61, 131.25, 131.03, 130.18, 130.13, 129.13, 129.05, 127.62, 126.54, 125.40, 125.26, 124.42, 120.77, 119.53, 116.69, 114.31, 106.16, 55.53, 36.15, 31.47 ppm. HR-MALDI-MS (DCTB) *m/z* calcd for $C_{37}H_{28}N_3O$ [M-CH_3^+] 530.2227, found 530.2221.

241c (*E*)-2-[4-(9,9-dimethyl-9,10-dihydroacridine)phenyl]-4-[(4-*N,N*-diphenylaminophenyl)ethenyl]pyrimidine

$C_{45}H_{36}N_4$

MW = 632.79

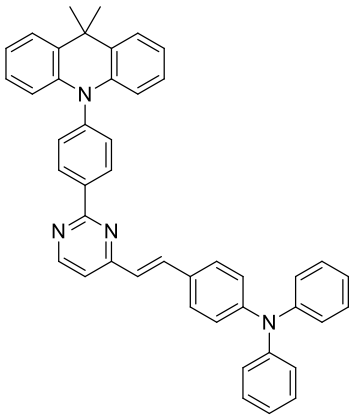

Compound **241c** was synthesized from compound **239** (228 mg, 0.60 mmol) and 4-diphenylaminobenzaldehyde (164 mg, 0.60 mmol) following the method B. The crude product was purified by column chromatography (CH_2Cl_2). Yield 182 mg (48 %); yellow solid; R_f = 0.8 (SiO_2; CH_2Cl_2); mp: 375 °C (dec.). ^{1}H NMR (400 MHz, $CDCl_3$) δ = 8.87–8.84 (m, 3H),

8.09 (d, $^{3}J_{H\text{-}H}$ = 16 Hz, 1H), 7.61–7.56 (m, 6H), 7.41–7.01 (m, 18H), 6.49–6.47 (m, 2H), 1.81 (s, 6H) ppm. ^{13}C NMR (100 MHz, $CDCl_3$) δ = 163.92, 163.08, 157.70, 149.22, 147.21, 143.50, 140.85, 138.13, 137.04, 131.53, 130.97, 130.13, 129.56, 129.16, 128.90, 126.51, 125.35, 123.86, 123.76, 122.38, 120.74, 116.43, 114.28, 36.10, 31.44 ppm. HR-MALDI-MS (DCTB) *m/z* calcd for $C_{44}H_{33}N_4$ [M-CH_3^+] 617.2700, found 617.2689.

242a (*E,E*)-2-[4-(9,9-dimethyl-9,10-dihydroacridine)phenyl]-4,6-bis[(4-methoxyphenyl)ethenyl]pyrimidine

$C_{43}H_{37}N_3O_2$

MW = 627.77

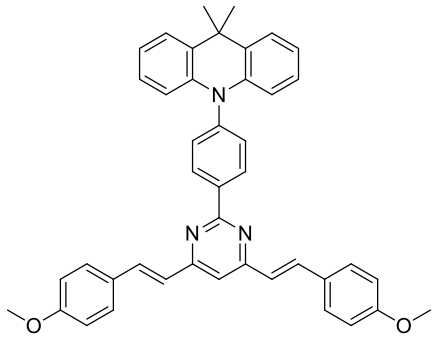

Compound **242a** was synthesized from compound **230** (158 mg, 0.40 mmol) and 4-methoxybenzaldehyde (110 mg, 0.81 mmol) following the method B. The crude product was purified by recrystallization. Yield 186 mg (73 %); yellow solid; R_f = 0.4 (SiO_2; CH_2Cl_2); mp: 201 °C. ^{1}H NMR (500 MHz, $CDCl_3$) δ = 8.85–8.83 (m, 2H), 8.04 (d, $^{3}J_{H\text{-}H}$ = 16 Hz, 2H), 7.63–7.62 (m, 4H), 7.52–7.48 (m, 4H), 7.19 (s, 1H), 7.06 (d, $^{3}J_{H\text{-}H}$ = 16 Hz, 2H), 7.00–6.93 (m, 8H), 6.41–6.39 (m, 2H), 3.87 (s, 6H), 1.73 (s, 6H) ppm. ^{13}C NMR (125 MHz, $CDCl_3$) δ = 163.69, 163.45, 160.74, 143.27, 140.90, 138.60, 136.50, 131.49, 131.17, 130.07, 129.33, 128.80, 126.53, 125.40, 124.20, 120.70, 114.46, 114.33, 114.17, 55.52, 36.13, 31.51 ppm. HR-MALDI-MS (DCTB) *m/z* calcd for $C_{42}H_{34}N_3O_2$ [M-CH_3^+] 612.2646, found 612.2637.

242b (*E,E*)-2-[4-(9,9-dimethyl-9,10-dihydroacridine)phenyl]-4,6-bis[(6-methoxynaphtalen-2-yl)ethenyl]pyrimidine

$C_{51}H_{41}N_3O_2$

MW = 727.89

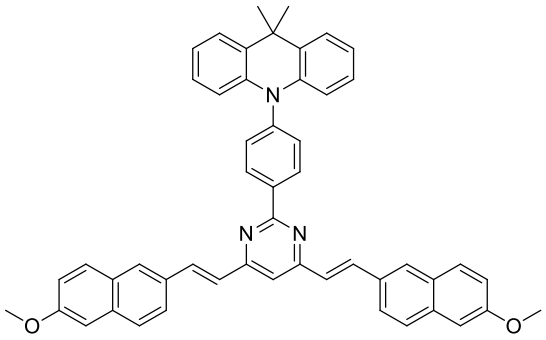

Compound **242b** was synthesized from compound **240** (100 mg, 0.26 mmol) and 6-methoxy-2-naphtalenaldehyde (96 mg, 0.51 mmol) following the method B. The crude product was purified by recrystallization. Yield 133 mg (72 %); yellow solid; R_f = 0.3 (SiO_2; hexane/EtOAc 8:2); mp: 271 °C. ^{1}H NMR (500 MHz, $CDCl_3$) δ = 8.90–8.88 (m, 2H), 8.22 (d, $^3J_{H\text{-}H}$ = 16 Hz, 2H), 7.99 (s, 2H), 7.84–7.77 (m, 6H), 7.54–7.49 (m, 4H), 7.27–7.24 (m, 3H), 7.19–7.15 (m, 4H), 7.02–6.94 (m, 4H), 6.44–6.42 (m, 2H), 3.94 (s, 6H), 1.74 (s, 6H) ppm. ^{13}C NMR (125 MHz, $CDCl_3$) δ = 163.74, 163.39, 158.60, 143.35, 140.92, 138.54, 137.18, 135.29, 131.52, 131.42, 131.22, 130.12, 130.10, 129.04, 127.57, 126.56, 125.59, 125.43, 124.44, 120.73, 119.48, 114.58, 114.34, 106.10, 55.52, 36.15, 31.53 ppm. HR-MALDI-MS (DCTB) *m/z* calcd for $C_{50}H_{38}N_3O_2$ [M-CH_3^+] 712.2959, found 712.2944.

242c (*E,E*)-2-[4-(9,9-dimethyl-9,10-dihydroacridine)phenyl]-4,6-bis[(4-*N,N*-diphenylaminophenyl)ethenyl]pyrimidine

$C_{65}H_{51}N_5$

MW = 902.13

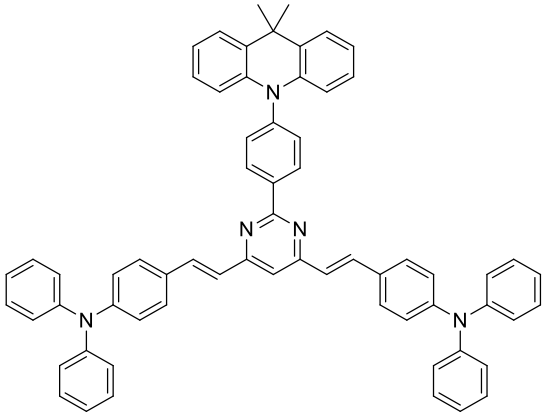

Compound **242c** was synthesized from compound **240** (196 mg, 0.50 mmol) and 4-diphenylaminobenzaldehyde (274 mg, 1.00 mmol) following the general procedure for Knoevenagel condensation. The crude product was purified by column chromatography (hexane/CH_2Cl_2 1:1) and recrystallization. Yield 110 mg (22 %); yellow solid; R_f = 0.6 (SiO_2;

hexane/CH_2Cl_2 1:1); mp: 233°C. ^{1}H NMR (500 MHz, $CDCl_3$) δ = 8.85–8.84 (m, 2H), 8.02 (d, $^3J_{H\text{-}H}$ = 16 Hz, 2H), 7.55–7.49 (m, 8H), 7.33–7.30 (m, 8H), 7.21–7.16 (m, 9H), 7.12–7.05 (m, 10H), 7.00–6.94 (m, 4H), 6.42–6.40 (m, 2H), 1.74 (s, 6H) ppm. ^{13}C NMR (125 MHz, $CDCl_3$) δ = 163.74, 163.44, 149.05, 147.81, 147.29, 143.25, 140.90, 138.66, 136.40, 131.49, 131.17, 130.07, 129.56, 129.47, 128.84, 126.52, 125.38, 125.26, 124.23, 123.93, 123.80, 122.51, 120.69, 114.34, 114.11, 36.13, 31.50 ppm. HR-MALDI-MS (DCTB) *m/z* calcd for $C_{64}H_{48}N_5$ [M-CH_3^+] 886.3904, found 886.3892.

244a 2-phenylpyrimidine

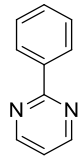

$C_{10}H_8N_2$

MW = 156.18

Compound **244a** was synthesized from 2-chloropyrimidine (458 mg, 4 mmol) and phenylboronic acid (586 mg, 4.8 mmol) following the method C and purified by column chromatography (8:2, petroleum ether/EtOAc) Yield 524 mg (84 %); pale orange solid. R_f = 0.5 (8:2, petroleum ether/EtOAc). ^{1}H NMR (300 MHz, $CDCl_3$) δ = 8.81 (d, $^3J_{H\text{-}H}$ = 5 Hz, 2H), 8.46–8.42 (m, 2H), 7.52–7.47 (m, 3H), 7.19 (t, $^3J_{H\text{-}H}$ = 5 Hz, 1H) ppm. 13C NMR (75 MHz, CDCl3) δ = 164.50, 157.04, 137.44, 130.68, 128.48, 128.08, 118.94, ppm. Data are in accordance with literature.[289]

244b 2-(3-cyanophenyl)pyrimidine

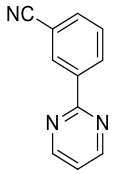

$C_{11}H_7N_3$

MW = 181.19

Compound **244b** was synthesized from 2-chloropyrimidine (458 mg, 4 mmol) and 3-cyanophenylboronic acid (706 mg, 4.8 mmol) following the general procedure for the synthesis of ligands and purified by column chromatography (7:3, petroleum ether/EtOAc) Yield 508 mg (70 %); white solid. R_f = 0.5 (7:3, petroleum ether/EtOAc). ^{1}H NMR (300 MHz, $CDCl_3$) δ = 8.84 (d, $^3J_{H\text{-}H}$ = 5 Hz, 2H), 8.79–8.78 (m, 1H), 8.71–8.68 (m, 1H), 7.78–7.75 (m, 1H), 7.63–7.58 (m, 1H), 7.28 (t, $^3J_{H\text{-}H}$ = 5 Hz, 1H) ppm. ^{13}C NMR (75 MHz, $CDCl_3$) δ = 162.80, 157.60, 138.91, 133.99, 132.36, 132.12, 129.57, 120.14, 118.80, 113.09 ppm. HR-MALDI-MS (DCTB) *m/z* calcd for $C_{11}H_8N_3$ [M+H^+] 182.0713, found 182.0713. Data are in accordance with literature.[289]

244c 2-(3-methoxyphenyl)pyrimidine

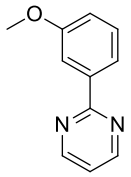

$C_{11}H_{10}N_2O$

MW = 186.21

Compound **244c** was synthesized from 2-chloropyrimidine (606 mg, 5.29 mmol) and 3-methoxyphenylboronic acid (965 mg, 6.35 mmol) following the general procedure for the synthesis of ligands and purified by column chromatography (CH_2Cl_2) Yield 651 mg (66 %); pale orange solid. R_f = 0.2 (CH_2Cl_2). ^{1}H NMR (300 MHz, $CDCl_3$) δ = 8.81 (d, $^3J_{H,H}$ = 5 Hz, 2H), 8.07–8.00 (m, 2H), 7.43–7.38 (m, 1H), 7.19 (t, $^3J_{H,H}$ = 5 Hz, 1H), 7.07–7.03 (m, 1H), 3.91 (s, 3H) ppm. ^{13}C NMR (75 MHz, $CDCl_3$) δ = 164.66, 160.12, 157.28, 139.12, 129.71, 120.81, 119.26, 117.58, 112.68, 55.50 ppm. HR-MALDI-MS (DCTB) *m/z* calcd for $C_{11}H_{11}N_2O$ [M+H$^+$] 187.0866, found 187.0866. Data are in accordance with literature.[289]

244d 2-(3-*N,N*-diphenylaminophenyl)pyrimidine

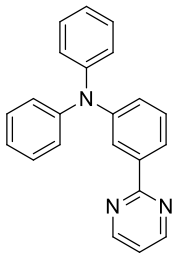

$C_{22}H_{17}N_3$

MW = 323.39

Compound **244d** was synthesized from 2-chloropyrimidine (96 mg, 0.83 mmol) and 3-*N,N*-diphenylaminophenylboronic acid (289 mg, 1 mmol) following the general procedure for the synthesis of ligands and purified by column chromatography (CH_2Cl_2) Yield 122 mg (45 %); white solid. R_f = 0.6 (CH_2Cl_2). ^{1}H NMR (300 MHz, $CDCl_3$) δ = 8.75–8.73 (m, 2H), 8.22–8.21 (m, 1H), 8.10–8.07 (m, 1H), 7.40–7.35 (m, 1H), 7.28–7.19 (m, 4H), 7.17–6.99 (m, 8H) ppm. ^{13}C NMR (75 MHz, $CDCl_3$) δ = 164.70, 157.31, 148.50, 148.00, 139.14, 129.67, 129.40, 126.98, 124.32, 124.17, 122.86, 119.22 ppm. HR-MALDI-MS (DCTB) *m/z* calcd for $C_{22}H_{17}N_3$ [M$^+$] 323.1417, found 323.1405.

244e 2-(4-methoxyphenyl)pyrimidine

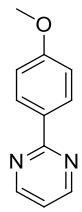

$C_{11}H_{10}N_2O$

MW = 186.21

Compound **244e** was synthesized from 2-chloropyrimidine (615 mg, 5.36 mmol) and 4-methoxyphenylboronic acid (978 mg, 6.44 mmol) following the general procedure for the synthesis of ligands and purified by column chromatography (CH_2Cl_2) Yield 706 mg (71 %); pale yellow solid. R_f = 0.2 (CH_2Cl_2). ^{1}H NMR (300 MHz, $CDCl_3$) δ = 8.75 (d, $^3J_{H-H}$ = 5 Hz, 2H), 8.41–8.37 (m, 2H), 7.11 (t, $^3J_{H-H}$ = 5 Hz, 1H), 7.03–6.98 (m, 2H), 3.88 (s, 3H) ppm. ^{13}C NMR (75 MHz, $CDCl_3$) δ = 164.61, 162.03, 157.21, 130.37, 129.87, 118.41, 114.03, 55.43 ppm. HR-MALDI-MS (DCTB) *m/z* calcd for $C_{11}H_{11}N_2O$ [M+H$^+$] 187.0866, found 187.0866. Data are in accordance with literature.[289]

245a

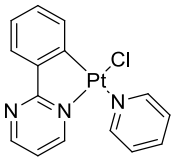

$C_{15}H_{12}ClN_3Pt$
MW = 464.81

Compound **245a** was synthesized from K_2PtCl_4 (100 mg, 0.24 mmol) and **244a** (46 mg, 0.29 mmol) following the general procedure for the synthesis of Pt^{II} complexes. Yield 40 mg (36 %) yellow solid. R_f = 0.5 (1:1, EtOAc/CH_2Cl_2). ^{1}H NMR (300 MHz, $CDCl_3$) δ = 9.87–9.73 (m, $^3J_{H-Pt}$ = 38 Hz, 1H), 9.08–8.91 (m, $^3J_{H-Pt}$ = 47 Hz, 2H), 8.79–8.77 (m, 1H), 7.94–7.85 (m, 2H), 7.47–7.42 (m, 2H), 7.17–7.05 (m, 3H), 6.47–6.28 (m, $^3J_{H-Pt}$ = 49 Hz, 1H) ppm. ^{13}C NMR (75 MHz, $CDCl_3$) δ = 175.83, 158.56, 157.56 (m, $^2J_{C-Pt}$ = 8 Hz), 154.18 (m, $^2J_{C-Pt}$ = 6 Hz), 141.66, 141.09, 138.13 (m, $^2J_{C-Pt}$ = 6 Hz), 132.46 (m, $^3J_{C-Pt}$ = 29 Hz), 130.37 (m, $^3J_{C-Pt}$ = 23 Hz), 127.79 (m, $^3J_{C-Pt}$ = 23 Hz), 126.22 (m, $^3J_{C-Pt}$ = 26 Hz), 124.23, 117.65 (m, $^4J_{C-Pt}$ = 14 Hz) ppm. HR-MALDI-MS (DCTB) *m/z* calcd for $C_{15}H_{12}ClN_3Pt$ [M$^+$] 464.0362, found 464.0365.

245b

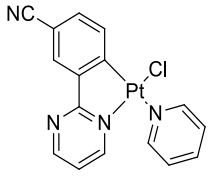

$C_{16}H_{11}ClN_4Pt$
MW = 489.82

Compound **245b** was synthesized from K_2PtCl_4 (200 mg, 0.48 mmol) and **244b** (105 mg, 0.58 mmol) following the general procedure for the synthesis of Pt^{II} complexes. Yield 40 mg (36 %) yellowish solid. R_f = 0.6 (1:1, EtOAc/CH_2Cl_2). ^{1}H NMR (300 MHz, $CDCl_3$) δ = 9.93–9.79 (m, $^3J_{H-Pt}$ = 38 Hz, 1H), 9.01–8.86 (m, 3H), 8.22–8.03 (m, 1H), 8.00–7.91 (m, 1H), 7.53–7.49 (m, 2H), 7.31–7.24 (m, 2H), 6.60–6.42 (m, $^3J_{H-Pt}$ = 49 Hz, 1H) ppm. (75 MHz, $CDCl_3$) δ = 158.96, 157.84, 153.99 (m, $^2J_{C-Pt}$ = 6 Hz), 148.15, 138.67, 134.89 (m, $^3J_{C-Pt}$ = 29 Hz), 131.14,

130.69, 129.88, 126.58 (m, $^{3}J_{C\text{-}Pt}$ = 25 Hz), 119.63, 118.72 (m, $^{4}J_{C\text{-}Pt}$ = 14 Hz), 107.38 ppm (One quaternary carbon is not observed due to the low solubility of this complex). HR-MALDI-MS (DCTB) *m/z* calcd for $C_{16}H_{11}ClN_4Pt$ [M^+] 489.0315, found 489.0317.

245c

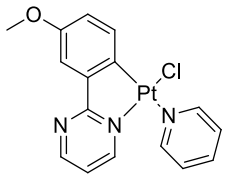

$C_{16}H_{14}ClN_3OPt$
MW = 494.84

Compound **245c** was synthesized from K_2PtCl_4 (100 mg, 0.24 mmol) and **244c** (54 mg, 0.29 mmol) following the general procedure for the synthesis of Pt^{II} complexes. Yield 55 mg (46 %) orange solid. R_f = 0.6 (1:1, EtOAc/CH_2Cl_2). ^{1}H NMR (300 MHz, $CDCl_3$) δ = 9.85–9.70 (m, $^{3}J_{H\text{-}Pt}$ = 34 Hz, 1H), 9.07–8.91 (m, $^{3}J_{H\text{-}Pt}$ = 45 Hz, 2H), 8.77–8.74 (m, 1H), 7.93–7.87 (m, 1H), 7.46–7.41 (m, 3H), 7.10–7.07 (m, 1H), 6.76–6.72 (m, 1H), 6.36–6.17 (m, $^{3}J_{H\text{-}Pt}$ = 48 Hz, 1H), 3.62 (s, 3H) ppm. ^{13}C NMR (75 MHz, $CDCl_3$) δ = 175.63, 158.33, 157.63 (m, $^{2}J_{C\text{-}Pt}$ = 10 Hz), 157.14, 154.17 (m, $^{2}J_{C\text{-}Pt}$ = 6 Hz), 142.08, 138.04 (m, $^{2}J_{C\text{-}Pt}$ = 6 Hz), 131.96, 131.04 (m, $^{3}J_{C\text{-}Pt}$ = 28 Hz), 126.17 (m, $^{3}J_{C\text{-}Pt}$ = 26 Hz), 120.07 (m, $^{3}J_{C\text{-}Pt}$ = 31 Hz), 117.69 (m, $^{4}J_{C\text{-}Pt}$ = 17 Hz), 111.38 (m, $^{3}J_{C\text{-}Pt}$ = 25 Hz) 55.55 ppm. HR-MALDI-MS (DCTB) *m/z* calcd for $C_{16}H_{14}ClN_3OPt$ [M^+] 494.0468, found 494.0472.

245d

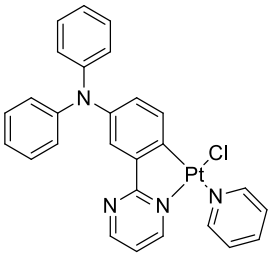

$C_{27}H_{21}ClN_4Pt$
MW = 632.02

Compound **245d** was synthesized from K_2PtCl_4 (100 mg, 0.24 mmol) and **244d** (94 mg, 0.29 mmol) following the general procedure for the synthesis of Pt^{II} complexes. Yield 115 mg (76 %) orange solid. R_f = 0.8 (1:1, EtOAc/CH_2Cl_2). ^{1}H NMR (300 MHz, $CDCl_3$) δ = 9.86–9.74 (m, $^{3}J_{H\text{-}Pt}$ = 34 Hz, 1H), 9.07–8.92 (m, $^{3}J_{H\text{-}Pt}$ = 44 Hz, 2H), 8.70–8.68 (m, 1H), 7.91–7.86 (m, 1H), 7.70–7.69 (m, 1H), 7.45–7.41 (m, 2H), 7.23–7.18 (m, 4H), 7.10–7.06 (m, 5H), 7.98–6.88 (m, 3H), 6.40–6.22 (m, $^{3}J_{H\text{-}Pt}$ = 48 Hz, 1H) ppm. ^{13}C NMR (75 MHz, $CDCl_3$) δ = 175.26, 158.43, 157.64 (m, $^{2}J_{C\text{-}Pt}$ = 10 Hz), 154.11, 147.84, 144.50, 142.58, 138.09, 135.36, 131.19 (m, $^{3}J_{C\text{-}Pt}$ = 28 Hz), 129.77 (m, $^{3}J_{C\text{-}Pt}$ = 31 Hz), 129.28, 126.16 (m, $^{3}J_{C\text{-}Pt}$ = 26 Hz), 124.49 (m, $^{3}J_{C\text{-}Pt}$ = 24

Hz), 123.54, 122.36, 117.73 (m, $^{4}J_{C\text{-}Pt}$ = 13 Hz) ppm. HR-MALDI-MS (DCTB) *m/z* calcd for $C_{27}H_{22}ClN_4Pt$ [M^+] 632.1175, found 632.1094.

245e

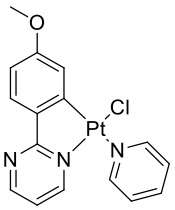

$C_{16}H_{14}ClN_3OPt$

MW = 494.84

Compound **245e** was synthesized from K_2PtCl_4 (100 mg, 0.24 mmol) and **244e** (54 mg, 0.29 mmol) following the general procedure for the synthesis of Pt^{II} complexes. Yield 54 mg (45 %) yellow solid. R_f = 0.4 (1:1, EtOAc/CH_2Cl_2). ^{1}H NMR (300 MHz, $CDCl_3$) δ = 9.78–9.64 (m, $^{3}J_{H\text{-}Pt}$ = 39 Hz, 1H), 9.08–8.89 (m, $^{3}J_{H\text{-}Pt}$ = 46 Hz, 2H), 8.72–8.69 (m, 1H), 7.93–7.87 (m, 1H), 7.84–7.82 (m, 1H), 7.47–7.42 (m, 2H), 7.02–6.99 (m, 1H), 6.71–6.68 (m, 1H), 5.95–5.76 (m, $^{3}J_{H\text{-}Pt}$ = 56 Hz, 1H), 3.68 (s, 3H) ppm. ^{13}C NMR (75 MHz, $CDCl_3$) δ = 175.20, 162.79, 158.57, 157.50 (m, $^{2}J_{C\text{-}Pt}$ = 11 Hz), 154.17 (m, $^{2}J_{C\text{-}Pt}$ = 6 Hz), 142.79, 138.13 (m, $^{2}J_{C\text{-}Pt}$ = 6 Hz), 134.41, 129.56 (m, $^{3}J_{C\text{-}Pt}$ = 27 Hz), 126.17 (m, $^{3}J_{C\text{-}Pt}$ = 26 Hz), 116.50 (m, $^{3}J_{C\text{-}Pt}$ = 24 Hz), 116.43 (m, $^{4}J_{C\text{-}Pt}$ = 19 Hz), 108.86, 55.17 ppm. HR-MALDI-MS (DCTB) *m/z* calcd for $C_{16}H_{14}ClN_3OPt$ [M^+] 494.0468, found 494.0476.

ANNEXES

Annex 1.*Calculated absorption and emission data for compounds* ***48****,* ***49****,* ***61****,* ***62****,* ***232i*** *and* ***232m****. f is oscillator strength.*

	Absorption: λ_{abs} (nm)/f (orbitals contributions)		*Emission: λ_{em} (nm)/f*	
Compd	PBE0	CAM-B3LYP	PBE0	CAM-B3LYP
48	357 / 1.05 (HOMO → LUMO)	326 / 1.17 (HOMO → LUMO)	376 / 1.11	363 / 1.22
49	402 / 0.93 (HOMO → LUMO)	348 / 1.20 (HOMO → LUMO)	538 / 0.07	387 / 1.21
61 Confo1	403 / 1.60 (HOMO → LUMO)	351 / 2.24 (HOMO → LUMO)	427 / 1.65	377 / 2.27
	316 / 0.79 (HOMO-1 → LUMO+1)	313 / 0.14 (HOMO-1 → LUMO)		
61 Confo2	390 / 1.09 (HOMO → LUMO)	344 / 1.67 (HOMO → LUMO)	421 / 1.11	373 / 1.66
	343 / 0.58 (HOMO → LUMO+1)	305 / 0.57 (HOMO-1 → LUMO) (HOMO → LUMO+1)		
	329 / 0.37 (HOMO-1 → LUMO) (HOMO → LUMO+1)			
62 Confo1	442 / 1.71 (HOMO → LUMO)	370 / 2.49 (HOMO → LUMO)	481 / 1.47	396 / 2.54
	346 / 0.51 (HOMO-1 → LUMO+1)	335 / 0.16 (HOMO-1 → LUMO) (HOMO → LUMO+1)		
62 Confo2	428 / 1.34 (HOMO → LUMO)	364 / 1.89 (HOMO → LUMO)	471 / 1.15	390 / 1.92
	393 / 0.22 (HOMO-1 → LUMO)	331 / 0.53 (HOMO-1 → LUMO) (HOMO → LUMO+1)		
	371 / 0.30 (HOMO-1 → LUMO+1)			
	366 / 0.16 (HOMO → LUMO+1)			
232i Confo1	416 / 0.43 (HOMO → LUMO)	351 / 1.81 (HOMO → LUMO)	504 / 0.05	378 / 1.90
	389 / 1.11 (HOMO-1 → LUMO)	331 / 1.33 (HOMO-2 → LUMO) (HOMO → LUMO+1)		
	374 / 0.66 (HOMO-2 → LUMO) (HOMO → LUMO+1)	308 / 0.34 (HOMO-1 → LUMO) (HOMO → LUMO)		
	342 / 0.40 (HOMO-2 → LUMO+1) (HOMO-1 → LUMO+1)			
232i Confo2	405 / 0.27 (HOMO → LUMO)	344 / 1.34 (HOMO → LUMO) (HOMO-1 → LUMO)	490 / 0.06	374 / 1.38
	376 / 1.27 (HOMO-1 → LUMO) (HOMO → LUMO+1)	329 / 2.09 (HOMO → LUMO+1)		
	373 /0.80 (HOMO-1 → LUMO) (HOMO → LUMO+1)	306 / 0.29 (HOMO-2 → LUMO+1) (HOMO → LUMO)		

	358/ 0.29 (HOMO-2 → LUMO+1) (HOMO-2 → LUMO) (HOMO-1 → LUMO+1)			
232i Confo3	410 / 0.39 (HOMO → LUMO)	347 / 1.67 (HOMO → LUMO+1)	500 / 0.07	377 / 1.68
	382 / 0.76 (HOMO-1 → LUMO)	329 / 1.70 (HOMO → LUMO+1) (HOMO-2->LUMO)		
	371 / 1.19 (HOMO-2 → LUMO) (HOMO → LUMO+1)	307 / 0.36 (HOMO-1 → LUMO) (HOMO → LUMO)		
	350 / 0.55 (HOMO-1 → LUMO+1)			
232m Confo1	444 / 0.97 (HOMO → LUMO)	369 / 2.26 (HOMO → LUMO) (HOMO-1 → LUMO)	536 / 0.06	400 / 2.17
	428 / 0.75 (HOMO-1 → LUMO)	353 / 1.41 (HOMO-2 → LUMO) (HOMO → LUMO+1)		
	414 / 0.68 (HOMO-2 → LUMO)	322 / 0.14 (HOMO-2 → LUMO) (HOMO → LUMO+1)		
	380 / 0.42 (HOMO → LUMO+1) (HOMO-2 → LUMO) (HOMO-1 → LUMO+1)			
232m Confo2	431 / 0.65 (HOMO → LUMO)	363 / 1.73 (HOMO-1 → LUMO) (HOMO → LUMO) (HOMO-2 → LUMO+1)	525 / 0.07	395 / 1.72
	418 / 1.33 (HOMO-1 → LUMO) (HOMO → LUMO+1)	352 / 2.14 (HOMO → LUMO+1) (HOMO → LUMO+2)		
	410 / 0.76 (HOMO → LUMO+1) (HOMO-1 → LUMO)			
232m Confo3	437 / 0.87 (HOMO → LUMO) (HOMO-1 → LUMO)	365 / 2.09 (HOMO → LUMO) (HOMO-1 → LUMO)	535 / 0.07	396 / 2.06
	420 / 0.65 (HOMO-1 → LUMO) (HOMO → LUMO)	352 / 1.77 (HOMO-2 → LUMO) (HOMO → LUMO+1)		
	412 / 1.12 (HOMO-2 → LUMO) (HOMO → LUMO+1)			
	384 / 0.28 (HOMO-2 → LUMO) (HOMO-1 → LUMO+1)			

Annex 2. *Overlap of normalized TD-DFT calculated (red) and experimental (black) electronic absorption spectra of* ***241*** *and* ***242****. The vertical red lines represent oscillator strengths.*

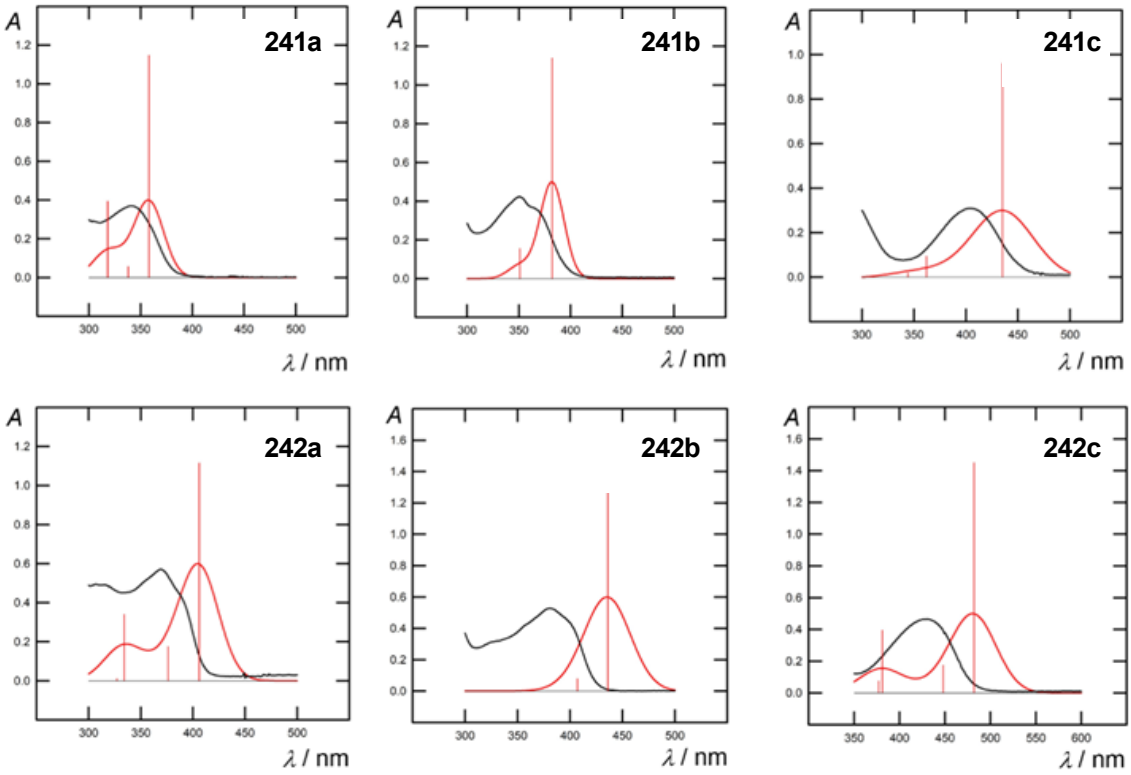

Annex 3. *TD-DFT calculated parameter of* ***241*** *and* ***242****.*

Compd	*λ nm (eV)*	*f*	*orbitals contribution*
241a	511 (2.42)	0.0001	HOMO→LUMO HOMO→LUMO+1
	358 (3.46)	1.1470	HOMO-1→LUMO
	338 (3.67)	0.0565	HOMO–1→LUMO+1 HOMO-4→LUMO
	318 (3.89)	0.3929	HOMO–1→LUMO+1 HOMO–4→LUMO
241b	539 (2.30)	0.0000	HOMO→LUMO
	382 (3.25)	1.1391	HOMO–1→LUMO
	351 (3.53)	0.1550	HOMO–1→LUMO+1 HOMO–1→LUMO HOMO–3→LUMO HOMO–1→LUMO+2
241c	510 (2.43)	0.0000	HOMO→LUMO HOMO→LUMO+1
	435 (2.85)	0.9606	HOMO–1→LUMO
	362 (3.43)	0.0940	HOMO–1→LUMO+1
	344 (3.61)	0.0181	HOMO–1→LUMO+2
	340 (3.65)	0.0013	HOMO→LUMO+2 HOMO–1→LUMO+3
242a	517 (2.40)	0.0000	HOMO→LUMO
	406 (3.05)	1.1153	HOMO–1→LUMO
	376 (3.30)	0.1756	HOMO–2→LUMO+1 HOMO→LUMO+2
	334 (3.72)	0.3406	HOMO–2→LUMO+1
242b	529 (2.34)	0.0000	HOMO→LUMO
	436 (2.84)	1.4466	HOMO–1→LUMO
	407 (3.05)	0.0794	HOMO–2→LUMO HOMO–1→LUMO+1
242c	495 (2.50)	0.0000	HOMO→LUMO
	482 (2.57)	1.4500	HOMO–1→LUMO
	448 (2.77)	0.1747	HOMO–2→LUMO
	381 (3.26)	0.3942	HOMO–2→LUMO+1
	377 (3.29)	0.0753	HOMO–1→LUMO+1

Annex 4. *Excited-state dynamics of* ***241a*** *(A) and* ***241b*** *(B) in neat film with detection in two emission bands.*

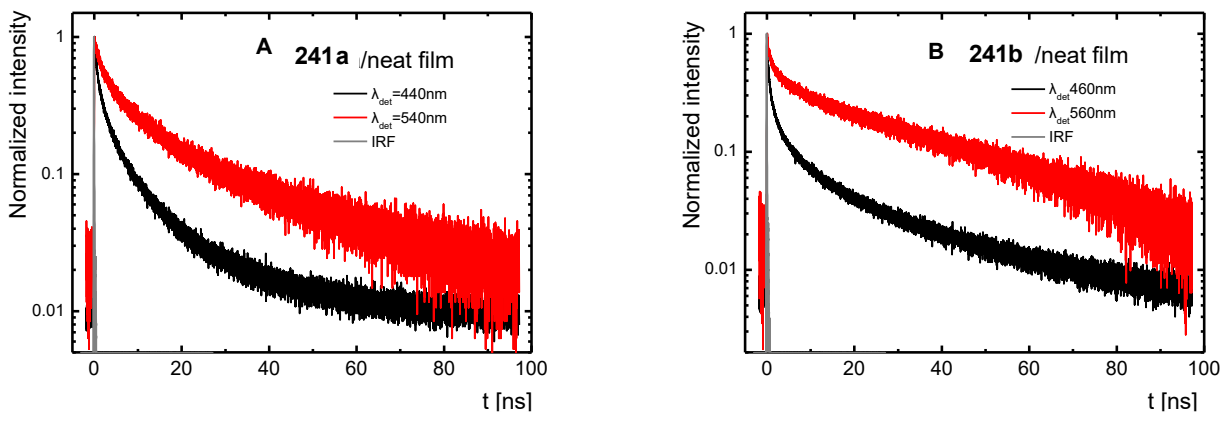

Annex 5. *Relevant computed data for complexes* ***245****.*

Compound		***245a***	***245b*** *CN*	***245c*** *OMe*	***245d*** *NPh_2*	***245e*** *OMe*
HOMO-LUMO gap (eV)		4.15	4.19	3.80	3.28	4.23
Pt-Cl (Å)		2.454	2.440	2.454	2.453	2.454
[Wiberg bond indice]		[0.301]	[0.312]	[0.301]	[0.303]	[0.302]
Pt-N(py) (Å)		2.020	2.020	2.019	2.019	2.021
[Wiberg bond indice]		[0.396]	[0.399]	[0.398]	[0.398]	[0.395]
Pt-N(ppy) (Å)		2.016	2.019	2.017	2.017	2.016
[Wiberg bond indice]		[0.411]	[0.408]	[0.411]	[0.410]	[0.412]
Pt-C(ppy) (Å)		1.978	1.971	1.981	1.978	1.977
[Wiberg bond indice]		[0.689]	[0.696]	[0.679]	[0.687]	[0.686]
Py/Pt(ppy) torsion angle (°)		66	67	65	65	65
NAO charges	Pt	0.63	0.65	0.63	0.64	0.63
	Cl	-0.69	-0.68	-0.69	-0.69	-0.69
	N(py)	-0.52	-0.52	-0.52	-0.52	-0.52
	N(ppy)	-0.54	-0.54	-0.54	-0.54	-0.55
	C(ppy)	-0.19	-0.17	-0.22	-0.20	-0.17

REFERENCES

[1] T. W. Kelley, P. F. Baude, C. Gerlach, D. E. Ender, D. Muyres, M. A. Haase, D. E. Vogel, S. D. Theiss, *Chem. Mater.* **2004**, *16*, 4413–4422.

[2] J. M. Shaw, P. F. Seidler, *IBM J. Res. Dev.* **2001**, *45*, 3–9.

[3] M. Reyes-Reyes, D. L. Carroll, W. Blau, R. López-Sandoval, *J. Nanotechnol.* **2011**, *2011*, 589241.

[4] C. H. (Fred) Chen, W.-S. Wen, C.-T. Chen, in *Encyclopedia of Modern Optics*, Elsevier, **2018**, pp. 64–69.

[5] T. Tsujimura, In *OLED Display Fundamentals and Applications*, John Wiley & Sons, Inc., Hoboken, New Jersey, **2017**, pp. 1–5.

[6] N. T. Kalyani, H. Swart, S. J. Dhoble, in *Principles and Applications of Organic Light Emitting Diodes (OLEDs)*, Elsevier, **2017**, pp. 205–225.

[7] G. Zissis, in *LEDs for Lighting Applications* (Ed.: P. Mottier), ISTE, London, UK, **2009**, pp. 1–27.

[8] E. Wiedemann, *Ann. Phys. Chem.* **1888**, *270*, 446–463.

[9] B. Valeur, in *New Trends in Fluorescence Spectroscopy: Applications to Chemical and Life Sciences* (Eds.: B. Valeur, J.-C. Brochon), Springer Berlin Heidelberg, Berlin, Heidelberg, **2001**, pp. 3–6.

[10] E. N. Harvey, *A History of Luminescence: From the Earliest Times until 1900*, American Philosophical Society, Philadelphia, **1957**.

[11] G. G. Stokes, *Philos. Trans.* **1852**, *142*, 463–562.

[12] E. Becquerel, *Ann. Phys. Chem.* **1842**, 257–322.

[13] E. Becquerel, *La Lumière, Ses Causes et Ses Effets. Effets de La Lumière*, Firmin Didot, Paris, **1868**.

[14] A. Jabłoński, *Acta Phys. Pol.* **1970**, 453–458.

[15] In *Membership Lists of IUPAC Bodies 1977–1979*, Elsevier, **1978**, pp. 139–140.

[16] I. P. Herman, in *Optical Diagnostics for Thin Film Processing*, Elsevier, **1996**, pp. 619–636.

[17] H. Rekhi, R. Kaur, A. K. Malik, in *Advances in Animal Biotechnology and Its Applications* (Eds.: S.K. Gahlawat, J.S. Duhan, R.K. Salar, P. Siwach, S. Kumar, P. Kaur), Springer Singapore, Singapore, **2018**, pp. 383–401.

[18] J. Lee, *J. Sib. Fed. Univ., Bio.* **2008**, 194–205.

[19] Y. Horowitz, R. Chen, L. Oster, I. Eliyahu, in *Encycl. Spectrosc. Spectrom.*, Elsevier, **2017**, pp. 444–451.

[20] B. P. Chandra, A. S. Rathore, *Cryst. Res. Technol.* **1995**, *30*, 885–896.

[21] J. S. Klein, C. Sun, G. Pratx, *Phys. Med. Biol.* **2019**, *64*, 04TR01.

[22] J. I. Zink, B. P. Chandra, *J. Phys. Chem.* **1982**, *86*, 5–7.

[23] G. T. Reynolds, *J. Lumin.* **1992**, *54*, 43–69.

[24] M. Schott, *Comptes Rendus de l'Académie des Sciences - Series IV - Physics* **2000**, *1*, 381–402.

[25] D. Stowe, M. Bertilson, Ja. Hunt, *Microsc. Microanal.* **2017**, *23*, 1034–1035.

[26] K. Yasui, T. Tuziuti, M. Sivakumar, Y. Iida, *Appl. Spectrosc. Rev.* **2004**, *39*, 399–436.

[27] A. Braeuer, in *Supercritical Fluid Science and Technology*, Elsevier, **2015**, pp. 41–192.

[28] B. Valeur, *Molecular Fluorescence Principles and Applications*, Wiley-VCH, New York, **2001**.

[29] J. W. Lichtman, J.-A. Conchello, *Nat. Methods* **2005**, *2*, 910–919.

[30] J. R. Lakowicz, *Principles of Fluorescence Spectroscopy*, Springer US, **2006**.

[31] M. G. Vivas, L. De Boni, C. R. Mendonça, in *Mol. Laser Spectrosc.*, Elsevier, **2018**, pp. 165–191.

[32] N. W. Barnett, P. S. Francis, in *Encyclopedia of Analytical Science (Second Edition)* (Eds.: P. Worsfold, A. Townshend, C. Poole), Elsevier, Oxford, **2005**, pp. 305–315.
[33] B. Valeur, *Molecular Fluorescence Principles and Applications*, Springer Berlin Heidelberg, Berlin, Heidelberg, **2001**.
[34] J. N. Demas, S. E. Demas, in *Reference Module in Chemistry, Molecular Sciences and Chemical Engineering*, Elsevier, **2014**, p. 36.
[35] J. W. Verhoeven, *Pure Appl. Chem.* **1996**, *68*, 2223–2286.
[36] D. A. Skoog, F. J. Holler, S. R. Crouch, *Principles of Instrumental Analysis*, Thomson Brooks/Cole, Belmont, CA, **2007**.
[37] S. E. Braslavsky, *Pure Appl. Chem.* **2007**, *79*, 293–465.
[38] J. R. Albani, in *Structure and Dynamics of Macromolecules: Absorption and Fluorescence Studies* (Ed.: J.R. Albani), Elsevier Science, Amsterdam, **2004**, pp. 141–192.
[39] V. P. Gupta, in *Principles and Applications of Quantum Chemistry*, Elsevier, **2016**, pp. 291–337.
[40] B. Valeur, *Molecular Fluorescence*, Wiley-VCH Verlag GmbH & Co. KGaA, Weinheim, Germany, **2009**.
[41] P. Klán, J. Wirz, *Photochemistry of Organic Compounds*, John Wiley & Sons, Ltd, Chichester, UK, **2009**.
[42] J. C. del Valle, J. Catalán, *Phys. Chem. Chem. Phys.* **2019**, *21*, 10061–10069.
[43] X. Zhu, Q. Su, W. Feng, F. Li, *Chem. Soc. Rev.* **2017**, *46*, 1025–1039.
[44] J. Klikorka, B. Hájek, J. Votinský, *Obecná a anorganická chemie*, SNTL - Nakladatelství Technické Literatury, Praha, **1985**.
[45] R. McDiarmid, *J. Phys. Chem.* **1980**, *84*, 64–70.
[46] Y. Yamaguchi, Y. Matsubara, T. Ochi, T. Wakamiya, Z. Yoshida, *J. Am. Chem. Soc.* **2008**, *130*, 13867–13869.
[47] F. Masetti, U. Mazzucato, G. Galiazzo, *J. Lumin.* **1971**, *4*, 8–12.
[48] P. T. C. So, C. Y. Dong, B. R. Masters, K. M. Berland, *Annu. Rev. Biomed. Eng.* **2000**, *2*, 399–429.
[49] O. V. Przhonska, S. Webster, L. A. Padilha, H. Hu, A. D. Kachkovski, D. J. Hagan, E. W. Van Stryland, in *Advanced Fluorescence Reporters in Chemistry and Biology I: Fundamentals and Molecular Design* (Ed.: A.P. Demchenko), Springer, Berlin, Heidelberg, **2010**, pp. 105–147.
[50] J. M. Hales, S.-H. Chi, V. W. Chen, J. W. Perry, in *The WSPC Reference on Organic Electronics: Organic Semiconductors*, WORLD SCIENTIFIC, **2016**, pp. 397–442.
[51] B. Strehmel, A. M. Sarker, H. Detert, *ChemPhysChem* **2003**, *4*, 249–259.
[52] S. Marder, D. Neher, Eds. , *Photoresponsive Polymers I*, Springer-Verlag, Berlin Heidelberg, **2008**.
[53] S. Barlow, S. R. Marder, in *Funct. Org. Mater.* (Eds.: T.J.J. Mller, U.H.F. Bunz), Wiley-VCH Verlag GmbH & Co. KGaA, Weinheim, Germany, **2006**, pp. 393–437.
[54] P. Audebert, K. Kamada, K. Matsunaga, K. Ohta, *Chem. Phys. Lett.* **2003**, *367*, 62–71.
[55] L. Antonov, K. Kamada, K. Ohta, F. S. Kamounah, *Phys. Chem. Chem. Phys.* **2003**, *5*, 1193–1197.
[56] C. Katan, F. Terenziani, O. Mongin, M. H. V. Werts, L. Porrès, T. Pons, J. Mertz, S. Tretiak, M. Blanchard-Desce, *J. Phys. Chem. A* **2005**, *109*, 3024–3037.
[57] S. G. Schulman, Q. Q. Di, J. Juchum, in *Encycl. Spectrosc. Spectrom.* Elsevier, **2017**, pp. 641–646.
[58] A. Pereira, S. Martins, A. Teresa Caldeira, in *Phytochemicals in Human Health* (Eds.: V. Rao, D. Mans, L. Rao), IntechOpen, **2020**.
[59] R. M. Christie, in *Handbook of Textile and Industrial Dyeing: Principles, Processes and Types of Dyes.*, Woodhead Publishing Ltd., **2011**, p. 26.

[60] T. Maindron, in *OLED Microdisplays* (Ed.: F. Templier), John Wiley & Sons, Inc., Hoboken, NJ, USA, **2014**, pp. 1–33.
[61] N. T. Kalyani, H. Swart, S. J. Dhoble, in *Principles and Applications of Organic Light Emitting Diodes (OLEDs)*, Elsevier, **2017**, pp. 1–37.
[62] N. T. Kalyani, H. Swart, S. J. Dhoble, in *Principles and Applications of Organic Light Emitting Diodes (OLEDs)*, Elsevier, **2017**, pp. 39–64.
[63] H. J. Round, *Electr. World* **1907**, *49*, 309.
[64] A. Bernanose, M. Comte, P. Vouaux, *J. Chem. Phys.* **1953**, *50*, 64–69.
[65] C. W. Tang, S. A. VanSlyke, *Appl. Phys. Lett.* **1987**, *51*, 913–915.
[66] Z. Dechun, in *Organic Light-Emitting Diodes (OLEDs)*, Elsevier, **2013**, pp. 114–142.
[67] A. Boudrioua, M. Chakaroun, A. Fischer, in *Organic Lasers*, Elsevier, **2017**, pp. 1–47.
[68] M. Mussini, S. Toffanin, In *Organic Light-Emitting Transistors*, John Wiley & Sons, Inc, Hoboken, NJ, **2016**, pp. 5–43.
[69] F.-C. Chen, in *Encyclopedia of Modern Optics*, Elsevier, **2018**, pp. 220–231.
[70] Adrian Kitai, in *Principles of Solar Cells, LEDs and Related Devices*, John Wiley & Sons, Ltd, **2018**, pp. 307–357.
[71] C. Reese, M. Roberts, M. Ling, Z. Bao, *Mater. Today* **2004**, *7*, 20–27.
[72] S. Ahmad, *J. Polym. Eng.* **2014**, *34*, 279–338.
[73] A. Facchetti, *Mater. Today* **2007**, *10*, 28–37.
[74] N. T. Kalyani, H. Swart, S. J. Dhoble, in *Principles and Applications of Organic Light Emitting Diodes (OLEDs)*, Elsevier, **2017**, pp. 141–170.
[75] C. Adachi, S. Lee, T. Nakagawa, K. Shizu, K. Goushi, T. Yasuda, W. J. Potscavage, in *Organic Electronics Materials and Devices* (Ed.: S. Ogawa), Springer Japan, Tokyo, **2015**, pp. 43–73.
[76] U. Wurfel, A. Cuevas, P. Wurfel, *IEEE J. Photovoltaics* **2015**, *5*, 461–469.
[77] D.-G. Moon, in *Encyclopedia of Modern Optics*, Elsevier, **2018**, pp. 232–239.
[78] S. H. Ko, Ed. , *Organic Light Emitting Diode - Material, Process and Devices*, InTech, **2011**.
[79] T. Tsujimura, In *OLED Display Fundamentals and Applications*, John Wiley & Sons, Inc., Hoboken, New Jersey, **2017**, pp. 7–59.
[80] C. Li, J. Wei, J. Han, Z. Li, X. Song, Z. Zhang, J. Zhang, Y. Wang, *J. Mater. Chem. C* **2016**, *4*, 10120–10129.
[81] B. Geffroy, P. le Roy, C. Prat, *Polym. Int.* **2006**, 572–582.
[82] D. Vaufrey, in *OLED Microdisplays* (Ed.: F. Templier), John Wiley & Sons, Inc., Hoboken, NJ, USA, **2014**, pp. 53–94.
[83] N. T. Kalyani, H. Swart, S. J. Dhoble, in *Principles and Applications of Organic Light Emitting Diodes (OLEDs)*, Elsevier, **2017**, pp. 227–252.
[84] D. R. Bull, in *Communicating Pictures* (Ed.: D.R. Bull), Academic Press, Oxford, **2014**, pp. 99–132.
[85] *Commission Internationale de l'Éclairage Proceedings*, Cambridge University Press, Cambridge, **1931**.
[86] T. D. Schmidt, W. Brütting, in *Highly Effic. OLEDs* (Ed.: H. Yersin), Wiley-VCH Verlag GmbH & Co. KGaA, Weinheim, Germany, **2018**, pp. 199–228.
[87] R. Komatsu, H. Sasabe, J. Kido, *J. Photon. Energy* **2018**, *8*, 1.
[88] T.-T. Bui, F. Goubard, M. Ibrahim-Ouali, D. Gigmes, F. Dumur, *Beilstein J. Org. Chem.* **2018**, *14*, 282–308.
[89] X. Zhao, S. T. Chaudhry, J. Mei, in *Heterocyclic Chemistry in the 21st Century* (Eds.: E.F.V. Scriven, C.A. Ramsden), Academic Press, **2017**, pp. 133–171.
[90] C. W. Bird, *Tetrahedron* **1992**, 335–340.

[91] V. P. Mamaev, O. P. Shkurko, S. G. Baram, in *Adv. Heterocycl. Chem.*, Elsevier, **1987**, pp. 1–82.
[92] Corwin. Hansch, A. Leo, R. W. Taft, *Chem. Rev.* **1991**, *91*, 165–195.
[94] H. Szatylowicz, O. A. Stasyuk, T. M. Krygowski, in *Adv. Heterocycl. Chem.* (Eds.: E.F.V. Scriven, C.A. Ramsden), Academic Press, **2015**, pp. 137–192.
[94] A. R. Katritzky, C. A. Ramsden, J. A. Joule, V. V. Zhdankin, in *Handbook of Heterocyclic Chemistry*, Elsevier, **2010**, pp. 242–382.
[95] J. Spanget-Larsen, *J. Chem. Soc., Perkin Trans. 2* **1985**, 417–419.
[97] K. Mills, J. A. Joule, in *Heterocycl. Chem., 5th Edition*, Wiley-Blackwell, **2010**.
[92] V. P. Mamaev, O. P. Shkurko, S. G. Baram, in *Adv. Heterocycl. Chem.*, Elsevier, **1987**, pp. 1–82.
[98] A. P. Sadimenko, in *Adv. Heterocycl. Chem.*, Elsevier, **2013**, pp. 91–239.
[99] A. P. Sadimenko, O. O. Okoh, in *Adv. Heterocycl. Chem.*, Elsevier, **2018**, pp. 51–120.
[100] A. P. Sadimenko, O. O. Okoh, in *Adv. Heterocycl. Chem.*, Elsevier, **2019**, pp. 315–390.
[101] W. Kaim, *Coord. Chem. Rev.* **2002**, *230*, 127–139.
[102] I. Haiduc, *J. Coord. Chem.* **2019**, *72*, 2805–2903.
[103] S. Achelle, J. Rodríguez-López, F. Robin-le Guen, *ChemistrySelect* **2018**, *3*, 1852–1886.
[104] K. Itami, D. Yamazaki, J. Yoshida, *J. Am. Chem. Soc.* **2004**, *126*, 15396–15397.
[105] S. Achelle, Y. Ramondenc, F. Marsais, N. Plé, *Eur. J. Org. Chem.* **2008**, *2008*, 3129–3140.
[106] S. Kato, Y. Yamada, H. Hiyoshi, K. Umezu, Y. Nakamura, *J. Org. Chem.* **2015**, *80*, 9076–9090.
[107] L. Pascal, J. J. Vanden Eynde, Y. Van Haverbeke, P. Dubois, A. Michel, U. Rant, E. Zojer, G. Leising, L. O. Van Dorn, N. E. Gruhn, J. Cornil, J. L. Brédas, *J. Phys. Chem. B* **2002**, *106*, 6442–6450.
[108] S. Achelle, A. Barsella, C. Baudequin, B. Caro, F. Robin-le Guen, *J. Org. Chem.* **2012**, *77*, 4087–4096.
[109] S. Achelle, J. Rodríguez-López, C. Katan, F. Robin-le Guen, *J. Phys. Chem. C* **2016**, *120*, 26986–26995.
[110] S. Achelle, A. Barsella, B. Caro, F. Robin-le Guen, *RSC Adv.* **2015**, *5*, 39218–39227.
[111] S. Achelle, I. Nouira, B. Pfaffinger, Y. Ramondenc, N. Plé, J. Rodríguez-López, *J. Org. Chem.* **2009**, *74*, 3711–3717.
[112] C. Denneval, S. Achelle, C. Baudequin, F. Robin-le Guen, *Dyes Pigm.* **2014**, *110*, 49–55.
[113] M. Fecková, P. le Poul, F. Bureš, F. Robin-le Guen, S. Achelle, *Dyes Pigm.* **2020**, *182*, 108659.
[114] L. Li, Y.-P. Tian, J.-X. Yang, P.-P. Sun, J.-Y. Wu, H.-P. Zhou, S.-Y. Zhang, B.-K. Jin, X.-J. Xing, C.-K. Wang, M. Li, G.-H. Cheng, H.-H. Tang, W.-H. Huang, X.-T. Tao, M.-H. Jiang, *Chem. - Asian J.* **2009**, *4*, 668–680.
[115] B. Liu, X.-L. Hu, J. Liu, Y.-D. Zhao, Z.-L. Huang, *Tetrahedron Lett.* **2007**, *48*, 5958–5962.
[116] Q. Zhang, L. Luo, H. Xu, Z. Hu, C. Brommesson, J. Wu, Z. Sun, Y. Tian, K. Uvdal, *New J. Chem.* **2016**, *40*, 3456–3463.
[117] Q. Zhang, X. Tian, H. Wang, Z. Hu, J. Wu, H. Zhou, S. Zhang, J. Yang, Z. Sun, Y. Tian, K. Uvdal, *Sens. Actuators, B* **2016**, *222*, 574–578.
[118] C. Tang, Q. Zhang, D. Li, J. Zhang, P. Shi, S. Li, J. Wu, Y. Tian, *Dyes Pigm.* **2013**, *99*, 20–28.
[119] D. Cvejn, S. Achelle, O. Pytela, J.-P. Malval, A. Spangenberg, N. Cabon, F. Bureš, F. Robin-le Guen, *Dyes Pigm.* **2016**, *124*, 101–109.

[120] P. Savel, H. Akdas-Kilig, J.-P. Malval, A. Spangenberg, T. Roisnel, J.-L. Fillaut, *J. Mater. Chem. C* **2014**, *2*, 295–305.
[121] C. Denneval, O. Moldovan, C. Baudequin, S. Achelle, P. Baldeck, N. Plé, M. Darabantu, Y. Ramondenc, *Eur. J. Org. Chem.* **2013**, *2013*, 5591–5602.
[122] Z. Liu, T. Chen, B. Liu, Z.-L. Huang, T. Huang, S. Li, Y. Xu, J. Qin, *J. Mater. Chem.* **2007**, *17*, 4685.
[123] S. Achelle, J. Malval, S. Aloïse, A. Barsella, A. Spangenberg, L. Mager, H. Akdas-Kilig, J. Fillaut, B. Caro, F. Robin-le Guen, *ChemPhysChem* **2013**, *14*, 2725–2736.
[124] D. J. Brown, *The Pyrimidines*, Interscience Publishers, New York, **1962**.
[125] "Pyrimidines - Halogenated Heterocycles | Sigma-Aldrich," can be found under https://www.sigmaaldrich.com/chemistry/chemistry-products.html?TablePage=16271203, **2020**.
[126] G. W. Rewcastle, in *Comprehensive Heterocyclic Chemistry III* (Eds.: A.R. Katritzky, C.A. Ramsden, E.F.V. Scriven, R.J.K. Taylor), Elsevier, Oxford, **2008**, pp. 117–272.
[127] J. W. Goodby, M. Hird, R. A. Lewis, K. J. Toyne, *Chem. Commun.* **1996**, 2719.
[128] Norio. Miyaura, Akira. Suzuki, *Chem. Rev.* **1995**, *95*, 2457–2483.
[129] J. M. Schomaker, T. J. Delia, *J. Org. Chem.* **2001**, *66*, 7125–7128.
[130] J. J. Vanden Eynde, L. Pascal, Y. Van Haverbeke, P. Dubois, *Synth. Commun.* **2001**, *31*, 3167–3173.
[131] C. Reichardt, *Chem. Rev.* **1994**, *94*, 2319.
[132] H. Muraoka, T. Obara, S. Ogawa, *Tetrahedron Lett.* **2016**, *57*, 3011.
[133] E. V. Verbitskiy, A. V. Schepochkin, N. I. Makarova, I. V. Dorogan, A. V. Metelitsa, V. I. Minkin, S. A. Kozyukhin, V. V. Emets, V. A. Grindberg, O. N. Chupakhin, G. L. Rusinov, V. N. Charushin, *J. Fluoresc.* **2015**, *25*, 763–775.
[134] S. S. Mati, S. Chall, S. Konar, S. Rakshit, S. C. Bhattacharya, *Sens. Actuators, B* **2014**, *201*, 204–212.
[135] S. Das, A. Sahana, A. Banerjee, S. Lohar, D. A. Safin, M. G. Babashkina, M. Bolte, Y. Garcia, I. Hauli, S. K. Mukhopadhyay, D. Das, *Dalton Trans.* **2013**, *42*, 4757–4763.
[136] B. Das, S. Dey, G. P. Maiti, A. Bhattacharjee, A. Dhara, A. Jana, *New J. Chem.* **2018**, *42*, 9424–9435.
[137] D. Karak, S. Lohar, A. Sahana, S. Guha, A. Banerjee, D. Das, *Anal. Methods* **2012**, *4*, 1906–1908.
[138] Y. Maimaiti, X. Maimaitiyiming, *Fibers Polym.* **2020**, *21*, 7–18.
[139] J. Weng, Q. Mei, Q. Ling, Q. Fan, W. Huang, *Tetrahedron* **2012**, *68*, 3129–3134.
[140] S. Goswami, A. K. Das, S. Maity, *Dalton Trans.* **2013**, *42*, 16259–16263.
[141] L. Luo, P. Wang, Y. Wang, F. Wang, *Sens. Actuators, B* **2018**, *273*, 1640–1647.
[142] M. Kaur, Y.-H. Ahn, K. Choi, M. J. Cho, D. H. Choi, *Org. Biomol. Chem.* **2015**, *13*, 7149–7153.
[143] C. Hadad, S. Achelle, I. López-Solera, J. C. García-Martínez, J. Rodríguez-López, *Dyes Pigm.* **2013**, *97*, 230–237.
[144] S. S. Mati, D. Singharoy, B. Samai, S. Konar, N. Santra, S. Pal, P. Das, S. Murmu, *J. Mol. Struct.* **2019**, *1184*, 102–109.
[145] L. Zhu, X. Yang, X. Luo, B. Hu, W. Huang, *Inorg. Chem. Commun.* **2020**, *114*, 107823.
[146] S. R. Thakur, R. Behura, S. Behura, R. B. Sayala, A. K. Barick, D. S. Ramakrishna, R. J. Jali, *Indian J. Chem.* **2020**, 1809–1813.
[147] A. Boländer, D. Kieser, C. Voss, S. Bauer, C. Schön, S. Burgold, T. Bittner, J. Hölzer, R. Heyny-von Haußen, G. Mall, V. Goetschy, C. Czech, H. Knust, R. Berger, J. Herms, I. Hilger, B. Schmidt, *J. Med. Chem.* **2012**, *55*, 9170–9180.
[148] X. Qiu, C. Xin, W. Qin, Z. Li, D. Zhang, G. Zhang, B. Peng, X. Han, C. Yu, L. Li, W. Huang, *Talanta* **2019**, *199*, 628–633.

[149] X. Xie, M. Li, F. Tang, Y. Li, L. Zhang, X. Jiao, X. Wang, B. Tang, *Anal. Chem.* **2017**, *89*, 3015–3020.
[150] E. V. Verbitskiy, G. L. Rusinov, O. N. Chupakhin, V. N. Charushin, *Dyes Pigm.* **2020**, *180*, 108414.
[151] P. H. Doan, D. R. G. Pitter, A. Kocher, J. N. Wilson, T. Goodson, *J. Am. Chem. Soc.* **2015**, *137*, 9198–9201.
[152] Q. Zhang, X. Tian, Z. Hu, C. Brommesson, J. Wu, H. Zhou, J. Yang, Z. Sun, Y. Tian, K. Uvdal, *Dyes Pigm.* **2016**, *126*, 286–295.
[153] Q. Zhang, R. Guan, X. Tian, L. Luo, H. Zhou, S. Li, J. Wu, Y. Tian, *RSC Adv.* **2017**, *7*, 20068–20075.
[154] D. Zhang, W. Du, B. Peng, Y. Ni, H. Fang, X. Qiu, G. Zhang, Q. Wu, C. Yu, L. Li, W. Huang, *Sens. Actuators, B* **2020**, *323*, 128673.
[155] J. Yang, W. Hu, H. Li, H. Hou, Y. Tu, B. Liu, *Photochem. Photobiol. Sci.* **2018**, *17*, 474–481.
[156] S. Achelle, J. Rodríguez-López, N. Cabon, F. Robin-Le Guen, *RSC Adv.* **2015**, *5*, 107396–107399.
[157] S. Achelle, J. Rodríguez-López, M. Larbani, R. Plaza-Pedroche, F. Robin-le Guen, *Molecules* **2019**, *24*, 1742.
[158] J. Wang, F. Tang, Y. Wang, S. Liu, L. Li, *Adv. Opt. Mater.* **2020**, *8*, 1901571.
[159] G. Hughes, C. Wang, A. S. Batsanov, M. Fern, S. Frank, M. R. Bryce, I. F. Perepichka, A. P. Monkman, B. P. Lyons, *Org. Biomol. Chem.* **2003**, *1*, 3069–3077.
[160] C. C. Wu, Y. T. Lin, H. H. Chiang, T. Y. Cho, C. W. Chen, K. T. Wong, Y. L. Liao, G. H. Lee, S. M. Peng, *Appl. Phys. Lett.* **2002**, *81*, 577–579.
[161] G. Ge, J. He, H. Guo, F. Wang, D. Zou, *J. Organomet. Chem.* **2009**, *694*, 3050–3057.
[162] G. Ge, X. Yu, H. Guo, F. Wang, D. Zou, *Synt. Met.* **2009**, *159*, 1178–1182.
[163] X. Yang, Z. Feng, J. Zhao, J.-S. Dang, B. Liu, K. Zhang, G. Zhou, *ACS Appl. Mater. Interfaces* **2016**, *8*, 33874–33887.
[164] M. Sarma, W.-L. Tsai, W.-K. Lee, Y. Chi, C.-C. Wu, S.-H. Liu, P.-T. Chou, K.-T. Wong, *Chem* **2017**, *3*, 461–476.
[165] W. Zhang, J. Ma, G.-J. Liu, X.-Y. Liu, J. Fan, L.-S. Liao, *J. Mater. Chem. C* **2017**, 9496–9503.
[166] Y.-H. Zhou, J. Xu, Z.-G. Wu, Y.-X. Zheng, *J. Organomet. Chem.* **2017**, *848*, 226–231.
[167] X.-F. Ma, J.-C. Xia, Z.-P. Yan, X.-F. Luo, Z.-G. Wu, Y.-X. Zheng, W.-W. Zhang, *J. Mater. Chem. C* **2019**, *7*, 2570–2576.
[168] H. Ma, D. Liu, J. Li, Y. Mei, D. Li, Y. Ding, W. Wei, *New J. Chem.* **2020**, *44*, 8743–8750.
[169] H.-B. Han, Z.-G. Wu, Y.-X. Zheng, *Inorg. Chem. Front.* **2018**, *5*, 1545–1552.
[170] H.-B. Han, Z.-G. Wu, Z.-P. Yan, Y. Zhao, Y.-X. Zheng, *Dalton Trans.* **2018**, *47*, 16543–16550.
[171] H.-B. Han, Z.-L. Tu, Z.-G. Wu, Y.-X. Zheng, *Dyes and Pigments* **2019**, *160*, 863–871.
[172] H. Y. Shin, S. Jeong, S. H. Kim, J.-I. Hong, *Bull. Korean Chem. Soc.* **2017**, *38*, 830–837.
[173] Q.-L. Xu, X. Liang, L. Jiang, Y. Zhao, Y.-X. Zheng, *Dalton Trans.* **2016**, *45*, 7366–7372.
[174] B. Tong, Q. Mei, R. Tian, M. Yang, Q. Hua, Y. Shi, S. Ye, *RSC Adv.* **2016**, *6*, 34970–34976.
[175] L.-S. Cui, Y. Liu, X.-Y. Liu, Z.-Q. Jiang, L.-S. Liao, *ACS Appl. Mater. Interfaces* **2015**, *7*, 11007–11014.
[176] W. Cheng, L.-D. Wang, Y.-Y. Zhou, Z.-Q. Bian, B.-H. Tong, Z.-W. Liu, S. Wang, *Dyes Pigm.* **2020**, *177*, 108257.

[177] Y.-K. Chen, H.-H. Kuo, D. Luo, Y.-N. Lai, W.-C. Li, C.-H. Chang, D. Escudero, A. K.-Y. Jen, L.-Y. Hsu, Y. Chi, *Chem. Mater.* **2019**, *31*, 6453–6464.
[178] P. Ganesan, W. Hung, J. Tso, C. Ko, T. Wang, P. Chen, H. Hsu, S. Liu, G. Lee, P. Chou, A. K. -Y. Jen, Y. Chi, *Adv. Funct. Mater.* **2019**, *29*, 1900923.
[179] S. F. Wang, Y. Yuan, Y. Wei, W. Chan, L. Fu, B. Su, I. Chen, K. Chou, P. Chen, H. Hsu, C. Ko, W. Hung, C. Lee, P. Chou, Y. Chi, *Adv. Funct. Mater.* **2020**, *30*, 2002173.
[180] M. Z. Shafikov, R. Daniels, P. Pander, F. B. Dias, J. A. G. Williams, V. N. Kozhevnikov, *ACS Appl. Mater. Interfaces* **2019**, *11*, 8182–8193.
[181] M. Z. Shafikov, P. Pander, A. V. Zaytsev, R. Daniels, R. Martinscroft, F. B. Dias, J. A. G. Williams, V. N. Kozhevnikov, *J. Mater. Chem. C* **2021**, *9*, 127–135.
[182] A. Endo, M. Ogasawara, A. Takahashi, D. Yokoyama, Y. Kato, C. Adachi, *Adv. Mater.* **2009**, *21*, 4802–4806.
[183] A. Endo, K. Sato, K. Yoshimura, T. Kai, A. Kawada, H. Miyazaki, C. Adachi, *Appl. Phys. Lett.* **2011**, *98*, 083302.
[184] H. Uoyama, K. Goushi, K. Shizu, H. Nomura, C. Adachi, *Nature* **2012**, *492*, 234–238.
[185] R. Komatsu, H. Sasabe, Y. Seino, K. Nakao, J. Kido, *J. Mater. Chem. C* **2016**, *4*, 2274.
[186] T. H. Ha, E.-H. Cho, C. W. Lee, H. J. Choi, O. Y. Kim, B. D. Chin, *J. Korean Phys. Soc.* **2019**, *74*, 1059–1066.
[187] Q. Zhang, S. Xiang, Z. Huang, S. Sun, S. Ye, X. Lv, W. Liu, R. Guo, L. Wang, *Dyes Pigm.* **2018**, *155*, 51–58.
[188] T. Serevičius, R. Skaisgiris, I. Fiodorova, V. Steckis, J. Dodonova, D. Banevičius, K. Kazlauskas, S. Juršėnas, S. Tumkevičius, *Org. Electron.* **2020**, *82*, 105723.
[189] T. Serevičius, J. Dodonova, R. Skaisgiris, D. Banevičius, K. Kazlauskas, S. Juršėnas, S. Tumkevičius, *J. Mater. Chem. C* **2020**, *8*, 11192–11200.
[190] K. Nakao, H. Sasabe, R. Komatsu, Y. Hayasaka, T. Ohsawa, J. Kido, *Adv. Opt. Mater.* **2017**, *5*, 1600843.
[191] B. Li, Z. Li, T. Hu, Y. Zhang, Y. Wang, Y. Yi, F. Guo, L. Zhao, *J. Mater. Chem. C* **2018**, *6*, 2351–2359.
[192] I. S. Park, J. Lee, T. Yasuda, *J. Mater. Chem. C* **2016**, *4*, 7911–7916.
[193] Q. Zhang, S. Sun, W. Liu, P. Leng, X. Lv, Y. Wang, H. Chen, S. Ye, S. Zhuang, L. Wang, *J. Mater. Chem. C* **2019**, *7*, 9487–9495.
[194] K.-C. Pan, S.-W. Li, Y.-Y. Ho, Y.-J. Shiu, W.-L. Tsai, M. Jiao, W.-K. Lee, C.-C. Wu, C.-L. Chung, T. Chatterjee, Y.-S. Li, K.-T. Wong, H.-C. Hu, C.-C. Chen, M.-T. Lee, *Adv. Funct. Mater.* **2016**, *26*, 7560–7571.
[195] I. S. Park, H. Komiyama, T. Yasuda, *Chem. Sci.* **2017**, *8*, 953–960.
[196] K. Wu, T. Zhang, L. Zhan, C. Zhong, S. Gong, N. Jiang, Z.-H. Lu, C. Yang, *Chem. Eur. J.* **2016**, *22*, 10860–10866.
[197] T. Serevičius, R. Skaisgiris, J. Dodonova, L. Jagintavičius, D. Banevičius, K. Kazlauskas, S. Tumkevičius, S. Juršėnas, *ACS Appl. Mater. Interfaces* **2020**, *12*, 10727–10736.
[198] N. Aizawa, Y.-J. Pu, H. Sasabe, J. Kido, *Org. Electron.* **2012**, *13*, 2235–2242.
[199] C. Cai, S.-J. Su, T. Chiba, H. Sasabe, Y.-J. Pu, K. Nakayama, J. Kido, *Org. Electron.* **2011**, *12*, 843–850.
[200] S.-J. Su, C. Cai, J. Kido, *Chem. Mater.* **2011**, *23*, 274–284.
[201] G. H. Kim, R. Lampande, J. H. Kong, J. M. Lee, J. H. Kwon, J. K. Lee, J. H. Park, *RSC Adv.* **2015**, *5*, 31282–31291.
[202] S.-W. Li, C.-H. Yu, C.-L. Ko, T. Chatterjee, W.-Y. Hung, K.-T. Wong, *ACS Appl. Mater. Interfaces* **2018**, *10*, 12930–12936.
[203] R. Braveenth, H. Jung, K. Kim, B. M. Kim, I.-J. Bae, M. Kim, K. Y. Chai, *Appl. Sci.* **2020**, *10*, 519.

[204] H. Wang, C. Zang, G. Shan, Z. Yu, S. Liu, L. Zhang, W. Xie, H. Zhao, *Adv. Opt. Mater.* **2019**, *7*, 1801718.
[205] S. Jang, S. H. Han, J. Y. Lee, Y. Lee, *Synt. Met.* **2018**, *239*, 43–50.
[206] S. Gabriel, J. Colman, *Ber. Dtsch. Chem. Ges.* **1903**, *36*, 3379–3385.
[207] H. Yamanaka, S. Ogawa, S. Konno, *Chem. Pharm. Bull.* **1980**, *28*, 1526.
[208] G. A. Molander, C. R. Bernardi, *J. Org. Chem.* **2002**, *67*, 8424–8429.
[209] B. Li, R. Tong, R. Zhu, F. Meng, H. Tian, S. Qian, *J. Phys. Chem. B* **2005**, *109*, 10705–10710.
[210] L. Zou, Z. Liu, X. Yan, Y. Liu, Y. Fu, J. Liu, Z. Huang, X. Chen, J. Qin, *Eur. J. Org. Chem.* **2009**, *2009*, 5587–5593.
[211] Y. M. Poronik, V. Hugues, M. Blanchard-Desce, D. T. Gryko, *Chem. - Eur. J.* **2012**, *18*, 9258–9266.
[212] G. Argouarch, R. Veillard, T. Roisnel, A. Amar, H. Meghezzi, A. Boucekkine, V. Hugues, O. Mongin, M. Blanchard-Desce, F. Paul, *Chem. - Eur. J.* **2012**, *18*, 11811–11827.
[213] C. Liu, K.-C. Tang, H. Zhang, H.-A. Pan, J. Hua, B. Li, P.-T. Chou, *J. Phys. Chem. A* **2012**, *116*, 12339–12348.
[214] Y. Wang, S. Yin, J. Liu, L. Yao, G. Wang, D. Liu, B. Jing, L. Cheng, H. Zhong, X. Shi, Q. Fang, S. Qian, *RSC Adv.* **2014**, *4*, 10960–10967.
[215] J. Hu, Y. Li, H. Zhu, S. Qiu, G. He, X. Zhu, A. Xia, *ChemPhysChem* **2015**, *16*, 2357–2365.
[216] R. J. Perner, C.-H. Lee, M. Jiang, Y.-G. Gu, S. DiDomenico, E. K. Bayburt, K. M. Alexander, K. L. Kohlhaas, M. F. Jarvis, E. L. Kowaluk, S. S. Bhagwat, *Bioorg. Med. Chem. Lett.* **2005**, *15*, 2803–2807.
[217] C. Reichardt, *Angew. Chem. Int. Ed. Engl.* **1979**, *18*, 98–110.
[218] F. Kournoutas, I. K. Kalis, M. Fecková, S. Achelle, M. Fakis, *J. Photochem. Photobiol., A* **2020**, *391*, 112398.
[219] F. Terenziani, C. Katan, E. Badaeva, S. Tretiak, M. Blanchard-Desce, *Adv. Mater.* **2008**, *20*, 4641–4678.
[220] A. S. Davydov, *Theory of Molecular Excitons*, Springer US, Boston, MA, **1971**.
[221] E. Ishow, G. Clavier, F. Miomandre, M. Rebarz, G. Buntinx, O. Poizat, *Phys. Chem. Chem. Phys.* **2013**, *15*, 13922–13939.
[222] M. J. Frisch, G. W. Trucks, H. B. Schlegel, G. E. Scuseria, M. A. Robb, J. R. Cheeseman, G. Scalmani, V. Barone, G. A. Petersson, H. Nakatsuji, X. Li, M. Caricato, A. V. Marenich, J. Bloino, B. G. Janesko, R. Gomperts, B. Mennucci, H. P. Hratchian, J. V. Ortiz, A. F. Izmaylov, J. L. Sonnenberg, D. Williams-Young, F. Ding, F. Lipparini, F. Egidi, J. Goings, B. Peng, A. Petrone, T. Henderson, D. Ranasinghe, V. G. Zakrzewski, J. Gao, N. Rega, G. Zheng, W. Liang, M. Hada, M. Ehara, K. Toyota, R. Fukuda, J. Hasegawa, M. Ishida, T. Nakajima, Y. Honda, O. Kitao, H. Nakai, T. Vreven, K. Throssell, J. A. Montgomery Jr., J. E. Peralta, F. Ogliaro, M. J. Bearpark, J. J. Heyd, E. N. Brothers, K. N. Kudin, V. N. Staroverov, T. A. Keith, R. Kobayashi, J. Normand, K. Raghavachari, A. P. Rendell, J. C. Burant, S. S. Iyengar, J. Tomasi, M. Cossi, J. M. Millam, M. Klene, C. Adamo, R. Cammi, J. W. Ochterski, R. L. Martin, K. Morokuma, O. Farkas, J. B. Foresman, D. J. Fox, *Gaussian16 Revision C.01*, Gaussian, Inc., Wallingford CT, **2016**.
[223] K. Seintis, D. Agathangelou, D. Cvejn, N. Almonasy, F. Bureš, V. Giannetas, M. Fakis, *Phys. Chem. Chem. Phys.* **2017**, *19*, 16485–16497.
[224] M. Klikar, I. V. Kityk, D. Kulwas, T. Mikysek, O. Pytela, F. Bureš, *New J. Chem.* **2017**, *41*, 1459–1472.
[225] M. Klikar, K. Seintis, I. Polyzos, O. Pytela, T. Mikysek, N. Almonasy, M. Fakis, F. Bureš, *ChemPhotoChem* **2018**, *2*, 465–474.
[226] C. Adamo, V. Barone, *J. Chem. Phys.* **1999**, *110*, 6158–6170.

[227] C. Xu, W. W. Webb, *J. Opt. Soc. Am. B* **1996**, *13*, 481–491.
[228] D. Cvejn, E. Michail, K. Seintis, M. Klikar, O. Pytela, T. Mikysek, N. Almonasy, M. Ludwig, V. Giannetas, M. Fakis, F. Bureš, *RSC Adv.* **2016**, *6*, 12819–12828.
[229] G. U. Mahoro, J. Fernandez-Cestau, J.-L. Renaud, P. B. Coto, R. D. Costa, S. Gaillard, *Adv. Opt. Mater.* **2020**, *8*, 2000260.
[230] X. Liang, Z.-L. Tu, Y.-X. Zheng, *Chem. - Eur. J.* **2019**, *25*, 5623–5642.
[231] W. Chen, F. Song, *Chin. Chem. Lett.* **2019**, *30*, 1717–1730.
[232] M. Y. Wong, E. Zysman-Colman, *Adv. Mater.* **2017**, *29*, 1605444.
[233] Z. Yang, Z. Mao, Z. Xie, Y. Zhang, S. Liu, J. Zhao, J. Xu, Z. Chi, M. P. Aldred, *Chem. Soc. Rev.* **2017**, *46*, 915–1016.
[234] D. Volz, *J. Photonics Energy* **2016**, *6*, 020901.
[235] B. Wex, B. R. Kaafarani, *J. Mater. Chem. C* **2017**, *5*, 8622–8653.
[236] P. Ledwon, *Org. Electron.* **2019**, *75*, 105422.
[237] H. Tanaka, K. Shizu, H. Miyazaki, C. Adachi, *Chem. Commun.* **2012**, *48*, 11392–11394.
[238] M. Okazaki, Y. Takeda, P. Data, P. Pander, H. Higginbotham, A. P. Monkman, S. Minakata, *Chem. Sci.* **2017**, *8*, 2677–2686.
[239] S. Xiang, R. Guo, Z. Huang, X. Lv, S. Sun, H. Chen, Q. Zhang, L. Wang, *Dyes Pigm.* **2019**, *170*, 107636.
[240] C. Tu, W. Liang, *Org. Electron.* **2018**, *57*, 74–81.
[241] A. Khan, Y.-K. Wang, C.-C. Huang, S. Kumar, M.-K. Fung, Z.-Q. Jiang, L.-S. Liao, *Org. Electron.* **2020**, *77*, 105520.
[242] X.-D. Zhu, C.-C. Peng, F.-C. Kong, S.-Y. Yang, H.-C. Li, S. Kumar, T.-T. Wang, Z.-Q. Jiang, L.-S. Liao, *J. Mater. Chem. C* **2020**, *8*, 8579–8584.
[243] M. Stanoppi, A. Lorbach, *Dalton Trans.* **2018**, *47*, 10394–10398.
[244] L. Gan, Z. Xu, Z. Wang, B. Li, W. Li, X. Cai, K. Liu, Q. Liang, S.-J. Su, *Adv. Funct. Mater.* **2019**, *29*, 1808088.
[245] X. Cao, D. Zhang, S. Zhang, Y. Tao, W. Huang, *J. Mater. Chem. C* **2017**, *5*, 7699–7714.
[246] Y. Chen, J. W. Y. Lam, R. T. K. Kwok, B. Liu, B. Z. Tang, *Mater. Horiz.* **2019**, *6*, 428–433.
[247] J. Luo, Z. Xie, J. W. Y. Lam, L. Cheng, H. Chen, C. Qiu, H. S. Kwok, X. Zhan, Y. Liu, D. Zhu, B. Z. Tang, *Chem. Commun.* **2001**, 1740–1741.
[248] J.-Y. Kim, H.-J. Noh, in-A. Shin, J.-H. Yang, D.-W. Yoon, K.-J. Yoon, *Delayed Fluorescence Compound, and Organic Light Emitting Diode and Display Device Using the Same*, **2016**, EP3020783A1.
[249] X. Cai, Z. Qiao, W. Qiu, S. Su, *Organic Micromolecule Material Based on 2,6-Dimethyl-4-Cyanophenyl Receptor Unit, Preparation and Application*, **2018**, CN108530376A.
[250] J. Tydlitát, M. Fecková, P. le Poul, O. Pytela, M. Klikar, J. Rodríguez-López, F. Robin-le Guen, S. Achelle, *Eur. J. Org. Chem.* **2019**, *2019*, 1921–1930.
[251] F. Y. Kwong, A. Klapars, S. L. Buchwald, *Org. Lett.* **2002**, *4*, 581–584.
[252] F. Bureš, D. Cvejn, K. Melánová, L. Beneš, J. Svoboda, V. Zima, O. Pytela, T. Mikysek, Z. Růžičková, I. V. Kityk, A. Wojciechowski, N. AlZayed, *J. Mater. Chem. C* **2016**, *4*, 468–478.
[253] H.-J. Park, S. H. Han, J. Y. Lee, *Chem. - Asian J.* **2017**, *12*, 2494–2500.
[254] G. Xie, X. Li, D. Chen, Z. Wang, X. Cai, D. Chen, Y. Li, K. Liu, Y. Cao, S.-J. Su, *Adv. Mater.* **2016**, *28*, 181–187.
[255] D. Blakemore, in *Synthetic Methods in Drug Discovery: Volume 1*, The Royal Society Of Chemistry, **2016**, pp. 1–69.
[256] M. Fecková, P. le Poul, F. Robin-le Guen, T. Roisnel, O. Pytela, M. Klikar, F. Bureš, S. Achelle, *J. Org. Chem.* **2018**, *83*, 11712–11726.

[257] M. Taniguchi, J. S. Lindsey, *Photochem. Photobiol.* **2018**, *94*, 290–327.
[258] J. Zhao, F. Dang, Z. Feng, B. Liu, X. Yang, Y. Wu, G. Zhou, Z. Wu, W.-Y. Wong, *Chem. Commun.* **2017**, *53*, 7581–7584.
[259] A. Santoro, A. C. Whitwood, J. A. G. Williams, V. N. Kozhevnikov, D. W. Bruce, *Chem. Mater.* **2009**, *21*, 3871–3882.
[260] J. Zhao, Z. Feng, D. Zhong, X. Yang, Y. Wu, G. Zhou, Z. Wu, *Chem. Mater.* **2018**, *30*, 929–946.
[261] A. C. Cope, R. W. Siekman, *J. Am. Chem. Soc.* **1965**, *87*, 3272–3273.
[262] H. Fukuda, Y. Yamada, D. Hashizume, T. Takayama, M. Watabe, *Appl. Organomet. Chem.* **2009**, *23*, 154–160.
[263] J. Kang, R. Zaen, K.-M. Park, K. H. Lee, J. Y. Lee, Y. Kang, *Cryst. Growth Des.* **2020**, *20*, 6129–6138.
[264] V. Barone, J. Bloino, M. Biczysko, F. Santoro, *J. Chem. Theory Comput.* **2009**, *5*, 540–554.
[265] V. Barone, A. Baiardi, M. Biczysko, J. Bloino, C. Cappelli, F. Lipparini, *Phys. Chem. Chem. Phys.* **2012**, *14*, 12404–12422.
[266] R. Schira, C. Latouche, *Dalton Trans.* **2021**, *50*, 746–753.
[267] G. M. Sheldrick, *Acta Crystallogr. Sect. A* **2015**, *71*, 3–8.
[268] G. M. Sheldrick, *Acta Crystallogr. Sect. C* **2015**, *71*, 3–8.
[269] N. Droseros, K. Seintis, M. Fakis, S. Gardelis, A. G. Nassiopoulou, *J. Lumin.* **2015**, *167*, 333–338.
[270] M. A. Albota, C. Xu, W. W. Webb, *Appl. Opt.* **1998**, *37*, 7352–7356.
[271] M. Thompson, *ArgusLab*, **2004**.
[272] T. Yanai, D. P. Tew, N. C. Handy, *Chem. Phys. Lett.* **2004**, *393*, 51–57.
[273] J. P. Perdew, K. Burke, M. Ernzerhof, *Phys. Rev. Lett.* **1996**, *77*, 3865–3868.
[274] J. P. Perdew, K. Burke, M. Ernzerhof, *Phys. Rev. Lett.* **1997**, *78*, 1396–1396.
[275] Thom. H. Dunning, P. J. Hay, in *Methods of Electronic Structure Theory* (Ed.: H.F. Schaefer), Springer US, Boston, MA, **1977**, pp. 1–27.
[276] P. J. Hay, W. R. Wadt, *J. Chem. Phys.* **1985**, *82*, 270–283.
[277] W. R. Wadt, P. J. Hay, *J. Chem. Phys.* **1985**, *82*, 284–298.
[278] P. J. Hay, W. R. Wadt, *J. Chem. Phys.* **1985**, *82*, 299–310.
[279] M. Cossi, V. Barone, R. Cammi, J. Tomasi, *Chem. Phys. Lett.* **1996**, *255*, 327–335.
[280] V. Barone, M. Cossi, J. Tomasi, *J. Chem. Phys.* **1997**, *107*, 3210–3221.
[281] S. I. Gorelsky, *AOMix: Program for Molecular Orbital Analysis*, York University, Toronto, **1997**.
[282] E. D. Glendening, J. K. Badenhopp, A. E. Reed, J. E. Carpenter, J. A. Bohmann, C. M. Morales, F. Weinhold, *NBO*, Theorethical Chemistry Institute, University Of Wisconsin, Madison, **2013**.
[283] R. Dennington, T. Keith, J. Millam, K. Eppinnett, W. L. Hovell, R. Gilliland, *GaussView*, **2009**.
[284] F. Santoro, R. Improta, A. Lami, J. Bloino, V. Barone, *J. Chem. Phys.* **2007**, *126*, 084509.
[285] F. Santoro, A. Lami, R. Improta, V. Barone, *J. Chem. Phys.* **2007**, *126*, 184102.
[286] F. Santoro, A. Lami, R. Improta, J. Bloino, V. Barone, *J. Chem. Phys.* **2008**, *128*, 224311.
[287] J. Stanek, G. Caravatti, H. G. Capraro, P. Furet, H. Mett, P. Schneider, U. Regenass, *J. Med. Chem.* **1993**, *36*, 46–54.
[288] T. Sakamoto, K. Tanji, S. Niitsuma, T. Ono, H. Yamanaka, *Chem. Pharm. Bull.* **1980**, *28*, 3362–3368.
[289] J.-M. Bégouin, C. Gosmini, *J. Org. Chem.* **2009**, *74*, 3221–3224.

UNIVERSITÉ DE RENNES 1

UNIVERSITY OF PARDUBICE

Titre : Matériaux luminescents hétérocycliques organiques et organométalliques: vers des applications OLEDs

Mots clés : diode électroluminescente organique (OLED), chromophore push-pull, pyrimidine, platine, luminescence

Résumé : Depuis 1987, date à laquelle la première diode électroluminescente organique (OLED) a été préparée par C. W. Tang et S. V. Slyke (Eastman Kodak company), il y a eu un grand intérêt pour le développement de dispositifs d'éclairage à base de matériaux organiques. Dans ce manuscrit, des luminophores organiques et organométalliques portant un hétérocycle pyrimidine en tant que groupement attracteur d'électrons sont discutés. Trois séries avec des caractéristiques structurelles différentes ont été préparées: (i) Une série de 2,4-di (arylvinyl)- et de 2,4,6-tri(arylvinyl)pyrimidines avec des groupes électro-donneurs périphériques identiques ou différents, (ii) Une série de 4-arylvinyl- et de 4,6-di(arylvinyl)pyrimidines portant un groupement phénylacridine torsadé en position 2 du cycle pyrimidine (iii) Des complexes de platine (II) cyclométalé à base de 2-phénylpyrimidine. Les propriétés de photoluminescence de tous les dérivés finaux ont été mesurées. Des relations structure-photoluminescence au sein de chaque série ont été tirées de ces résultats et discutées en détail. Des phénomènes de luminescence intéressants, tels que l'émission accordable par protonation, l'émission induite par l'agrégation, l'émission duale, l'émission à l'état solide ou l'émission de lumière blanche, ont été observés pour certains de ces dérivés.

Title : Organic and organometallic heterocyclic luminescent materials: towards OLED applications

Keywords : organic light-emitting diode (OLED), push-pull chromophore, pyrimidine, platinum, luminescence

Abstract : Since 1987, when the first organic light-emitting diode (OLED) was prepared by C. W. Tang and S. V. Slyke (Eastman Kodak company), there has been a great interest in the development of lighting devices based on organic materials. In this dissertation, organic and organometallic luminophores bearing pyrimidine heterocycle as electron-withdrawing moiety are discussed. Three series with different structural features were prepared: (i) 2,4-di(arylvinyl)- and 2,4,6-tri(arylvinyl)-pyrimidines with identical or different peripheral electron-donating groups, (ii) 4-arylvinyl- and 4,6-di(arylvinyl)pyrimidines with twisted phenylacridan structure in position 2 of pyrimidine ring and (iii) 2 phenylpyrimidine cyclometalated platinum (II) complexes. Photoluminescence properties of all final derivatives were measured. Structure-photoluminescence relationships within each series were drawn from these results and thoroughly discussed. Interesting luminescence phenomena, such as tuneable emission by protonation, aggregation-induced emission, dual emission, solid-state emission or white light emission, were observed for certain derivatives across the series.